

**2016 SUMMER RESEARCH PROGRAM FOR HIGH SCHOOL JUNIORS**

**AT THE**

**UNIVERSITY OF ROCHESTER'S**

**LABORATORY FOR LASER ENERGETICS**

**STUDENT RESEARCH REPORTS**

**PROGRAM DIRECTOR**

**Dr. R. Stephen Craxton**

**February 2018**

**Lab Report 391**

**2016 SUMMER RESEARCH PROGRAM FOR HIGH SCHOOL JUNIORS**

**AT THE**

**UNIVERSITY OF ROCHESTER'S**

**LABORATORY FOR LASER ENERGETICS**

**STUDENT RESEARCH REPORTS**

**PROGRAM DIRECTOR**

**Dr. R. Stephen Craxton**

**LABORATORY FOR LASER ENERGETICS**

University of Rochester

250 East River Road

Rochester, NY 14623-1299

During the summer of 2016, 13 students from Rochester-area high schools participated in the Laboratory for Laser Energetics' Summer High School Research Program. The goal of this program is to excite a group of high school students about careers in the areas of science and technology by exposing them to research in a state-of-the-art environment. Too often, students are exposed to "research" only through classroom laboratories, which have prescribed procedures and predictable results. In LLE's summer program, the students experience many of the trials, tribulations, and rewards of scientific research. By participating in research in a real

environment, the students often become more excited about careers in science and technology. In addition, LLE gains from the contributions of the many highly talented students who are attracted to the program.

The students spent most of their time working on their individual research projects with members of LLE's scientific staff. The projects were related to current research activities at LLE and covered a broad range of areas of interest including laser physics, computational modeling of implosion physics, experimental diagnostic development, experimental modeling and data analysis, physical chemistry, optical design, tritium capture and storage, cryogenic target characterization, and scientific web page development. The students, their high schools, their LLE supervisors, and their project titles are listed in the table. Their written reports are collected in this volume. By working through several iterations of their project reports, incorporating feedback from their supervisors and the Program Director, the students experience most of the steps involved in preparing a scientific paper for publication.

The students attended weekly seminars on technical topics associated with LLE's research. Topics this year included laser physics, fusion, holography, nonlinear optics, atomic force microscopy, optical instruments, and pulsed power. The students also received safety training, learned how to give scientific presentations, and were introduced to LLE's resources, especially the computational facilities.

The program culminated on 24 August with the "High School Student Summer Research Symposium," at which the students presented the results of their research to an audience including parents, teachers, and LLE staff. Each student spoke for approximately ten minutes and answered questions. At the symposium LLE presented its 20th annual William D. Ryan Inspirational Teacher Award. The recipient this year was Mrs. Shayne Watterson, a chemistry

teacher at Penfield High School. This award honors a teacher, nominated by alumni of the LLE program, who has inspired outstanding students in the areas of science, mathematics, and technology. Mrs. Watterson was nominated by Emma Garcia and Felix Weilacher, participants in the 2014 Summer Program.

A total of 353 high school students have participated in the program since it began in 1989. The students this year were selected from approximately 60 applicants. Each applicant submitted an essay describing their interests in science and technology, a copy of their transcript, and a letter of recommendation from a science or math teacher.

In the past, several participants of this program have gone on to become semifinalists (now designated as “scholars”) and finalists in the prestigious Regeneron (formerly Intel) Science Talent Search. This tradition of success continued this year with the selection of Webster Kehoe and Nathan Morse as two of the 300 Regeneron Scholars chosen from over 1700 applicants nationwide. In addition, Grace Lenhard qualified to attend the Intel International Science and Engineering Fair on the basis of her LLE project.

LLE plans to continue this program in future years. The program is strictly for students from Rochester-area high schools who have just completed their junior year. Application information is mailed to schools and placed on the LLE website in early February with an application deadline near the middle of March. For more information about the program, please contact Dr. R. Stephen Craxton at LLE.

This program was supported by the U.S. Department of Energy Office of Inertial Confinement Fusion under Cooperative Agreement No. DE-NA0001944.

Table I: High School Students and Projects—Summer 2016.

| Name               | High School          | Supervisor           | Project Title  |
|--------------------|----------------------|----------------------|--|
| Kyle Bensink       | Victor               | D. W. Jacobs-Perkins | Post-Shot Data Analysis Tools for Cryogenic Target Shots   |
| Lindsay Browning   | Penfield             | R. S. Craxton        | Development of a Standardized Saturn Ring for Proton Backlighting on the National Ignition Facility      |
| James Hu           | Brighton             | R. W. Kidder         | Using Social Media Technologies for Online Scientific Analysis and Collaboration                         |
| Webster Kehoe      | Wilson Magnet        | R. S. Craxton        | Beam Pointing Optimizations for Omega Implosions   |
| Grace Lenhard      | Prattsburgh          | W. T. Shmayda        | Characterizing a Cu/Mn Alloy for Extracting Oxygen from Inert Gas Streams                                |
| Joseph Mastrandrea | Webster Thomas       | W. T. Shmayda        | Measuring Hydrogen Pressure over a Palladium Bed   |
| Nathan Morse       | Allendale Columbia   | M. J. Guardalben     | Frequency Conversion Crystal Designs for Improved Ultraviolet Power Balance on the 60-Beam OMEGA Laser   |
| Sapna Ramesh       | Pittsford Mendon     | K. L. Marshall       | Characterization of the Electrical Properties of Contaminated Dielectric Oils for Pulsed Power Research  |
| Archana Sharma     | Webster Schroeder    | A. Kalb              | Design and Optimization of a Portable Wavefront Measurement System for Short-Coherent-Length Laser Beams |
| Jonah Simpson      | Brighton             | C. Stoeckl           | Validating the Ion Slowing Model in the <i>Geant4</i> Toolkit  |
| Matthew Wang       | Pittsford Sutherland | C. Stoeckl           | Impulse Response Calibration of a Neutron Temporal Diagnostic Using the Multi-Terawatt Laser             |
| Leah Xiao          | Webster Schroeder    | R. S. Craxton        | Simulations of Laser-Driven Magnetized-Liner Inertial Fusion   |
| Joy Zhang          | Penfield             | R. T. Janezic        | Development of a Digital Microscope for the Characterization of Defects in Cryogenic DT-Filled Targets   |

*Post-Shot Data Analysis Tools for Cryogenic Target Shots*

**Kyle Bensink**

Victor Senior High School

Victor, NY

Advisor: Douglas Jacobs-Perkins

**Laboratory for Laser Energetics**

University of Rochester

Rochester, NY

January 2017

## **1. Abstract**

A series of Matlab programs were developed that can systematically parse and analyze data from multiple cryogenic target positioning control and sensor subsystems on OMEGA. The most involved analysis programs were written to monitor the pressure and leak rate of helium exchange gas within the inner shroud, both of which must be relatively stable in order to tightly control target temperature. Many interrelated factors influence the condition of the deuterium-tritium ice layer within the target as well as target position. Most data sources log data at dissimilar rates - for example, high-speed video logging of target position records rapidly and intermittently in contrast to diagnostic equipment on the moving cryostat transfer cart. As a result, programs that incorporate multiple subsystem data sets needed to correlate time logs in order to parse effectively. As more programs are developed, they will be integrated into the post-shot analysis cycle to generate statistical data, and ultimately will allow subsystem “health” to be closely monitored.

## **2. Introduction**

The University of Rochester Laboratory for Laser Energetics (LLE) is pursuing an effort to demonstrate that it is possible to develop 100 GBar internal target pressure during an inertial confinement target implosion. Physicists believe that 100 GBar performance on OMEGA would scale to ignition if repeated at the National Ignition Facility (NIF).<sup>1</sup> One requirement of the 100 GBar effort is consistent target conditions for each shot. The target position accuracy requirements have been tightened from 10  $\mu\text{m}$  to within 5  $\mu\text{m}$  of the target chamber center, and additionally, the temperature of the target must be maintained within  $\pm 5$  mK in order to maintain the quality of the deuterium-tritium (DT) ice layer within the target. A variety of interrelated

factors influence these conditions, most of which are currently not regularly monitored and assessed.

The goal of this work was to start developing programs that can help scientists and engineers determine the sensitivity of target performance to operating variables. Once sensitivities are understood, variables with greatest sensitivity will be the focus of improvement efforts.

### **3. Internal Environment**

Figure 1 schematically depicts the construction of the target and the immediate surrounding environment, which are exaggerated for illustrative purposes. The environment is drawn to scale in Figure 2. The target is a small (860  $\mu\text{m}$  diameter) shell filled with a mixture of DT. Part of this mixture is frozen at 19.5 K and forms an ice layer on the inner surface of the shell, surrounding the remaining gas mixture. By nature, tritium is radioactive and produces heat as it decays; thus, the environment surrounding the target needs to conduct excess heat out of the chamber. The target is surrounded by helium exchange gas at a pressure of about 2 torr, which conducts heat away from the target and toward the walls of the inner shroud.

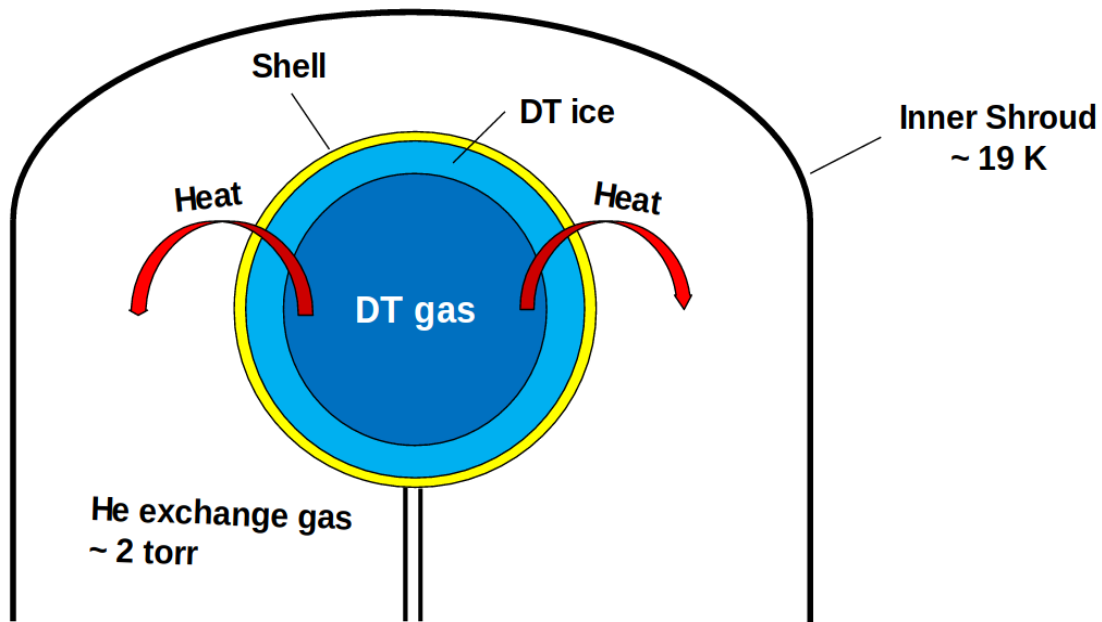


**Figure 1. Schematic (not to scale) of target and surrounding environment.** Heat is conducted away by the inner shroud as tritium in the target decays.

### 3.1 The Shroud

Figure 2 is a computer-aided design (CAD) rendition of the upper section of the moving cryostat transfer cart (MCTC). Shown at top is a gripper mechanism that is attached to a linear induction motor (LIM, not shown). The gripper attaches to the shroud, and the linear motor lifts the shroud clear of the laser beams immediately before the laser fires. The shroud is a 3-part assembly which provides a graduated thermal buffer from the external environment, ensuring that the target remains at a stable temperature. In Figure 2, the shroud is depicted in gray, salmon, and orange portions; the latter of the three is the inner shroud that contains the target.

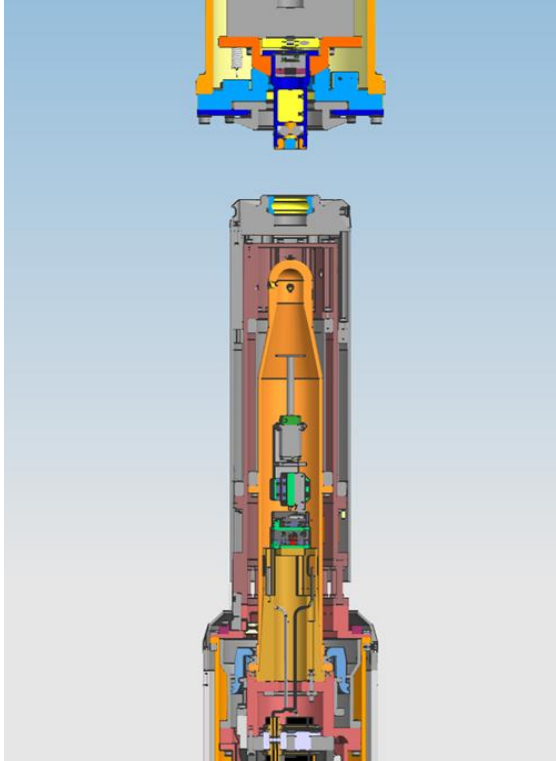


**Figure 2. CAD assembly of the upper section of the moving cryostat transfer cart (MCTC) and gripper.**

The shroud is shown clamped to the moving cryostat as the gripping mechanism is lowered to the shroud.

### **3.2 The Shot Cycle**

For the majority of the shot cycle, the inner shroud is secured by the parting-joint clamp (shown in blue near the bottom of Fig. 2) applying approximately 500 lbs of force. These clamps maintain a gas-tight seal along the bottom of the shroud, limiting the release of He gas. Small amounts leak out, which is expected, and new gas is introduced to the shroud by a “puffer” circuit intended to maintain the pressure of the He.

When the command is given, the LIM lowers and grips the shroud. At this time, the LIM provides a preload of 250 lb and the inner shroud clamps release. This maintains the seal at the bottom of the shroud. About 5 minutes before the shot is taken, this preload is reduced to 90 lb,

maintaining the seal but less so. As a result, the leak rate of exchange gas increases. One goal of this analysis is to determine if the leak rate is abnormally high, indicating that repairs are necessary before a new target is loaded into the cryostat.

Figure 3 depicts the same assembly as Figure 2, but shortly after the Shroud Pull command is given. The LIM has lifted up the shroud partway, and the clamps at the bottom (shown in sky blue) are fully unclamped. In practice, the movement of the LIM is quite swift in fully uncovering the target; this figure illustrates which pieces are removed in the process.

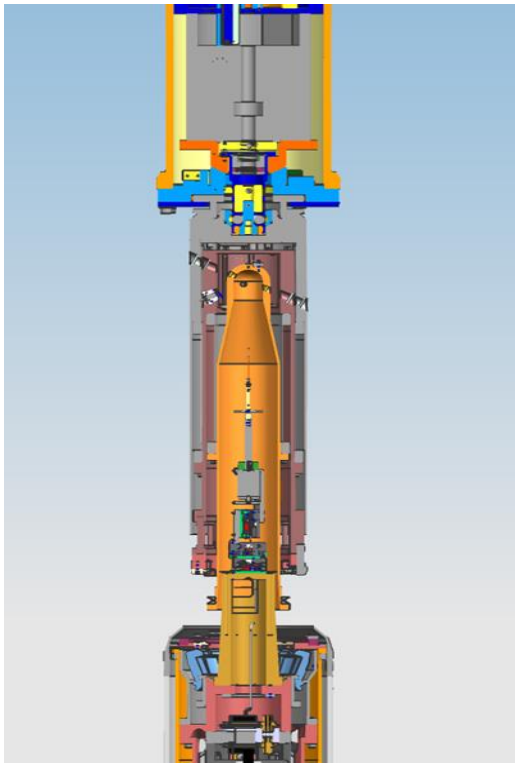


**Figure 3. Linear induction motor (LIM) gripped onto shroud.**  
Clamps are unclamped, and the shroud is being removed.

### **3.3 Data Sources Used**

Every time a test shot is performed on OMEGA, records of all gathered data are stored in LLE's databases. Each data set is saved in the form of a Matlab structure for simple access. Four of the Matlab structures compiled from each shot were used in this work. The MCTC Control Module (MCM) gathers information from the MCTC, providing over 200 unique sets of data. The Linear Motor Control Module (LCM) records from the LIM and contains around 50 data sets. The High-Speed Video (HSV) structure consists of information gathered by the two HSV cameras. Finally, the Cryogenic Shot Command Log (Cryoshot) contains a record of every shot command issued from the control room. These logs consist of three parts: a legend, an array of datetime values, and a substructure which contains the data itself. The MCM and LCM log at a constant rate of 40 Hz, whereas HSV cameras are more variable (see sections 5.1 and 5.2 for more on this difference in logging methods).

### **4. Characterizing Exchange Gas Leak Rate**

Ultimately, the task at hand is to understand the relationship between the load applied to the seal and the leak rate of the He gas, and to determine when an unusual amount of leakage is occurring.

There are four stages of interest when examining the He leak rate: prior to the Shroud Engage; after the shroud is engaged; when the LIM preload is at 250 lb; and when the LIM preload is at 90 lb. Each of these stages has different conditions which characterize its beginning and end. Some of these are data-based, such as the preload reaching a certain value, but others are command-based.

During post-shot data analysis, subroutines parse the requisite sections of data by searching for the starting and ending conditions. The parsed data is then sent through a zero-phase digital filtering function to eliminate unnecessary noise. The filtered data is then searched for local maxima, which correspond to when the puffer circuit introduces new He gas. The distance from maximum to maximum constitutes the period of the gas pressure oscillation, a value which is highly linked to the leak rate itself. For each observed period in the parsed data, the average leak rate is recorded, as well as the maximum and minimum pressure values.

Figure 4 depicts a graph of exchange gas pressure while the LIM preload is at 250 lb (blue) and at 90 lb (yellow). The long, vertical violet line indicates the time at which the command was given to reduce the preload to 90 lb, thus increasing the leak rate. Short multicolored vertical lines in the 250 lb section indicate local maxima identified by the program.

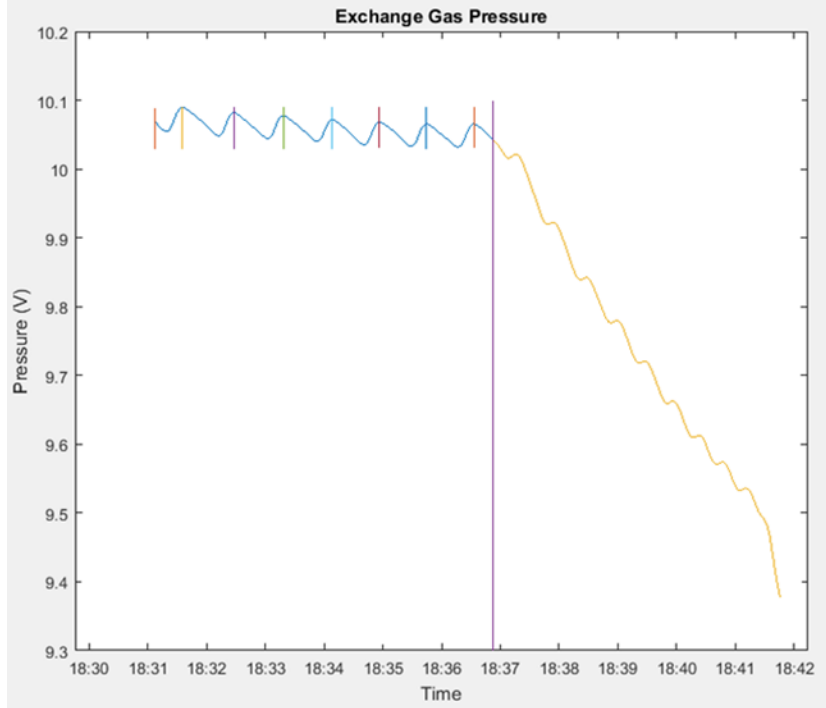


**Figure 4. Exchange Gas Pressure during 250 lb and 90 lb Preloads vs. Time (hours:minutes).**

Vertical lines divide sections which have been parsed by the program. The leak rate changes abruptly when the preload is reduced from 250 to 90 lb. A periodic pressure increase results from the puffer circuit introducing replacement gas. (Note: for this manometer, a reading of 10 V indicates a pressure of 2 torr).

## 5. Determining Target Support Stiffness

The target's position is influenced by a variety of factors, one critical factor being the stiffness of the moving cryostat and its associated support structure. When the force applied by the LIM changes, the structure deflects accordingly. In order to have the target precisely positioned after the shroud is removed and these forces are absent, the structure must be characterized in advance so that its deflection is accurately known. The goal of this program is to correlate HSV data with other data to determine the structure's stiffness, and to accurately

predict target location once the shroud is removed. If the stiffness changes over time, it could also be indicative of needed maintenance.

### 5.1 HSV Cameras

During the shot cycle, the target position is recorded by two HSV cameras. The cameras are positioned nearly orthogonal to each other, so as to accurately determine the target's position in 3-dimensional space. Figure 5 is a graph plotting the target's z-axis position as a function of time. HSV cameras record ensembles of images in ~500 ms bursts at a fixed frame rate between 500-2000 Hz. After each acquisition, analysis is performed and the acquisition/analysis cycle repeats.

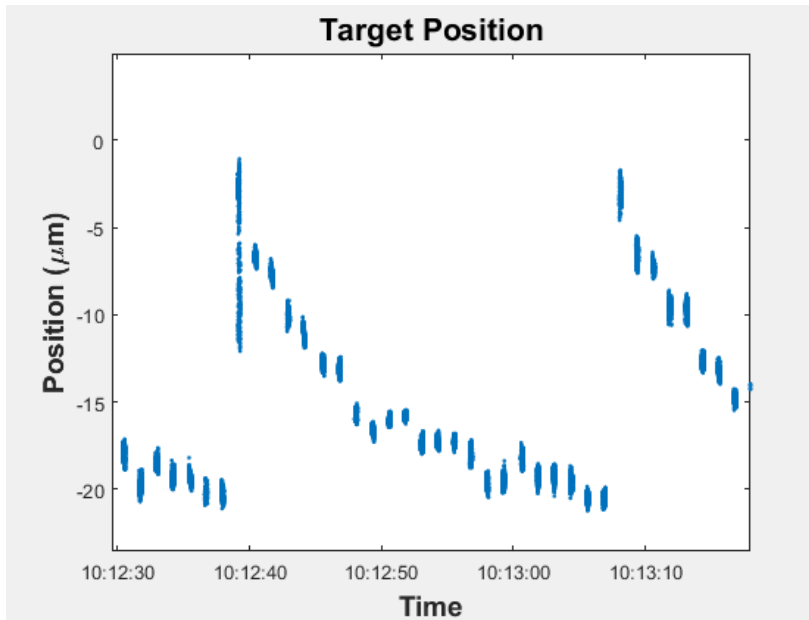


**Figure 5. Target position vs. Time (hours:minutes:seconds).**

High-speed video images are typically recorded as ensembles at 1-2 kHz frame rate for ~500 ms, then analyzed before the next ensemble is acquired. This leads to the data clusters (above), followed by data gaps. This is in contrast to MCM and LCM data that is sampled at regular intervals.

## 5.2 Challenges with Aligning HSV to Other Data

In order to properly correlate HSV data with other sources, the timestamps for both data sets need to be equivalent. Data logged from most sources (MCM, LCM, Cryoshot) have timestamps that come from the same clock; however, HSV cameras operate on a different clock that may or may not be synchronized. Figure 6 shows an example of this time mismatch -- for this data set, the HSV timestamps recorded the target moving about 2 seconds before the LIM changed preload.

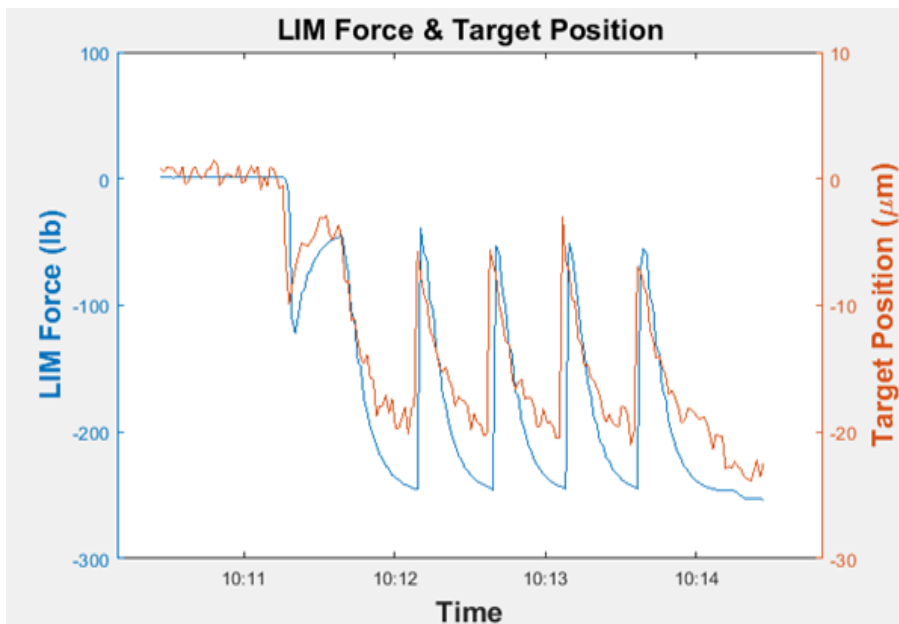


**Figure 6. LIM Force and Target Position vs. Time (hours:minutes).**

The timestamps for LIM Force and Target Position are not aligned; it appears as if the target moves before the LIM.

Correction of this misalignment is a work in progress. Figure 7 shows data for the same shot as Figure 6, but with the time misalignment manually corrected. Ultimately, the program will use a function to find local maxima in both the LIM Force and HSV data sets, and determine

the average mismatch between their time logs. The time log for HSV will then be altered to remedy the mismatch.

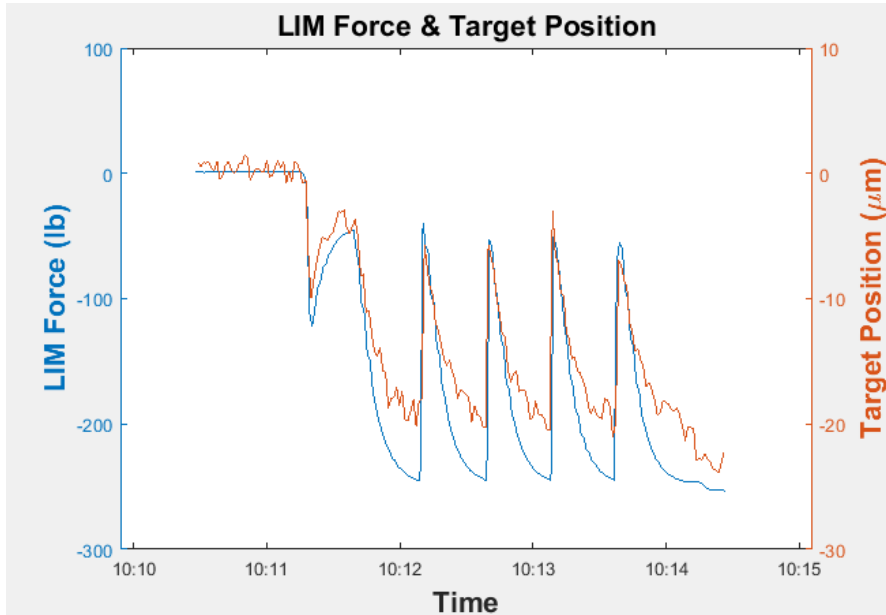


**Figure 7. Corrected version of Figure 6.**

The HSV camera time log has been manually aligned to match with that of the LIM.

### 5.3 Determining Target Support Stiffness

HSV target positioning records are correlated with other data sets to ultimately determine how the target reacts to certain changes in its environment. In the case of correlating target position with LIM Force, the goal is to determine the relationship that occurs between the two variables. Figure 8 is a plot of these variables, along with a least-squares regression line (LSRL) to indicate the linear relationship that exists between the two. The trendline predicts that the target will move by 8  $\mu\text{m}$  once the 90 lb LIM preload is removed from the target support structure; this prediction is consistent with prior observations.<sup>2</sup> This correlation will eventually

be performed on each moving cryostat to determine the difference in target support stiffness from one cart to the next.

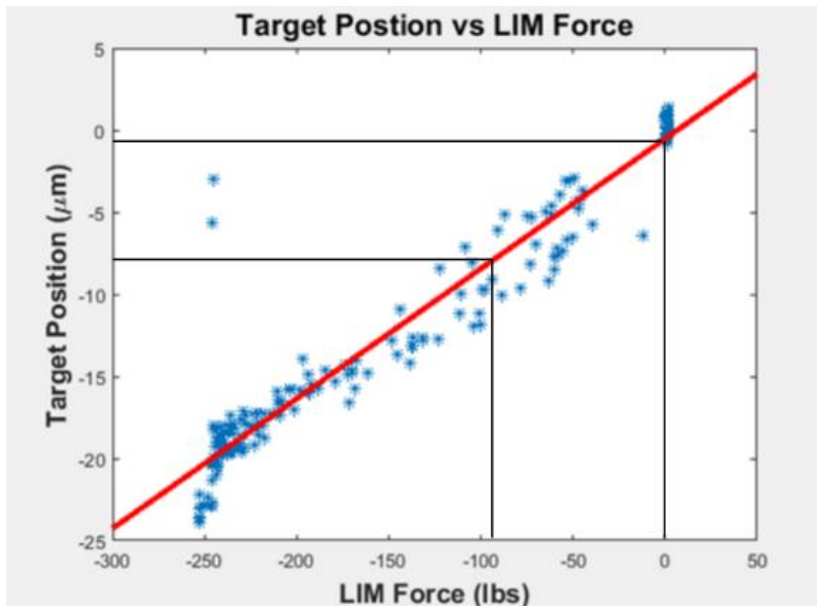


**Figure 8. Target Position vs. LIM Force.**

The least-squares regression line indicates that the target will move by an average of 8 μm once the 90 lb preload is removed from the support structure.

## 6. Stored Data

Once data logged from a shot is entered into LLE's databases, the programs developed from this work parse appropriate data from the logs, analyze the results, and save the output back into the databases. Currently, there is no self-acting part in any of the programs that will alert a user when an abnormal shot occurred; one ultimate goal, however, is to determine acceptable thresholds for each statistic.

## **7. Conclusion**

A series of programs were written to systematically parse and analyze data from multiple cryogenic target positioning control and sensor subsystems on OMEGA. The focus of this work was to determine the target's response to certain operating variables, many of which are not currently monitored. Regular assessment of these conditions can lead to quick diagnoses of problems and more consistent shot performance.

One of the most involved programs examines the leak rate of helium exchange gas within the shroud. For each shot, the program parses sections of data, and analyzes the leak rate under each of four conditions. Other values of interest are recorded as well, such as the period of oscillation and the range of pressure values. These findings are recorded in the database for later reference.

The other main program involves correlating target positioning imaging with the LIM force applied to the shroud, so as to determine the stiffness of the target support structure. Since HSV timestamps are not always aligned with other sources, a sub-function is being written to correct the average error in the HSV timestamp. This allows for stronger correlation between data, and a better prediction of where the target will be located when the shot is fired.

## **8. Acknowledgements**

I thank Dr. Craxton for managing this program, which provides students like myself with an opportunity to work in a research-based environment. I also thank Jeffrey Ulreich for providing the CAD images in this report. Finally, I thank Dr. Jacobs-Perkins for his endless guidance and patience in working with me on this project.

## 9. References

<sup>1</sup> “Implosion Dynamics in Direct-Drive Experiments.” *LLE Review 139*, pp. 158-159 (2014).

<sup>2</sup> S. X. Hu, V. N. Goncharov, P. B. Radha, J. A. Marozas, S. Skupsky, T. R. Boehly, T. C. Sangster, D. D. Meyerhofer, and R. L. McCrory, *Phys. Plasmas 17*, 102706 (2010).

*Development of a Standardized Saturn Ring for Proton Backlighting on the National Ignition  
Facility*

**Lindsay Browning**

Penfield High School

Advisor: Dr. R. S. Craxton

Laboratory for Laser Energetics

University of Rochester

January 2017

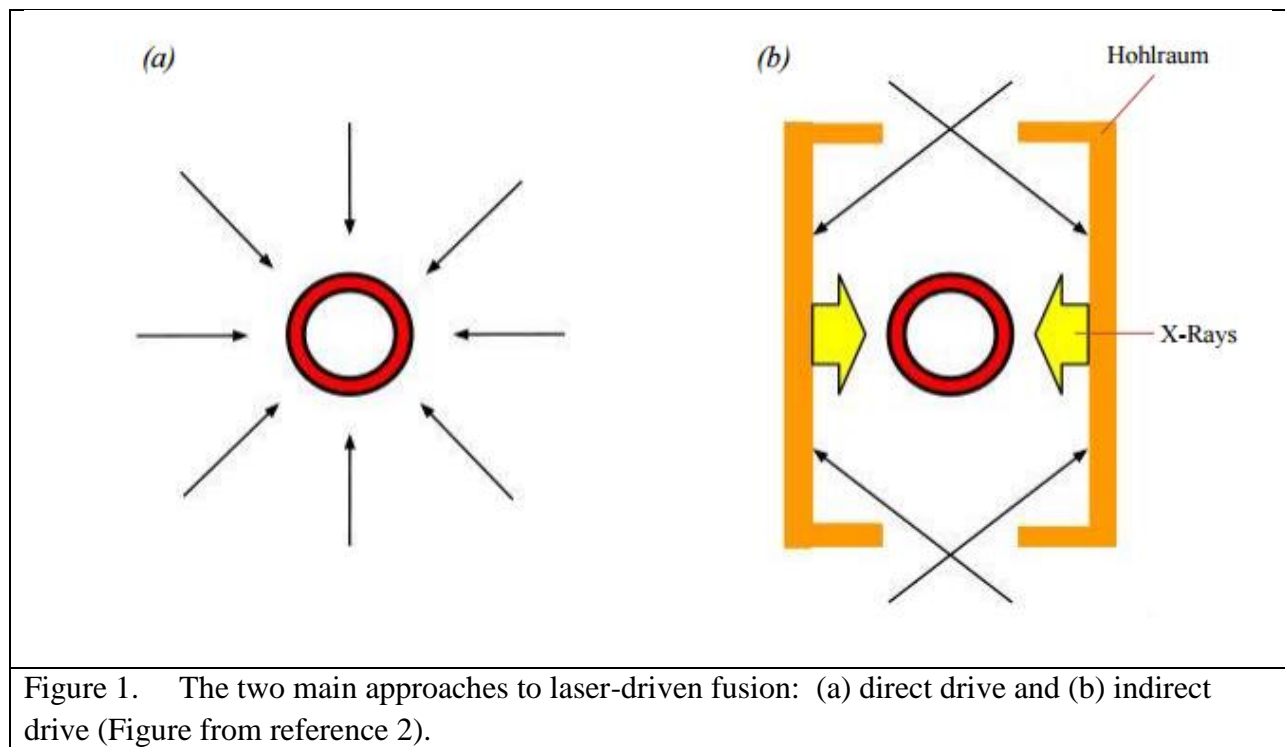
## 1. Abstract

Proton backlighter targets are of interest at the National Ignition Facility (NIF), where a small number of laser beams are pointed at a proton backlighter target filled with  $D^3He$ . The backlighter target produces a burst of protons upon implosion that irradiate a primary target. This provides a variety of diagnostics as the protons are either deflected or absorbed by the primary target while passing through it. Due to the small diameter of backlighter targets, unabsorbed light travels past the target and could potentially damage laser optics on the opposite side of the target chamber. Saturn rings have been proposed to be placed around the targets to minimize the effects of passing light. A Saturn ring has been developed, using the hydrodynamics simulation code SAGE, for a design on the NIF that will fit all backlighter target diameters from 440 to 1100 microns. Adjustments have been made to laser pointings where necessary to maintain a uniform implosion. This will allow for the manufacturing of a standardized Saturn ring that will prevent laser damage for a wide range of proton backlighter targets on the NIF while maintaining implosion uniformity.

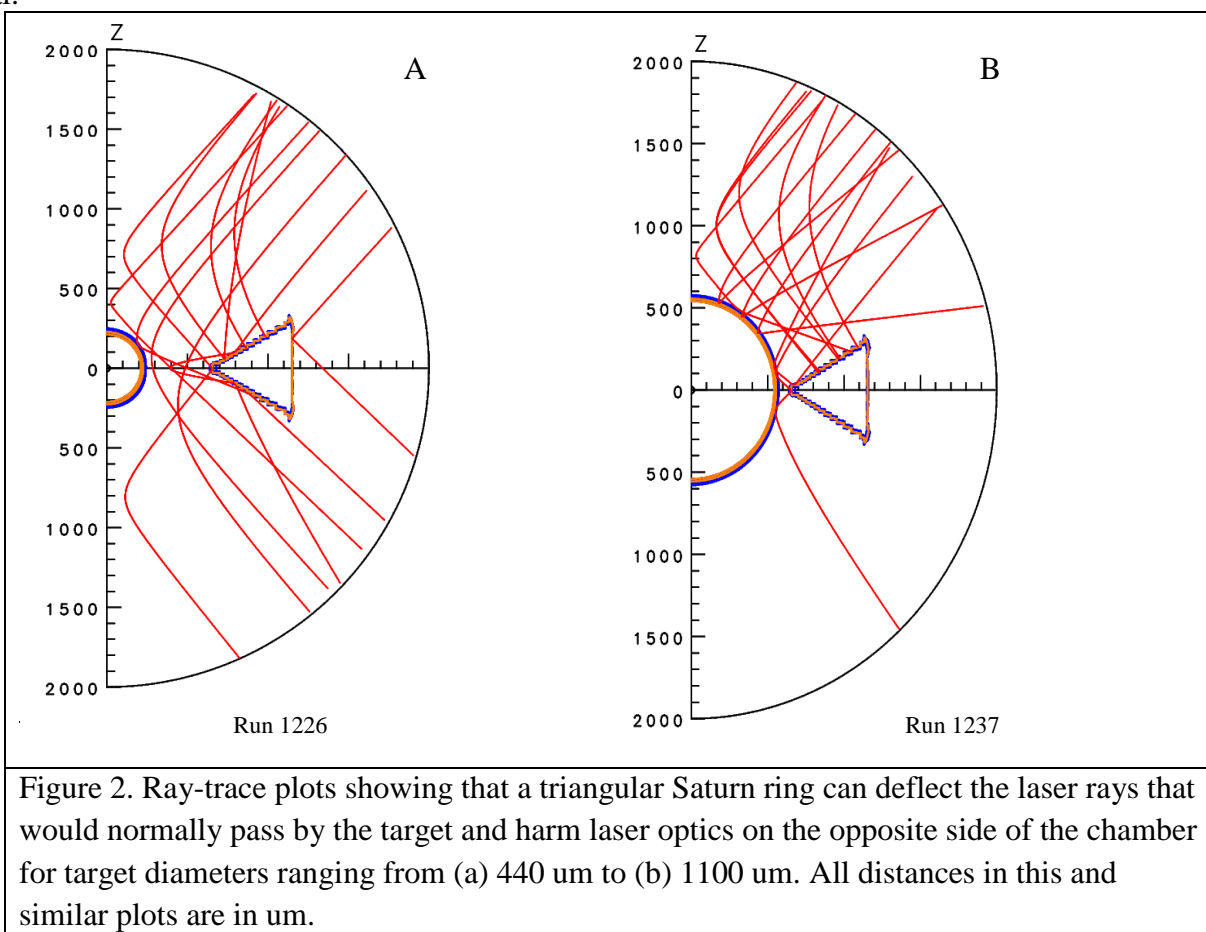
## 2. Introduction

Nuclear fusion holds a promising future as a powerful, safe, and clean energy source. Instead of relying on natural gas or oil, fusion draws on the energy found in hydrogen atoms, specifically the deuterium and tritium isotopes. One method of achieving fusion involves using lasers to irradiate a spherical glass or plastic shell filled with cryogenic deuterium and tritium, as shown in Figure 1(a). As the shell heats and ablates outward, the hydrogen is compressed inward, experiencing a high temperature and density at peak compression. The resulting energy overcomes repulsive forces between the nuclei, and the deuterium and tritium fuse to form a helium nucleus and an energetic neutron. If the density and the radius of the fuel are great

enough, the energy of the helium nucleus will also be redeposited in the fuel. This is known as ignition.<sup>1</sup> Ignition is the first step toward achieving breakeven, where the energy outputted by the fusion reactions exceeds the energy inputted by the laser. The approach shown in Figure 1(a) is known as direct drive, because laser beams are pointed directly at the target and their energy is directly deposited. This method is used at the University of Rochester Laboratory for Laser Energetics. Figure 1(b) depicts indirect drive, where laser beams are shot into the sides of a hohlraum, causing it to emit x rays. These x rays irradiate the target. Indirect drive is used at the National Ignition Facility (NIF). To enable the laser beams to enter the hohlraum, the NIF beams are located at angles 23.5 degrees to 50 degrees from the vertical. The lack of beams near the target's equator makes it difficult for direct drive targets to be imploded on the NIF. However, uniform implosions can be achieved using the NIF laser optics and repointing and defocusing the laser beam.<sup>3</sup>



One important diagnostic technique that can be used to diagnose target implosions and a variety of other laser-target experiments is proton backlighting.<sup>4</sup> In proton backlighting, a small number of laser beams are taken off the primary target and used to irradiate a small spherical shell filled with deuterium and helium-3. Upon implosion, the backlighter target emits protons that pass through the primary target. This allows for a variety of diagnostic possibilities, such as the shape of the primary target implosion and the deflection of protons in the electric and magnetic fields of the primary target. The first proton backlighting design for the NIF was developed by Kong<sup>2</sup> and the first proton backlighting shot on the NIF was reported by Rygg et al.<sup>5</sup>



A significant problem with proton backlighter targets is that many applications require them to have a small size. They are so small that the laser beams are often wider than the target

itself. As a result, portions of the laser beams pass by the target, directly into laser optics on the opposite side of the target chamber. This can cause severe damage to the laser optics due to the extremely high energy of the laser beams. Figure 2a shows a raytrace plot of laser rays (red lines) aimed at a small proton backlighter target, together with a solution to the scattered light problem, which is to place a Saturn ring<sup>6</sup> around the backlighter target. If the triangular ring circling around the target were not present, the laser rays would pass directly past the target without any deflection. Figure 2 is rotationally symmetric about the vertical (z) axis.

In Reference 6, the Saturn ring was proposed to increase the equatorial drive on the NIF for direct-drive targets. Here, however, the primary purpose of the ring is to block or deflect laser rays away from the opposite laser ports in the target chamber. Figure 3 shows a cross section of a target with an elliptical Saturn ring. The design was proposed by Garcia.<sup>7</sup> It consists of a target 440  $\mu\text{m}$  in diameter and a ring with a diameter of 600  $\mu\text{m}$ , with the innermost edge placed 360  $\mu\text{m}$  away from the center of the target. The target is irradiated by four laser quads (one quad contains four beams) from the top at 45 degrees from the z axis and four quads from the bottom at 135 degrees. Garcia also designed a Saturn ring (of larger size) for an 860  $\mu\text{m}$  diameter target. Huang<sup>8</sup> showed that standard targets (i.e., targets without a Saturn ring) with diameter below 1000  $\mu\text{m}$  produce scattered light about the safety level of 60 kJ/sr.

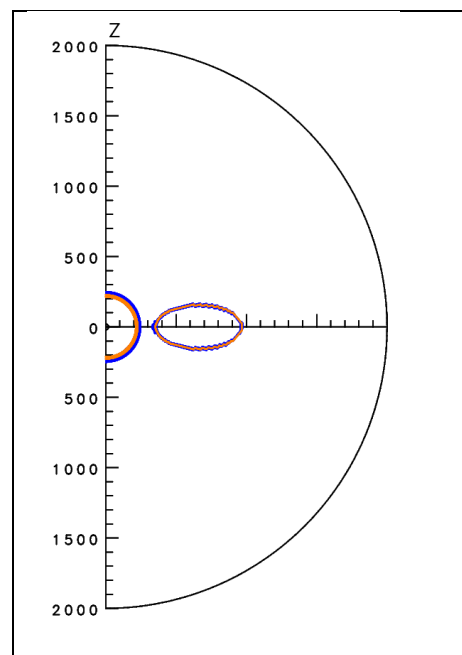


Figure 3. The initial ring set up, proposed by E. Garcia.<sup>7</sup> The ellipse is 600  $\mu\text{m}$  in diameter and 360  $\mu\text{m}$  away from the center of the target, whose radius is 220  $\mu\text{m}$ . (Distances in the figure are shown in  $\mu\text{m}$ .) The figure shows one problem with the ring; it cannot accommodate larger target sizes.

The rings used by Garcia were successful in minimizing the scattered light to 30 kJ/sr, below the safety level. However, the ring for the 440  $\mu\text{m}$  target could not accommodate targets larger than 440  $\mu\text{m}$  because the inner edge of the ring would interfere with the implosion of the target. The purpose of this work was to develop a standardized ring that could fit all sizes of proton backlighter targets while maintaining a uniform target implosion and minimizing scattered light below 60 kJ/sr.

### 3. Designs

A design was developed wherein the cross-sectional shape of the ring was changed from an ellipse to a triangle. The idea was that the ring would better deflect laser beams towards the equator of the target, causing a more uniform implosion. A similar shaped ring was used in Reference 9 for a different application. After experimenting with triangle dimensions and sizes, it was determined that an equilateral triangle with a height of 500  $\mu\text{m}$  placed with its inner tip at a radius of 650  $\mu\text{m}$  was the most effective at blocking scattered light while allowing for uniform implosion. Figure 2 shows that this design blocks a significant number of laser rays for target diameters ranging from 440  $\mu\text{m}$  to 1100  $\mu\text{m}$ .

Figure 2 also demonstrates why the target size is limited from 440  $\mu\text{m}$  to 1100  $\mu\text{m}$ . The target diameter cannot be smaller than 440  $\mu\text{m}$  because otherwise too many laser rays (represented by the red lines) will pass through the gap between the ring and the target. Note that some of the rays in Figure 2a that go through the gap are actually close to straight (minimal deflection) because the figure plots the rays' projections in the  $(r,z)$  plane. Figure 2a shows the largest gap possible between the ring and the target without having too many undeflected laser rays. Figure 4 is the same as Figure 2 except that it is for a later time. Figure 4 shows that the target size cannot exceed 1100  $\mu\text{m}$  in diameter because the Saturn ring will interfere with the

implosion uniformity of the target. Plasma ablated from the ring's inner tip will press into the equator of targets larger than 1100  $\mu\text{m}$ , resulting in an overdriven equator.

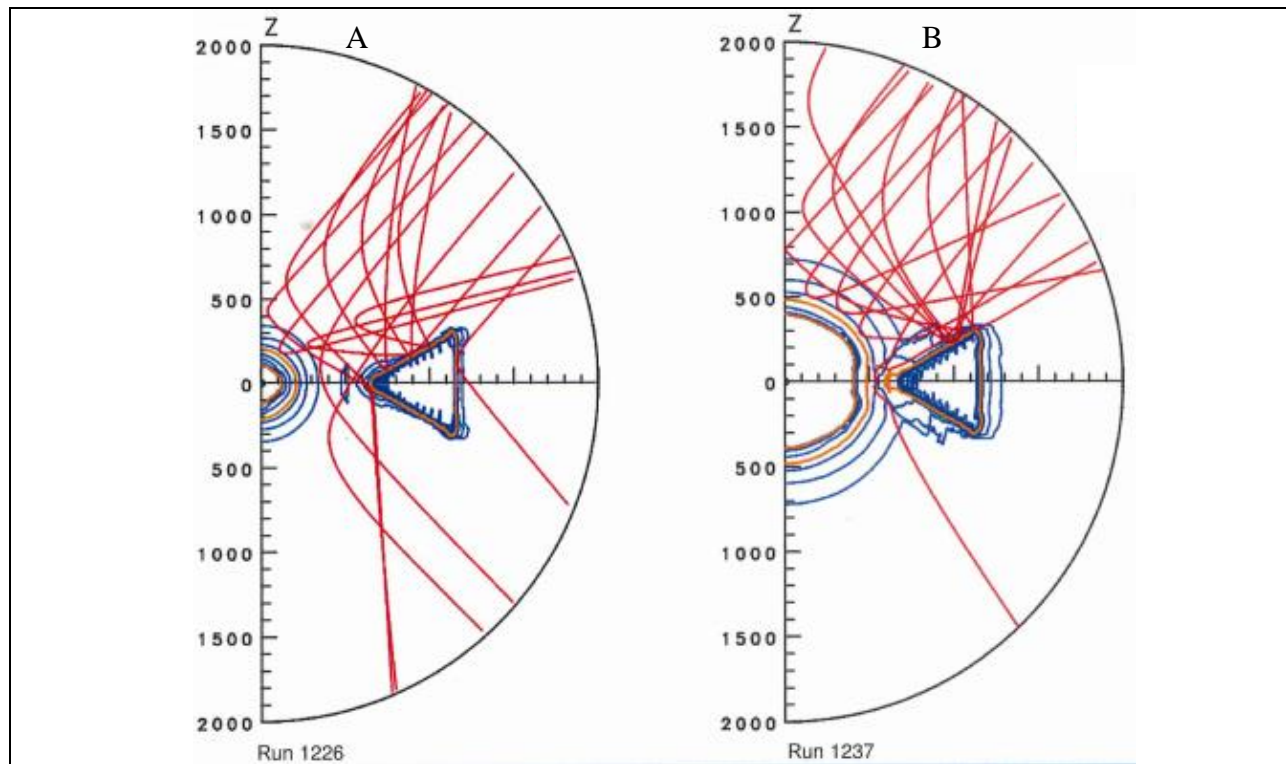


Figure 4. The same two runs as Figure 2, except at a later time in the implosion (500 ps). (a) shows the plasma on the ring expanding to further deflect laser rays. (b) shows how the expanding plasma of the ring interferes with target implosion at the equator. The ring blocks rays from reaching the equator, but plasma from the ring pushes the equator inward, causing a slightly overdriven equator.

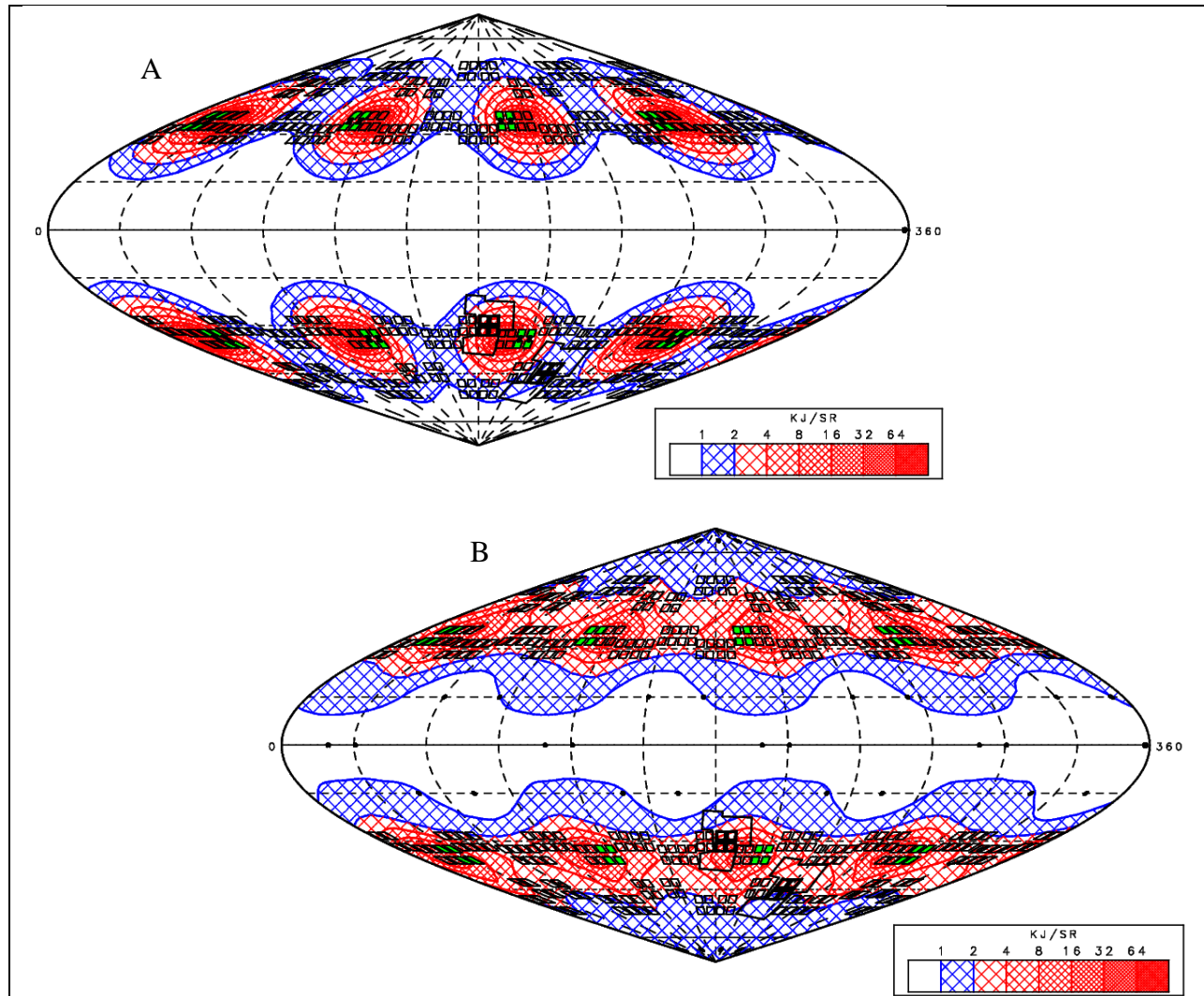


Figure 5. (a) A contour plot of scattered light around the target chamber for a target of 440  $\mu\text{m}$  diameter. The small green squares represent the quads of laser beams that are used to irradiate the target. The adjacent squares indicate the projections of beams (coming from the opposite hemisphere) through the center of the chamber. High concentrations of scattered light focused on these adjacent squares indicate light that has passed through the center of the chamber with minimal deflection.

(b) Same as (a) except that a Saturn ring of inner radius 650  $\mu\text{m}$  was placed around the target. The scattered light is much more dispersed and less focused on the laser quads.

Figure 5 shows contour plots of scattered light around the target chamber for a target of 440  $\mu\text{m}$  diameter. Figure 5a shows the scattered light around the chamber without a Saturn ring. The light is concentrated directly on squares representing laser optics on the opposite side of the

target chamber. The maximum scattered light intensity on the laser optics is higher than 64 kJ/sr, exceeding the safety limit. Figure 5b shows the same 440  $\mu\text{m}$  target, except with a Saturn ring.

The ring has deflected the laser rays, diffusing the scattered light away from the laser optics and reducing the maximum scattered light to less than 32 kJ/sr, well below the safety limit.

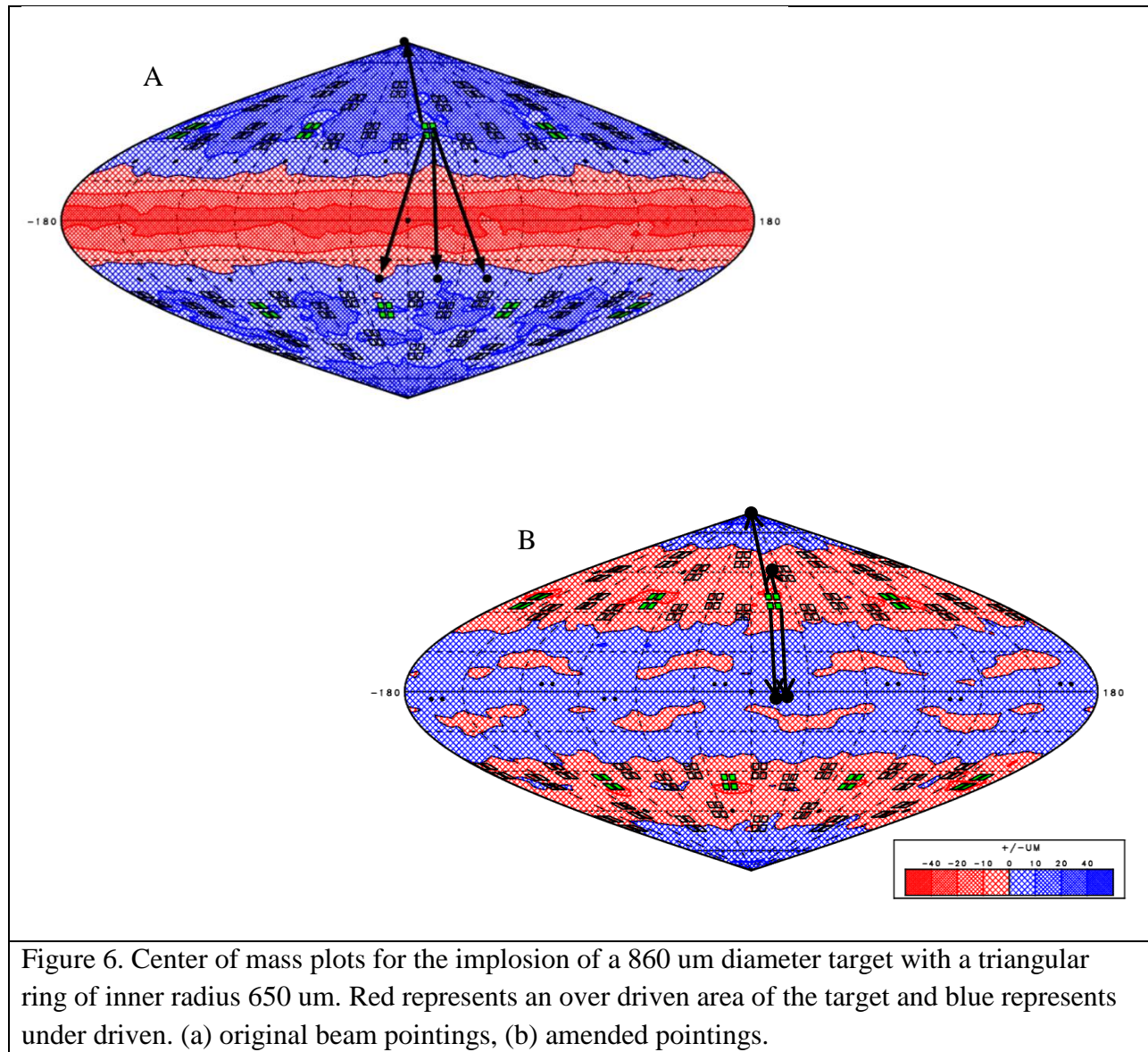
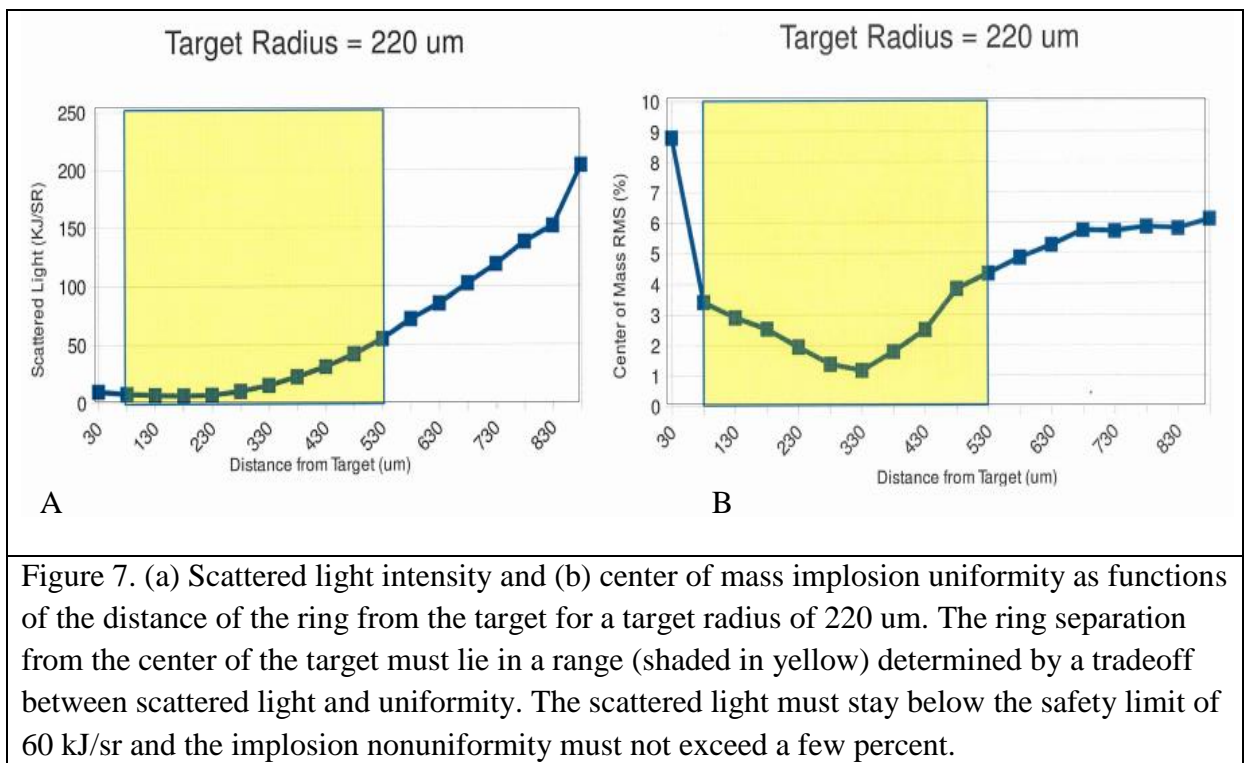


Figure 6. Center of mass plots for the implosion of a 860  $\mu\text{m}$  diameter target with a triangular ring of inner radius 650  $\mu\text{m}$ . Red represents an over driven area of the target and blue represents under driven. (a) original beam pointings, (b) amended pointings.

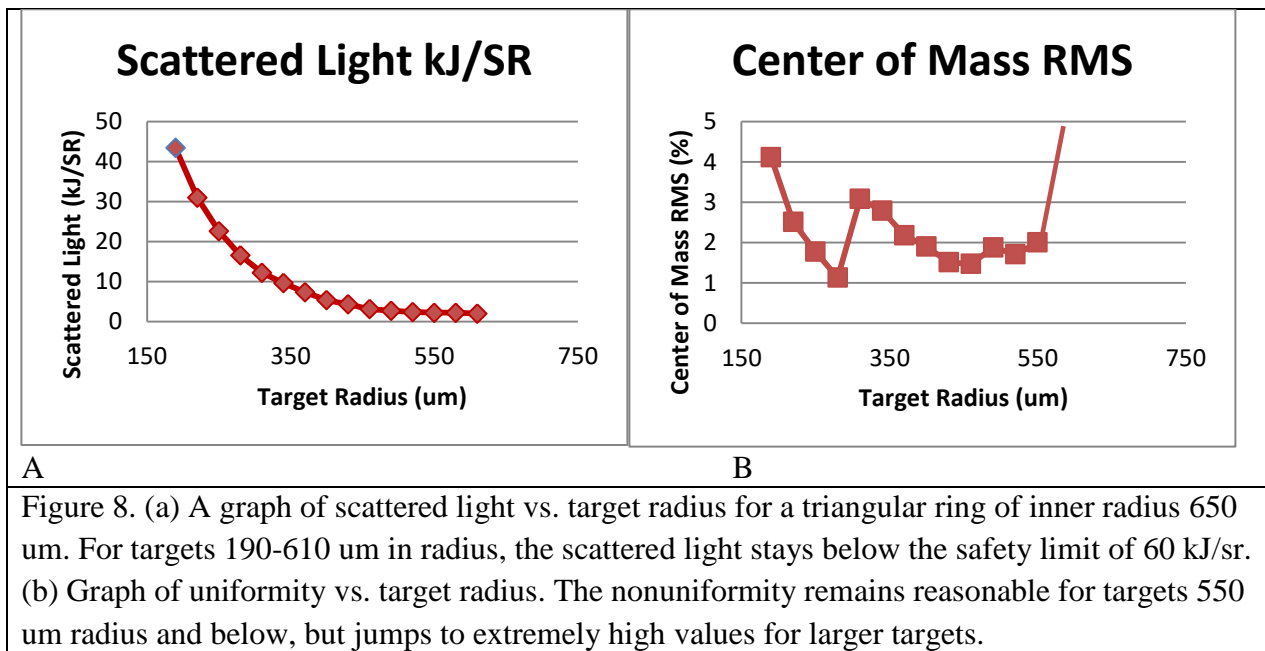
After finding the optimal ring size for targets 440  $\mu\text{m}$  to 1100  $\mu\text{m}$  in diameter, it was noticed that at target diameter 620  $\mu\text{m}$  there was a jump in nonuniformity. The cause of the jump was determined to be laser beam pointings. Targets smaller than 620  $\mu\text{m}$  were so small that laser

pointings made no significant difference to the implosion uniformity, but larger targets were impacted by laser pointings because the beam was no longer wider than the target itself. Figure 6a shows the initial top four laser beam pointings for targets 620  $\mu\text{m}$  and larger. One beam is pointed at the pole and the other three are spread along the 120 degree line. The deep red at the equator shows that the equator is severely overdriven, resulting in a high RMS of 3.12%. Figure 6b shows the corrected laser beam pointings. One beam is pointed at the pole, a second at the 45 degree mark, and two beams at the equator. This resulted in a much more uniform implosion with an RMS of 1.43%.



The distance the ring is from the target has a profound effect on scattered light intensity and target implosion uniformity. Figure 7 shows how ring separation affects both scattered light and implosion uniformity. When the ring is moved very close to the target (Figure 7a), essentially no scattered light is detectable. However, when the ring is moved too far away, it

allows laser rays to pass between the target and ring, resulting in high intensities of scattered light. Regarding implosion uniformity (Figure 7b), moving the ring too close causes it to interfere with target implosion, resulting in high nonuniformity. As the ring moves too far away, it no longer deflects laser rays into the equator of the target. This causes the target equator to be underdriven, and the implosion has a higher nonuniformity. Thus a tradeoff between scattered light and uniformity determines the range of distances the ring can be placed from the target. Figure 7 shows that for a 220  $\mu\text{m}$  radius target, the tradeoff range (shaded in yellow) is between 80  $\mu\text{m}$  and 530  $\mu\text{m}$  from the target. The ranges were determined for targets from 440  $\mu\text{m}$  to 1100  $\mu\text{m}$  in diameter, and compared to find a ring distance that reduced scattered light and maintained uniformity for all target sizes in the range.

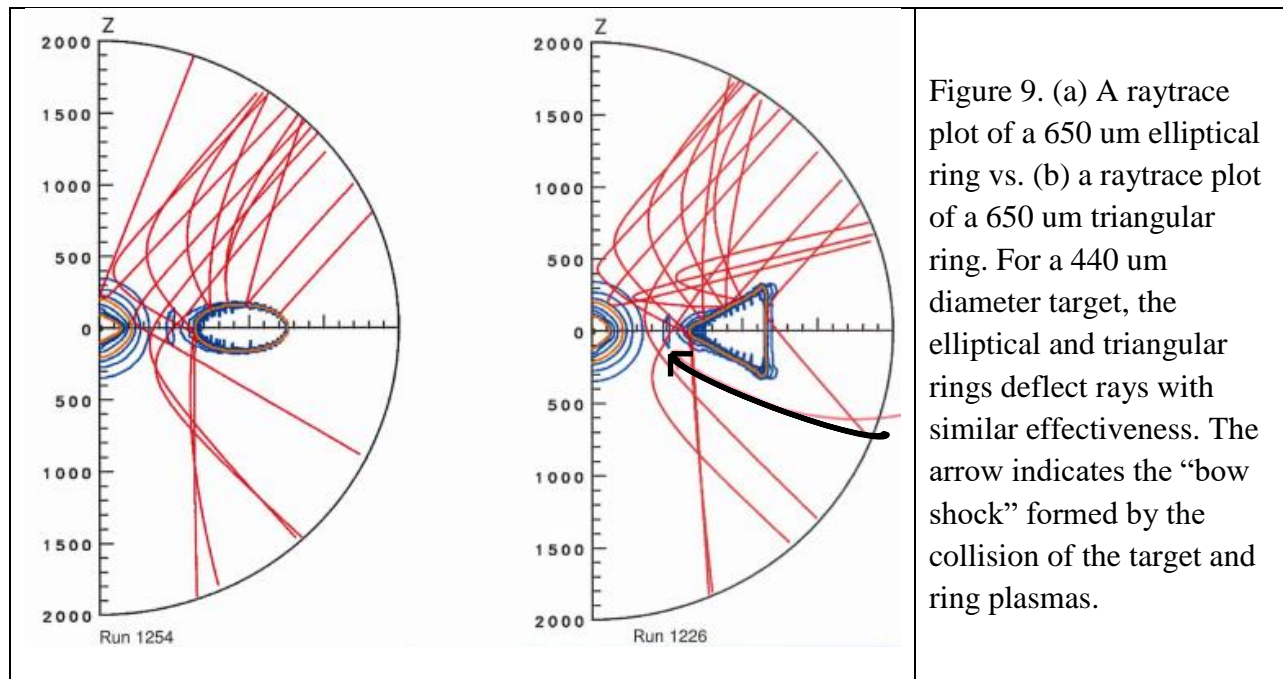


It was determined that an equilateral triangular ring with a diameter of 500  $\mu\text{m}$  and placed 650  $\mu\text{m}$  from the center of the target effectively reduced scattered light to below 30 kJ/sr while maintaining a uniform implosion for all proton backlighter targets sized from 440  $\mu\text{m}$  to 1100  $\mu\text{m}$  in diameter. Figure 8 shows the scattered light and nonuniformity values obtained using this ring

for target diameters 380  $\mu\text{m}$  to 1220  $\mu\text{m}$  at 60  $\mu\text{m}$  increments. At the smallest targets, the scattered light becomes too high for safety, and at the largest targets the nonuniformity becomes too high, for the same reasons that the ring can only lie in a certain range of distances from the target. Thus, there is another tradeoff between scattered light and nonuniformity that determines the range of targets for which the ring is effective.

#### 4. Comparison between Triangular and Elliptical Saturn Rings

Comparisons were made between triangular and elliptical rings. The elliptical ring was set to have a 600  $\mu\text{m}$  diameter in the horizontal direction and 300  $\mu\text{m}$  diameter along the z axis, as in Garcia's design<sup>7</sup>. The inner edge of the ring was set to be 650  $\mu\text{m}$  from the center of the target, as for the triangular ring. Several simulations were run using targets in the range effective with the triangular ring.



Raytrace plots of both the elliptical ring and triangular ring were compared, as shown in Figure 9. The elliptical ring deflected rays less toward the equator of the target, resulting in a

slightly underdriven equator. Otherwise, the 650  $\mu\text{m}$  elliptical ring had similar effectiveness to the triangular ring in minimizing scattered light while maintaining implosion uniformity. An interesting feature seen between the target and the ring in both cases (shown by the arrow in Figure 9) is a contour of higher density known as the “bow shock.” The bow shock is formed by the collision of the expanding plasmas from the target and the ring. The plasmas collide, and produce a higher density area.

It was determined that the elliptical ring had a similar effectiveness to the triangular ring, as shown in Figure 10. The elliptical ring did not block as much scattered light as the triangular ring for target radii above 310  $\mu\text{m}$  radius, but this was irrelevant because the scattered light was still well below the 60  $\text{kJ}/\text{sr}$  limit for all target sizes. This may have occurred because the laser beam pointings used were the optimal pointings for the triangular ring. In addition, the uniformity of implosion was similar to that for the triangular ring.

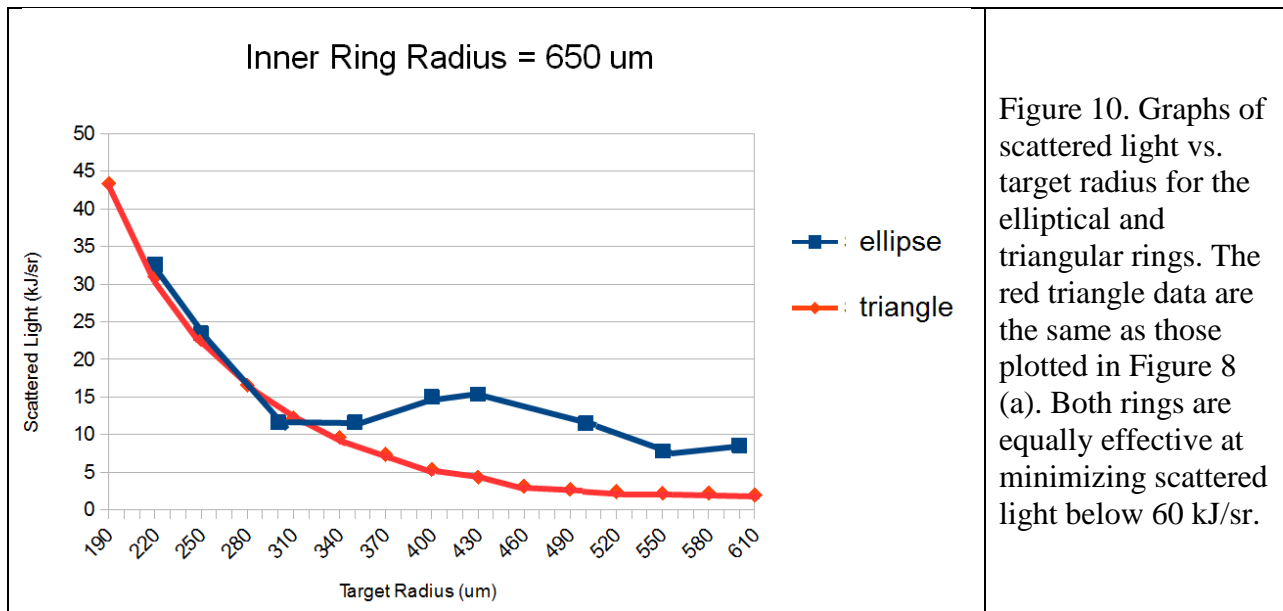


Figure 10. Graphs of scattered light vs. target radius for the elliptical and triangular rings. The red triangle data are the same as those plotted in Figure 8 (a). Both rings are equally effective at minimizing scattered light below 60  $\text{kJ}/\text{sr}$ .

## **5. Conclusion**

The purpose of this work was to develop a standardized ring that could be used with all sizes of proton backlighter targets while maintaining a uniform target implosion and minimizing scattered light below 60 kJ/sr. A triangular ring with an inner radius of 650  $\mu\text{m}$  was developed that effectively worked with all target diameters from 440  $\mu\text{m}$  to 1100  $\mu\text{m}$ . An elliptical ring was found to be equally effective in blocking scattered light and maintaining implosion uniformity for this range of target diameters.

## **6. Acknowledgements**

I would like to thank Dr. Craxton for allowing me to participate in the summer research program. His teaching, feedback and incredible patience were consistent guidance throughout the project process. Thank you as well to Emma Garcia for providing the initial Saturn ring set up and suggestions for proton backlighter targets. Lastly I would like to thank the LLE community for supporting the summer research program and offering us an opportunity like no other.

## 7. References

1. J. Nuckolls, L. Wood, A. Thiessen, and G. Zimmerman, *Laser compression of matter to super-high densities: Thermonuclear CTR applications*, *Nature* 239, 139 (1972).
2. Kong, Y., *Beam-Pointing Optimization for Proton Backlighting on the NIF*, Laboratory for Laser Energetics High School Research Program (2013).
3. Cok, A. M., Craxton, R. S., & McKenty, P. W., *Polar-drive designs for optimizing neutron yields on the National Ignition Facility*, *Physics of Plasmas* 15, 082705 (2008).
4. C.K. Li, F.H. Séguin, J.A. Frenje, J.R. Rygg, and R.D. Petrasso, *Monoenergetic proton backlighter for measuring E and B fields and for radiographing implosions and high-energy density plasmas (invited)*, *Review of Scientific Instruments* 77, 10E725 (2006).
5. Rygg, J.R., Zylstra, A.B., Séguin, F.H., LePape, S., Bachman, B., Craxton, R.S., Garcia, E.M., Kong, Y.Z., Gatu-Johnston, M., Khan, S.F., Lahmann, B.J., McKenty, P.W., Petrasso, R.D., Rinderknecht, H.G., Rosenberg, M.J., Sayre, D.B., and Sio, H.W., *Note: A monoenergetic proton backlighter for the National Ignition Facility*, *Review of Scientific Instruments* 86, 116104 (2015).
6. Craxton, R. S., & Jacobs-Perkins, D. W., *The Saturn Target for Polar Direct Drive on the National Ignition Facility*, *Physical Review Letters* 94, 095002 (2005).
7. E. Garcia, private communication.
8. Huang, P. (2016, March). *Analysis of Unabsorbed Light from Exploding-Pusher Targets Used for Proton Backlighting on the National Ignition Facility*, Laboratory for Laser Energetics High School Research Program (2015).
9. Kinney, J, *Optimization of Backlighter Targets Using a Saturn Ring on the National Ignition Facility*, Laboratory for Laser Energetics High School Research Program (2015).

*Using Social Media Technologies for Online Scientific Analysis and Collaboration*

**James Hu**

Brighton High School

Advisor: Richard Kidder

**Laboratory for Laser Energetics**

University of Rochester

Rochester, New York

June 2017

## 1. Abstract

A web page that demonstrates a concept for a scientific analysis worksheet for data from experiments on the OMEGA and OMEGA EP lasers has been improved upon with the implementation of social features to create a more collaborative scientific environment for users. This interface was created with the purpose of allowing principal investigators and guest users to collaboratively analyze data in web-based live sessions and communicate with their peers through a group chat system. Users are able to connect with other principal investigators, diagnostic specialists and facility managers associated with scientific campaigns of interest. Collaborators are able to view and analyze data or develop code using Python functions. Principal investigators can invite remote colleagues to join a session to conveniently share data. The work demonstrates that features commonly found in social media can be successfully implemented into a scientific environment to promote collaborative analysis of data.

## 2. Introduction

The Laboratory for Laser Energetics has an informatics website that allows principal investigators (PIs) to view their laser shot and diagnostic data online in a user-friendly interface. Additionally, there are web tools available to assist in the analysis of the data, such as the ability to upload analysis routines written in Python to manipulate the data and compare data between multiple diagnostics. However, no features exist on the web page that allow PIs to share their data easily without manually sending the data to another person. **Figure 1** illustrates the current interface for exporting shot data. It provides for downloading only with no collaborative tools. For example, if a PI were to be working with a graduate student, he would need to manually download the shot data after searching for it via an identification number, and then send it to his student through email or another messenger system. The system only provides the raw data and no

analytical tools. Additionally, most OMEGA data is archived with custom formats and metadata that is unfamiliar for many and requires prior knowledge to utilize effectively. The analysis process can be tedious in that it may require going back and forth between the PI and his colleague to resolve problems, which can lead to delays. As such, social features were implemented to the LLE diagnostics web page to allow online collaboration between users directly on the web page in the form of group communication and simultaneous viewing and analysis of data.

## LLE Image Archive Query Results

Select the files to download from the following list. You can use *control-click* to select multiple files or *shift-click* for groups of files. You may also choose to convert any non-SEPIA selected files. Although the conversions are generally reliable, they may not work in all cases. For information on extracting files from

| Shot # | Diagnostic  | Acquired   | Original Data File                                    | <i>Click on button to reorder the list</i> |
|--------|-------------|------------|---|--|
| 82596  | AWG         | 08/23/2016 | /archive/tmp/drivers/psc/s82596fePHX.hdf              |  |
| 82596  | AWG         | 08/23/2016 | /archive/tmp/drivers/psc/s82596feSSD.hdf              |  |
| 82596  | BLOTDR      | 08/23/2016 | /archive/tmp/drivers/OTDR/new_bl_otdr82596.hdf        |  |
| 82596  | C-NEARFIELD | 08/23/2016 | /archive/tmp/NF_Camera/Stage_C/s82596.hdf             |  |
| 82596  | DRVOTDR     | 08/23/2016 | /archive/tmp/drivers/OTDR/new_ssd_otdr82596.hdf       |  |
| 82596  | FF_CAMERA   | 08/23/2016 | /archive/tmp/alignment_cameras/ff/s82596_dl-asp_p.hdf |  |
| 82596  | HED         | 08/23/2016 | /archive/tmp/hed/sn82596n.hdf                         |  |
| 82596  | HED         | 08/23/2016 | /archive/tmp/hed/sn82596s.hdf                         |  |
| 82596  | IR_PULSE2   | 08/23/2016 | /archive/tmp/ir_pulse2/s82596_ssd.hdf                 |  |
| 82596  | IR_PULSE3   | 08/23/2016 | /archive/tmp/ir_pulse3/s82596_dl_psm.hdf              |  |
| 82596  | LDED        | 08/23/2016 | /archive/tmp/drivers/energy_diag/s82596.hdf           |  |
| 82596  | NEARFIELD   | 08/23/2016 | /archive/tmp/NF_Camera/s82596.hdf                     |  |
| 82596  | NF_CAMERA   | 08/23/2016 | /archive/tmp/alignment_cameras/nf/s82596_dl-asp_c.hdf |  |
| 82596  | NF_CAMERA   | 08/23/2016 | /archive/tmp/alignment_cameras/nf/s82596_out_c.hdf    |  |
| 82596  | NF_CAMERA   | 08/23/2016 | /archive/tmp/alignment_cameras/nf/s82596_slara_c.hdf  |  |

Conversions only performed on SEPIA selected files:

- NONE (no format conversion)
- TIFF (Tag Image File Format; no floating point)
- HDF (Hierarchical Data Format)
- FITS (16-bit data only)
- GIF (Graphics Interchange Format; 8-bit, 2D only)

Download

*Figure 1: Current LLE page to download and export shot data*

### 3. Development

The design of the new interface was created following the familiar aesthetics of popular social media sites, such as modeling the chat system after Facebook’s messenger system to create an intuitive design. Although the LLE web site does not necessarily count as “social media,” implementing attributes from successful social media sites can be beneficial in improving the usability of the new technologies.

In order to implement the live web sessions that would allow PIs to work collaboratively, Node.js was chosen as the base platform. Node.js is a cross-platform runtime environment that can process inputs asynchronously on the server side without performance loss, an important aspect of the live web session's functionality. This means that multiple inputs are processed separately from each other, which allows them to be executed simultaneously and processed quickly. With JavaScript being the primary language that the web page was already written in, Node.js allows easy integration into the preexisting code. Node.js has also built up a reputation of being used by some of the biggest technology companies in the world. For instance, social media site LinkedIn is entirely built on Node.js and allows its users to connect and build professional relationships, while serving external applications that can be embedded in LinkedIn's framework. Google also uses Node.js to connect its social media Google+ accounts to its other services, allowing users to share documents and data, join circles to organize users, and even stream media. Most importantly, Google uses Node.js to allow the simultaneous editing of files seamlessly by users on their Google Docs, Sheets, and Slides platforms.

## 4. Interface Capabilities

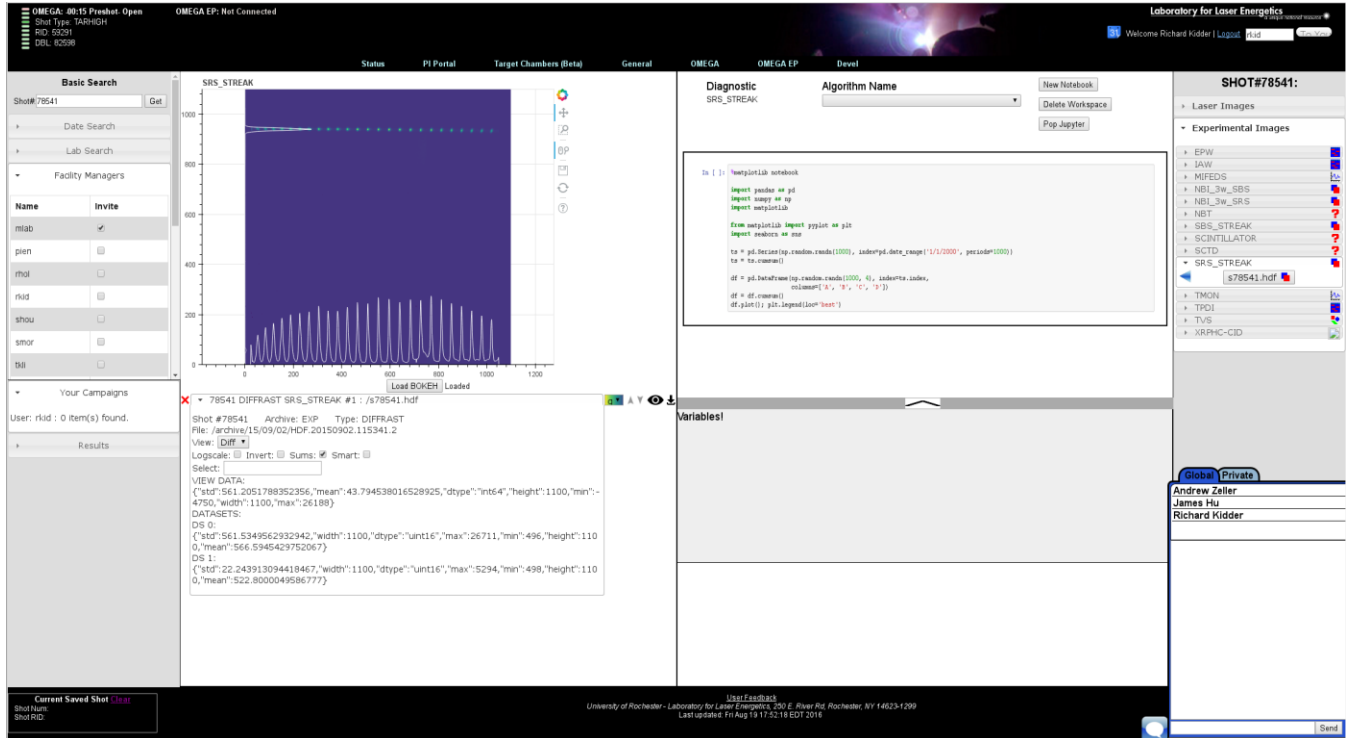


*Figure 2: Example of the diagnostics web page in use*

At LLE, Node.js was used to develop ways to enable users to interact on the informatics website and specifically on the diagnostics page. The web-based live sessions on the diagnostics page will not only allow collaborators to be able to simultaneously view the data, but also allow users to simultaneously write Python code in the embedded Jupyter notebook, seen in the upper right box in **Figure 2**, similar to how Google Docs functions. Furthermore, users will be able to upload their code routines to the web page so that their code will be saved onto their account on the server and no longer need to be transferred locally.

A new interface was added to display online users, who can be invited to another user's live session with a simple click. If they are online, denoted by whether or not the circle next to their user ID is green, they will receive an invitation to join the session and have the option of accepting or declining. There is a list of facility support personnel who are not directly associated

with any specific diagnostic, but are there for general assistance regarding any of the diagnostics, seen in **Figure 3**.



| Name   |   | Invite                   |
|--------|---|--------------------------|
| mlab   | ● | <input type="checkbox"/> |
| pien   | ● | <input type="checkbox"/> |
| rhol   | ● | <input type="checkbox"/> |
| rkid   | ● | <input type="checkbox"/> |
| shou   | ● | <input type="checkbox"/> |
| smor   | ● | <input type="checkbox"/> |
| tkli   | ● | <input type="checkbox"/> |
| zuegel | ● | <input type="checkbox"/> |
| ehil   | ● | <input type="checkbox"/> |
| jkwi   | ● | <input type="checkbox"/> |

Your Campaigns

Results

*Figure 3: List of facility support staff who are always displayed under the tab “Facility Managers”*

When a shot is looked up by its identification number, it will display two tabs, one for laser images and one for experimental images. Within each tab there are diagnostics, each of which has its own sets of data. For each diagnostic, a list of staff members associated with the diagnostic will appear when the arrow is clicked on, and they too can be invited by simply checking the box under the “Invite” column, illustrated in **Figure 4**. This allows the staff list to be organized in a logical manner, as users will most likely want to collaborate with internal users who are associated with

the specified shot. However, if internal users want to collaborate with external users, meaning personnel not affiliated with LLE, the process is different.

|             |                                  |                                     | SHOT#23826:   |
|-------------|----------------------------------|-------------------------------------|---|
| <b>Name</b> | <b>Position</b>                  | <b>Invite</b>                       | ▶ Laser Images  |
| asor ●      | Instrument Specialist Technician | <input checked="" type="checkbox"/> | ▼ Experimental Images   |
| cmil ●      | Instrument Specialist            | <input type="checkbox"/>            | ▶ EMPMON           |
| pnil ●      | Diagnostic PI                    | <input type="checkbox"/>            | ▼ PJX              |
| uhxr ●      | Diagnostic PI                    | <input type="checkbox"/>            | ▶ s23826_pjx2.hdf  |
|             |                                  |                                     | ▶ TMON             |
|             |                                  |                                     | ▶ TVS              |

*Figure 4: Example of a list of personnel associated with a diagnostic*

Previously, colleagues who are not in the LLE system could not use the web page at all because they simply did not have access. This was resolved by allowing internal users to invite external guest users to view their live session temporarily. In order for external users to join a live session, an internal user must give the external users a randomly generated link that will expire after a set duration. It is important to maintain a high level of security when allowing external users to collaborate, as there is confidential data that should not be seen by unwanted personnel. When an external user joins, he will be set as a guest by default and will have restricted access to the features of the web page, such as not being able to change the diagnostic, as seen in **Figure 5**. On the other hand, the web page for an internal user is seen in **Figure 6**, where he has full access to all the shot data. This is an important security feature, as only the internal user should have control over what data is being shown in order to provide another level of security.

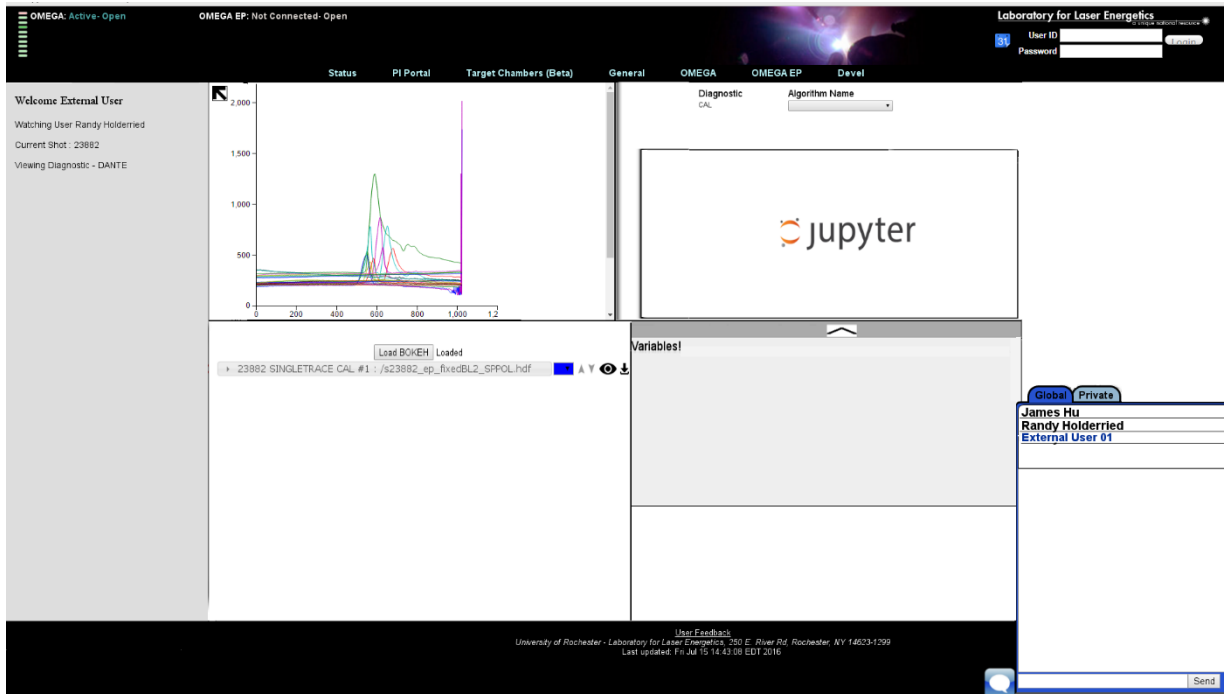


*Figure 5: Diagnostics page for an external user, who has restricted access to the features of the web page*

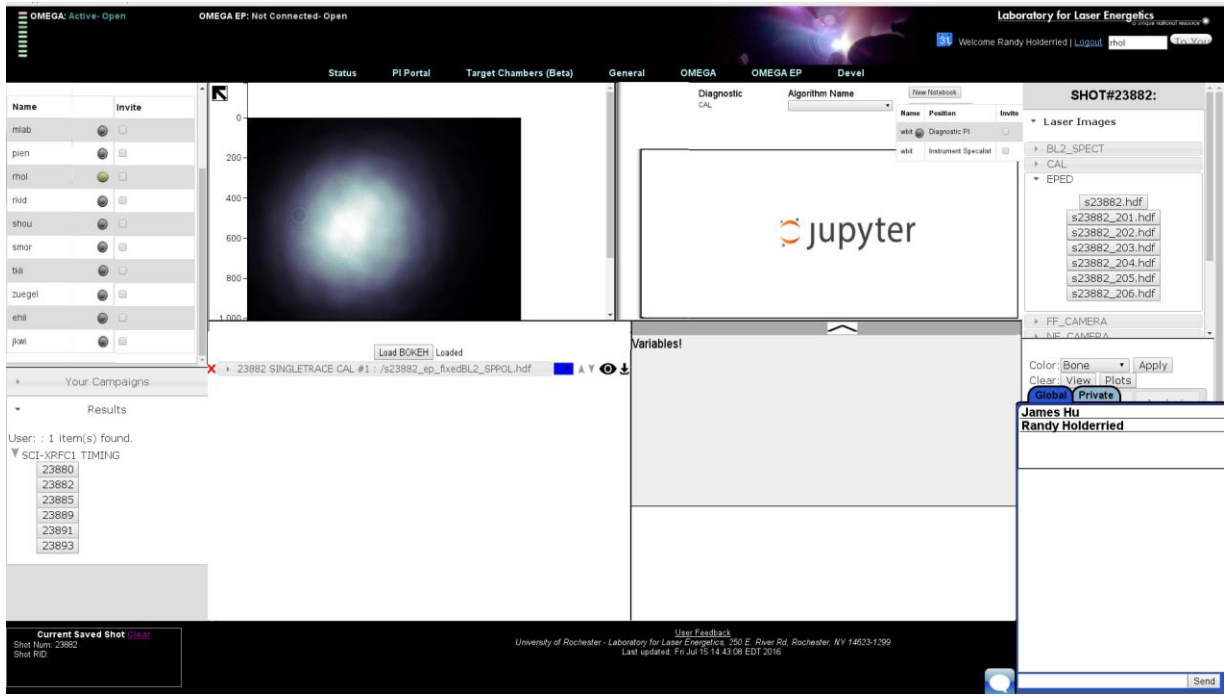


*Figure 6: Diagnostics page for an internal user, who has complete access to all shot data and web features*

Formerly there was only one chat, which meant that anybody online could see what was being typed, which would not be ideal for a live collaboration. As such, the chat system was revamped to allow users of a particular live session to communicate in a group chat, but to also allow private messages between individual online users. A messaging system is an important piece of any collaborative tool, and, using the chat system, users can see when others are available and can communicate when reviewing data. Although the chat system is quite simple, seen in **Figure 7** which displays both the private and group (global) chat, updates will be made to improve the usability and clarity of the chat.

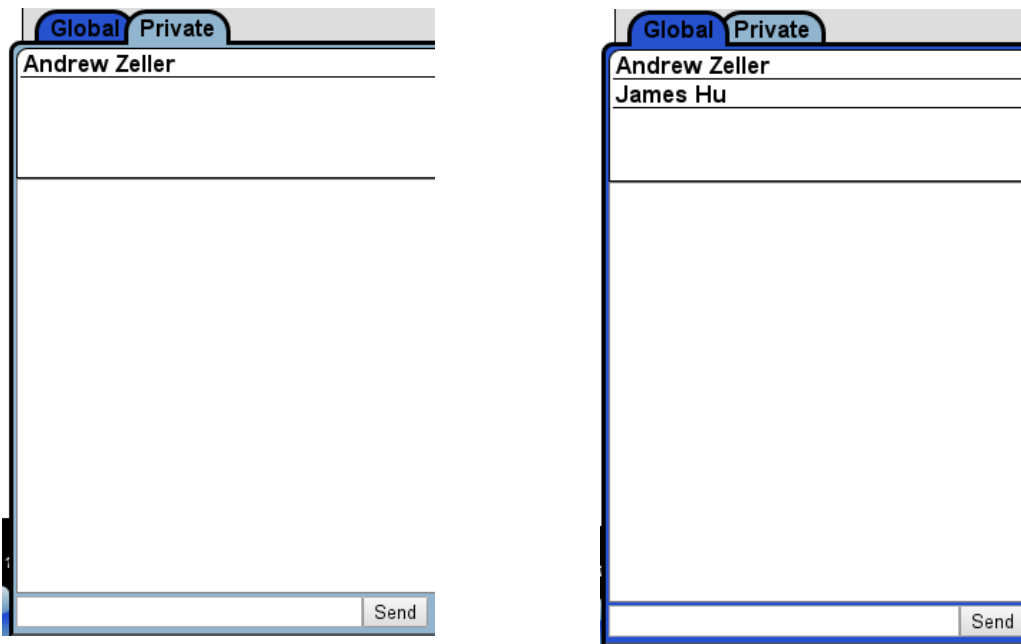


*Figure 7: Chat system*

## 6. Conclusion

Live web-based sessions with a private chat system have been implemented to help PIs with their collaborative endeavors in analyzing diagnostic data. Accessibility to shot data for guest users has been added while maintaining an adequate level of security. The ability for internal users to collaborate with their external colleagues directly on the web page is beneficial to PIs as they

no longer have to go through a longer and more difficult process to analyze data collectively. The features added demonstrate the practicality of social features and their advantageous role in a scientific environment. Social technologies can be implemented into a scientific environment to promote collaborative analysis of data.

## **7. Acknowledgements**

I would not have been able to accomplish this research without the help of my advisor Richard Kidder, who patiently guided me along the entire process and was responsive whenever I required assistance. I would also like to thank Andrew Zeller, Randy Holderried, Tyler Copenbarger, and Liam Smith for explaining the current framework of the web page to me and helping me with any coding issues. Finally, I would like to thank Dr. Craxton for his hard work in organizing the high school research program, as none of this would have been possible without him.

*Beam Pointing Optimizations for Omega Implosions*

**Webster Kehoe**

Joseph C. Wilson Magnet High School

Rochester, New York

Advisor: Dr. R. S. Craxton

**Laboratory for Laser Energetics**

University of Rochester

Rochester, New York

October 2016

## 1. Abstract

One essential requirement for successful laser driven fusion is target uniformity during compression. To ensure high uniformity, the OMEGA laser uses 60 beams aimed at the target in a specific geometric pattern, a truncated icosahedron. However, if some beams either lose functionality or are diverted for use with diagnostics, the target uniformity is severely decreased. To remedy this issue other beams can be repointed to compensate for those that are missing. In one experiment, six beams were aimed towards a secondary target, leaving only 54 beams to drive the implosion. As a result, the root-mean-square (RMS) nonuniformity increased from 0.40% for the perfect configuration with all 60 beams, to 10.33%. Using the hydrodynamics simulation code SAGE, the beam pointings of the remaining 54 beams were manually optimized to maximize uniformity, reducing the RMS to 0.67%. Since this method of optimization is very time intensive, an effort was made to explore whether it was possible to find an acceptable configuration in a much shorter amount of time given any combination of missing beams. An algorithm was created to find the optimal configuration given any single missing beam. This algorithm produced an RMS of 0.54%, which was equal to that of the non-algorithmic optimization. The algorithm was extended to the case of multiple missing beams, and applied to the case of six missing beams. With an RMS of 0.79%, the algorithm gave results very close to the manual optimization. This could also have implications for a fusion reactor, by enabling it to automatically repoint beams if some beams go out of service or need maintenance.

## 2. Introduction

Nuclear fusion has significant potential for a variety of reasons. It is safe, clean, and perhaps most important, it is fully renewable, as it relies on hydrogen, the most abundant element in the universe. One method of achieving nuclear fusion is direct drive inertial confinement fusion.<sup>1,2</sup> In inertial confinement fusion, laser beams are used to compress and heat a small capsule filled with fusion fuel, as shown in Fig. 1. The capsule typically consists of a thin plastic shell surrounding a shell of frozen deuterium and tritium, two isotopes of hydrogen. As the laser irradiates the capsule's outer shell it ablates material from the shell. The opposite reaction of this ablation is a force that pushes inwards, toward the center of the target. The ablation process is akin to creating a rocket, except that the rocket is spherical, with all sides of it pushing towards the center. This force creates an implosion, as the capsule collapses inward. This collapse creates extreme conditions. To produce a sufficient number of fusion reactions, temperatures must reach approximately 100 million degrees Celsius and the deuterium and tritium must have a density over 200 grams per cubic centimeter. These extreme conditions allow the two reacting nuclei to overcome their natural repulsion forces and combine to form a helium atom and a neutron, whose kinetic energy is the form of the energy being released.

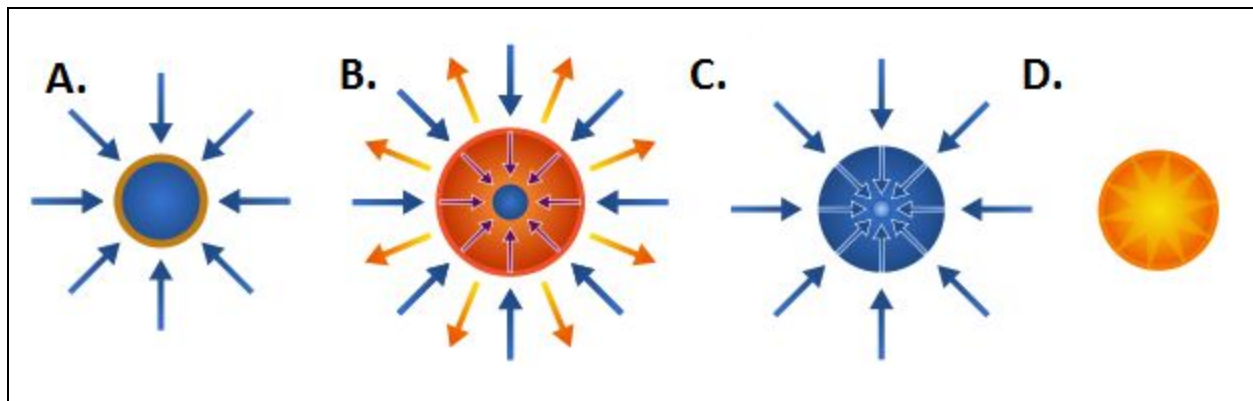
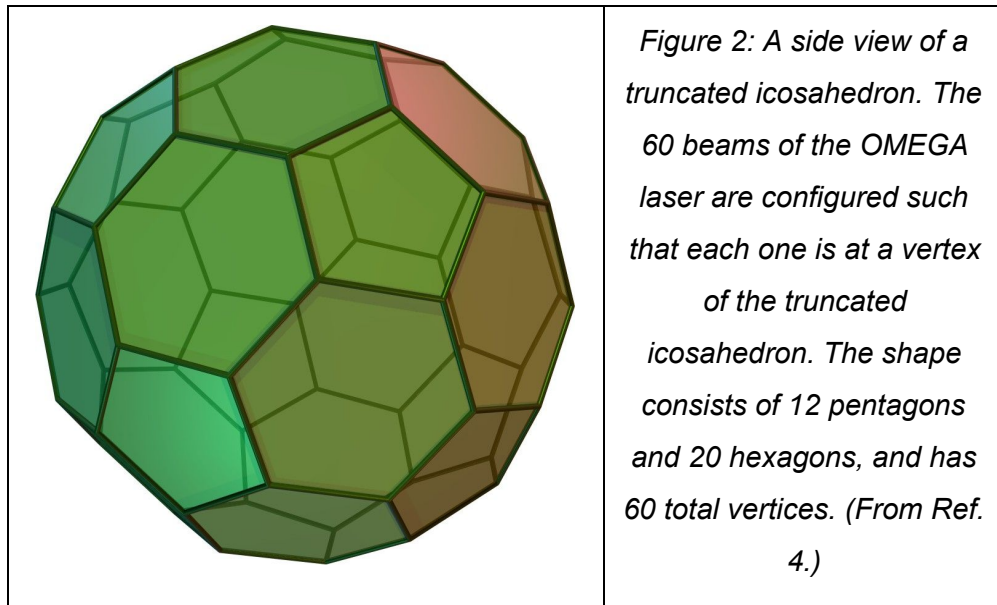


*Figure 1: A diagram of the steps that occur as the laser beams compress the target. The blue arrows represent the laser irradiation, while the orange arrows represent blowoff. The blue circle represents the target. The orange ring in part A represents the plasma surrounding the target. Figure D represents the target when it reaches thermonuclear burn. (From Ref. 3.)*

If the density of the fuel multiplied by the radius of the fuel is large enough, the energy from the reaction will be deposited in the fuel, initiating more reactions. This process is known

as ignition. If ignition occurs, the energy released by the fusion reactions will be greater than the energy input, which is referred to as “breakeven”. Once the energy released is 100 times that of the energy input, high energy gain will be achieved, allowing for a viable nuclear fusion reactor.



For fusion to occur, it is essential to have the beams irradiate the target uniformly. This will be a primary design criterion in future fusion reactors. The OMEGA laser uses 60 beams arrayed on the vertices of a truncated icosahedron (see Fig. 2), which resembles a soccer ball, to compress the target. The truncated icosahedron design was chosen for the OMEGA facility because it allows for a large number of beams in a symmetrical configuration.

Because of the good uniformity of the OMEGA design it may be used as the basis for a future fusion reactor. However, one problem that arises is what to do if one or more beams lose functionality. Since the region on the target where the beam is aimed no longer receives the same energy deposition as the other parts of the target, it will be less compressed. This problem also occurs in diagnostic experiments on OMEGA, in which some beams are diverted from the main implosion. In either scenario, there will be a severe drop in compression uniformity.

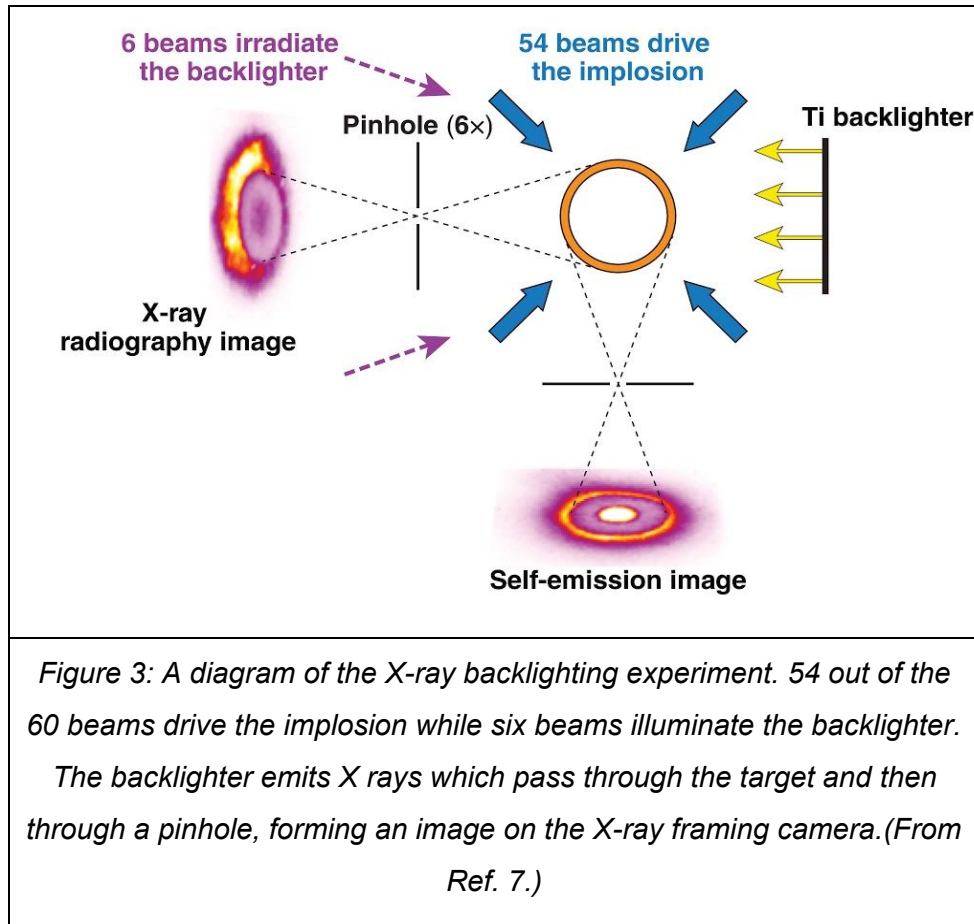
This problem can be minimized by repointing the other beams slightly towards the beams that are missing. However, the process of calculating the correct repointings can be extremely time consuming, as it is currently done through human optimization of a large number of parameters using the hydrodynamics simulation program SAGE.<sup>5</sup> If an effective algorithm was developed it would significantly decrease the amount of time required to find optimal configurations when diverting beams for diagnostic experiments, as well as allow a fusion

reactor to automatically repoint beams if one beam were to fail or be out of service for maintenance. This would enable the reactor to continue to produce energy while the beam was being repaired.

In this work a configuration was greatly improved upon for a specific diagnostic experiment, and an algorithm was developed that calculates beam repointings given any combination of missing beams.

### **3. X-ray Backlighting Experiment**

To gain more knowledge on how best to improve the compression scientists often use diagnostic experiments that allow them to see snapshots of what is going on during the compression. One common experiment is X-ray backlighting. As illustrated in Fig. 3, for an experiment carried out by T. Michel<sup>6</sup> and reported in Ref. 7, some laser beams (in this experiment six) are pointed at a secondary target, which emits x rays that pass through the target to a pinhole camera on the other side. Some of the X-rays are blocked by the dense target shell. This creates an absorption image on the X-ray framing camera. The other circle below the target in Fig. 3 shows the image that is created by the self-emission of the X-rays from the hot outer plasma surrounding the target. This image is used to diagnose the shape of the implosion.



As a result of pointing the six beams away from the main implosion, the regions that the beams were previously compressing become not nearly as compressed as the rest of the sphere. The predicted non-uniformity is illustrated in Fig. 4, which is a sinusoidal projection of the energy deposition on the sphere, that displays in a similar way to oval maps of the Earth. In this case the top is the “North Pole” and the bottom is the “South Pole”. The middle horizontal line is the entire equator with the leftmost and rightmost points being the same point because it wraps around. The deep blue represents an area of much lower energy deposition compared to the rest of the sphere. The missing beams are shown by orange circles. The uneven energy deposition depicted in this projection results in a very weak uniformity of 10.33% RMS (where the Root Mean Square is the square root of the arithmetic mean of the squared nonuniformity averaged over the surface of the sphere), compared to the 0.4% RMS that can be achieved with all 60 beams in their original configuration.

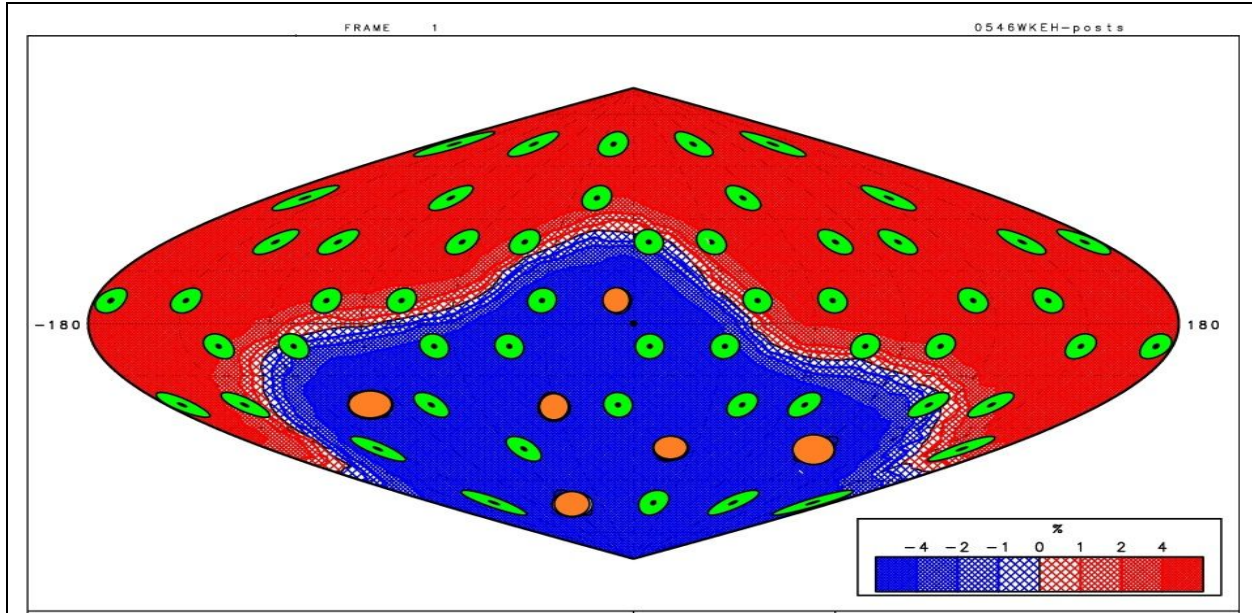


*Figure 4: 2-D energy deposition profile illustrating target non-uniformity. Blue indicates areas with a lack of energy deposition whereas red indicates areas of too much energy deposition. The more intense the color, the higher the non-uniformity. The green circles represent the beam port locations on the target chamber and the small black circles indicate the positions on the target where the beams are aimed. In this case no beams have been repointed. The orange circles indicate beams that are missing. The RMS energy deposition nonuniformity in this simulation is 10.3%.*

### 3.1 Prior Design

To compensate for the missing beams, an experiment was carried out<sup>7</sup> in which some of the remaining beams were repointed towards the areas in Fig. 4 where there is not enough energy deposited. It is important to note that each beam spreads its energy over a large region on the target, with the highest absorption being at the center of the beam. The design moved only the 18 beams closest to the six missing beams. The design also took advantage of the natural tri-fold symmetry of the truncated icosahedron (see Fig. 2). Each beam repointing has two parameters, the distance it moves along a great circle of the sphere, and its direction, defined by a point on the sphere it moves towards. By utilizing the 3 fold symmetry, which is illustrated in Fig. 5, the number of parameters is reduced from 36, for all 18 beams, to just 12, for six beams. After these six beams are optimized, the same relative movements are applied to their symmetrical counterparts. In this case most of the beams moved towards the missing

beam closest to them except for the 3 beams in the central hexagon which all move toward the center.

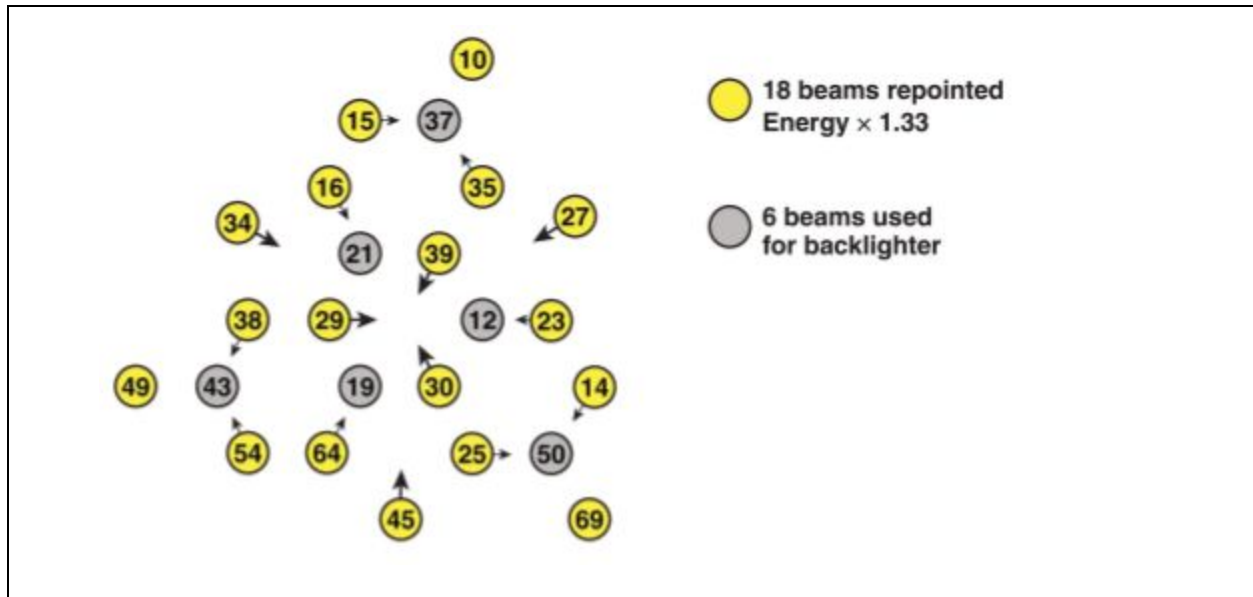
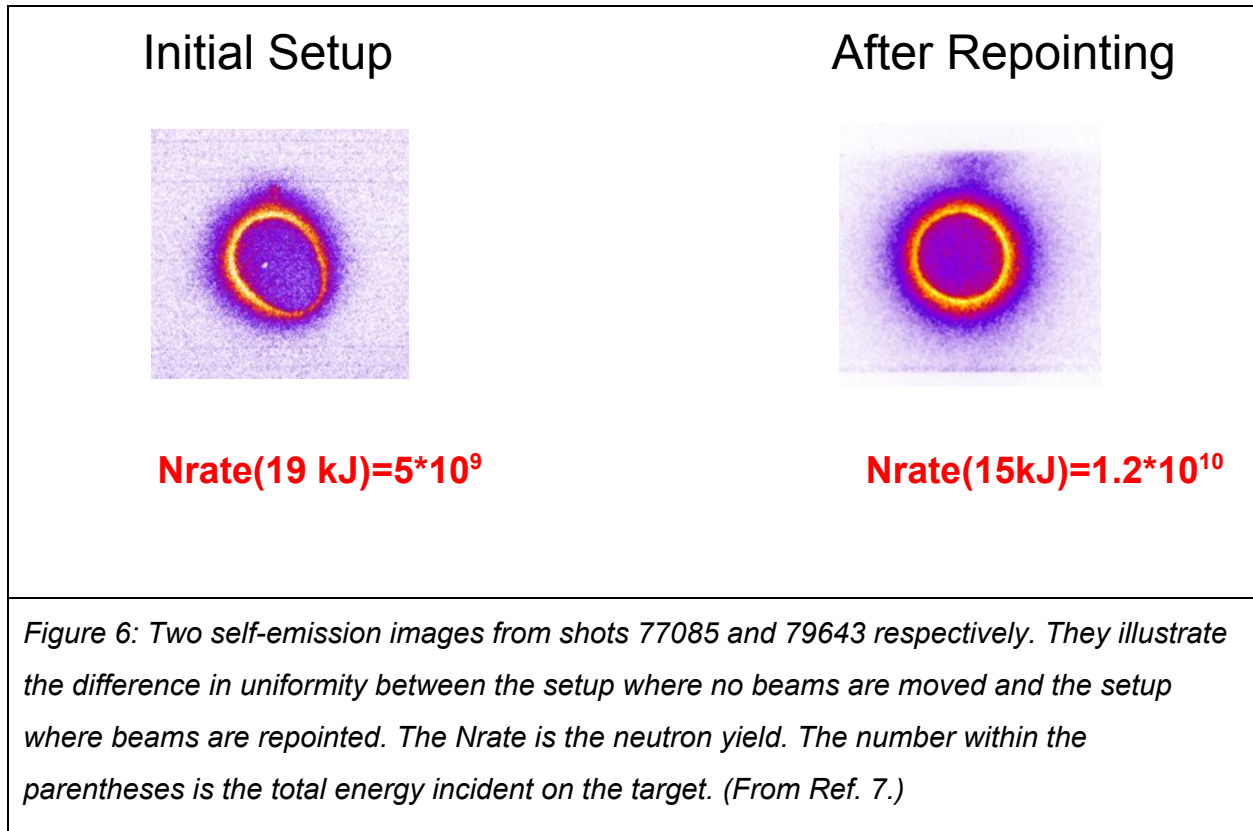


Figure 5: Flattened projection of the missing beams in the OMEGA backlighting experiment, and the 18 beams directly around them. Grey circles indicate missing beams. The number inside each circle is the designated number of each beam. The “x1.33” indicates that the beams indicated in yellow have had their relative energies multiplied by 1.33 to compensate for the missing beams. In practice, the unaltered beams were given 1/1.33x less energy. The arrows represent which direction each beam was moved in. (From Ref. 7.)

Unfortunately, merely changing the pointings of the 18 beams is not enough to compensate for the energy of the six missing beams. As a result, the 18 beams were given increased relative energies 33% higher than the other beams. However, since there is a limit on the amount of energy each laser beam can possess, and all the beams are operated at maximum energy, it is impossible to increase the energy of the 18 beams. Rather, the energy of all the other beams had to be decreased, so they were reduced to 75% energy. There is significantly better uniformity, as shown in Fig. 6.



In Fig. 6, the area of non-uniformity near the bottom right in the initial setup image corresponds directly to the area of deep blue in Fig. 4. The repointed configuration yielded very high uniformity, with a calculated RMS of only 0.74%. This high uniformity allows for a much higher neutron yield despite the fact that less energy is incident on the target (15 kJ compared to 19 kJ). The neutron yield is a key indicator of the success of the implosion. One of the primary goals of the experiment is to observe neutron yields as close as possible to the neutron yield from a full 60 beam implosion.

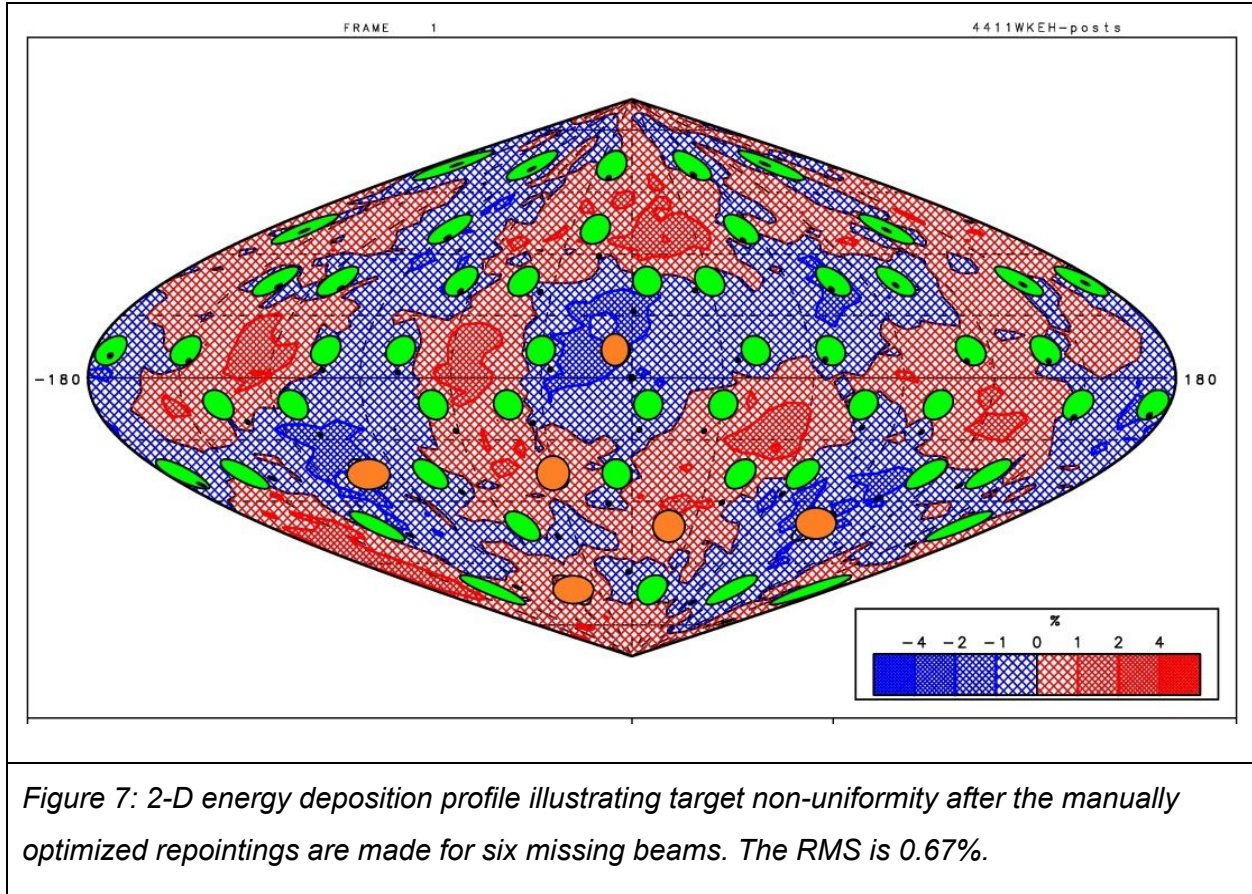
Optimally, to achieve a higher neutron yield the beam configuration needs to have strong uniformity while also depositing the full 19 kJ of energy.

### 3.2 Optimized Design for 6 Beams Missing

To pursue the goal of attaining the high uniformity of the previous design and also using the full 19 kJ of energy, all 54 beams were repointed, and all beams were kept on maximum energy. In the manual optimization process, a design was tested by running it through the hydrodynamics code SAGE to find the RMS value. The design was evaluated based on the sinusoidal projection of energy deposition and new pointings were input that addressed the problems of that configuration. This process was repeated until the RMS value ceased to

decrease through a large number of runs. Most of the adjustments were based on repointing the beams either directly toward a missing beam or toward the center of all the missing beams, as shown in Fig. 5. However, not all beams were pointed directly at one of those two places. Often there would be minor adjustments that directed energy towards places of low energy deposition based on the most recent sinusoidal projection. One of the major issues complicating the process is the fact that each beam is large enough that even after it is moved there will still be a large amount of energy deposited around its original area (denoted by the green circles in the energy deposition profiles). This is because the part of the beam that is hitting that area is hitting it at normal incidence, where rays experience the greatest absorption, whereas the other parts of the beam are not. Thus, the beam energy deposition profile will always trend toward its starting point. This phenomenon is part of the reason the optimizations have always been done manually.

To minimize the number of parameters this design also took advantage of the natural tri-fold symmetry, so 18 beams were repointed and the same relative repointings were applied to the other 36 beams. With each of the 18 beams having two parameters, 36 parameters had to be optimized. After hundreds of trials running various designs through SAGE the optimized design was found, shown in Fig. 7. Like all other such deposition figures used here it is on the same scale as Fig. 4. In this design almost all of the surface of the target is within 1% non-uniformity, resulting in a total RMS of 0.67%. This decrease in non-uniformity from the prior 0.74% could be due to the fact that more parameters were varied. Overall, since both designs have extremely high uniformity - the difference between the two being negligible - the largest improvement is the maximization of the total laser energy. This should result in a higher neutron yield. Because of this, the configuration will be used for future backlighting experiments.<sup>6</sup>



#### 4. One Beam Missing

Beyond X-ray backlighting, there are a variety of other reasons why some number of beams would be taken out from the original configuration. In the case of a future nuclear fusion reactor, it is possible that at some time a beam would lose functionality. However, if there was a set repointing that could be applied, the reactor could continue to function, with only slightly lower neutron yield. Since every beam is equivalent in the OMEGA geometry, with each beam being at the intersection of two hexagons and a pentagon (see Fig. 2), solving for the best configuration with any missing beam will have the same solution as for any other single missing beam. With one missing beam and no adjustments made to the other 59, the RMS value is raised to 2.80% from 0.40%. After another manual optimization process (similar to the one for six missing beams) the energy deposition was extremely uniform except for a few areas of non-uniformity between 1% and 2% (see Fig. 8). The overall RMS was reduced to 0.54%.

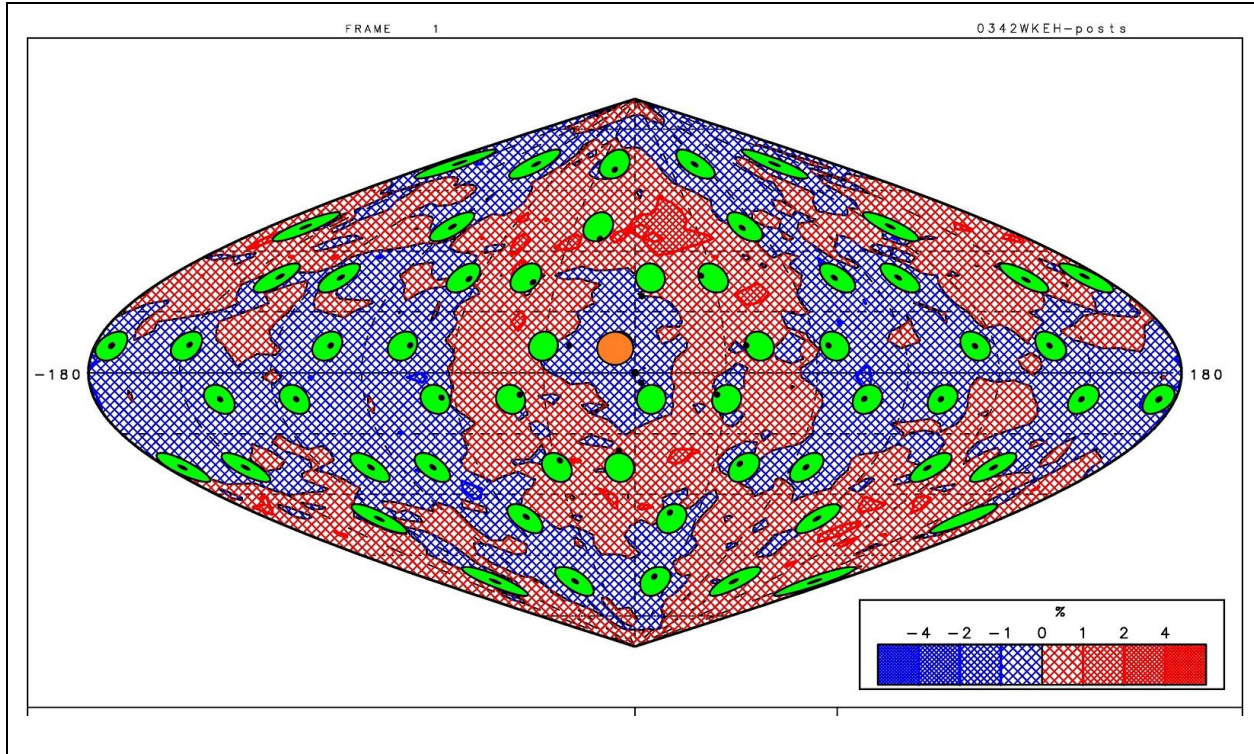


Figure 8: 2-D energy deposition profile illustrating the target non-uniformity for one beam missing after the manually optimized repointings are made. The RMS is 0.54%.

### 5. Developing the Algorithm

One concept that became evident through the optimization process is that there is basic logic that dictates what the optimal design will look like. The closer a beam is to a missing beam the more it will move. Also, small movements of all the beams are better than large movements of only a few. It seemed plausible that there could be a basic equation that describes how far the beams should be moved towards the missing beam. To continue with this idea, the movements toward the missing beams were graphed against the distance  $d$  between the beam and the missing beam, measured along a great circle on a unit sphere (Fig. 9). To find  $d$  the equation<sup>8</sup>

$$d = \arccos(\cos\theta_1 \times \cos\theta_2 \times \cos(\Phi_2 - \Phi_1) + \sin\theta_1 \times \sin\theta_2) \tag{Equation 1}$$

was used, where  $\theta$  is the latitude,  $\Phi$  is the longitude, and the subscripts 1 and 2 represent two beams, where 1 and 2 denote the missing beam and the beam to be moved, respectively.

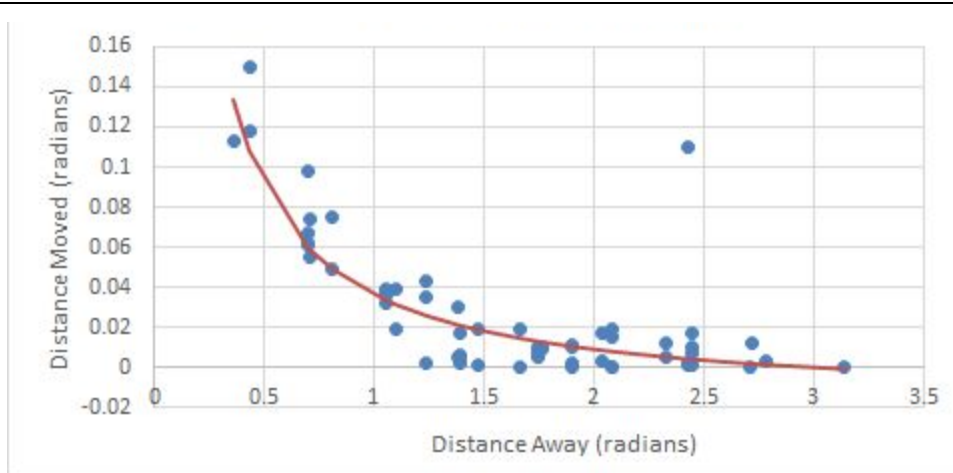
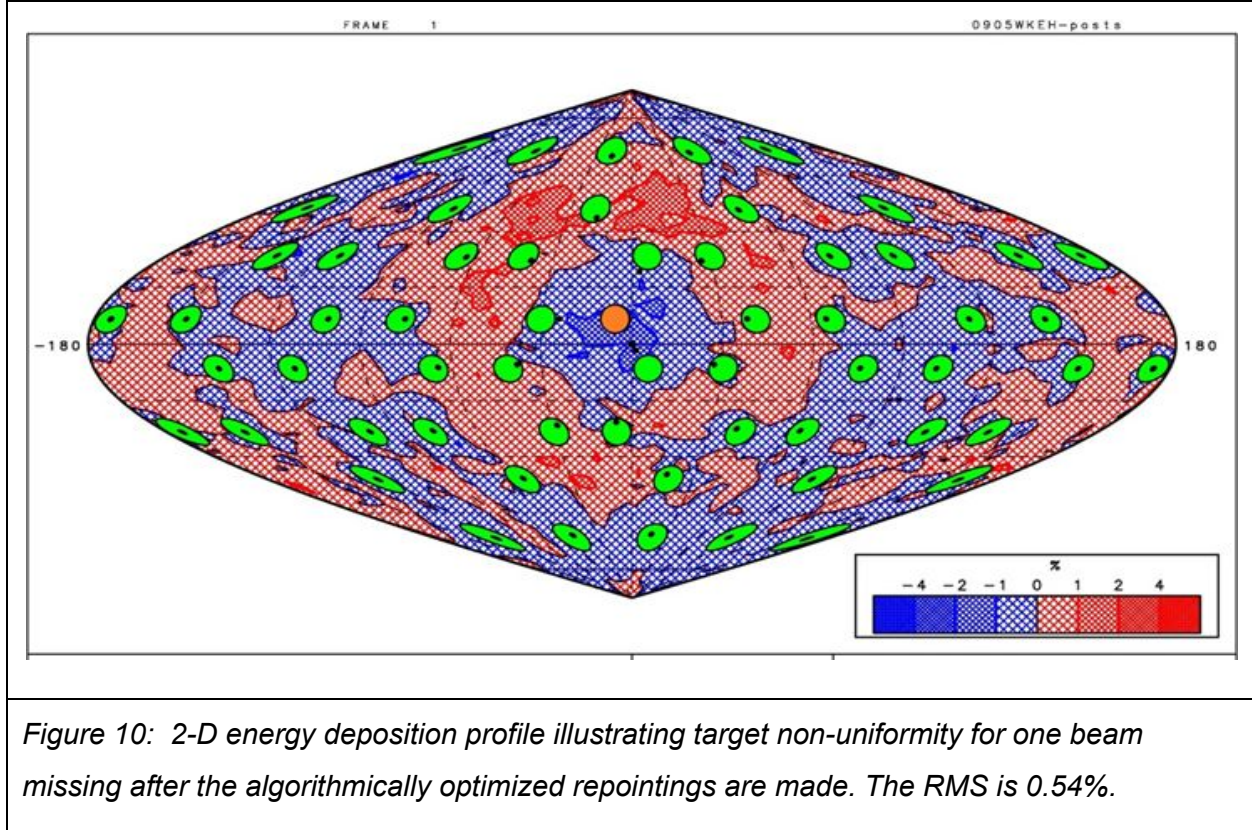


Figure 9: A graph of the distance moved ( $s$ ) vs. the distance away ( $d$ ) for the manual optimization. Both axes are in radians. Each blue dot indicates the values for one of the 59 beams. The red line is the trend line with the equation  $s = 0.0545/d - 0.018$

The line of best fit can be approximated through the equation

$$s = A/d - B \quad (\text{Equation 2})$$

where  $s$  is the distance the beam moves toward the missing beam along the great circle connecting the two of them, and where  $A = 0.0545$  and  $B = 0.018$ . Although there is an outlier, it is merely a result of a manual optimization decision, and since there is a high number of beams it does not have a large impact on the value of the equation coefficients. When the beam pointings were re-adjusted to follow this equation the configuration produced an extremely similar sinusoidal plot to the manually optimized one (see Fig. 10 versus Fig. 8). It also produced the same RMS value, 0.54%.



## 6. Extending the Algorithm

It seemed feasible that this single beam algorithm could be extended to multiple missing beams as well. A program was created to pursue this idea.

For each beam  $(\theta_2, \Phi_2)$ , the program calculates the distance  $s$  it would move toward one of the missing beams  $(\theta_1, \Phi_1)$  using equation 2. Then the new latitude  $\theta_3$  and longitude  $\Phi_3$  are found using the pair of equations<sup>8</sup>

$$\theta_3 = \arcsin(\sin\theta_2 \times \cos(s) + \cos\theta_2 \times \sin(s) \times \cos(\beta)) \quad (\text{Equation 3})$$

$$\Phi_3 = \Phi_2 + \text{atan2}(\sin(s) \times \sin(\beta) \times \cos\theta_2, \cos(s) - \sin\theta_2 \times \sin\theta_1)$$

where  $\theta$  is the latitude,  $\Phi$  is the longitude, and  $\beta$  is the bearing which is calculated using<sup>8</sup>

$$\beta = \text{atan2}(\sin(\Phi_1 - \Phi_2) \times \cos\theta_1, \cos\theta_2 \times \sin\theta_1 - \sin\theta_2 \times \cos\theta_1 \times \cos(\Phi_1 - \Phi_2)) \quad (\text{Equation 4})$$

By summing the changes in latitude and longitude for each missing beam the final latitude and longitude of the beam are found.

Using this algorithm the program is able to take any combination of missing beams and produce a suitable repointing configuration. When this algorithm was applied to the original case of six missing beams it produced a configuration with an RMS of 1.02%, shown in Fig. 11.

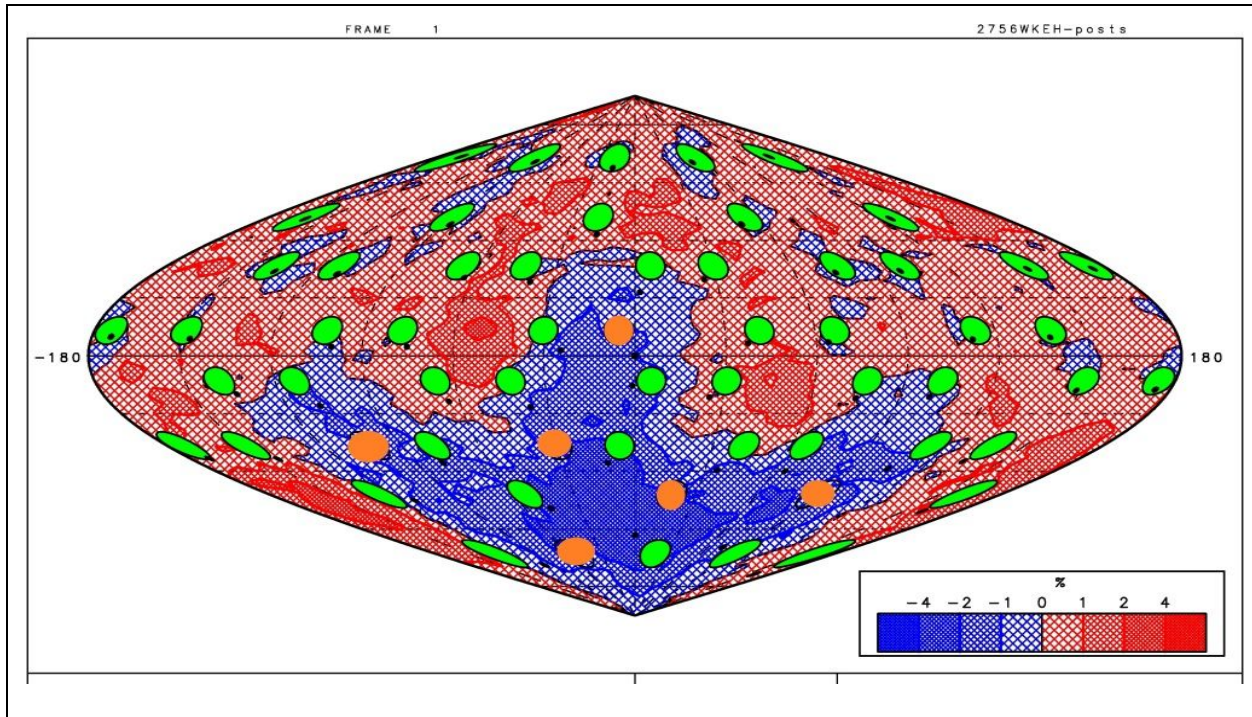
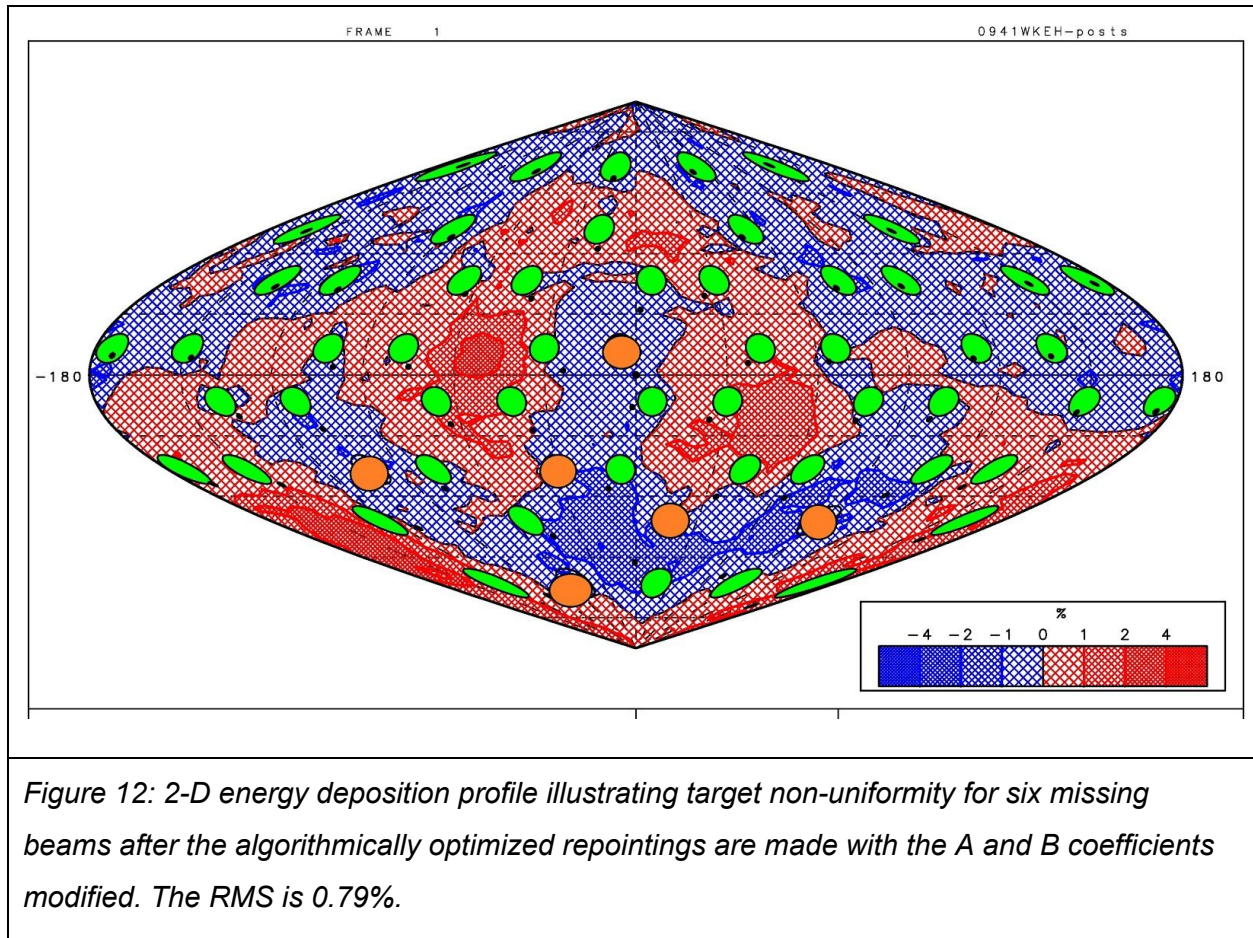


*Figure 11: 2-D energy deposition profile illustrating target non-uniformity for six beams missing after the algorithmically optimized repointings were made based on Equation 2 with the original A and B coefficients. The RMS is 1.02%.*

However, with the large area of lower energy deposition centered around the missing beams that is clearly visible in Fig. 11, it becomes clear that the repointings of the beams were not quite large enough. To account for this, the coefficients in the equation were changed so that each beam moved farther towards the missing beams. To find the correct coefficient values, A and B were optimized through a number of trials. However, this was a relatively quick process since there were only 2 parameters, one for each coefficient. In the optimized solution coefficient A was increased from 0.0545 to 0.0575 while coefficient B had a negligible change.

After this modification the configuration produced by the algorithm (shown in Fig.12) had an RMS of 0.79%, very close to the 0.67% of the manual optimization. By comparing the aim points (small black circles) in Fig. 12 to those in Fig. 7 one can see the similarities in the repointings, and the tri-fold symmetry is still evident. One interesting thing to note is that for both the six beam case and the one beam case the algorithm produces a configuration where there are certain areas that are much more non-uniform than the rest of the target, but the extremely

high uniformity in the remainder of the target allows the RMS value to stay about the same. The closeness of the algorithmic and manual values demonstrates the validity of the algorithm for multiple beams. This could drastically reduce the amount of time it takes to find a suitably uniform configuration when some beams are missing. For example, if 5 beams were missing with no symmetry, the 55 beams would make for a total of 110 parameters to optimize whereas with the algorithm there are only 2.



## 7. Future Work

To improve even further on the algorithm it would be beneficial if the program could recognize certain aspects of the pattern generated by the missing beams. One major factor that has a large effect on how far the beams should be moved is how clustered the beams are. To test out the nature of the relationship between clustering and the RMS the program was run with the original coefficient values ( $A=0.0545$ ,  $B=0.018$ ) for two, three, and four beams missing, each with two extreme cases, the most spread out and the most clustered.

| Number of Beams | RMS when beams are most spread out | RMS when beams are most clustered |
|-----------------|------------------------------------|-----------------------------------|
| 2               | 0.66%                              | 0.83%                             |
| 3               | 0.76%                              | 1.06%                             |
| 4               | 0.83%                              | 1.37%                             |

*Table 1: RMS values of configurations generated by the algorithm with the base coefficients for two, three, and four beams for the two extreme cases of the missing beams being most spread out or most clustered.*

The results are summarized in Table 1. Currently, with the base algorithm the program gives worse results when the beams are clustered, demonstrating that it could be beneficial to have coefficient A increase to account for the beams not moving enough in those cases.

Through analyzing these relationships it may be possible to have the program recognize these patterns and choose the appropriate coefficient values accordingly. This would eliminate all human optimization from the process and decrease the time needed for repointing calculations even further.

## 8. Conclusion

In conclusion, an optimal six beam configuration was found for an X-ray backlighting experiment on OMEGA. This configuration had an RMS of 0.67% and improved on the previous design by not requiring the energy to be reduced on any beams. An optimal configuration for any single missing beam was also created, and had an RMS of 0.54%. An algorithm was developed for the case of one missing beam and yielded the same RMS value. This algorithm was extended to be able to produce a suitable configuration given any number of missing beams. The algorithm was tested on the original six beam case and had an RMS of 0.79%, extremely close to the 0.67% of the manually optimized configuration. However, the manual method had 36 separate parameters while the algorithmic optimization only had 2, making it much more time efficient. This time savings is even more apparent when there is a set of missing beams with no symmetry, where there would likely be over 100 parameters to optimize if it were to be done manually.

Overall, it appears that the algorithm allows suitable configurations for a wide range of combinations of missing beams with limited human input. The algorithm could be very beneficial for a future reactor that could automatically repoint if one or more of the beams were to lose functionality.

## **9. Acknowledgements**

First, I would like to thank Roger Janezic for telling me about the Summer High School Program at the Laboratory for Laser Energetics and encouraging me to apply. I would also like to thank the Laboratory for providing this program and making this opportunity possible. Most of all, I would like to thank Dr. R. Stephen Craxton for being extremely helpful and supportive as my advisor, and for running the entire program.

## 10. References

1. J. Nuckolls, L. Wood, A. Thiessen, and G. Zimmerman, "Laser compression of matter to super-high densities: Thermonuclear (CTR) applications," *Nature*, vol. 239, p. 139, 1972.
2. R.S Craxton et al., "Direct-drive inertial confinement fusion: A review," *Physics of Plasmas*, vol. 22, p. 110501, 2015.
3. B.D. Esham, Inertial Confinement Fusion. Digital image. Wikipedia. N.p., 5 July 2007. Web. 10 Sept. 2016.
4. Truncated Icosahedron. Digital image. Wikipedia. N.p., 22 May 2005. Web. 10 Sept. 2016.
5. R.S. Craxton and R. L. McCrory, "Hydrodynamics of thermal self-focusing in laser plasmas", *Journal of Applied Physics*, vol. 56, p. 108, 1984.
6. T. Michel, private communication.
7. R.S. Craxton, M. Hohenberger, W. Kehoe, F.J. Marshall, D.T. Michel, P.B. Radha, M.J. Rosenberg, *Bulletin of the American Physical Society*, Vol. 61, p. 231, 2016.
8. C. Veness, [www.movable-type.co.uk](http://www.movable-type.co.uk). "Movable Type Scripts." Calculate Distance and Bearing between Two Latitude/Longitude Points Using Haversine Formula in JavaScript. MIT, 2002. Web. 12 Nov. 2016.

***Characterizing a Cu/Mn Alloy for Extracting Oxygen from Inert Gas  
Streams***

**Grace Lenhard**

Prattsburgh Central School

LLE advisors: Walter Shmayda and Matthew Sharpe

Laboratory for Laser Energetics

University of Rochester

Summer High School Research Program 2016

July 2017

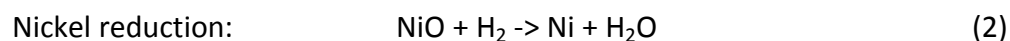
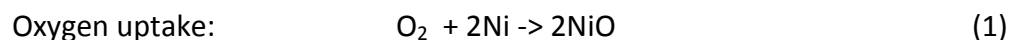
## **Abstract**

Gloveboxes filled with inert gases are used to reduce the release of tritium, a radioactive isotope of hydrogen used in fusion studies at LLE, into the atmosphere. A zirconium/iron (Zr-Fe) alloy is used to remove tritium chronically released into the gloveboxes. However, some atmosphere permeates into the gloveboxes through the gloves and seals. Oxygen and water deactivate the Zr-Fe bed, so they must be removed from the gas stream. A copper/manganese (Cu/Mn) alloy was investigated as an alternative to nickel, the current oxygen getter. Oxygen in a carrier stream of helium is flowed over the alloy, allowing it to getter oxygen. The amount of oxygen exiting the bed is measured as a function of time to determine the bed capacity. When the amount of oxygen leaving the bed is nearly equal to the amount of oxygen being flowed into the bed, the bed is considered full. This procedure was repeated for alloy temperatures of 200°C, 300°C, and 400°C with a helium flow rate of 1 LPM containing 1% oxygen. As the temperature increased, the bed capacity increased. However, a change in the bed temperature had no significant effect on the bed efficiency. Flowing oxygen over the bed also produced a small quantity of water, even if the bed had been dried beforehand, suggesting water creation from hydrogen within the alloy.

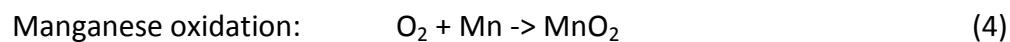
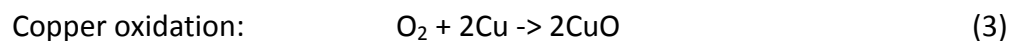
## **1. Introduction**

At LLE, gloveboxes are used to reduce tritium escape into the environment [1]. Tritium and inert gasses are run through a system which utilizes a Zr-Fe bed to recapture escaped tritium. However, small amounts of oxygen and water that seep into the gloveboxes can

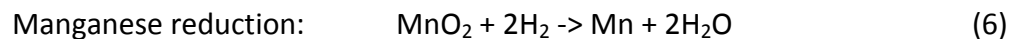
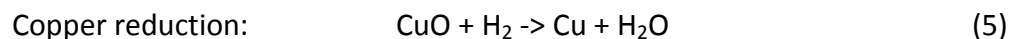
deactivate the Zr-Fe bed. A molecular sieve collects the water vapor and an oxygen getter collects the oxygen before the gas stream is passed over the Zr-Fe bed [2, 3, 4, 5]. The current oxygen getter is a nickel bed [6], but alternatives such as a copper/zinc alloy have been tested [4]. After the bed is full, it is regenerated with hydrogen, forming water. The reactions are:



In this experiment, Cu/Mn was tested as a possible oxygen getter for tritium gloveboxes. Its gettering capacity (the amount of O<sub>2</sub> absorbed by the bed) was tested at 200°C, 300°C, and 400°C with a constant flow rate of 10 sccm oxygen to determine the most efficient temperature for oxygen gettering with Cu/Mn. At lower temperatures, the copper oxidized, but at higher temperatures the manganese also oxidized. The reactions are:



After the bed is loaded (filled to capacity), it is regenerated with hydrogen, yielding the reactions:



## 2. Experimental

A system was built to test the gettering capacity of Cu/Mn (fig. 2.1). The flow of the gasses used (He, H<sub>2</sub>, and 1% O<sub>2</sub> in He) was controlled using mass flow controllers (MFC) and valves (1-6) allowed the gas to be flowed either through the Cu/Mn bed or through a bypass. At the end, the gasses were sent through a dew point sensor to record temperature and relative humidity. A residual gas analyzer (RGA) determined the composition of the gas. The RGA monitored for helium, hydrogen, and oxygen. Nitrogen was also monitored to ensure against leaks into the gas system.

The stainless-steel piping was heated to 100°C to prevent condensation on the plumbing surfaces. The temperature of the Cu/Mn bed could be adjusted. Temperatures of 200°C, 300°C, and 400°C were used.

The bed contained 174 ml Cu/Mn in a ratio of 14% Cu (0.29 mol), 56% Mn (1.22 mol), and 30% inert medium. The pellets were 2-3 mm in diameter with a surface area of 200 m<sup>2</sup>/g.<sup>1</sup>

Helium was used to purge the system and as a carrier gas for hydrogen. It was flowed at a rate of 1 L/min at most times. Hydrogen was flowed with the helium to unload the bed. Various flow rates were tested until it was determined that the best flow rate for hydrogen was 10 sccm hydrogen in 1 L/min helium. The hydrogen flow rate was inhibited by water production because if the humidity rose above 40% water would begin to condense out of the gas stream. 1% oxygen in helium was run at 1 L/min to test the capacity of the bed for absorbing oxygen.

---

<sup>1</sup> Surface area of gettering material is measured by the total surface area of all particles in a certain mass of the material. In this case, the total surface area of one gram of particles is 200 m<sup>2</sup>.

This resulted in an oxygen flow rate of 10 sccm. When the 1% oxygen in helium was flowed, the flow of pure helium was shut off.

The RGA used to measure the partial pressures of the gas in the stream had to be calibrated because the RGA works under a partial vacuum and the proportions of gasses in the RGA are not the same as in the gas stream. Correction factors had to be calculated for each gas using the equations

$$\text{Hydrogen: } C_{H_2} = \frac{F_{H_2}^{avg}(LPM) \cdot 101325(Pa)}{F_{total}(LPM) \cdot P_{H_2}^{RGA}(Pa)} \quad (7)$$

$$\text{Oxygen: } C_{O_2} = \frac{0.01 \cdot 101325(Pa)}{P_{O_2}^{RGA}(Pa)} \quad (8)$$

$$\text{Water: } C_{H_2O} = \frac{P_{H_2O}^{carrier}(Pa)}{P_{H_2O}^{RGA}(Pa)} \quad (9)$$

where 101325 Pa is the total system pressure,  $C_{H_2}$  is the correction factor for hydrogen,  $C_{O_2}$  is the correction factor for oxygen,  $C_{H_2O}$  is the correction factor for water,  $F_{H_2}^{avg}$  is the average flow of hydrogen,  $F_{total}$  is the total gas flow,  $P_{H_2}^{RGA}$  is the partial pressure of hydrogen in the RGA,  $P_{O_2}^{RGA}$  is the partial pressure of oxygen in the RGA,  $P_{H_2O}^{RGA}$  is the partial pressure of water in the RGA, and  $P_{H_2O}^{carrier}$  is the partial pressure of water in the carrier stream found from the relative humidity and the vapor pressure of water at the given temperature using the equation

$$\text{Partial pressure of water: } P_{H_2O}^{carrier}(Pa) = RH \cdot P_{vap}(Pa) \quad (10)$$

where  $RH$  is relative humidity and  $P_{vap}$  is the vapor pressure of water at a given temperature.

The partial pressure of gasses in the RGA are multiplied by the conversion factors to get the partial pressure of the gasses in the carrier stream.

### **3. Results and discussion**

#### *3.1 Oxygen absorption*

The main objectives of this work were to test the rate of oxygen absorption and to measure the capacity of Cu/Mn at multiple temperatures to determine its usefulness in scavenging oxygen from inert gas streams. To test this, multiple steps were taken. First, 1% oxygen in helium was flowed through the bypass to determine the partial pressure measured by the RGA for that specific run so the conversion factor could be found using equation 8. The bed was then opened to the gas flow. The concentration of oxygen in the outflow quickly dropped to nearly 0, before increasing and eventually leveling out at about the same concentration as when the gas was running through the bypass, creating a breakthrough curve like the one in figure 3.1. After the measured oxygen concentration was level for several minutes, the gas flow was switched back to bypass before the bed was unloaded by flowing hydrogen over it producing water as shown in equations 5 and 6.

The volume of oxygen absorbed was found using the flow rate into the bed (known) and the flow rate out of the bed (determined using the partial pressure of oxygen in the RGA multiplied by the correction factor found using equation 8). The oxygen flow out of the bed (the shaded area in figure 3.1) was determined using

Oxygen flow out: 
$$V_{O_2}^{out}(\mu mol) = \int F_{O_2}^{out} \left( \frac{\mu mol}{s} \right) dt \quad (11)$$

where  $V_{O_2}^{out}$  is the volume of oxygen not captured by the bed and  $F_{O_2}^{out}$  is the flow rate of oxygen out of the bed.

Theoretically, subtracting the amount of oxygen flowed out of the bed from the amount of oxygen flowed into the bed would equal the amount of oxygen gettered by the bed.

However, there was also water output when the oxygen was being flowed through the bed (discussed in section 3.2 below), so the volume of water production also had to be taken into consideration using the equation

Oxygen gettered:

$$V_{O_2}^{get}(\mu mol) = V_{O_2}^{in}(\mu mol) - V_{O_2}^{out}(\mu mol) - \frac{V_{H_2O}^{out}(\mu mol)}{2} \quad (12)$$

where  $V_{O_2}^{get}$  is the total volume of oxygen gettered by the bed,  $V_{O_2}^{in}$  is the volume of oxygen that entered the getter bed, and  $V_{H_2O}^{out}$  is the total volume of water produced by the bed. The last factor is divided by two because one  $\mu mol$  of oxygen is needed to form two  $\mu mol$ s of water.

Using these equations, the volume of oxygen gettered by the bed at each temperature was determined. As the temperature increased, the amount of oxygen the bed could hold, or bed capacity, increased, as shown in figure 3.2.

An important extension of this information is the efficiency of the bed. The percentage of oxygen flow that was gettered or converted to water over time was calculated using the equation

$$Efficiency(\%) = \frac{F_{O_2}^{in}(\frac{mol}{s}) - F_{O_2}^{out}(\frac{mol}{s})}{F_{O_2}^{in}(\frac{mol}{s})} \cdot 100\% \quad (13)$$

where  $F_{O_2}^{in}$  is the flow rate of oxygen in. As seen in figure 3.3, bed efficiency exceeds 98% when the getter is operating at 200 °C and improves slightly with increasing temperature. When the bed approaches capacity, the gettering efficiency drops off rapidly.

Bed efficiency is a critical consideration in how well a material can perform as an oxygen getter in glove boxes. Although the calculations above provide a total bed capacity, the useful bed capacity is the amount of oxygen absorbed before breakthrough. Breakthrough is defined as the point at which more than 1% of the oxygen above background levels gets through. In other words, it is when efficiency drops 1% below the highest efficiency recorded. For Cu/Mn at 200°C, oxygen absorbed before breakthrough is approximately 4% of the theoretical bed capacity (the amount of oxygen that could be absorbed if every atom of copper and manganese were oxidized) and at 400°C oxygen absorbed before breakthrough is 24% of the theoretical bed capacity. For the Ni beds currently used, however, oxygen absorbed before breakthrough is roughly 12% of the theoretical bed capacity at 200°C and 50% of the theoretical bed capacity at 400°C [6]. It is clear that the useful capacity compared to the theoretical capacity of the nickel beds currently used is much higher than that of Cu/Mn.

### 3.2 Water production during unloading

An interesting artifact of bed loading was water production. Although no water should have been produced during the oxidation of the alloy, approximately 30 mmol of water were

produced during each loading run as shown in Table 1. This is substantial considering that average oxygen uptake was between 54 mmol and 324 mmol, depending on the alloy temperature. Water production did not appear to depend on the alloy temperature, as shown in figure 3.4.

Water production was measured using two methods: with a dew point sensor installed in the main stream and by sampling the stream with the RGA. In the first case, the relative humidity is directly proportional to the vapor pressure of water in the carrier provided the carrier temperature is fixed. In the second case the vapor pressure in the carrier can be inferred from the RGA signal once the RGA is calibrated using equation 9.

In the first approach the quantity of water produced in the getter bed is:

$$V_{H_2O}(mol) = \int \frac{P_{H_2O}^{carrier}(Pa)}{101325} * F_{total} \left( \frac{mol}{s} \right) dt \quad (14)$$

where  $F_{total}$  is the total gas flow.

The source of water production is unclear but is most likely related to reactions of the hydrogen with the manganese or the binder in the Cu/Mn bed.

#### 4. Conclusion

This experiment measured the oxygen gettering capacity of a Cu/Mn bed at different temperatures to determine if it would be a good alternative to nickel, the current oxygen getter used in tritium glove boxes. As temperature increased, the bed was able to getter more oxygen. The efficiency rose slightly from 98% to 99.5% as the temperature of the alloy increased from 200 to 400°C. The useful gettering capacity was between 4% and 24% of the theoretical bed

capacity at temperatures of between 200°C and 400°C. Water was also produced during the oxidation of the bed. The latter two observations suggest that Cu/Mn would be a poor replacement for the current Ni beds because of the production of water and the significantly lower useful gettering capacity per amount of material.

## 5. Acknowledgements

Thanks to Dr. Shmayda and Dr. Sharpe for their help with my project, to Dr. Craxton for organizing the high school program, and to the other high school interns for the good times we spent together.

## 6. References

1. "Technologies for Mitigating Tritium Releases to the Environment." *LLE Review* **103**, 142 (2005).
2. A. G. Heics and W. T. Shmayda. "Design of a Second Generation Secondary Enclosure Clean-Up System." *Fusion Technol* **28**, 1509 (1995).
3. A. G. Heics and W. T. Shmayda. "Development of a Secondary Enclosure Clean-Up System for Tritium Systems." IEEE 93CH3348-0 65 (1993).
4. Gnolek, Sara. "Catalytic Oxidation of Hydrogen in Air Streams." Laboratory for Laser Energetics High School Summer Research Program (2013).
5. W. T. Shmayda, N.P. Kherani, B. Wallace, and F. Mazza. "Inert Gas Secondary Enclosure Clean-Up System." *Fusion Technol* **21**, 616 (1992).
6. W. T. Shmayda, S. J. Loucks, R. Janezic, T. W. Duffy, D. R. Harding, and L. D. Lund. "Tritium Operations at the Laboratory for Laser Energetics." *Fusion Sci. Technol* **49**, 851-858 (2006).

Figures

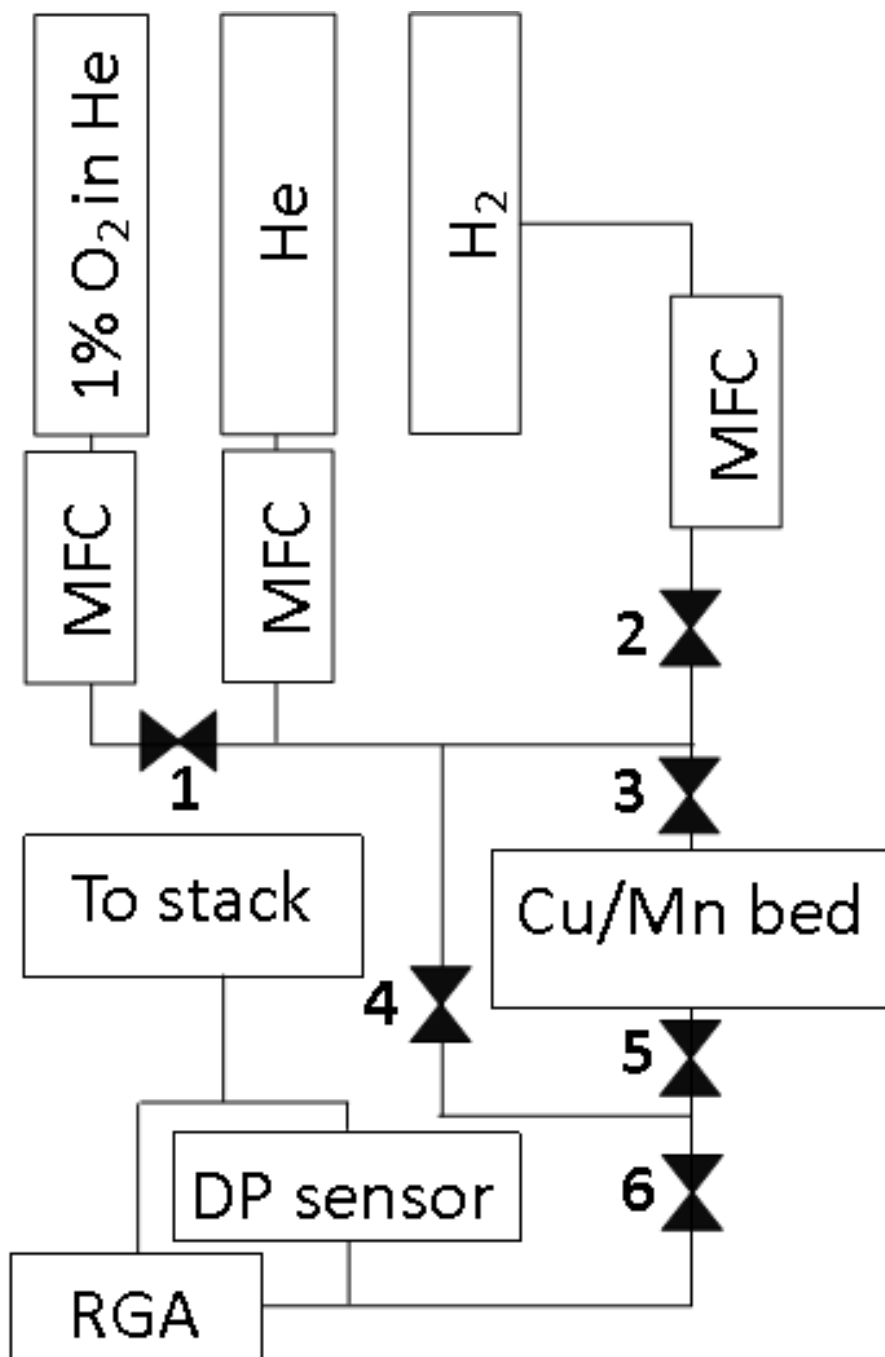


Figure 2.1 Experimental setup. MFC is mass flow controller; RGA is residual gas analyzer; DP is dewpoint

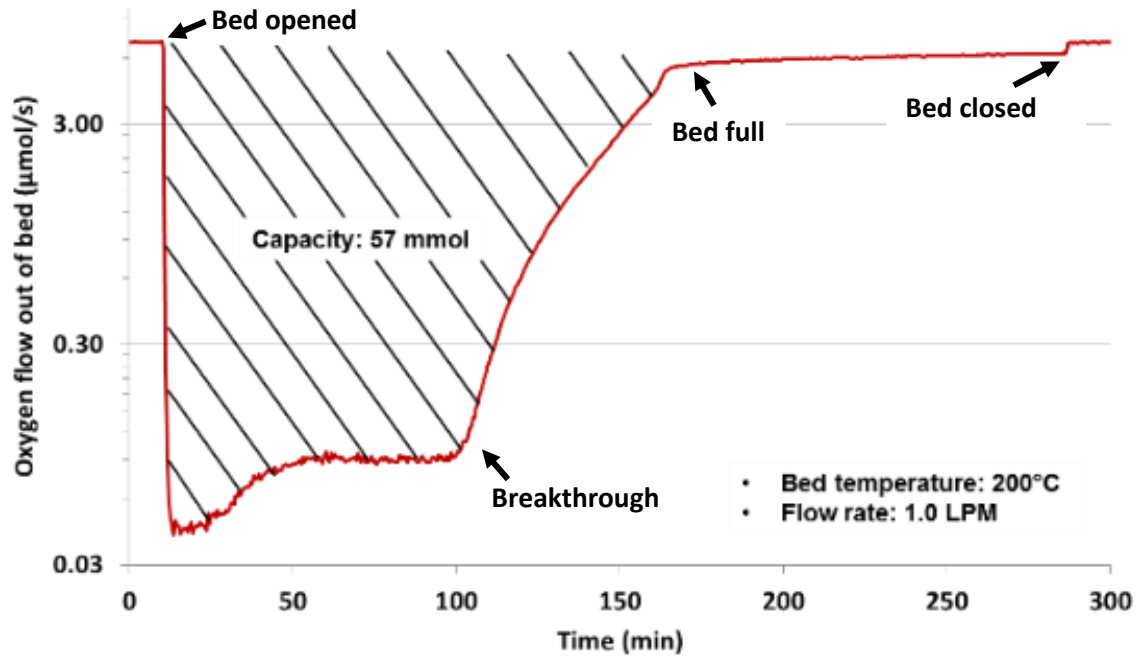


Figure 3.1 Typical oxygen collection profile for Cu/Mn. The shaded area provides an estimate of the bed oxygen capacity. Note that the oxygen concentration in the carrier stream increases when the bed is closed because collection efficiency is not 100%.

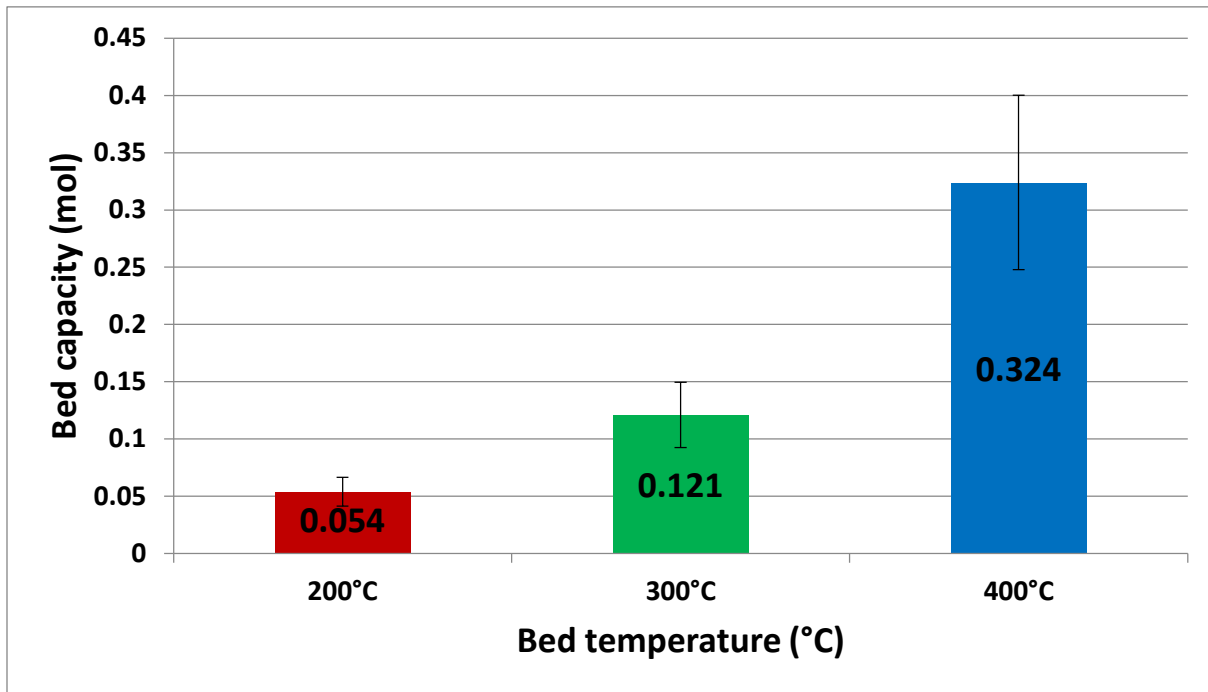


Figure 3.2 Bed capacity versus temperature. As bed temperature increases, bed capacity also increases.

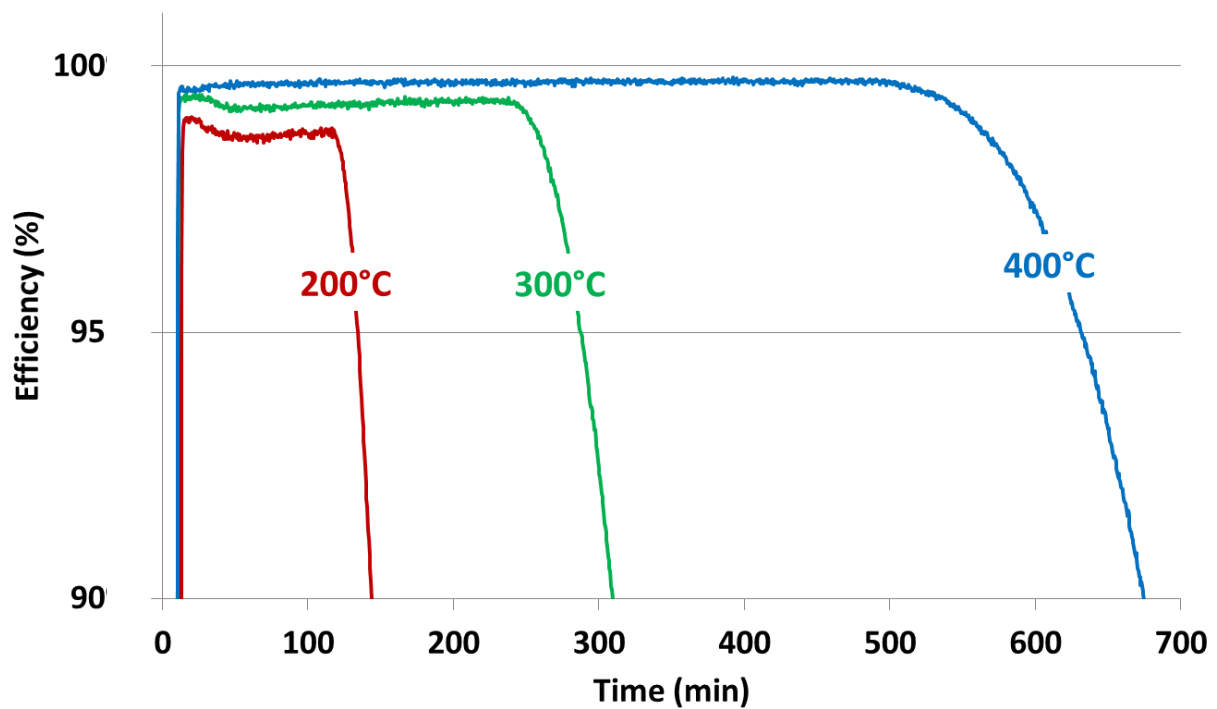


Figure 3.3 Dependency of gettering efficiency on temperature

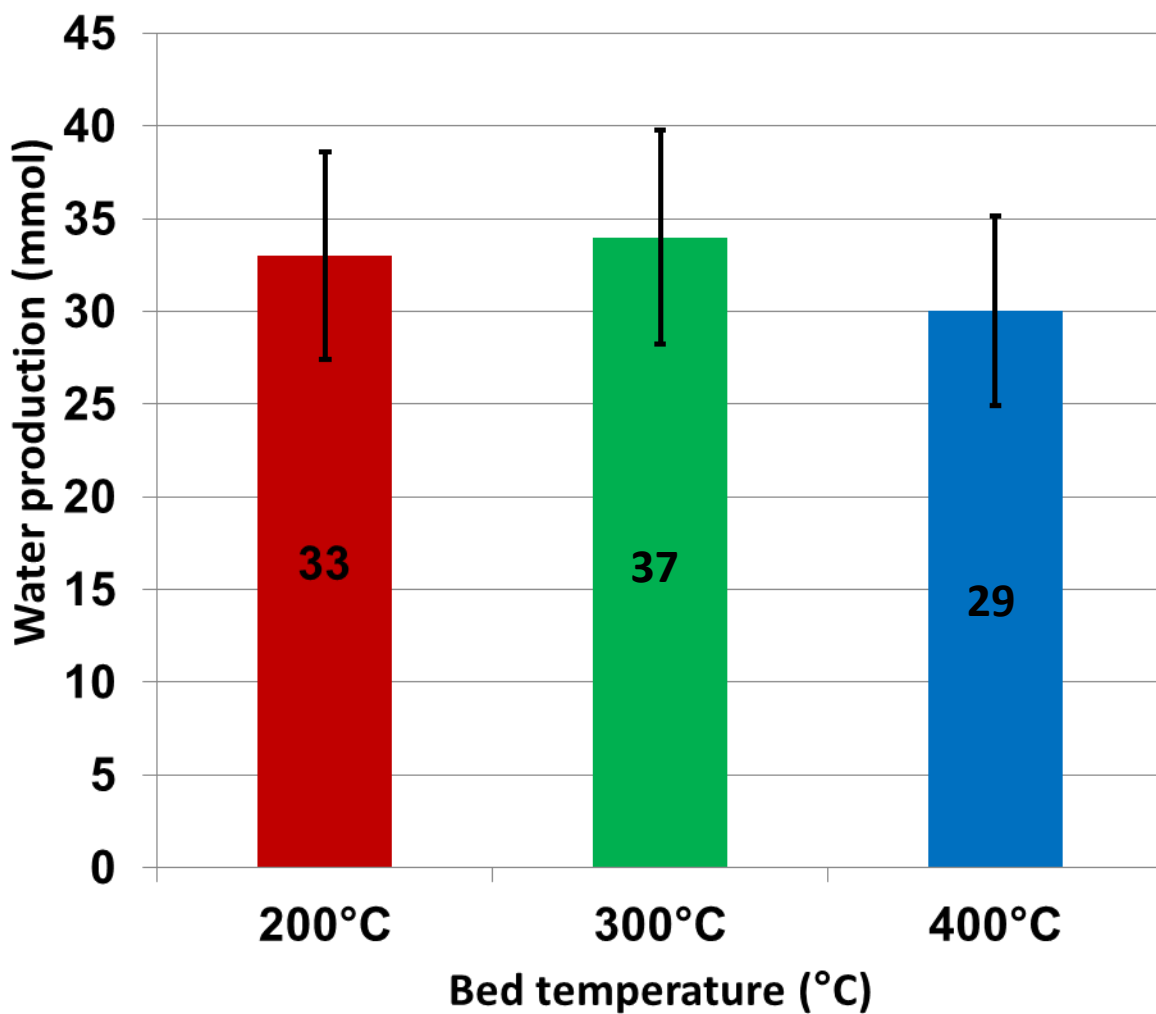


Figure 3.4 Dependency of water production on bed temperature

| Temperature (°C) | Oxygen consumed (mmol) | Water production (mmol) |
|------------------|------------------------|-------------------------|
| 200              | 65.0                   | 38.6                    |
| 200              | 40.2                   | 27.6                    |
| 200              | 57.2                   | 31.2                    |
| 300              | 121.0                  | 34.2                    |
| 300              | 122.0                  | 39.6                    |
| 400              | 324.0                  | 31.1                    |
| 400              | 325.0                  | 26.6                    |

Table 1: Oxygen consumption and water production for all runs organized by temperature.

## *Measuring Hydrogen Pressure over a Palladium Bed*

**Joseph Mastrandrea**

Webster Thomas High School

LLE Advisor: Walter Shmayda

### **Abstract:**

An experimental setup that utilized a Pd bed connected to a heater and a cryocooler, which operates according to the Stirling Cycle, was used to collect data on the formation of palladium hydride. Palladium is a member of a group of metals which have been found to absorb the different isotopes of hydrogen to form metal hydrides. Due to this, palladium is of interest on account of its ability to collect and store large volumes of hydrogen, deuterium, and tritium. Measuring the change in hydrogen pressure above the palladium at equilibrium at a fixed temperature provides the amount of hydrogen absorbed into the palladium. Pressure data was recorded for H/Pd ratios between 0.0 and 0.8 and temperatures between -40 C and 200 C. This extends the prior minimum temperature of study from 20 C to -40 C and expands the upper bound of the H/Pd ratio studied from 0.6 to 0.8. The absorption data indicates that palladium is an effective absorber of hydrogen at lower temperatures and can deliver hydrogen over a broad temperature range.

## Section 1: Introduction

The ability to form a hydride is a unique characteristic of palladium metal which makes it valuable in hydrogen collection processes. The focus of this particular experiment was on the formation of palladium hydride (PdH) at low temperatures. The study and understanding of the behavior of PdH at low temperatures is of importance at LLE because of its mission to study inertial confinement fusion reactions. The fuel delivery method employed during typical campaigns involves filling a cryogenic target, approximately one millimeter in diameter, with a mixture of deuterium ( $D_2$ ) and tritium ( $T_2$ ) in order to provide the fuel density required to create fusion conditions. In order to do this, a stock of gaseous tritium and deuterium must be kept for target charging purposes. Currently, the targets are being filled by permeation of DT through the outer plastic shell of the target (fig. 1). As the gas permeates through the outer skin, the pressure of DT inside the plastic shell increases until it is equal to the pressure surrounding it, at which point the target is full.

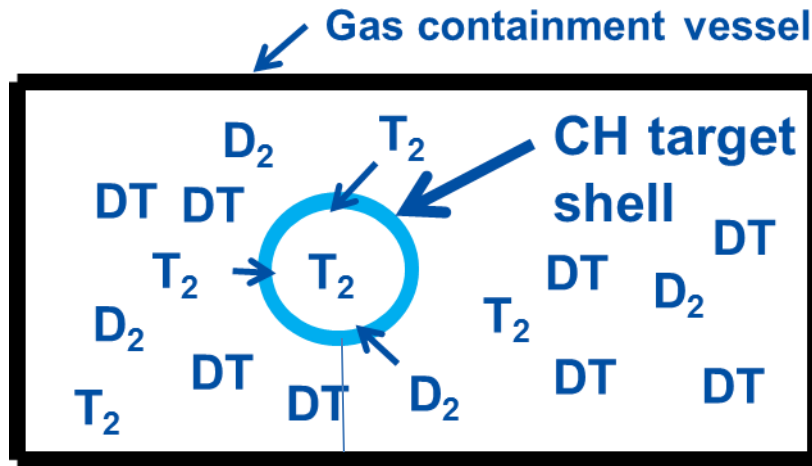


[Fig-1: Permeation filling process in which a target is filled with DT,  $D_2$ , and  $T_2$  at high pressure]

Tritium is a radioactive gas, making it difficult to safely use in experiments and collect once released into the environment. Although this research was focused on the formation of palladium hydride, it can be extended to the hydrogen isotopes deuterium and tritium, forming palladium deuteride and palladium tritide, respectively. It is believed that heating palladium hydride to desorb the precise amount of gas required, and flowing the gas through a fill tube into

the plastic shell as shown in fig. 2, would be less damaging to the targets and simplify the method of target filling.

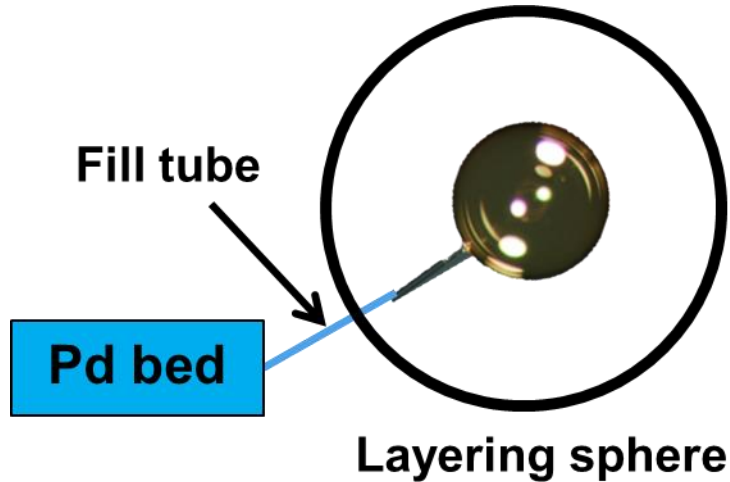


[Fig-2: Proposed less hazardous method of target filling using a palladium bed]

## **Section 2: Theory and literature review**

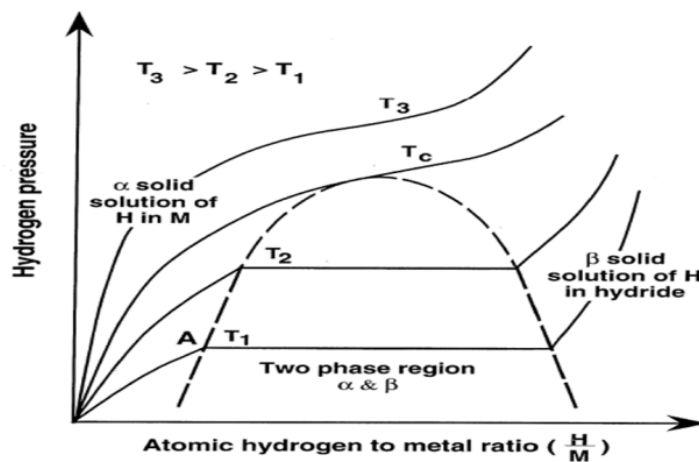
Palladium belongs to a unique group of metals which are capable of absorbing hydrogen into their lattice structure to form hydrides. This absorption process is complex and essentially occurs in three steps. This unique ability allows palladium to act as a hydrogen compressor, which means that palladium, at low temperatures, will absorb hydrogen resulting in a low vapor pressure above the metal. Then, upon heating, the vapor pressure of the hydrogen increases as it is desorbed from the palladium bed.

### (2.1) Palladium hydride formation:

The hydrogen pressure over the palladium is plotted in fig. 3(a) against the ratio of hydrogen to palladium in the palladium bed at a number of temperatures. As hydrogen is introduced into the palladium bed at a given temperature, the vapor pressure above the palladium increases to form the Alpha ( $\alpha$ ) region of the curve. Throughout this region, hydrogen atoms are dissolving into the palladium by fitting into the interstitial spaces within the hydrogen lattice in increasing quantities as the H/Pd ratio increases, as shown in the left part of fig. 3(b). At the end of the Alpha region, energetic favorability shifts from spontaneous absorption of hydrogen atoms into the lattice structure, to reactions with the palladium to form palladium hydride. This continues throughout the two-phase region ( $\alpha$  &  $\beta$ ), so called because there is both bonded and

dissolved hydrogen. As the hydrogen atoms introduced in each successive loading react to form palladium hydride and the H/Pd ratio increases, the reaction approaches the end of the two-phase region. At the end of the two-phase region, all of the palladium has been reacted to form palladium hydride, meaning that any further hydrogen introduced into the palladium bed is forced into solution within the newly formed palladium hydride lattice. This phenomenon continues throughout the Beta ( $\beta$ ) region until all of the spaces within the palladium hydride lattice are full and no additional hydrogen can be absorbed. With increasing temperature, the length of the two-phase region of the isotherm decreases until  $T_c$  is reached after which point there is no extended two-phase region. This is due to the fact that the formation of PdH is an exothermic process and is slowed as the temperature of the palladium is increased.

(a)



(b)

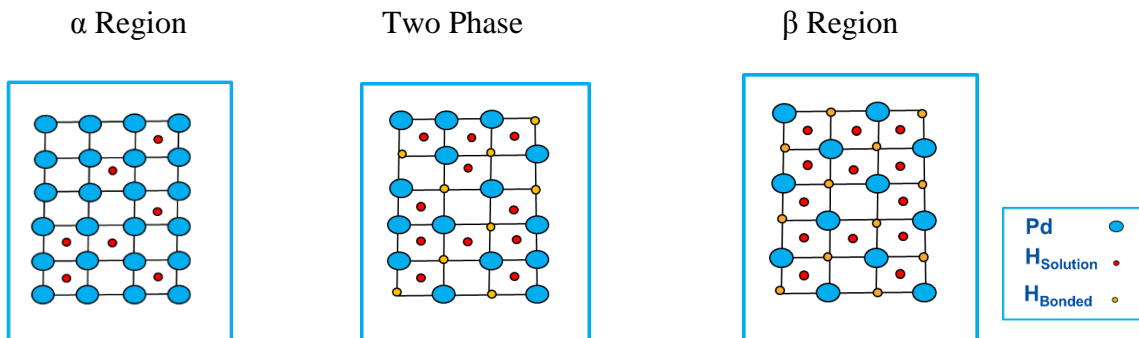


[Fig-3: (a) Phase diagram of PdH isotherms at increasing temperatures from  $T_1$  to  $T_3$ . (b) Structure of PdH in each of the three phases]

(2.2) Prior published research:

Previous research has shown a trend toward increased hydrogen pressure above a palladium bed as temperature is increased. This phenomenon is illustrated in figure 4, which is Gillespie's [Ref. 2] plot of isotherms between 20 C and 298 C. From this plot, it can also be observed that the length of the two-phase region decreases with increasing temperature, as in fig. 3.

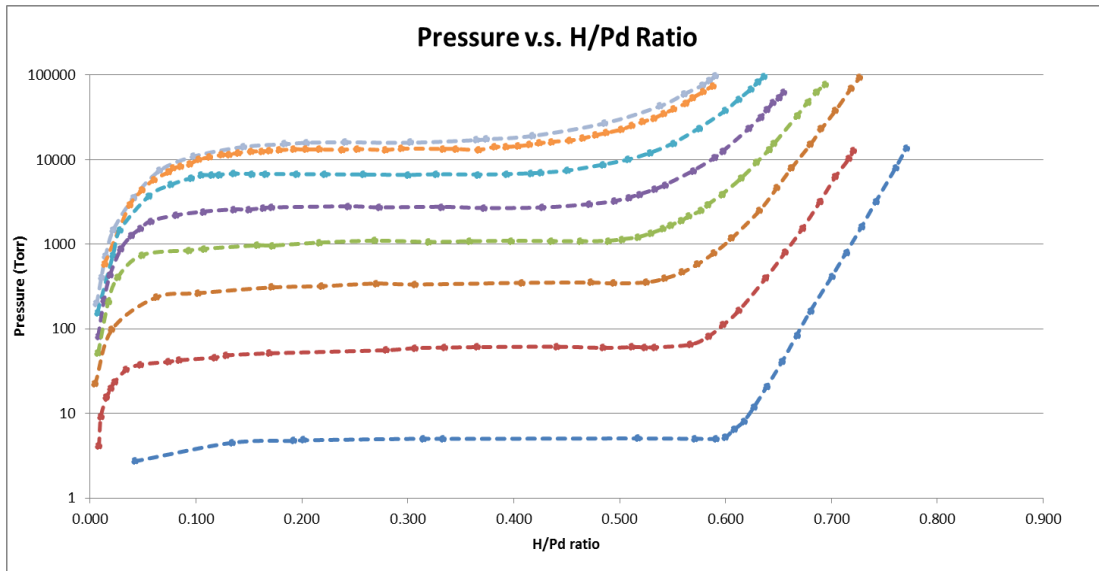


[Fig-4: Isotherms from Gillespie<sup>2</sup> for the pressure of hydrogen above a Pd Bed. Temperatures range from 20 C (bottom) to 298 C (top)]

### **Section 3: Experimental setup**

The experiment was designed to study the formation of PdH at lower temperatures: 20 C and below. A vacuum system was constructed to introduce hydrogen in discrete steps into an evacuated bed containing palladium powder so that the mass of hydrogen delivered to the bed could be measured. Between 10 and 14 psia of hydrogen was flowed through evacuated tubing from the hydrogen supply to the Pd bed as shown in Fig. 5. Each charge of hydrogen was isolated between the valves  $V_{Pd}$  and  $V_1$  before the bed was opened, to ensure that the initial pressure could be precisely measured. The measurement was taken using an MKS capacitance manometer measuring in Torr.

The experimental setup of figure 5 was designed to introduce a precisely measured quantity of hydrogen gas into the palladium bed. The palladium bed was surrounded by an evacuated secondary containment maintained between  $10^{-6}$  and  $10^{-7}$  Torr by a turbomolecular drag pump (labeled VAC in fig. 5). Vacuum pressures were measured with an ion gauge while the pressure of the hydrogen used to charge the system was measured using the two pressure transducers. For each step of the loading, hydrogen was introduced through the hydrogen supply line into the space between  $V_{iso}$ ,  $V_{Pd}$  and  $V_{Hydrogen}$ , where the pressure was measured prior to the Pd bed being opened. This cycle was repeated multiple times for each complete loading of the Pd bed.

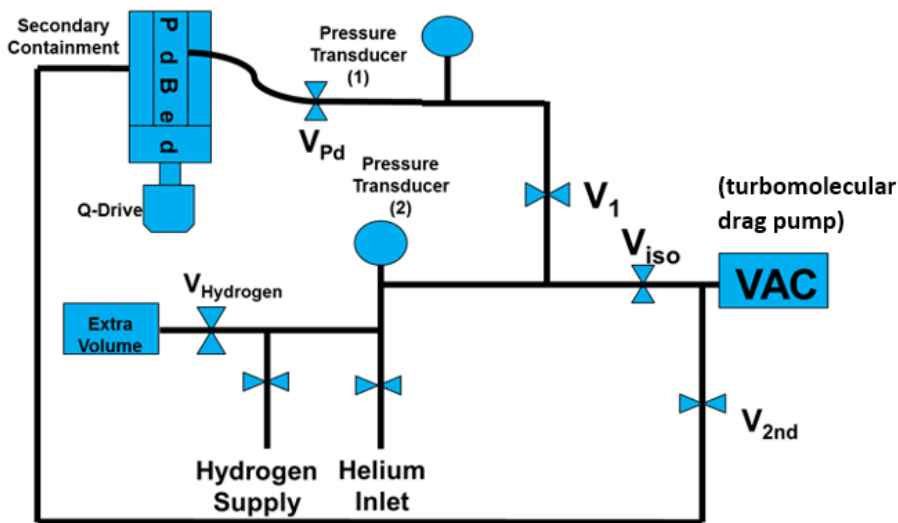


[Fig-5: Schematic of the experimental setup for introducing precisely measured quantities of hydrogen gas into a Pd bed]

In order to maintain isothermal conditions in the palladium bed, a Qdrive cryocooler was attached to the bottom of the Pd bed and all lines were evacuated with a turbomolecular vacuum pump to prevent air or water contamination from the surroundings. The hydrogen pressure measurements were taken using capacitance manometers (represented by pressure transducers 1 and 2 in fig. 5) and the vacuum pressure measurements were made using an ion gauge (near the intake of the vacuum pump at VAC in fig. 5) ensuring the highest level of precision. Figure 6 is an image of the experimental setup that is characterized by the above schematic.

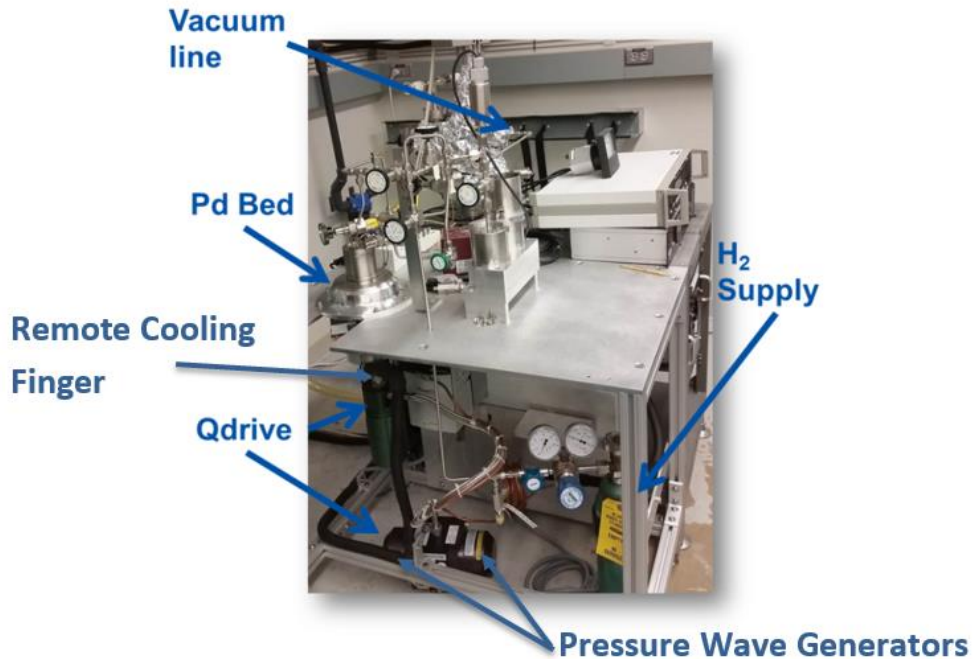


[Fig-6: The experimental setup including vacuum system and electronics]

### (3.1) Palladium bed:

Inside the palladium bed (fig. 7) is 2.5 grams (.0235 mol) of palladium sponge, which is contained within a stainless steel vessel with a free volume of 5.38 cc. The bed is contained in a large stainless steel cylinder connected to the turbomolecular vacuum pump that maintains a vacuum between  $10^{-6}$  and  $10^{-7}$  Torr. The vacuum is necessary to prevent ambient heat from entering and affecting the temperature inside the bed. Having highly resistive insulation is especially important as the focus of the experiment was on hydride formation at temperatures below 20 C. Additionally, at temperatures as low as -100 C, the rate of absorption of ambient heat is greater due to a greater temperature gradient between the Pd bed and the surrounding air, so thorough insulation is of great importance for good temperature control.

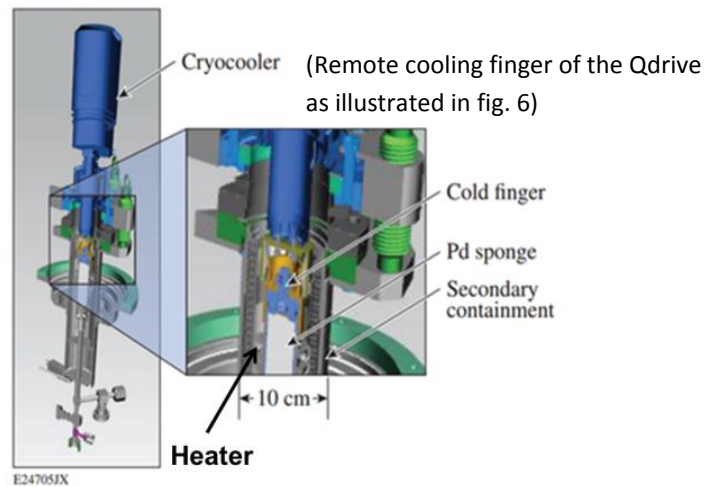


[Fig-7: Pd bed, thermally isolated by an evacuated secondary containment. The temperature is controlled with a Qdrive cryocooler and a trim heater]

### (3.2) Qdrive and Stirling cycle:

The Qdrive is a cryocooler which has a remote cooling finger attached to the bottom of the palladium bed, as shown in fig. 5, maintaining thermostatic conditions within the bed. As shown in fig. 8, the Qdrive uses a closed system of compressed helium (25 bar) which is passed through a series of heat exchangers in the cold head. The helium is forced through the heat exchangers and regenerator, labeled warm HX, cold HX, and regenerator in figure 8, under pressure generated by the pressure wave generators (PWG). These heat exchangers are all located in the cold head of the Qdrive, which is filled with the pressurized helium. The regenerator allows for the heat to be drawn from the helium to the cooling water with each cycle of the PWGs as it pumps the heat out of the helium into the cooling water. Each PWG is a linear motor connected to a piston, and as the piston is driven into the space containing the helium, the volume decreases, therefore increasing the pressure. In the Qdrive, the pressure wave generators are designed to oppose each other so that greater helium pressure can be achieved and vibration limited as each movement of a piston is opposed by that of the other piston to avoid colliding with each other.

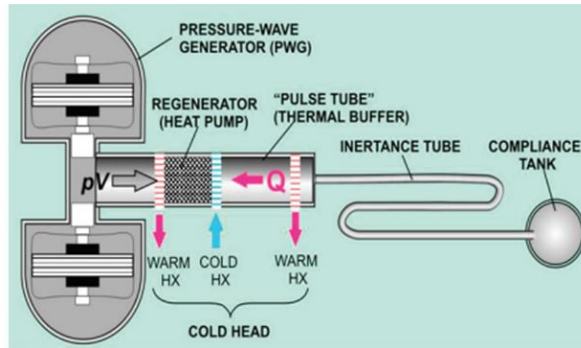


[Fig-8: Cross section of a Qdrive, which is a compressed helium, Stirling cycle, cryocooler. Image from [www. Chartindustries.com](http://www.Chartindustries.com)]

The Qdrive operates according to the principle of the Stirling Cycle which has four main thermodynamic steps beginning with an isothermal compression of the gas (from a to b in fig. 9) followed by an isochoric cooling of the gas (from b to c in fig. 9). Next is an isothermal expansion of the gas (from c to d in fig. 9). The final step is an isochoric heating of the gas (from d to a in fig. 9) after which the cycle repeats.

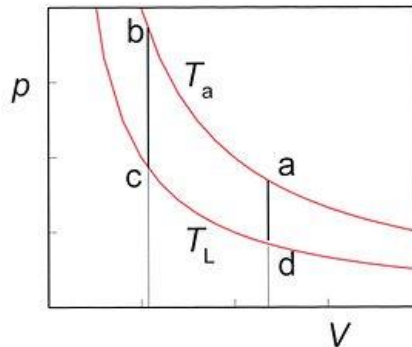


[Fig-9: Paths in the (P,V) plane taken by the He gas in a Qdrive cryocooler. The curved paths are isotherms. Image source: google images]

Inside the Qdrive, the cycle begins in stage 1 with the compression of the helium gas through the cold heat exchanger and into the pulse tube as the PWGs move towards each other. The helium is then forced into the inertance tube (see Fig. 8), where its velocity increases due to the smaller diameter of the opening to the tube relative to the diameter of the pulse tube. Due to the inertia of the helium and its momentum out the inertance tube, as well as its higher velocity towards the compliance tank, the helium undergoes the expansion step of the Stirling Cycle. As the helium expands, it absorbs the heat from the cold head which is attached to the palladium

bed. When the PWG's reverse directions, the helium is drawn back to the pulse tube through the hot heat exchanger, dissipating the heat from the helium before the cycle repeats.

### (3.3) Ion gauge:

The quality of the vacuum was measured using an ion gauge (fig. 10) driven by a Granville-Phillips 307 Vacuum Gauge Controller to obtain readings in the high vacuum region. The ion gauge uses a filament which, upon heating, thermionically emits electrons into an electric field, accelerating them, and providing them with the energy required to ionize any gas molecule within the cylindrical space defined by the grid. A wire called the collector runs down the middle of the grid and carries the current generated by the positively charged gas ions inside the grid volume. That current is directly proportional to the pressure of the gas inside. The ion gauge was used to measure the vacuum when gas pressures were below  $10^{-3}$  Torr.

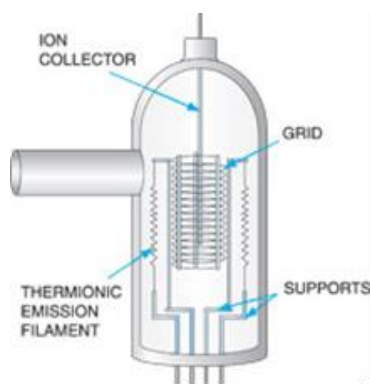


[Fig-10: Ion gauge used to measure pressures in the high vacuum range]

### (3.4) Capacitance manometer:

Initial and final hydrogen pressures were measured with an MKS Baratron pressure transducer, which utilizes a capacitance manometer (fig. 11), in the pressure range 0.01 to 800 Torr. This particular manometer is rated to measure over a pressure range of 0 to 1,000 Torr. The pressure measurements taken in these experiments were, therefore, well within the acceptable operating range of the device.

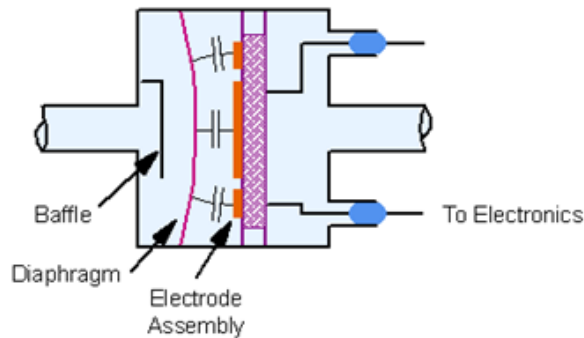


[Fig-11: Capacitance manometer used to measure accurately across multiple decades of pressure]

A capacitance manometer contains an air-gap capacitor that has one electrode attached to the stainless outer case and another attached to an interior diaphragm. Under increasing pressure from the input piping to the gas source being measured, the diaphragm deforms inward and the air gap between the two electrodes of the capacitor decreases, thereby decreasing the capacitance. Contained within the same circuit as the diaphragm are an oscillator and a demodulator, which measure the capacitance while the MKS Type 670 Signal Conditioner records the readings. The capacitance manometer is efficient at recording hydrogen gas pressure because the design is insensitive to gas species and can be configured to be linear over a broad pressure range.

### (3.5) Turbomolecular drag pump:

A turbomolecular drag pump (fig. 12) was used to evacuate all of the 1/4" dia. stainless steel piping within the system to pressures between  $10^{-6}$  and  $10^{-7}$  Torr to remove any impurities that may have entered from the surroundings. The turbomolecular drag pump uses between 10 and 40 different stages of blades to compress the input gas and remove it from the vacuum system. Each stage consists of a rotor and a stator pair, with the rotor spinning between 9000 and 90,000 rpm. The stator deflects the molecules propelled by the rotor into the next stage to compress the volume of air towards the exhaust. This pattern repeats as the gas travels through the pump until it is expelled from the exhaust. Turbomolecular pumps are capable of pumping between 100 and 800 liters per second. This pump was run continuously to ensure that the secondary containment of the Pd bed and all of the piping were evacuated and the system was rid of any leftover hydrogen gas from prior loadings.

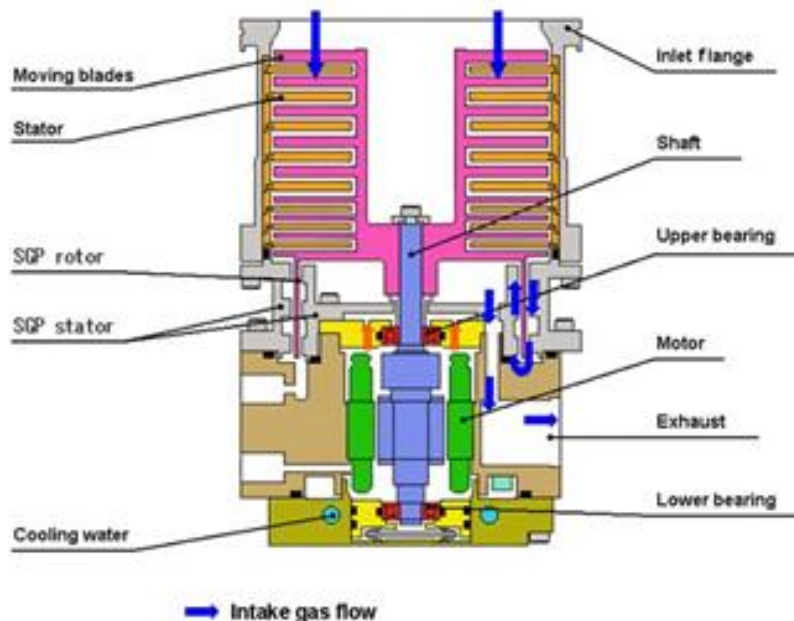


[Fig-12: Turbomolecular drag pump used to evacuate the system to between  $10^{-6}$  and  $10^{-7}$  Torr]

## **Section 4: Procedure**

### (4.1) Loading the palladium bed:

The palladium bed (fig. 5) was loaded in a stepwise fashion, allowing each known mass of hydrogen released into the bed to reach equilibrium. To measure the mass of hydrogen introduced into the bed, 18.2 cc of piping was loaded with hydrogen at 297 K and the pressure recorded. The pressure was adjusted to control the amount of gas desired for each loading but ranged from 3.8 to 13.8 psi (200 to 713 Torr). When the valve to the palladium bed was opened, the gas flowed into the bed and was absorbed into the palladium sponge until equilibrium was established, at which point the palladium bed was isolated and the pressure in the hydrogen line was recorded again. This process was repeated for each loading. Initial and final pressure measurements provided the equilibrium vapor pressure and allowed the mass of hydrogen introduced and the hydrogen to palladium ratio to be calculated for each loading.

#### (4.2) Unloading in steps:

In order to unload the bed in steps, all lines connected to the palladium bed were evacuated to  $10^{-6}$  Torr. The expansion volume was then isolated from the vacuum pump. Connected to the Pd bed, the expansion volume is composed of the piping from the bed to the tank labeled extra volume (see Fig-5), yielding a total volume of 544.8 cc when  $V_{\text{iso}}$  is closed. A larger volume was necessary to remove any additional gas during each step in order to expedite the unloading. Secondary containment of the palladium bed was open to the vacuum pump at all times except when the hydrogen was being pumped out of the expansion volume. The reason for this was to prevent hydrogen entering the secondary containment volume and creating a thermal short. Once the pressure inside the expansion volume stabilized and the palladium bed reached equilibrium, the bed was isolated and the pressure in the expansion volume was measured. Doing so provided data on the mass of gas removed from the bed and on the change in the hydrogen/palladium ratio. Following this, the secondary containment was isolated from the vacuum pump and the expansion volume was evacuated to  $10^{-6}$  Torr. This process was repeated for each step of the unloading to collect the data for each isotherm.

#### (4.3) Unloading by heating:

To clear the bed of all hydrogen prior to each run, the palladium bed and all of the hydrogen lines were evacuated. To enable this, the ion gauge was powered down to avoid burning out the filament from exposure to the high gas pressures (above  $10^{-3}$  Torr) released from the hydrogen supply lines. Next, the palladium bed and secondary containment vessel were isolated by closing  $V_{\text{Pd}}$  and  $V_{2\text{nd}}$ . Lastly, the valve to the vacuum pump was opened allowing the turbomolecular vacuum pump to remove the gas and evacuate those lines to below 1 Torr. Following this,  $V_{\text{Pd}}$  was opened and the hydrogen began to desorb from the palladium sponge. Once the pressure reading from the bed dropped below 0.3 Torr, the Qdrive was turned off and the temperature of the bed was raised in 10 to 20 degree increments to 200 C. The temperature of the bed was left at 200 C overnight to ensure desorption of all hydrogen from the palladium and to establish a hard vacuum ( $10^{-6}$  Torr) in all of the lines and the palladium bed. Once this was achieved, the temperature was decreased towards the desired temperature for the next loading by reducing the heat source. When the temperature dropped below 120 C, the Qdrive was re-

enabled, allowing the bed to be cooled to the new starting temperature. Once the temperature of the bed stabilized at the desired value, the palladium bed was isolated by closing  $V_{Pd}$  and opening  $V_{2nd}$  to evacuate the secondary containment vessel and insulate the bed from the environment. At this point, the system was ready for the palladium bed loading procedure to begin again.

## **Section 5: Data**

### (5.1) Experimental results:

For each loading of the palladium bed, pressure, bed temperature and H/Pd data were recorded. Isotherms were plotted on a hydrogen pressure versus hydrogen to metal ratio graph (fig. 13) to study the vapor pressure of hydrogen above the palladium sponge throughout the hydride formation process. Loadings were made from -40 C to 200 C. The data shown in Fig 13 reveal that the hydrogen vapor pressure increases as the palladium temperature is increased. From this observation, it was concluded that palladium will compress hydrogen well below 423 K (150 C) and throughout the two-phase region which extends from H/Pd ratio of 0.1 to 0.6. The length of the two phase region of each isotherm varies with temperature, providing an experimental illustration of the behavior shown in figure 3.

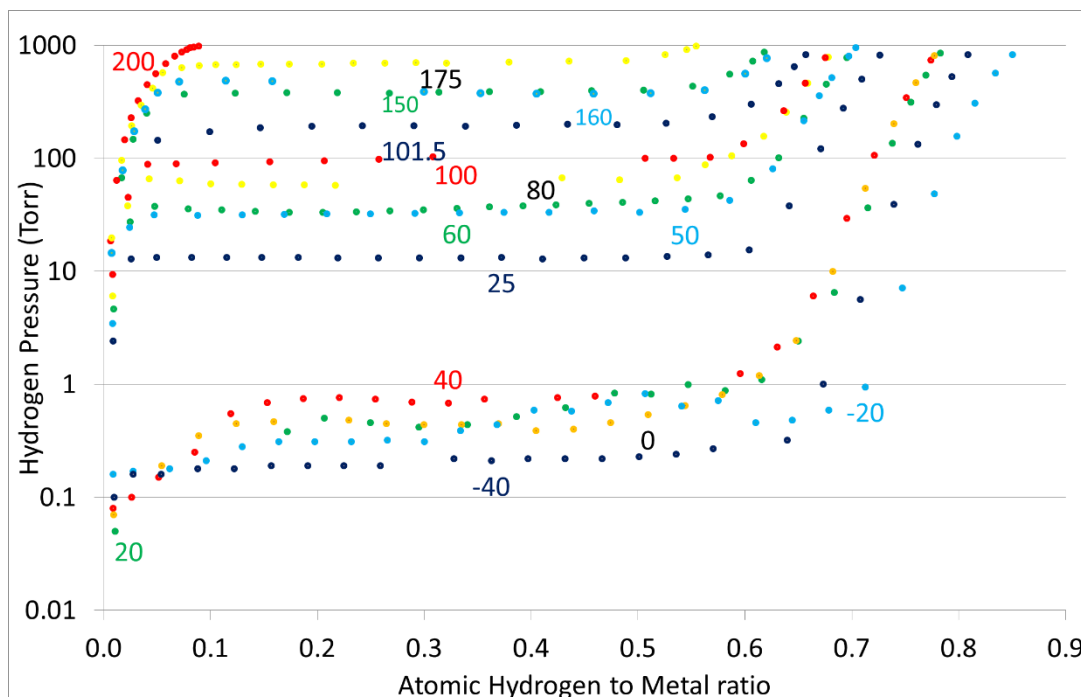


[Fig-13: Isotherms returned by this study with temperatures ranging from -40 C to 200 C]

The 25 C isotherm has a two-phase region of higher equilibrium pressure than the 40 C isotherm, which should not be the case. The probable cause of this could be premature pressure measurements made before the reaction reached equilibrium during the 25 C loading. Additionally, the low pressure of the two-phase region of the 40 C isotherm could be due to temperature fluctuations during the loading that may have caused the vapor pressure of the hydrogen over the palladium bed to decrease beyond expected the equilibrium for that temperature.

As the temperature of the isotherm increased, a decrease in the length of the two-phase region was observed. The theoretical limit to form palladium-hydride in the palladium hydrogen system occurs at PdH, that is to say one hydrogen for every palladium atom. At higher temperatures, it is energetically more favorable to dissolve hydrogen in palladium hydride when the H/Pd ratio is between 0.5 and 0.6. However, the data shows that as the temperature of the metal decreases below 20 C, the tendency to form palladium hydride beyond H/Pd ~ 0.6 is favored relative to dissolving hydrogen in the hydride because the H/Pd ratio at which the plot curves up after the two-phase region increases with decreasing temperature. The lower isotherms

shown in Fig. 13 indicate that the quantity of hydrogen that palladium is capable of capturing and storing increases as the temperature of the palladium decreases due to the longer two-phase region of the plot.

Each of the loadings was repeated to demonstrate the consistency with which the isotherms could be reproduced. Figure 14 provides examples of three sets of data taken at -20 C. Each data set indicates that the two-phase region spans a H/Pd range from 0.1 to 0.65, and an equilibrium pressure of approximately 0.2 to 0.5 Torr over that range.

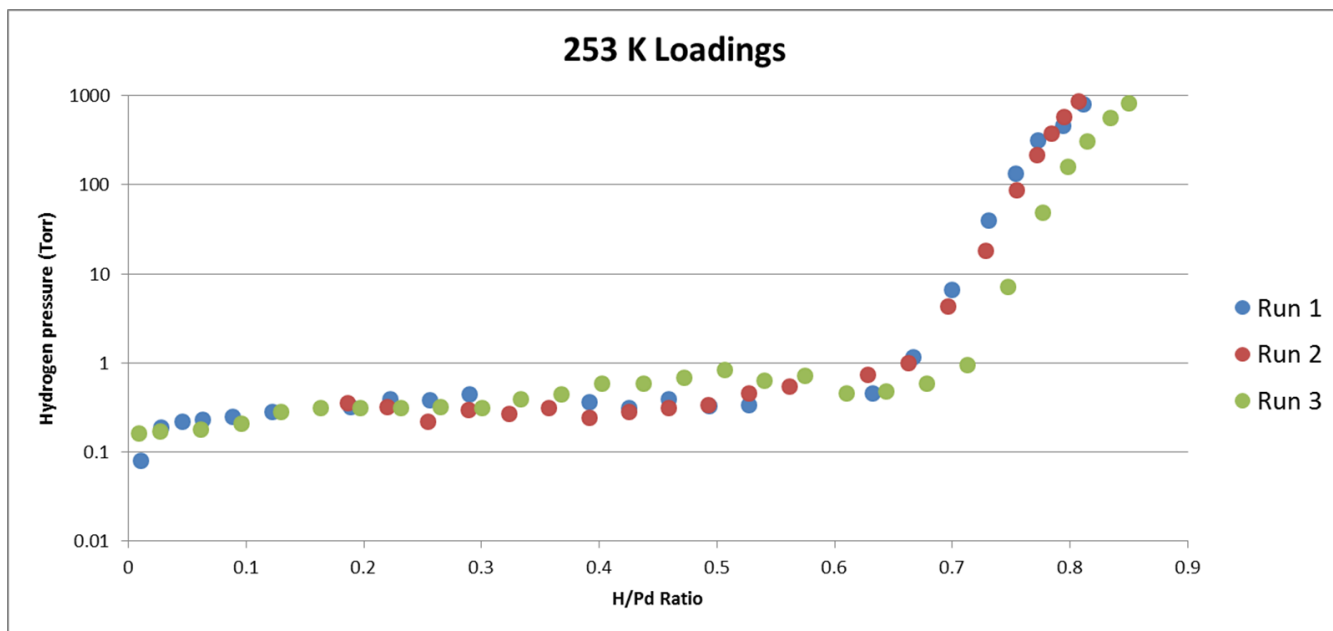


[ Fig-14: Three isotherms at -20 C, confirming reproducibility]

### (5.2) Van't Hoff curves:

To describe the vapor pressure dependence in the two-phase region, a mathematical relationship was needed to relate the temperature of the palladium bed to the vapor pressure of hydrogen above it. The Van't Hoff equation shown below (equation 1) was used.

The Van't Hoff equation relates the natural log of pressure,  $\ln(P)$ , to the enthalpy of formation of palladium hydride,  $\Delta H_f$ , and the entropy of formation,  $\Delta S_f$ , of palladium hydride for any given isotherm at temperature  $T$ .  $R$  is the ideal gas constant. The Van't Hoff equation was simplified by substituting constants  $A$  &  $B$  as shown in equation 2. The constant  $A$  represents the enthalpy of formation of palladium hydride divided by the ideal gas constant. The constant  $B$  represents the entropy of formation of palladium hydride divided by the ideal gas constant.

$$\ln(P) = \frac{-\Delta H_f}{RT} + \frac{\Delta S_f}{R} \quad (1)$$

$$\ln(P) = \frac{-A}{T} + B \quad (2)$$

To determine the constants  $A$  and  $B$ , plots were constructed of pressure dependence against inverse temperature using data from the two-phase region across each of the distinct isotherms at several fixed H/Pd ratios. As shown in Fig. 15, for two mole ratios 0.21 and 0.50, the data for each temperature were compiled on a plot of  $\ln(P)$  versus  $1/T$ . A best-fit line was then regressed returning the best-fit  $A$  and  $B$  coefficients.

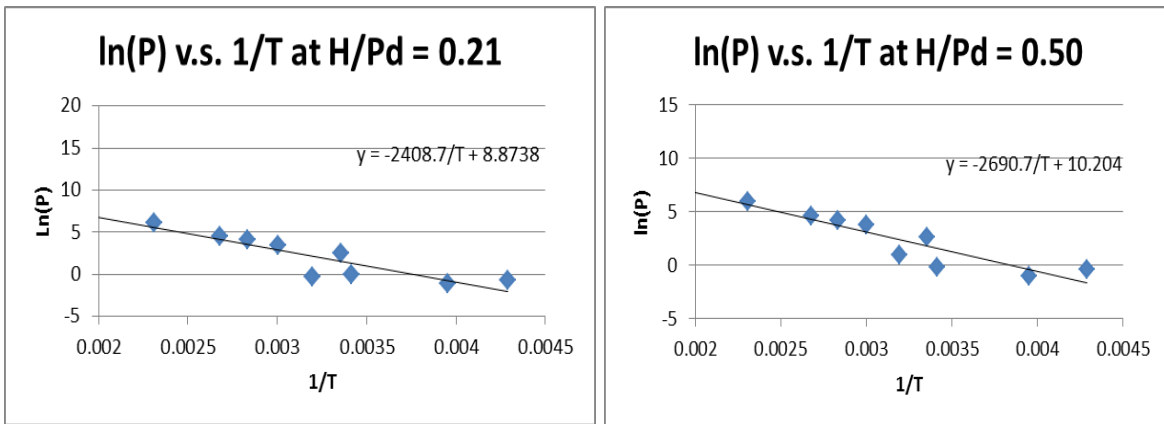


[Fig-15: Van't Hoff curves for H/Pd ratios of 0.21 (left) and 0.50 (right), showing a linear relationship across the length of the two-phase region]

Pressure measurements at  $H/Pd = 0.21$  were chosen because that ratio was common for the majority of the isotherms due to the quantity of gas added during each step of each loading.

The two sets of coefficients returned by these plots reveal the degree of correlation for the exponential fit for the two-phase region of the plot at the two extremes of the H/Pd ratios studied. It is noteworthy that the constants for the two cases are similar. The slight increase in the two constants for the higher H/Pd value is consistent with the observation that the slope of the plateau region between 0.2 and 0.5 is not zero but increases slightly as the H/Pd ratio increases.

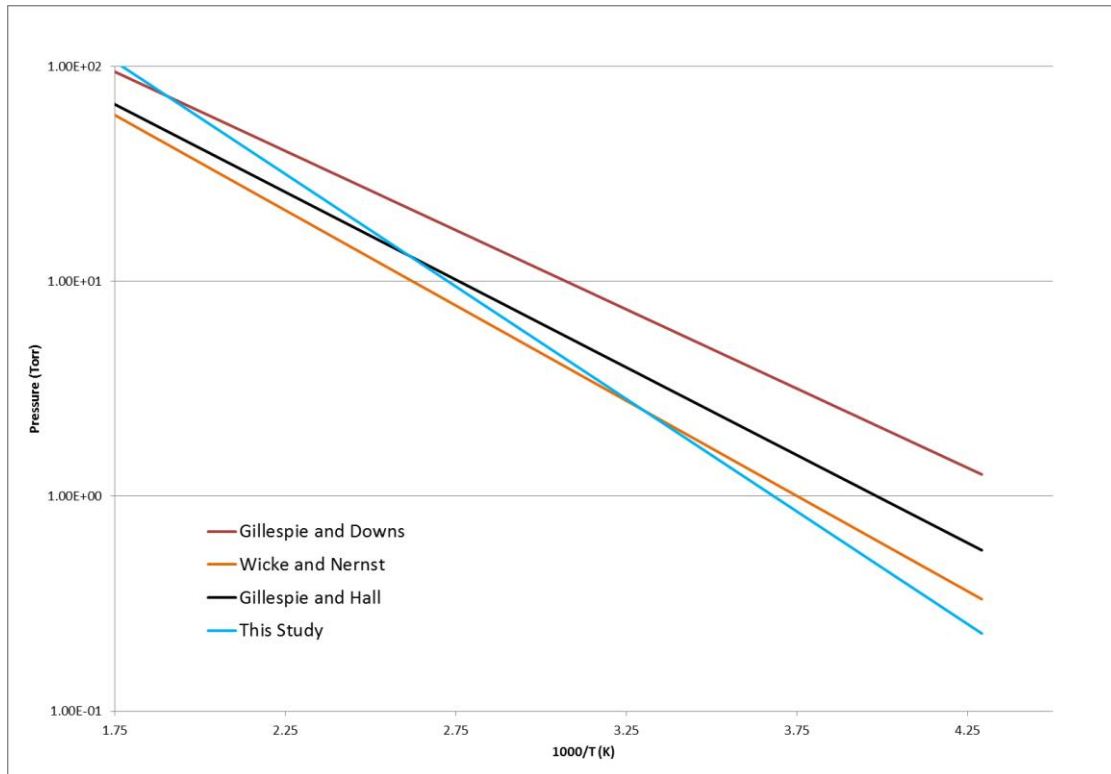
(5.3) Comparison with prior research:

Table 1 is a compilation of the data collected by previous researchers. This table includes the A and B constants as well as the temperature range over which isotherms were obtained. The constants returned by this study are close to those of previous experiments, although some variation is evident. This variation could have been the result of the significantly wider temperature range undertaken by this experiment. Alternately there may have been outliers on certain isotherms at the H/Pd ratios sampled to construct the Van't Hoff plots. Such values could have resulted from pressure measurements taken prior to equilibrium, or an environmental factor causing unstable temperatures, especially at the extreme ends of the temperature range.

| <b>Author</b>                              | <b>A (K)</b> | <b>B</b>    | <b>Temp. Range (K)</b> |
|--|--------------|-------------|------------------------|
| <b>Wicke and Nernst<sup>4</sup></b>        | <b>2039</b>  | <b>7.65</b> | <b>195 to 323</b>      |
| <b>Gillespie and Hall<sup>6</sup></b>      | <b>1878</b>  | <b>7.48</b> | <b>273 to 453</b>      |
| <b>Ratchford and Castellan<sup>5</sup></b> | <b>2028</b>  | <b>7.98</b> |                        |
| <b>This study</b>                          | <b>2409</b>  | <b>8.87</b> | <b>233 to 473</b>      |

Table 1: Comparison of constants derived from this study against values published in the literature

Figure 16 plots the pressure-temperature relationship given by Eq. 2 using the Van't Hoff constants from this study and those of the other researchers. The present curve is consistent with the findings of the prior research, although characterized by a slightly steeper slope. Overall, the variability observed between the Van't Hoff constants of this study and those of prior research was not found to be statistically significant.



[Fig-16: Dependence of pressure on temperature based on the Van't Hoff constants obtained from previous studies and this study]

The Van't Hoff curve also allows for a comparison between palladium and other hydrogen-compressing metals. In Fig. 17, the Van't Hoff curve for uranium is plotted along with the curves for palladium to illustrate that uranium must be heated to significantly higher temperatures to achieve comparable hydrogen vapor pressures with palladium. The fact that uranium provides lower vapor pressures at low temperatures indicates that uranium is better suited for longer-term hydrogen storage than palladium. However, palladium is better suited as a hydrogen compressor because higher pressures can be attained at lower temperatures compared to uranium.

Compressing tritium at lower temperatures means that less tritium will permeate through the containing vessels. Additionally, palladium is better suited to deliver tritium to targets because it desorbs the hydrogen at lower temperatures, allowing less stress on the cryogenic cooling equipment and easier maintenance of the temperature of the target.

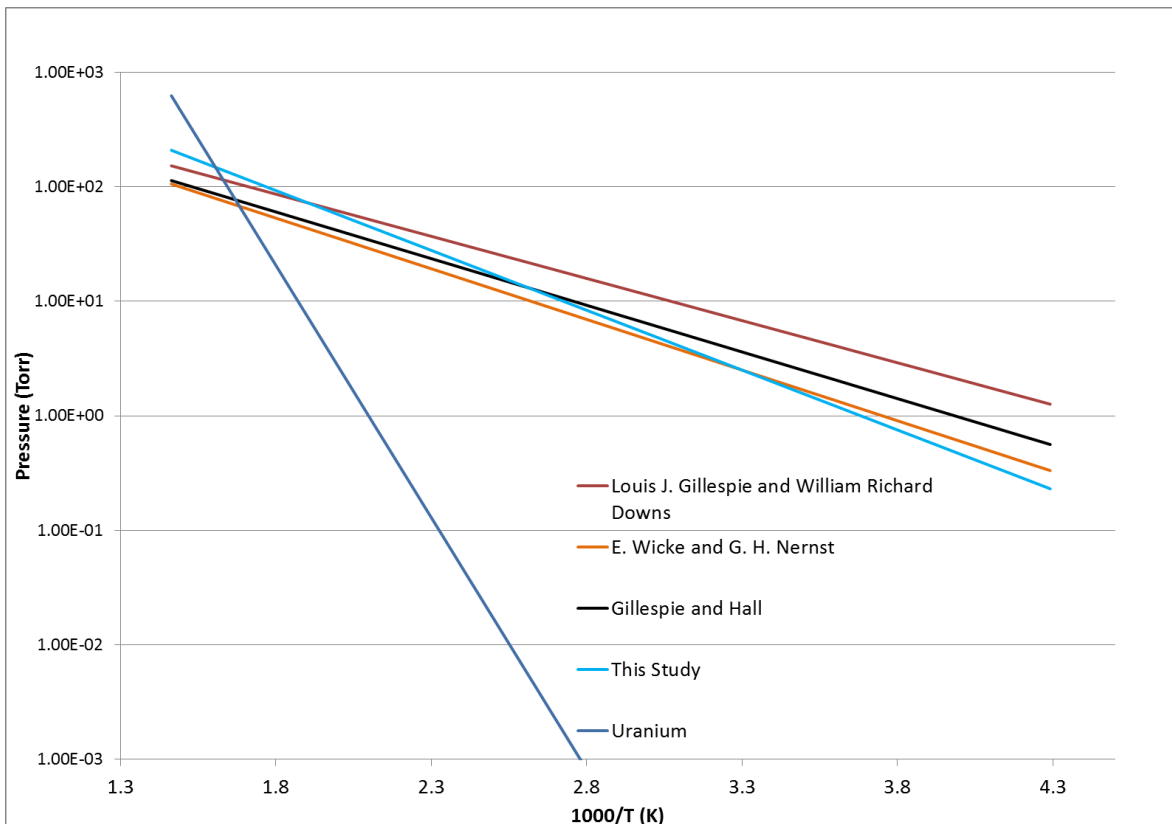


[Fig-17: As figure 16 except that data for uranium has been added. Gas is desorbed from palladium at lower temperatures than for uranium]

## **Section 6: Discussion and Conclusions**

Though the data correlated well with the results of prior experiments, there were slight differences between the Van't Hoff constants returned by this study and those of prior research. One of the potential causes for this variation in the results could have been temperature non-uniformity throughout the palladium bed.

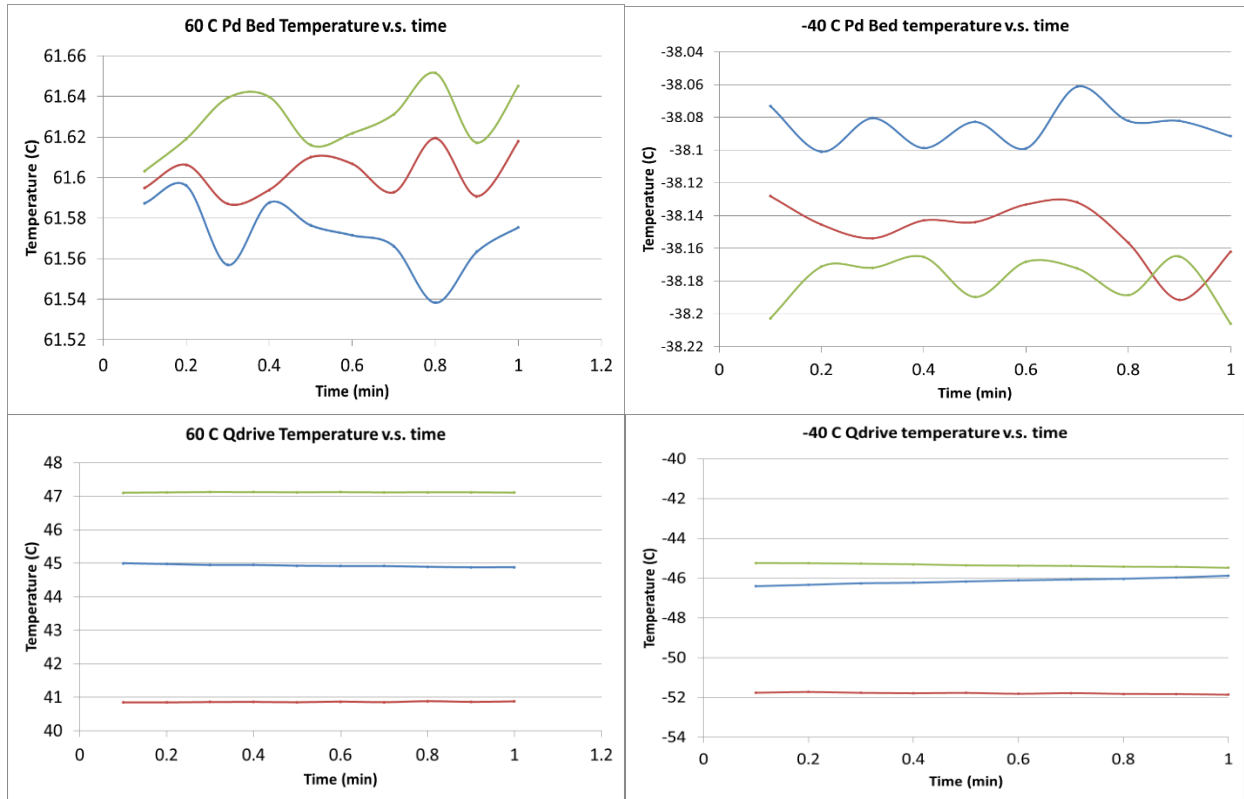


[Fig-18: Temperature of the Pd bed (top) and Qdrive (bottom). Temperature measurements from the Pd bed versus time for 3 loadings at 60 C (left) and -40 C (right), demonstrate temperature variability of the Pd bed. There was difficulty maintaining completely thermostatic conditions in the Pd bed with the Qdrive and the trim heater opposing each other]

The plots in Fig. 18 indicate the temperature fluctuations that were present in the palladium during a given step of a loading with each line representing the rate of change of the palladium bed during that particular step. Each color line is plotted with the temperature readings from the thermocouples at the Qdrive and Pd bed at 60 and -40 C, respectively. Each line shows a varying slope which indicates that throughout each step, the temperature changed but at a different rate from step to step. Such fluctuations in the temperature of the palladium bed are likely the result of the Qdrive opposing the trim heater. This effect became more apparent at the outer bounds of the temperature range studied. Figure 18 shows an approximately 7 degree spread in the Qdrive temperatures for the three loadings performed at -40 C. Based on the plots in Fig. 18, the variation in equilibrium pressures in the two-phase region between multiple loadings at a particular temperature is most likely due to the fact that the Qdrive temperature varied between, as well as during, each loading. This effect may also have contributed to the

length of time required for the reaction to equilibrate in the two-phase region, resulting in pressure readings being taken too early.

Overall, based on the data returned by this study, it can be concluded with a high degree of confidence that palladium is a good compressor of hydrogen at lower temperatures. In addition, the fill-tube method for charging targets by desorbing hydrogen from a palladium bed would be a safe and viable alternative to the current method of permeation filling with a gaseous mixture.

### **Section 7: Acknowledgements**

I would like to thank my advisor Dr. Shmayda, as well as Dr. Sharpe for sharing their knowledge and keen insights as well as their advice regarding the experimental procedure throughout my time at LLE. Additionally, I would like to thank Dr. Craxton for organizing the Summer Internship Program and making this experience possible.

### **References:**

- 1: D. H. W. Carstens and W. R. David. Equilibrium Pressure Measurements in the Beta region of Palladium Protide and Palladium Deuteride. National technical Information Service. March 1989
- 2: L. J. Gillespie and W. R. Downs. The Palladium-Deuterium Equilibrium. Research Laboratory of Physical Chemistry, Massachusetts Institute of Technology. Jul 10, 1939
- 3: F. D. Manchester, A. San-Martin, and J. M. Pitre. The H-Pd (Hydrogen palladium) System. Journal of Phase Equilibria. (15, 1) 1994
- 4: E. Wicke and G. H. Nernst. Zustandsdiagramm und thermodynamisches Verhalten der Systeme Pd/H<sub>2</sub> und Pd/D<sub>2</sub> bei normalen Temperaturen; H/D-Trenneffekte. Institut für Physikalische Chemie der Universität Münster. Nov 26, 1963
- 5: Mueller, Blackledge, and Libowitz. Metal Hydrides. Academic Press. Pg 641-3. 1968
- 6: L. J. Gillespie and F.P. Hall, The Palladium-Hydrogen Equilibrium and Palladium Hydride, American Chemical Society (1964)

**Frequency Conversion Crystal Designs for Improved Ultraviolet Power**

**Balance on the 60-Beam OMEGA Laser**

Nathan Morse

**Allendale Columbia School**

Rochester, NY

Advisor: Mark Guardalben

**Laboratory for Laser Energetics**

University of Rochester

May 21, 2017

**Summary:**

A Monte-Carlo-based method was developed and used to characterize the predicted performance of several different frequency conversion crystal designs for the 60-beam OMEGA laser located at the University of Rochester's Laboratory for Laser Energetics (LLE). The OMEGA laser is used to conduct implosion experiments and basic physics experiments in support of the National Inertial Confinement Fusion (ICF) program. A key element to achieving LLE's 100-Gbar implosion goal is improving the ultraviolet power balance of the OMEGA laser's 60 beams. The frequency conversion crystals (FCCs) on OMEGA convert an infrared laser pulse to an ultraviolet laser pulse using three crystals (a single doubler and two triplers), and were originally designed for higher laser input intensities and larger spectral bandwidth than are currently required. Less sensitivity of the ultraviolet laser power balance to beam-to-beam variations in the infrared energy and FCC angular alignment might be possible by using a different FCC design. A Monte-Carlo-based merit function was developed and used to characterize two different categories of FCC designs: 1) A reconfiguration of the current FCCs, and 2) FCC designs with alternative crystal lengths. Using an ultraviolet pulse designed for an 80-Gbar implosion campaign, improved power balance was achieved by eliminating OMEGA's second tripler. Additional improvement to power balance was obtained in a single-tripler design by changing OMEGA's crystal lengths from the current 12.2 mm to 15 mm.

## I. Introduction

At the University of Rochester's Laboratory for Laser Energetics (LLE), scientists are attempting to create fusion in the laboratory using the 60-beam OMEGA laser. The method chosen, direct drive inertial confinement fusion, is performed by impacting a small spherical deuterium/tritium (DT) target with high-power ultraviolet lasers, compressing it with extreme acceleration. When the lasers hit the target, the outer shell explodes outwards. Newton's Third Law (every action must have an equal and opposite reaction) dictates that the rest of the target accelerates inwards and implodes. The radius of the target decreases by approximately a factor of 30, and the resulting high density and temperature within the target cause the DT fuel to fuse. The main goal of this research is to achieve ignition, at which point the energy output from the fusion process is greater than the energy of the impacting lasers.<sup>1</sup> The current goal of LLE is to achieve 100 Gbar of pressure on the target in a direct-drive implosion, a value that is required for ignition at National Ignition Facility (NIF) scale energies.

There are many challenges to direct-drive inertial confinement fusion. One of the main difficulties is achieving implosion uniformity. Small beam-to-beam variations in on-target irradiance can produce hotter and colder spots on the target's surface, causing the target to deform from an exact spherical shape as it implodes, inhibiting fusion.<sup>2</sup> Several possible sources of irradiation nonuniformity are being investigated at LLE, including the frequency conversion crystals (FCCs) that convert each of OMEGA's 60 beams from infrared (IR) to ultraviolet (UV) laser energy.

Each of the frequency conversion systems on OMEGA originally consisted of a doubler crystal and a single tripler crystal.<sup>3</sup> The doubler crystal converts some of the incoming IR light into green light, and the tripler crystal converts the green and residual IR light to UV light. A technique called Smoothing by Spectral Dispersion (SSD) is implemented in OMEGA to increase implosion uniformity on the target by phase modulating the IR light to increase its spectral bandwidth, and then angularly dispersing this bandwidth on the fusion target using diffraction gratings.<sup>4</sup> In order to efficiently convert all IR wavelengths within the bandwidth to the UV, a second tripler had been added to the frequency conversion

system,<sup>5,6,7</sup> as shown in Figure 1. However, the current high-pressure implosion goal requires smaller bandwidth and lower IR intensities into the FCC than required for previous experiments.

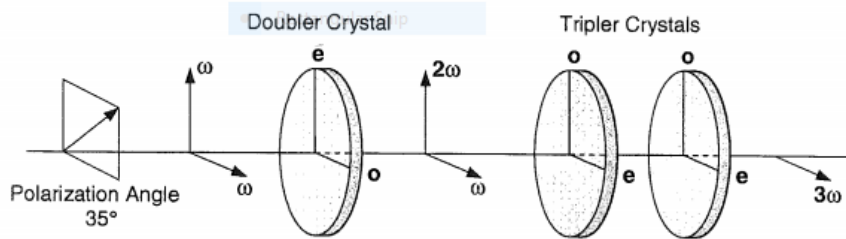


**Figure 1:** A diagram of the OMEGA frequency conversion system. The input IR beam has an electric field polarization that is at 35 degrees to the *o* (ordinary) axis of the doubler crystal and an angular frequency of  $\omega$ . The frequency of the green beam is  $2\omega$ , and the frequency of the ultraviolet beam is  $3\omega$ . The polarization angle determines how the photons will be distributed to the *e* (extraordinary) and *o* axes of the doubler crystal. In the nonlinear frequency conversion process, each crystal produces an output beam of light with electric field along its *e* axis whose angular frequency is the sum of the frequencies of the crystal's inputs. Conversion efficiency is maximized by tilting each crystal to an appropriate angle about its *o* axis.

In order to achieve a precise pressure on all points of a spherical target, all 60 of OMEGA's beams must be approximately equal in power, or power balanced, throughout the temporal width of the laser pulse (typical pulse width is 1 – 3 nanoseconds). Preliminary simulations by LLE scientists suggested that improved beam-to-beam power balance might be possible while maintaining sufficient IR-to-UV conversion efficiency under current FCC-input beam requirements by removing the second tripler. In the work reported here, the frequency conversion process was simulated using the smaller IR bandwidth and lower IR intensity conditions, and a Monte-Carlo-based model was developed and used to calculate the expected temporally dependent UV power nonuniformity across all 60 of OMEGA's beams for several different FCC designs. This approach allowed the different designs to be compared based upon the sensitivity of each design to variations in IR input and FCC configuration (e.g., IR input energy and polarization angle, angular alignment of the FCCs and differential tripler angle, and width of the air gap between the two tripling crystals) and an optimized design to be chosen. Two categories of FCC designs

were optimized: 1) A reconfiguration of the current FCCs, and 2) FCC designs with alternative crystal lengths.

In Section II, we describe the relationships between the parameters of the frequency conversion process and the ultraviolet pulse. In Section III, we discuss the Monte-Carlo method used to predict errors in UV power. In Section IV, we compare the best designs for OMEGA that were found using the Monte-Carlo method. In Section V, we show the process behind optimizing for crystal length, and observe the strengths and weaknesses of an FCC design with alternate length crystals. In Section VI, we conclude with a brief discussion of the impact of this study and future work.

## **II. Frequency Conversion Process**

Figures 2 and 3 show how the efficiency of converting IR light entering the FCCs to UV light depends on the tilt angle of the doubler and tripler, respectively, for several different values of IR intensity. These plots represent a single-tripler FCC design with crystal lengths of 15 mm. Similar plots of conversion efficiency were generated for several different FCC designs using the harmonic generation code Mixette,<sup>8</sup> which provided the ratio of UV output intensity to IR input intensity for each FCC design investigated. Using these plots, “look-up” tables were formed that mapped a given IR intensity to a UV intensity for beam propagation in the forward direction through the FCC, while for backward propagation, the tables provided the UV-to-IR mapping. Backward mapping was used to determine the required IR pulse shape for a desired UV pulse shape. Linear interpolation between discrete values within these tables provided intermediate values of intensity, so that only a limited number of Mixette simulations were required. In this study, a desired UV pulse shape for the 80-Gbar shot campaign was used, as shown in Figure 4 with its corresponding IR pulse in the absence of any crystal detuning.

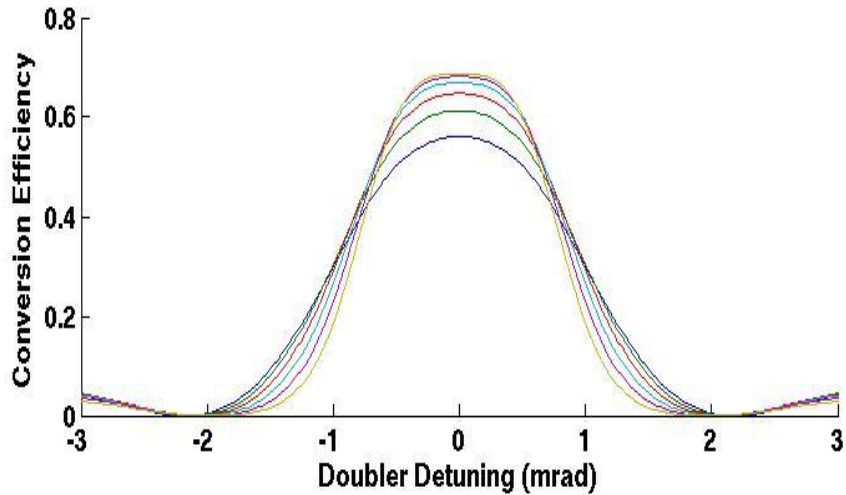


**Figure 2:** Graphs of IR to UV conversion efficiency v. doubler detuning for different IR intensities entering a 15-mm single tripler design. In this design, the second tripler was removed, and FCCs of 15 mm were used instead of the current 12.2-mm FCCs in OMEGA. A single IR intensity was used for each curve shown, with IR intensities ranging between  $0.5 \text{ GW/cm}^2$  and  $1.0 \text{ GW/cm}^2$  (inclusive), and an increment of  $0.1 \text{ GW/cm}^2$  between curves. For this set of IR intensities, greater IR intensity corresponds to greater conversion efficiencies at  $0^\circ$  doubler detuning. As the doubler is detuned, conversion efficiency decreases nonlinearly, and differently for each IR intensity.

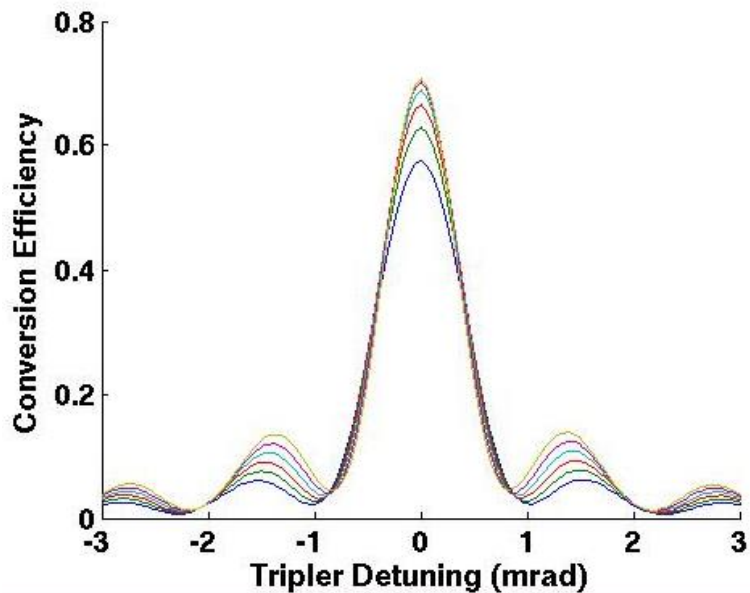


**Figure 3:** Graphs of IR to UV conversion efficiency v. tripler detuning for different IR intensities entering a 15-mm single tripler design. This is for the same FCC design and IR intensities used in Figure 2, where higher IR intensities also correspond to higher conversion efficiencies at  $0^\circ$  tripler detuning. Tripler detuning decreases conversion efficiency at a much greater rate than doubler detuning, as shown by the sharper efficiency peaks at  $0^\circ$  detuning in Figure 3 than in Figure 2. This implies that tripler detuning will be a larger source of error than doubler detuning.

Generation of an IR pulse that would, presuming no errors, convert to the desired UV pulse is necessary because the effects of frequency conversion parameters are dependent upon IR intensity. Among the FCC errors investigated, differential tripler detuning, IR polarization angle, and air gap distance were found to have less of an effect on the UV pulse than errors in IR energy, doubler detuning, and tripler detuning.

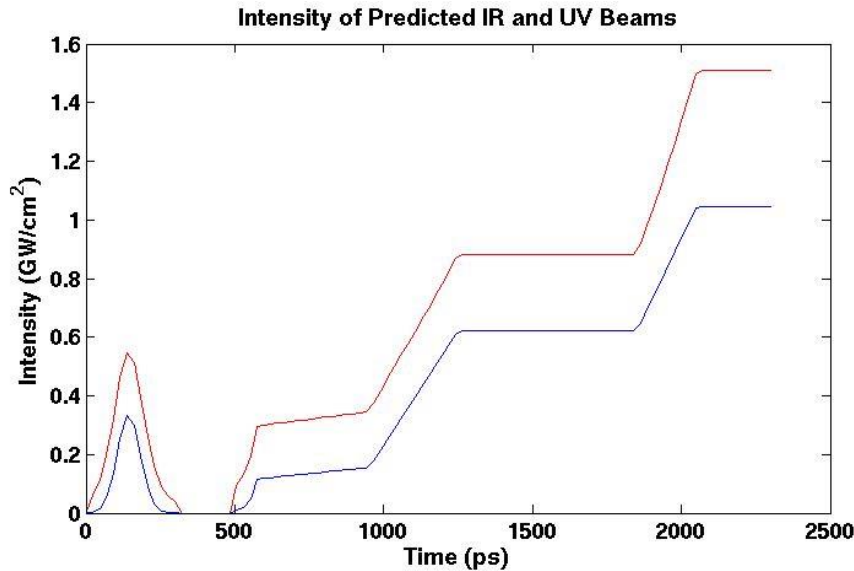


**Figure 4:** Desired pulse shape in IR (red) and UV (blue) for a 15-mm single-tripler design in the absence of crystal detuning. The relationship between the IR and the UV is nonlinear, shown clearly at the picket portion of the pulse (at ~200 ps). The relationship is slightly different for each FCC design, so a slightly different IR pulse is needed for each design to generate the same UV pulse.

### III. Monte-Carlo Method

Measurements on OMEGA in the past have shown that beam-to-beam variations in crystal detuning and IR energy can be approximately described by Gaussian random distributions. In the Monte-Carlo method, the errors in IR energy and crystal detuning for each of 60 beams were randomly drawn from normal distributions whose standard deviations were taken from experimental data, as shown in Figure 5. The error in IR energy was described as a constant multiplier for each beamline, that multiplied the IR power at each temporal point throughout the IR pulse.

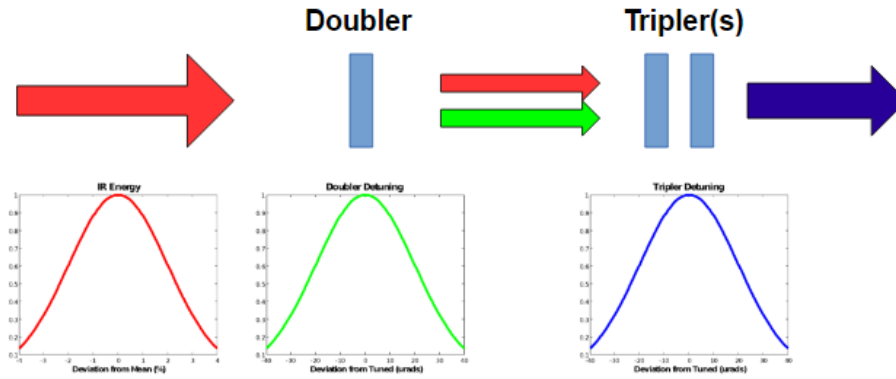


**Figure 5:** Visual depiction of Monte-Carlo error generation method used in the frequency conversion process. To represent the 60 beams of OMEGA, 60 samples from each Gaussian random distribution curve were drawn. The doubler and tripler detunings had a mean of 0  $\mu\text{rad}$  and a standard deviation of 20  $\mu\text{rad}$ . To model the IR energy error of each beam, an IR energy multiplier was drawn for each beam from a Gaussian random distribution with a standard deviation of 0.5% and mean value of 1.

The Monte-Carlo method assumes that each source of error independently contributes to the error in the UV pulse. For a given realization of 60 input IR pulses and FCC detunings, the look-up tables described in Section II were used to generate a set of 60 UV pulses. At each temporal point in the UV pulse, the variances of these three errors were added and the square root of this sum taken to obtain the root-sum-of-squares (RSS) error. This process allowed the calculation of the average UV pulse power and its standard deviation at each temporal point in the pulse across 60 OMEGA beams. This standard deviation is expressed as a percent of the UV power (RMS). The eventual goal of OMEGA is to achieve <1% RMS UV power imbalance.

#### IV. Configuration of Current FCCs

There were two main candidates for the optimized configuration of OMEGA's current FCCs: the single-tripler design, and the dual-tripler design. The single-tripler design was found to achieve better UV power balance overall, and roughly equivalent power balance at the picket, as shown in Figure 6. At low UV power, such as at the step portion of the pulse, the dual-tripler design has slightly lower RMS power

imbalance than the single-tripler design. However, at greater UV power, such as at the drive portion of the pulse, the dual-tripler RMS power imbalance is much greater than that of the single tripler. The major source of error for the dual-tripler design in this region of the pulse is from crystal detuning. The dual-tripler design thus requires tighter control of crystal alignment than the single tripler design to reach LLE's eventual goal of <1% RMS UV power imbalance, so the single-tripler design is favored. As shown in Figure 6, the dual-tripler design was unable to achieve <1% RMS UV power imbalance for an IR energy error of only 0.5% RMS. Therefore, despite generating slightly greater power balance at the picket, the dual-tripler design is less suitable for use on OMEGA under current conditions.

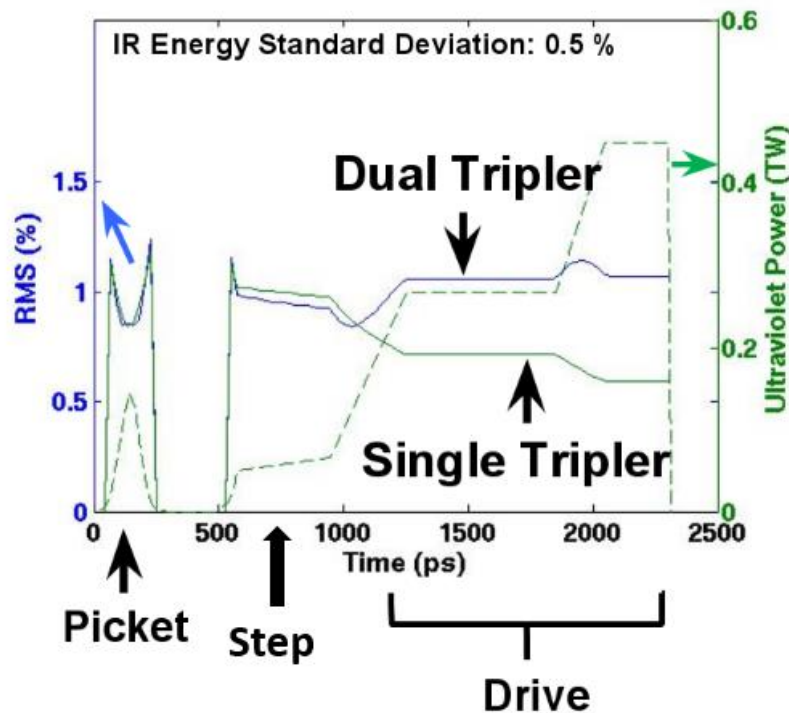


**Figure 6:** Predicted RMS power imbalance (left vertical axis) throughout the 80-Gbar pulse for dual-tripler (blue) and single-tripler (green) designs with current 12.2-mm FCCs on OMEGA. The right vertical axis plots the desired UV power in TW, shown dashed in green. UV power throughout the pulse is directly proportional to the desired UV intensities in Figure 4.

## V. Crystal Length Optimization

Since the current FCCs were designed for higher IR input intensities than required for the 80-Gbar pulse, it was suspected that they would be of suboptimal length for the single-tripler design modeled in Figure 6. Figure 7 shows that lengthening the FCCs in the single-tripler design decreases sensitivity to changes in IR energy. However, in the nonlinear frequency conversion process, the reconversion of UV light back to IR and green light limits the achievable UV power in long-crystal, single-tripler designs, as shown in Figure 8. The longest crystal length that was able to achieve the peak power in the 80-Gbar UV pulse was 15 mm. Therefore, the optimal FCC design for the 80-Gbar pulse used in this study is a single-tripler design with 15-mm crystals. This design achieves lower RMS UV pulse error than both dual- and single-tripler designs that use the current 12.2-mm length FCCs.

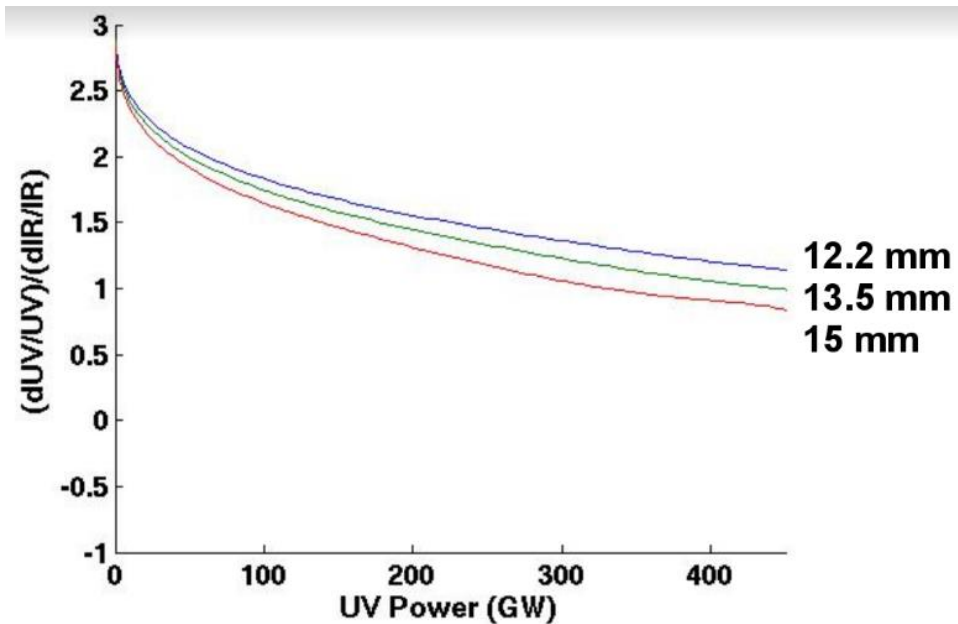


**Figure 7:** Sensitivity of UV power to changes in IR power is plotted on the vertical axis v. UV pulse power (horizontal axis) for single-tripler designs with crystal lengths of 12.2 mm, 13.5 mm, and 15 mm. The vertical axis is the numerical derivative of UV power with respect to IR power normalized by the ratio of IR and UV powers. The percent error in IR power multiplied by the vertical axis value gives the UV error in percent. The single-tripler design with longer FCCs has lower vertical axis values for all UV powers, implying that longer crystal designs provide less UV error, and thus greater power balance, for the range of UV intensities in the 80 Gbar pulse (0-450 GW).

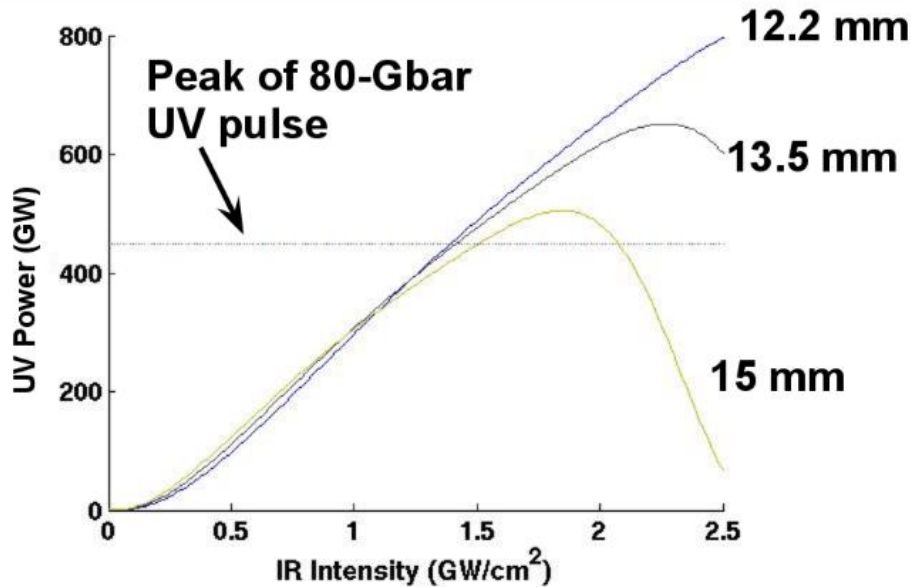


**Figure 8:** UV power v. IR intensity for single-tripler designs with different FCC lengths. Reconversion, in which UV converts back to IR and green light, happens at lower IR intensities for longer FCC single-tripler designs. This lowers the limit on achievable UV power. A single-tripler FCC design with 15-mm length crystals can achieve the 450 GW peak UV power in the 80-Gbar pulse, but cannot generate more than 500 GW of UV power.

## VI. Conclusion

Using a Monte-Carlo-based approach, the statistical performance of different FCC designs was compared and two optimized designs for LLE's 60-beam OMEGA laser were found. It is anticipated that these designs will provide enhanced UV power balance over the current FCC configuration for LLE's 100-Gbar implosion goal. The single-tripler design with the current FCC crystal thickness of 12.2 mm is being implemented on OMEGA by removing the second tripler. An improved single-tripler design for OMEGA consists of a 15-mm doubler crystal and a 15-mm tripler crystal, although this design would make OMEGA incapable of generating more than 500 GW of UV power per beam. With the Monte-Carlo merit function, LLE can now predict approximately how much error there will be in the UV pulse for given errors in the IR energy, doubler tuning, and tripler tuning, thus providing a tool to perform an error budget analysis, and to compare and optimize different FCC configurations. Future work may include

enhancing the Monte-Carlo method by adding other sources of UV pulse error, such as beam-to-beam differences in IR wavefront and beam-to-beam variations in crystal temperature.

### **Acknowledgements:**

I would like to thank my advisor, Mark Guardalben, for always pointing me in the right direction and giving me countless hours of help. I would also like to thank Dr. Jack Kelly for data on OMEGA crystal detuning and infrared energy errors. I would especially like to thank Dr. R. S. Craxton for all the work he puts into making the High School Summer Internship program work. Finally, I would like to thank the other participants in the summer program for their help.

---

<sup>1</sup> Craxton, R. S., McCrory, R. L., & Soures, J. M. (1986). *Progress in laser fusion*. New York: Scientific American, Inc. doi:10.1038/scientificamerican0886-68

<sup>2</sup> Skupsky S, Craxton R.S., “Irradiation uniformity for high-compression laser-fusion experiments,” *Physics Of Plasmas* 6 (5): 2157-2163 Part 2 May 1999

<sup>3</sup> Craxton, R. S. (1981). High efficiency frequency tripling schemes for high-power Nd: Glass lasers. *IEEE Journal of Quantum Electronics*, 17(9), 1771-1782. doi:10.1109/jqe.1981.1071318

<sup>4</sup> Skupsky, S., Short, R. W., Kessler, T., Craxton, R. S., Letzring, S., & Soures, J. M. (1989). Improved laser-beam uniformity using the angular dispersion of frequency-modulated light. *Journal of Applied Physics*, 66(8), 3456. doi:10.1063/1.344101

<sup>5</sup> Babushkin, A., Craxton, R. S., Oskoui, S., Guardalben, M. J., Keck, R. L., & Seka, W. (1998). Demonstration of the dual-tripler scheme for increased-bandwidth third-harmonic generation. *Optics Letters Opt. Lett.*, 23(12), 927. doi:10.1364/ol.23.000927

<sup>6</sup> Auerbach, J. M., Barker, C. E., Eimerl, D., Milam, D., & Milonni, P. W. (1997). Alternate frequency tripling schemes. *Solid State Lasers for Application to Inertial Confinement Fusion: Second Annual International Conference*. doi:10.1117/12.294267

<sup>7</sup> Eimerl, D., Auerbach, J. M., Barker, C. E., Milam, D., & Milonni, P. W. (1997). Multicrystal designs for efficient third-harmonic generation. *Optics Letters Opt. Lett.*, 22(16), 1208. doi:10.1364/ol.22.001208

<sup>8</sup> Private communication with Dr. R. S. Craxton.

# **Characterization of the Electrical Properties of Contaminated Dielectric Oils for Pulsed Power Research**

**Sapna Ramesh**

Pittsford Mendon High School

Pittsford, New York

Advisor: Kenneth L. Marshall

**Laboratory for Laser Energetics**

University of Rochester

Rochester, New York

Summer High School Research Program 2016

## 1. Abstract

The Z-machine at Sandia National Laboratory uses pulsed power to study magnetized inertial confinement fusion. In the Energy Storage Section of this apparatus, the high-voltage capacitors that store electrical charge are submerged in an insulating oil (Shell Diala S2 ZX-A) to minimize thermal and electric losses before and during system operation. Shell Diala S2 ZX-A has a density of  $890 \text{ kg/m}^3$  and is classified as a mineral oil. [1] Over time this oil becomes contaminated with both dielectric breakdown byproducts resulting from high-voltage “flash-over” discharges and extrinsic contaminants (atmospheric moisture and dust particles) introduced into the oil during maintenance and cleaning activities. The effect of these contaminants on the electrical properties of Shell Diala S2 ZX-A was evaluated using impedance spectroscopy measurements over a frequency range of  $50 \text{ } \mu\text{Hz} - 5 \text{ MHz}$  along with DC-regime measurements of resistivity and current flow. Oil samples exposed to electrical arc discharges were treated with either activated carbon or molecular sieve (13X) to remove dielectric breakdown contaminants; the absorbents in turn were removed by centrifugation followed by syringe-filtration through a submicron particle membrane filter. The electrical properties and transmittance spectra of both the contaminated and purified oil samples were analyzed and compared to similar data collected on pure oil samples that had never been subjected to arc discharge. The impedance spectroscopy results show that the oils contaminated with breakdown byproducts have both a higher dielectric constant and a higher loss factor across a wide frequency range, which suggests significant degradation in the insulating property of the oil. Both the DC resistivity measurements and the transmission spectra of the oil samples purified with absorbents showed recovery of the samples’ dielectric and spectroscopic properties to values roughly equivalent to those of the original pure material. Molecular sieve showed superior efficiency to activated carbon in purifying the oil,

suggesting that the contaminants are primarily charged particles. This work will provide the framework for future studies on characterizing the electrical properties of insulating oil directly from the Z-machine and on developing *in-situ* continuous purification systems for contaminated insulating oil.

## **2. Introduction**

The Z-machine is a pulsed power machine at Sandia National Laboratory in Albuquerque, New Mexico (Fig. 1). This powerful machine is being used to study the uses of pulsed power, such as nuclear weapons research and fusion energy. Pulsed power is the intense release of electrical energy over an extremely short period of time.

Each pulse generated by the Z-machine lasts 100-300 nanoseconds, and produces more than 80 trillion Watts of power. Before the apparatus fires, its capacitors charge to store around 20 Megajoules of energy [Fig. 1(a)]. These capacitors are submerged in 540,000 gallons of Shell Diala S2-ZX-A insulating oil in order to minimize thermal and electrical losses before the machine is fired [Fig. 1(b)].

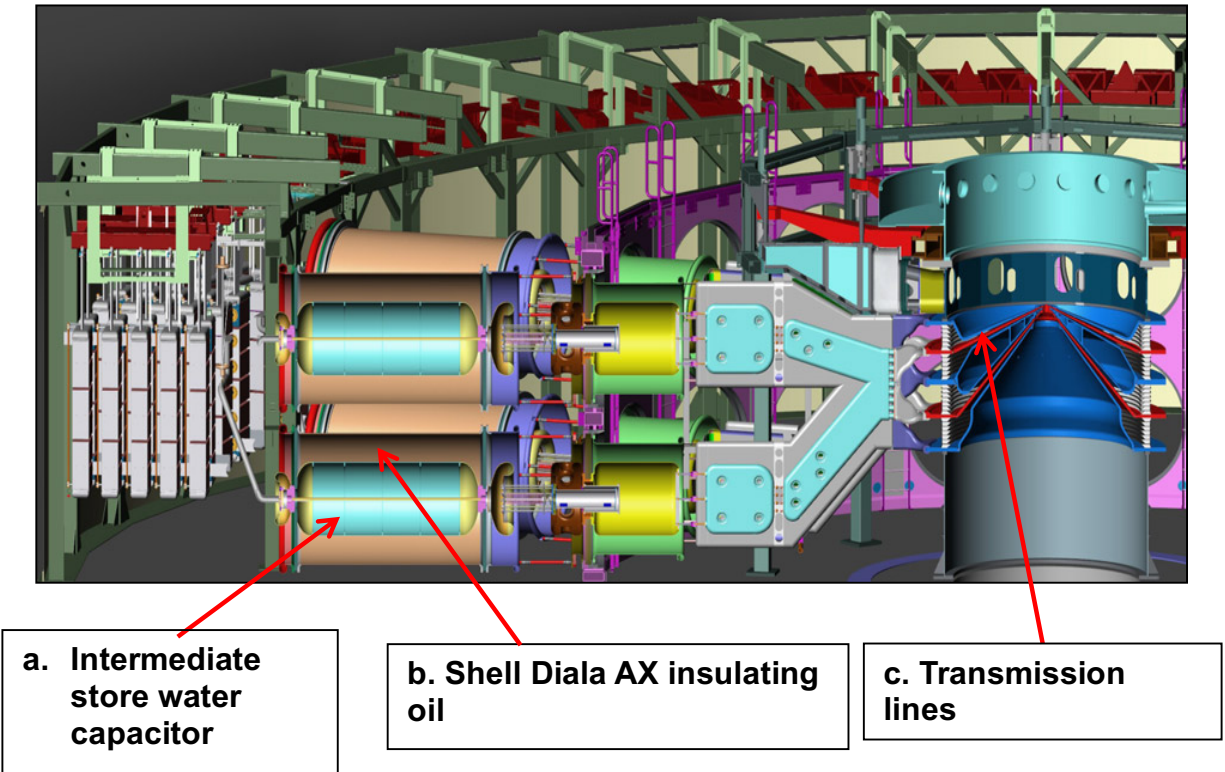


**Fig. 1:** A cross-sectional diagram of the Z-machine. The total diameter of the apparatus is 34 meters. [2]

Inside the vacuum chamber of the Z-machine, the electrical pulse is discharged through hundreds of parallel tungsten wires that transform into a plasma once the pulse arrives, creating a strong magnetic field that implodes the wire particles. These particles collide on the z-axis (which is where the instrument gets its name), producing intense amounts of radiation, pressure, and heat (up to 1.8 million degrees Celsius). As the collisions of the wire particles slow down, 2.7 million joules of x-rays are produced. [2]

The insulating oil used in the Z-machine becomes contaminated over time from both intrinsic and extrinsic sources. The 540,000-gallon insulating oil reservoir in the Z-machine is an uncovered tank and is susceptible to contamination through atmospheric moisture and dust from building access doors. Moisture can provide a low-resistance pathway for electricity through the

oil, thus deteriorating the quality of the insulating oil. The cleaning process for the transmission lines [Fig. 1(c)] involves physical grinding, and occurs only 30 feet away from the oil tank, resulting in metal particles becoming airborne and landing in the oil tank, producing another low resistance avenue for electricity to take when escaping from the oil. [3]

Figure 2 shows a photograph of the Z-machine while in operation. Significant arcing, called “flash-over” discharge or breakdown, occurs in the insulation oil due to the sheer magnitude of current that is trying to escape (26 million amps). [2]

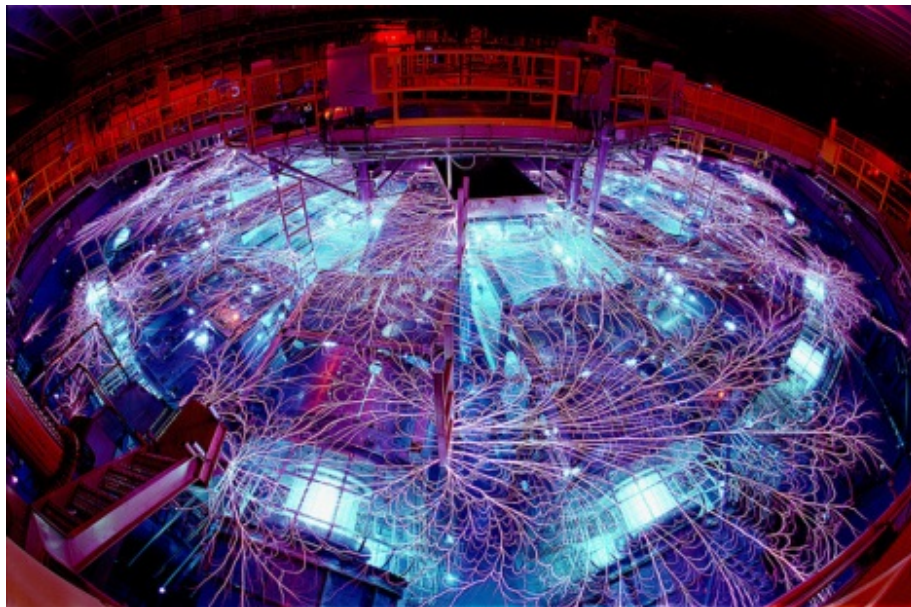


**Fig. 2:** An image of “flash-over” discharges in the Z-machine insulating oil. [2]

The goals of this work were to characterize the impact of breakdown products generated by dielectric discharge in the oil on the electrical properties of the oil and develop a scalable process suitable for *in-situ* continuous purification of the insulating oil for use in LLE’s own pulsed power laboratory.

### 3. Theory

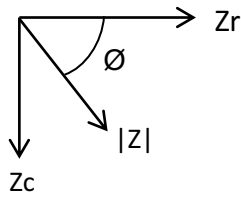
The process of dielectric breakdown produces various byproducts in the insulating oil, including hydrocarbon gases and polar compounds. When arcing occurs, a huge amount of energy is released and the hydrocarbon chains that make up the oil molecules are broken to produce gases such as hydrogen, methane, ethane, acetylene, and free carbon. Other breakdown contaminants include oxidation products, which pose a big problem to the function of the oil. Oxidation products can include organic carboxylic acids and formic acid, which decrease the surface tension of the oil and increase the number of bubbles. These bubbles can align between metal fragments and ionized particles to create a conductive bridge. Other common contaminants include dimethyl sulfide and ozone. All of these dielectric breakdown products that contaminate the oil have various impacts on the electrical properties of the oil such as resistivity, impedance, permittivity, dissipation factor, and dielectric constant. [4]

*Resistivity* ( $\rho$ ) is a fundamental property of a material that describes its resistance to current flow (**Eq.1**). Unlike resistance, resistivity takes into account the properties of the material. [5]

$$\rho = \frac{AR}{l} \quad \text{Eq. 1}$$

where  $A$  is the cross sectional area,  $l$  is the length and  $R$  is the resistance.

*Impedance* ( $Z$ ) is the complex form of resistance that applies to AC circuits.[5] Impedance includes an imaginary component on the y-axis, a real component on the x-axis, and a phase angle. Ohm's law still applies to AC circuits, but resistance is replaced by impedance (**Eq. 2**). In order to find the magnitude of impedance, one can simply use the Pythagorean theorem (**Eq. 3**).



$$Z = \frac{V}{I}$$

**Eq. 2**

$$|Z| = \sqrt{Z_r^2 + Z_c^2}$$

**Eq. 3**

where  $V$ = voltage,  $I$ = current,  $|Z|$ = magnitude of impedance,  $Z_r$ = real impedance (resistive), and  $Z_c$ = imaginary impedance (capacitive).

*Capacitance* ( $C$ ) is the ability to store charge. A simple parallel plate capacitor contains two conductive parallel plates with a dielectric, or insulating material between the plates. The dielectric material polarizes when a voltage ( $V$ ) is applied between the plates, pushing the positive charges ( $Q$ ) to one plate and the negative charges ( $-Q$ ) to the other (**Eq. 4**). The capacitor holds charge effectively when the dielectric material between the plates is a good insulator and doesn't allow the charges to migrate towards each other.<sup>[4]</sup> The capacitance of a parallel plate capacitor is shown in **Eq. 5**, where  $\epsilon$  is the permittivity of the dielectric,  $A$  is the cross sectional area of the capacitor and  $d$  is the distance between the conductive plates. The extent to which the dielectric is a good insulator is given by its permittivity.



$$C = \frac{Q}{V}$$

**Eq. 4**

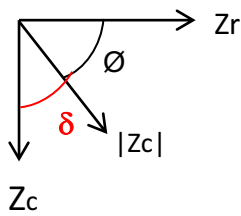
$$C_{parallel\ plate} = \epsilon \frac{A}{d}$$

**Eq. 5**

The *dielectric constant* ( $K$ ) of a material is the extent to which it concentrates electrical flux. A material with a higher dielectric constant can concentrate more charge. However, it is more likely to break down and thus is a poorer insulator than a material with a lower dielectric

constant. The dielectric constant of a material can be calculated by dividing the capacitance of a parallel-plate capacitor containing the material by the capacitance of a capacitor with the same plate area and gap spacing but filled with air, with both measurements conducted at the same voltage and frequency.[5]

The *loss factor* ( $\tan \delta$ ) is calculated using the complement of the phase angle of the impedance (**Eq. 6**). This value is commonly used in industry to characterize the condition of transformer oil. Usually, the  $\tan \delta$  of the oil is measured before use, and the deviation from this value is tracked and compared between batches to ensure that the oil has not deteriorated. In this experiment, impedance phase data was used to calculate and compare the  $\tan \delta$  values of the oil samples. The higher the  $\tan \delta$  of a material, the more energy loss occurs when a voltage is applied to the material, and the less effective is the material as an insulator.[5]



$$\text{Loss Factor} = \frac{Z_r}{Z_c} = \tan \delta$$

**Eq. 6**

where  $\delta$  = complementary angle to phase angle  $\phi$ .

In theory, the electrical properties of the oil responsible for its insulating ability should change measurably as the oil becomes contaminated with breakdown contaminants. Measuring these properties will corroborate the widely held view that breakdown products are indeed responsible for deterioration of the oil's insulating capability with time.

#### 4. Experimental Methods

All experiments were conducted on three samples of Shell Diala S2-ZX-A insulating oil [Fig. 3(a)] that were subjected to a high voltage discharge using a 50 kV Tesla coil with a 1mm spark gap for 0, 5, and 20 minutes [Fig. 3 (b)]. A pure sample of the oil that had not been subjected to dielectric discharge was used as a control sample.

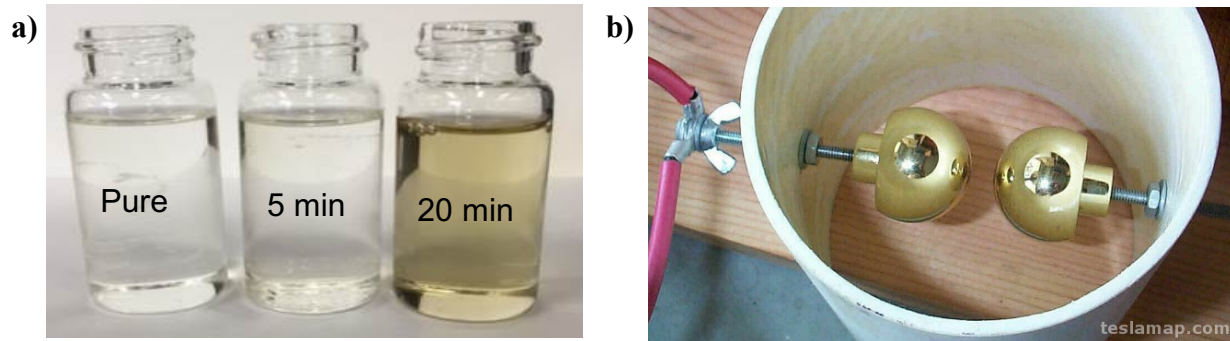


**Fig. 3:** (a) Two Shell Diala S2-ZX-A oil samples subjected to dielectric discharge for 5 min and 20 min compared to a sample of the pure material; darkening of the oil due to contamination is clearly evident. (b) Tesla coil setup that was used for the dielectric breakdown experiments; the spark gap is the distance between the two plates. [6]

#### 4 (a) Impedance spectroscopy measurements

A Solartron 1260 Impedance/Gain-Phase analyzer with a Solartron 1296 Dielectric Interface and Solartron 12962 sample holder (Fig. 4) was used to collect impedance spectroscopy data on both the pure oil and the samples exposed to high voltage arc-discharge (5 min and 20 min) to determine a relationship between various electrical properties (dielectric constant and  $\tan \delta$ ) and level of dielectric breakdown products. Both instruments were connected to a computer that used the SMaRT impedance software package from Ametek for data collection and processing. The measurement time was dependent on the range of frequencies over which the instrument was programmed to sweep; the lower the minimum frequency and the larger the range, the longer the

measurement duration. Typical impedance spectroscopy scans for the oil samples were collected over a frequency range of 50  $\mu\text{Hz}$  to 5 MHz; each measurement took  $\sim 44$  hours to complete.

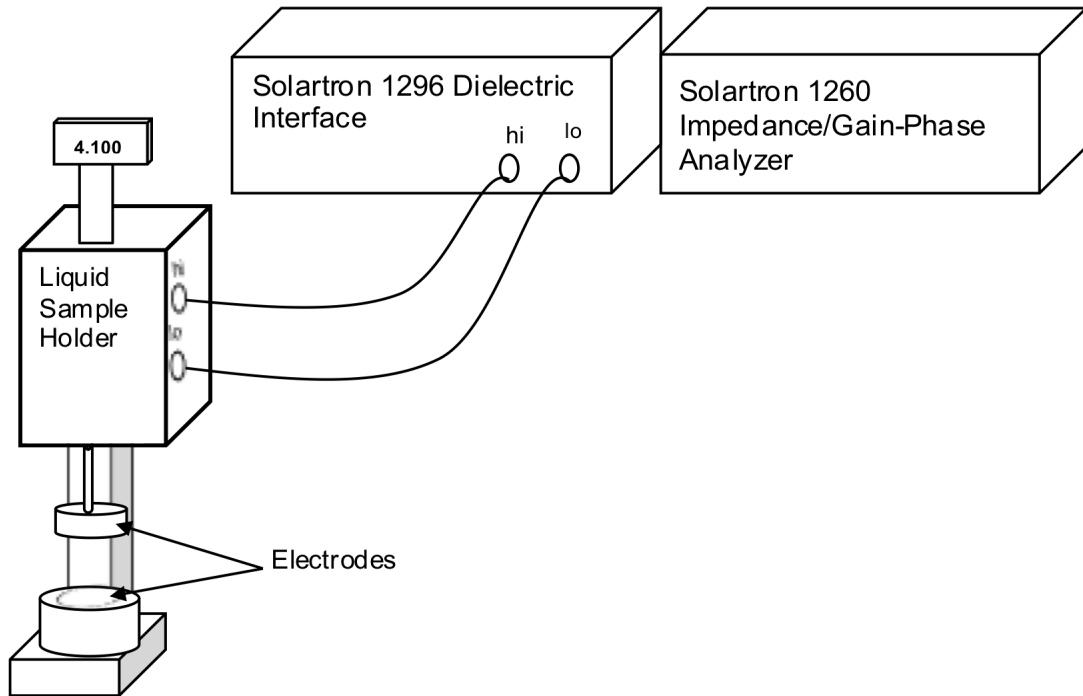


**Fig. 4:** Setup of the impedance spectroscopy instrumentation experiments. The instrument can sweep a maximum frequency range of 10  $\mu\text{Hz}$  to 5 MHz, measure impedance values from 100  $\Omega$  to 100 T $\Omega$ , and measure capacitance values from 1 pF to 0.1 F.

The instrument was checked for proper functionality by conducting frequency response analysis on a sample of deionized water, calculating its dielectric constant, and comparing the result to published literature values. The dielectric constant was determined by dividing the measured capacitance of deionized water at 100 KHz by the capacitance of the empty sample holder (air) determined at the same frequency and electrode gap setting. The accepted value for water at 100 kHz is 78 and the calculated value from the measurements was 76, which implies that the apparatus was working correctly.[7]

Prior to conducting measurements on the oil samples, the sample chamber and components (bottom electrode, guard ring, top and bottom surface of the mobile high electrode) were carefully wiped several times with methanol. The sample chamber was then wiped down with detergent, rinsed with deionized water and allowed to dry for two hours inside an incubator (Fig. 5) set to 40 °C.

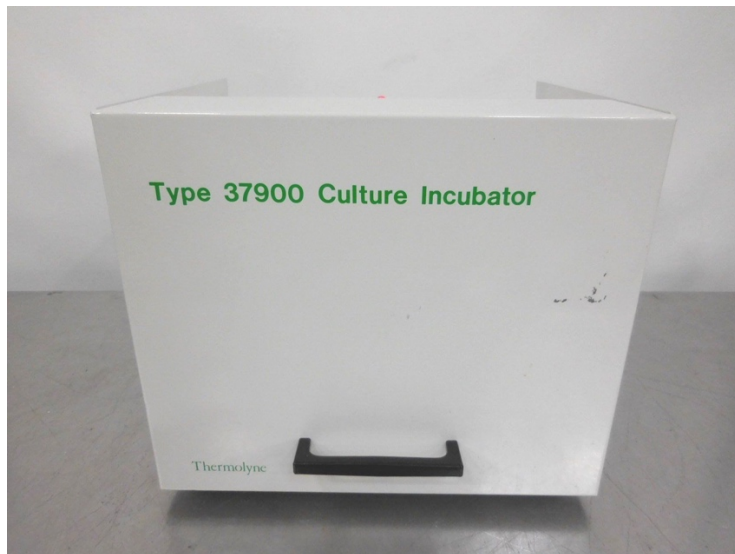


**Fig. 5:** Incubator used to dry the Solartron sample holder assembly at 40 °C.

After removing the sample holder from the incubator and allowing it to cool to room temperature, ~3 mL of the oil sample was transferred to the sample cell using a pipette. The mobile high electrode was lowered down towards the sample until the cell gap distance displayed on the sample holder scale was 4.100 mm. After allowing the sample to equilibrate in the sample holder for 0.5 to 0.75 hrs for temperature stabilization and to ensure the removal of any trapped air bubbles, the sample holder's high and low electrode ports were connected to the corresponding ports on the impedance analyzer, using the shortest possible wires to avoid stray impedance contributions. Figure 6 shows a screen shot of the measurement sequence used in the SMaRT software to acquire the impedance data.

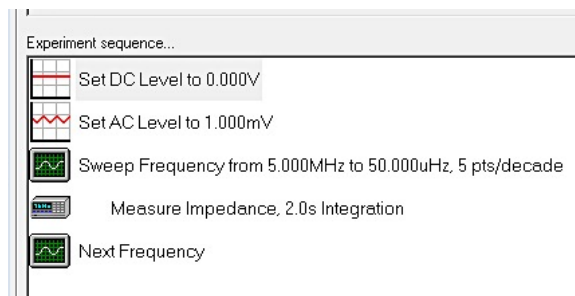


**Fig. 6:** Screen capture of the experiment sequence programmed with SMaRT for impedance data acquisition. The two-second integration period refers to the amount of time the instrument took to normalize the data for each measurement.

#### **4(b) DC resistivity measurements**

A Keithley Electrometer model 619 connected to a Yellow Springs Instruments Model 3403 conductivity probe with a cell constant of 100/m was used to determine the DC resistivity (Fig. 7). The electrometer measurement range is from 0.1  $\Omega$  to 200 G $\Omega$ . The probe leads were connected to the electrometer leads and secured with insulating tape. The instrument's functionality was verified by measuring the resistivity values for isopropyl alcohol and acetone (Table 1). The probe was cleaned using methanol and deionized water, followed by drying in the incubator for 1-2 hours. The resistivity of the sample was calculated by dividing the measured resistance by the cell constant.

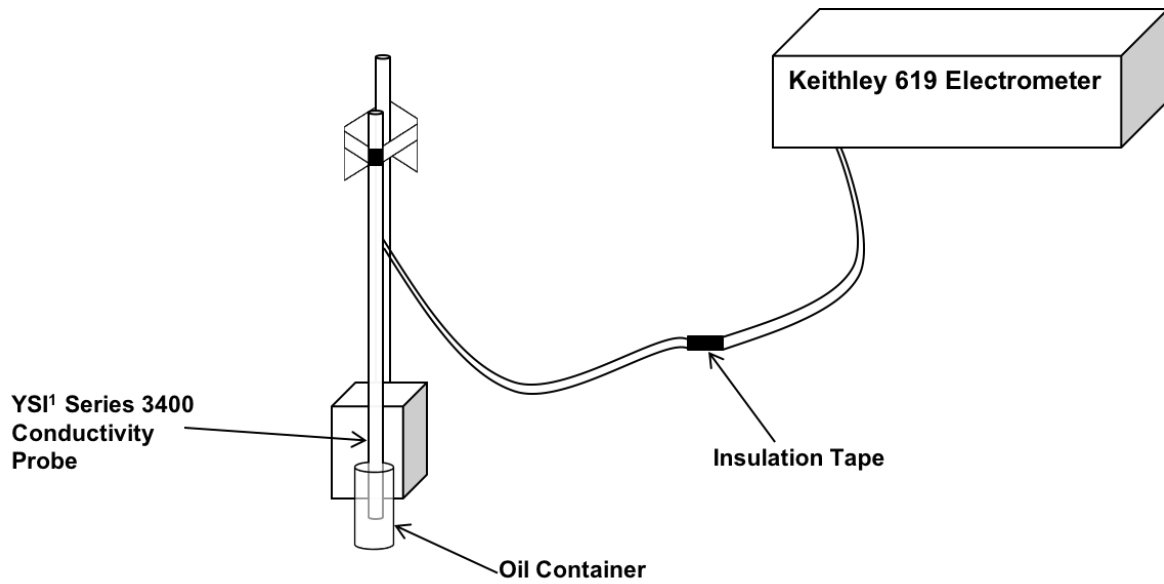


**Fig. 7:** Setup used to measure the resistivity of the various oil samples.

| Data Source | Acetone                            | Isopropyl Alcohol                  |
|-------------|------------------------------------|------------------------------------|
| Measured    | $7.65 \times 10^6 \Omega\text{-m}$ | $1.50 \times 10^5 \Omega\text{-m}$ |
| Literature  | $5.00 \times 10^6 \Omega\text{-m}$ | $1.67 \times 10^5 \Omega\text{-m}$ |

**Table 1:** Verification testing of the resistivity setup. Literature data was taken from material data sheets. [8] [9]

To minimize sensitivity of the probe and electrometer to vibrations, foam squares were cut and put under the four corners of the electrometer housing, the probe holder stand and the lead connections. For each measurement, ~16 ml of sample was used in a 25 ml glass vial. The probe was immersed in the sample until the bottom of the probe was ~ 3.5 cm above the bottom of the sample vial. A metal stand with a clamp was used to secure the probe in position during the measurement.

#### 4(c) Transmittance measurements

An Agilent 8452 diode array spectrophotometer was used to measure the transmittance spectra of the oil samples. Sample measurements were conducted using a 1 cm path length fused silica cuvette.

#### 4 (d) Purification process

Shell Diala S2 ZX-A oil samples exposed to high voltage discharge for 20 min were used for all of the purification process testing and development. Type 13X molecular sieve was used without activation as supplied by Chemicals Dynamics Corporation; Norit activated carbon was obtained from the University of Rochester Chemistry Department. Test samples were prepared by dispersing ~10 wt % of either molecular sieve or Norit in ~20 ml of oil in a Teflon beaker. The initial dispersion was conducted by hand using a spatula, followed by high-shear mixing using a Dremel Moto Tool equipped with a saw-tooth dispersion blade at 4000 rpm for 1 min. (Fig. 8).



**Fig. 8:** Dremel Moto tool setup used for high-shear dispersion of absorbents into the oil samples.

Following high-shear dispersion, the absorbent was separated from the oil sample by centrifugation at 3300 rpm for 4 min using a Fisher Scientific Centrifuge Model 228 centrifuge [Fig. 9(a)]. An identical weight of sample was transferred to each tube and the two tubes were placed opposite each other in the centrifuge rotor to eliminate vibration during the centrifuging process. For Norit-containing samples, it became necessary to centrifuge the sample an additional 2 min at 3300 rpm to eliminate the very fine black particles that remained suspended in the oil sample [Fig. 9(b)]. Remaining ultrafine suspended particles were removed by filtration of the oil sample through a 0.2  $\mu\text{m}$  disposable PTFE membrane syringe filter (0.2  $\mu\text{m}$  pore size) fitted to a glass syringe [Fig. 10].

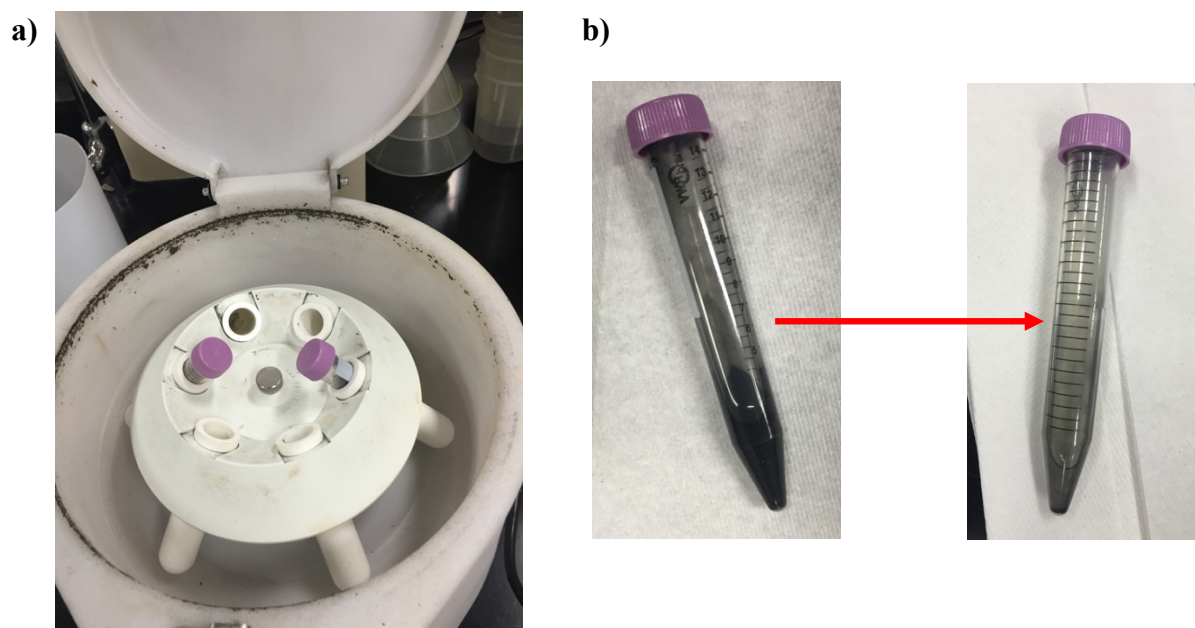


**Fig. 9:** Centrifuge used for bulk removal of absorbent from the oil samples. (a) Centrifuge rotor showing two centrifuge tubes containing identical weights of sample; (b) *Left:* Norit/oil sample after the first centrifugation step; note the large mass of Norit at the bottom of the tube. *Right:* centrifuge tube shown on the left after the oil sample was poured out. Fine particles of Norit such as those clinging to the walls still remained dispersed in the oil, requiring a second centrifugation step.

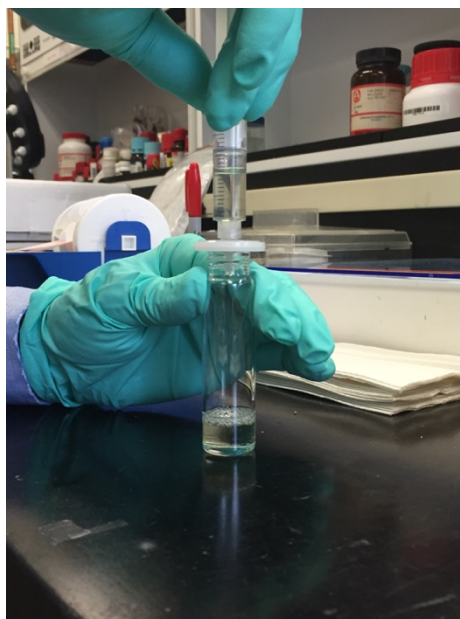


**Fig. 10:** Syringe filtration of a molecular sieve/oil dispersion through a disposable 0.2  $\mu\text{m}$  Teflon membrane filter.

## **5. Results and Discussion**

### **5 (a) Impedance measurements**

Figures 11 and 12 present electrical properties data obtained from impedance spectroscopy measurements taken on the contaminated insulating oil samples over a frequency range of 50  $\mu\text{Hz}$  to 5 MHz. The presence of dielectric breakdown products in the Shell Diala S2-ZX-A oil increases its dielectric constant in the high frequency range (from 1 Hz to 5 MHz); the presence of these dielectric breakdown products increases the loss factor ( $\tan \delta$ ) of the oil at 50 Hz (Fig. 11).

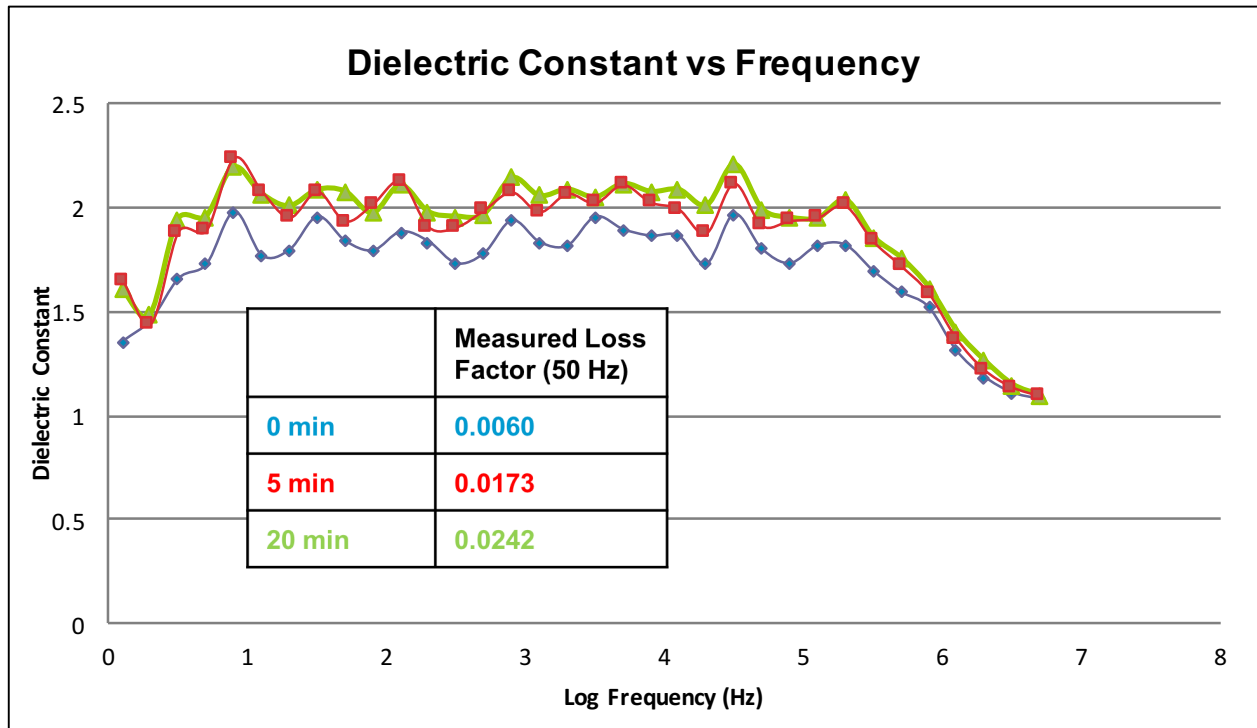


**Fig. 11:** The dielectric constant vs log of the frequency and the loss factor ( $\tan \delta$ ) data collected by impedance spectroscopy for samples exposed to dielectric discharge for 0, 5, and 20 min.

An analysis of the results in Fig. 11 shows that the dielectric constant of the contaminated insulating oil is increased at high frequencies, which indicates that dielectric breakdown products increase the conductive nature of the insulating oil. For the low frequency range ( $<10$  Hz, Fig. 12), no significant trends are discernible due to noise in the data. The higher  $\tan \delta$  of the contaminated oil indicates that breakdown products increase the amount of energy loss in the oil. The corroboration between both these trends confirms that dielectric breakdown products decrease the functionality of insulating oil.

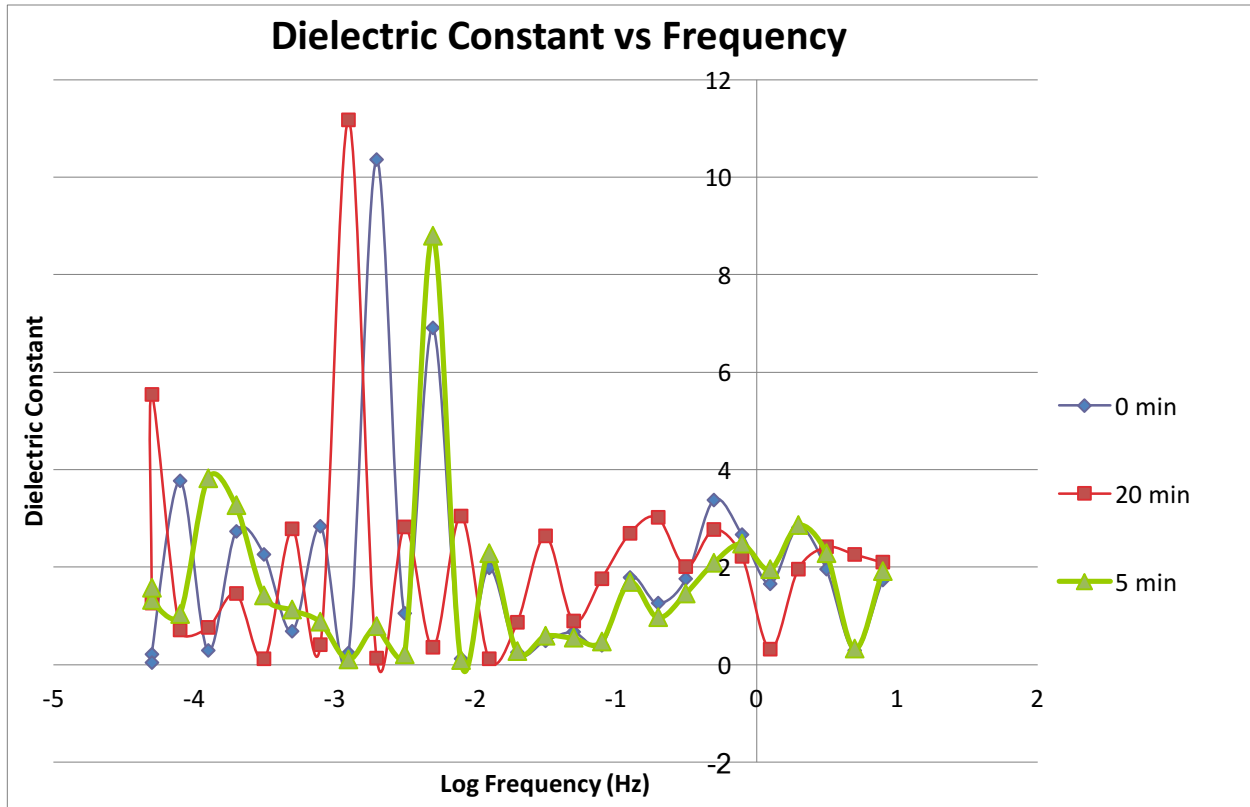


**Fig. 12:** Dielectric constant versus Log Frequency in the low frequency range (<10 Hz). No consistent trend is observed when compared to the high frequency range data in Fig. 11.

Impedance spectroscopy is also useful in obtaining the complex impedance plot (Fig.13), where the real impedance component of the sample is plotted on the x-axis and the imaginary impedance component is on the y-axis. Each curve in Fig. 13 represents a locus of impedance values for each of the three oil samples obtained during the frequency sweep. The positive x-axis represents positive resistive impedance (analogous to resistance in a DC circuit), while the negative x-axis represents negative resistive impedance. A material with a degree of positive resistive impedance will lose some of the electricity applied to it in the form of heat. The positive y-axis represents inductive impedance while the negative y-axis represents capacitive impedance, both of which are shown by the circuit symbols in the right side of Fig. 13. A material with a degree of inductive impedance will store some of the electricity applied to it in the form of a magnetic field. Conversely, a material with capacitive impedance will store some

of the electricity applied to it in the form of an electric field in a similar manner to a parallel plate capacitor. An ideal insulator would have a higher imaginary impedance, as this implies that it is storing electricity rather than losing it as heat [5].

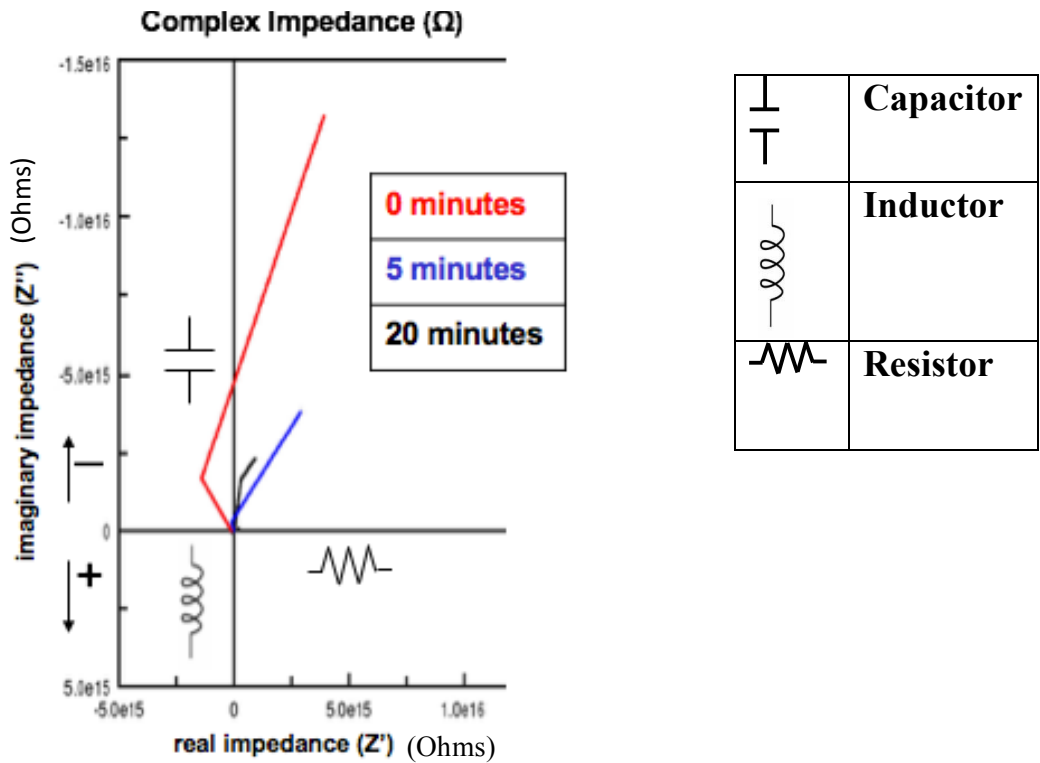


**Fig. 13:** Complex impedance plot with an inverted y-axis; the circuit symbols are identified on the right. The plot displays impedance spectroscopy data taken over a frequency range of 50  $\mu$ Hz to 5 MHz.

The complex impedance data collected in the experiment indicate that dielectric breakdown contaminants lower the imaginary (specifically, the capacitive) impedance because in Fig. 13, the capacitive impedance of the contaminated oil is lower than that of the pure oil. Dielectric breakdown products will therefore render the oil less functional. The small degree of negative resistance observed for the pure oil indicates that during some of the measurement, the pure oil exhibited a current-voltage relationship that was inverted; i.e., the current increased

when the voltage decreased. This effect can also occur in certain electronic devices and under certain conditions when an arc discharge (and resultant current flow) occurs in a gas [10].

### 5(b) Purification process evaluation

Optical spectroscopy and DC resistivity measurements were conducted to quantify the effectiveness of both molecular sieve and Norit absorbents in removing dielectric breakdown products from Shell Diala S2-ZX-A oil subjected to a high voltage arc discharge for 20 min. Figure 14 shows photographs of the original 20 min arc-discharged sample [Fig. 14(a)] and the same material after purification using molecular sieve [Fig. 14(b)] and Norit [Fig. 14(c)] absorbents. There is a visibly noticeable reduction in color in the purified samples, regardless of the absorbent used.

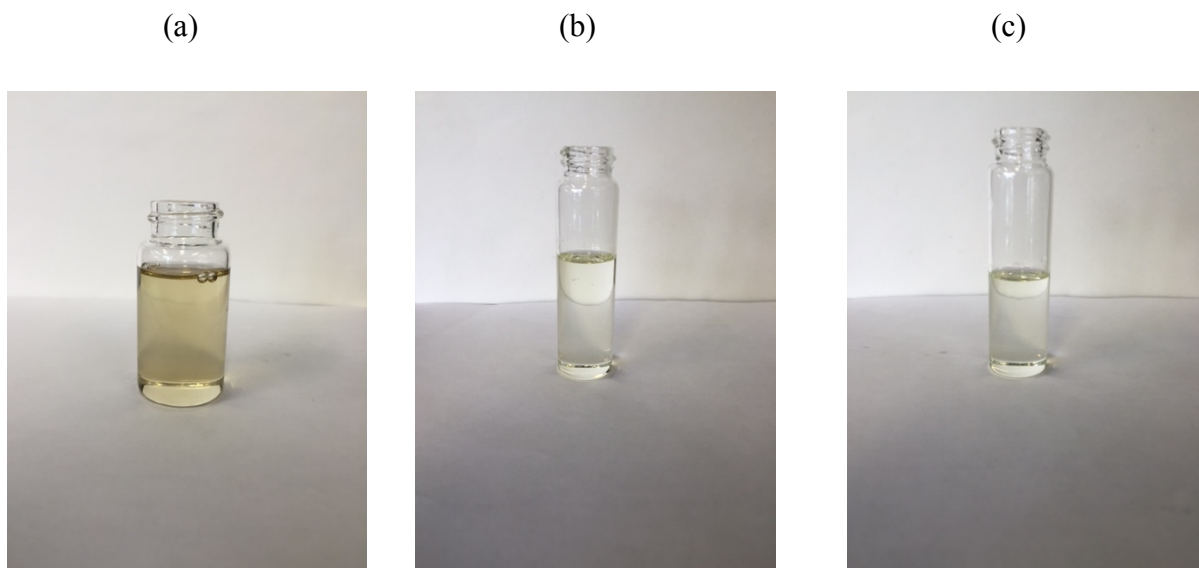


**Fig. 14:** (a) A sample of Shell Diala S2-ZX-A oil subjected to 20 min of high voltage discharge; (b) the same material shown in (a) after purification with molecular sieve; (c) the same material shown in (a) after purification with Norit.

Transmittance spectra for the three oil samples in Fig. 14 are compared in Fig. 15 along with the transmittance spectrum for a pure oil sample at the same optical path length. The pure oil has

the highest transmission, while the sample subjected to 20 min of high voltage discharge has the lowest transmission. Both purified oil samples show significantly improved transmission, approaching that of the pure oil.

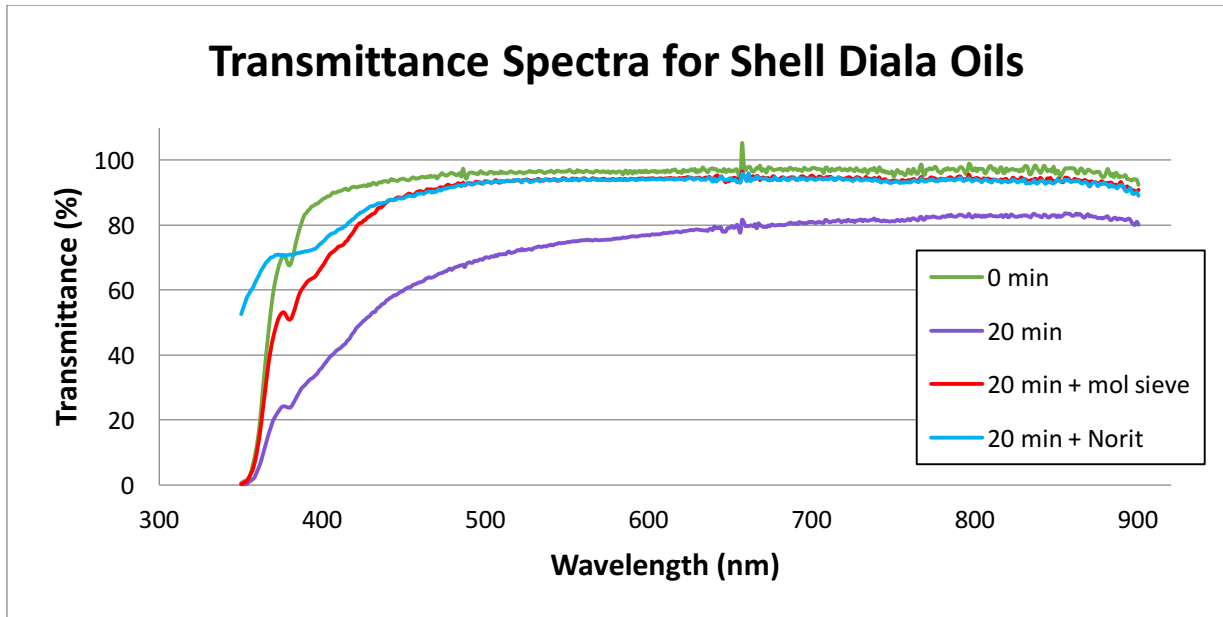
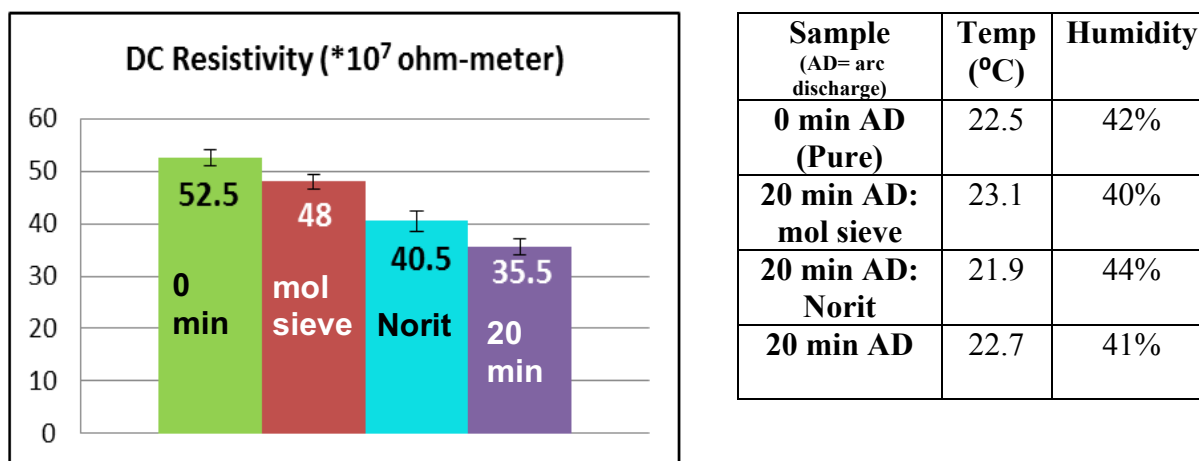


**Fig. 15:** Transmittance spectra from 350 nm to 900 nm of the four oil samples obtained in a 1 cm path length quartz cell.

DC resistivity data collected for the samples shown in Fig. 14 and the pure sample using the electrometer setup described in Section 4(b) are shown in Fig. 16. The resistivity data in Fig. 16 follow the same trend seen in the transmittance data in Fig. 15; the pure oil has both the highest resistivity and highest transmission, while the contaminated oil has the lowest resistivity and transmission. These results imply that the dielectric breakdown products responsible for the loss in resistivity are highly colored, and establish a direct correlation between the degree of coloration and resistivity, suggesting that optical spectroscopy may be an alternate and convenient method for monitoring the loss of the oil's insulating ability. In Fig. 15, the spectral

curve shape of the sample purified with molecular sieve more closely matches that of the pure oil sample than does the Norit-purified sample. This observation, together with the resistivity data of Fig. 16, demonstrates that molecular sieve absorbent is more effective than Norit in removing dielectric breakdown contaminants from the insulating oil and restoring its resistivity.



| Sample<br>(AD= arc discharge) | Temp (°C) | Humidity |
|-------------------------------|-----------|----------|
| 0 min AD (Pure)               | 22.5      | 42%      |
| 20 min AD: mol sieve          | 23.1      | 40%      |
| 20 min AD: Norit              | 21.9      | 44%      |
| 20 min AD                     | 22.7      | 41%      |

**Fig. 16:** DC resistivity data measured on the three oil samples shown in Fig. 14 plus the pure sample. Temperature and humidity were also monitored during each measurement and are shown in the table on the right. Because the electrometer is highly sensitive to vibration, the data is reported as a range of values.

The relative effectiveness of the two absorbents in removing dielectric breakdown products from the insulating oil as shown in Fig. 16 provides some insights into the chemical nature of these contaminants. Molecular sieve is a zeolite-based absorbent with a cage-like, highly porous structure and an alumino-silicate composition. The pore size of molecular sieves are precisely defined, and molecular sieves with different pore sizes can be used to selectively trap and absorb a wide variety of liquids and gases. The Type 13X molecular sieve used in the purification process described in this work has a pore diameter of 10 Å. Pore size can be altered by changing the cation in the negatively charged structure of the molecule. Type 13X has sodium cations in its structure (Fig. 17). A typical formula for Type 13X molecular sieve is  $\text{Na}_{86}[(\text{AlO}_2)_{86}(\text{SiO}_2)_{106}] \cdot n\text{H}_2\text{O}$ . In industry, Type 13X molecular sieve is normally used to

absorb  $\text{CO}_2$ ,  $\text{H}_2\text{O}$ ,  $\text{H}_2\text{S}$ , and other compounds, from gaseous and liquid process streams. Due to their highly charged internal field made of  $\text{AlO}_4$  and  $\text{SiO}_4$  tetrahedrons, zeolite materials are very effective at absorbing highly polar and charged particles. [11]

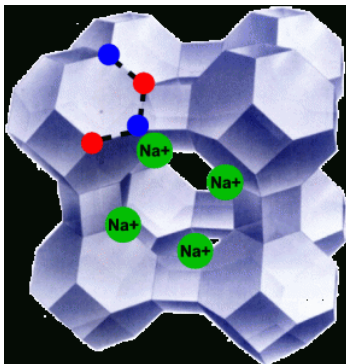


**Fig. 17:** Structure of Type 13X molecular sieve. Sodium cations contained inside the pores determine the pore size and attract charged particles. [12]

The molecular sieve used in this work was not activated; “activation” involves heating the material to very high temperatures ( $> 250\text{ }^\circ\text{C}$ ) in order to rid its structure of any water. This process maximizes the amount of material that the zeolite structure can absorb, because water molecules occupy space inside the pores.

Norit (activated carbon) is a common absorbent that has a high surface area and microporosity, which allows it to absorb very large amounts of materials (Fig. 18). This absorbent functions by binding to molecules that come into contact with its surface by means of van der Waals intermolecular forces. Because it is carbon-based, it does not have the capability to bind to inorganic materials, metals, strong acids and bases, and alcohols. [13]

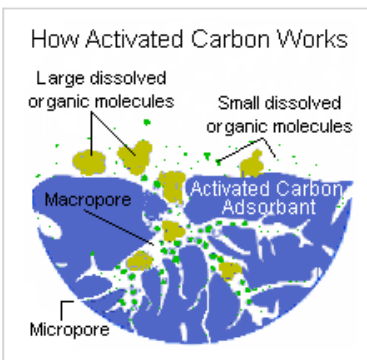


**Fig 18:** Structure of Norit, showing the presence of both macro and micropores. [14]

The finding that molecular sieves are more effective than Norit at removing dielectric breakdown contaminants from the insulating oil suggests that these contaminants may be small-to-medium molecular weight organic materials that bear a strong charge, as molecular sieve has a much higher affinity for such charged species than does Norit.

## 6. Future Work

Future efforts should be focused on ways to further improve the speed and efficiency of the purification process using absorbents. A simple first step would be to repeat the process using activated Type 13X molecular sieve. Molecular sieve activation is achieved by heating the material at 250 – 315 °C under a nitrogen flow or under vacuum for several days. Other absorbents could also be explored to evaluate their affinity for removing dielectric breakdown products. Some well-known examples are shown in Table 2 along with a comparison of their relative cost to molecular sieve and Norit.

In addition to testing different absorbents, different oils can be tested in order to find which oil is least affected by dielectric breakdown contaminants, as evidenced by changes in resistivity, dielectric constant, loss factor, complex impedance, and transmittance spectra. Other formulations of insulating oils, both from Shell and other sources, are widely available in industry. Conducting experiments on samples of contaminated oil taken directly from the Z-

machine could also lead to a more detailed understanding of all contaminants present and their individual roles in contributing to dielectric breakdown.

| Absorbent       | Cost per Kg |
|-----------------|-------------|
| Molecular Sieve | \$0.68      |
| Norit           | \$0.58      |
| Floridin Clay   | \$0.32      |
| Alumina         | \$1.00      |
| Silica Gel      | \$0.75      |

**Table 2:** Price comparison of absorbents. [15]

A key element of this project was developing a purification process for the oil that could be eventually applied to large-scale, continuous processing of oil in LLE's Pulsed Power laboratory that is currently under construction. Figure 19 shows a schematic diagram for a cartridge-based absorption/filtration set-up that could be run continuously so that the oil would never be overly contaminated during the operation of the pulsed-power apparatus. Submicron particle cartridge filters are installed after the absorption beds to capture fine particles, followed by a resistivity monitor to measure *in-situ* the effectiveness of the purification process and monitor oil quality. Because of the relationship established between optical transmission and resistivity, monitoring of the transmission of the oil in real-time is also an option.

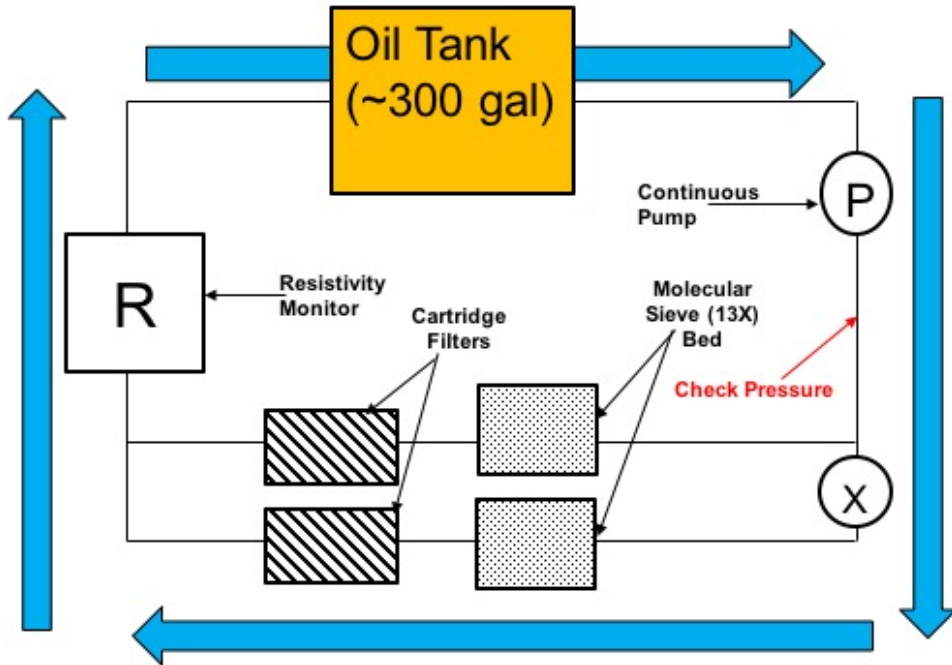


**Fig 19:** Schematic for a continuous absorption/filtration system for the purification of insulating oil in the pulsed-power systems. Flow through the purification system would be constant when the pulsed-power system is in an idle state.

## 7. Conclusion

An absorption-based purification process was developed to remove dielectric breakdown contaminants from insulating oils used in pulsed power research. The presence of dielectric breakdown products was shown to both increase the dielectric constant of the oil in the high frequency range, and decrease the complex component of the oil's impedance. Both of these values are indicators of a loss of insulating oil's functionality. DC resistivity measurements and transmittance spectra were used to evaluate the effectiveness of the purification process. Molecular sieve was shown to be very effective in restoring the contaminated oil's resistivity. Experiments on contaminated oil directly from the Z-machine could lead to further insights before a similar pulsed power apparatus is constructed at LLE.

## 8. Acknowledgements

I sincerely thank my advisor, Kenneth L. Marshall, for giving me valuable guidance and support on this research throughout my time at LLE. I also thank my undergraduate mentor, Akif Hosein, a chemical engineering student at the University of Rochester, for giving me background information on my project, teaching me how to operate all the instruments, and giving me a lot of support throughout my time at the lab. I thank my fellow peers in the high school internship program for constantly supporting me throughout this project. Lastly, I thank Dr. Craxton for giving me the opportunity to work at LLE.

## 9. References

- [1] "Shell Diala S2-ZX-A." *Technical Data Sheet*, [www.dayanoilco.com/upload/product/1451466774.pdf](http://www.dayanoilco.com/upload/product/1451466774.pdf). Table.
- [2] "How Does the Z Machine Work?" *Sandia National Laboratories*, [www.sandia.gov/z-machine/](http://www.sandia.gov/z-machine/).
- [3] Horry, M. L., et al. "Z" *Facility Dielectric Oil Clean-up*. [http://ieeexplore.ieee.org/xpl/tocresult.jsp?isnumber=17806&filter%3DAND\(p\\_IS\\_Number%3A17806\)&pageNumber=9](http://ieeexplore.ieee.org/xpl/tocresult.jsp?isnumber=17806&filter%3DAND(p_IS_Number%3A17806)&pageNumber=9).
- [4] *Breakdown of Liquid and Solid Insulation*. [www.elect.mrt.ac.lk/HV\\_Chap2.pdf](http://www.elect.mrt.ac.lk/HV_Chap2.pdf).
- [5] Nave, R. "Electricity and Magnetism." *Hyper Physics Concepts*, Georgia State University, [hyperphysics.phy-astr.gsu.edu/hbase/emcon.html#emcon](http://hyperphysics.phy-astr.gsu.edu/hbase/emcon.html#emcon).
- [6] "Tesla Coil Schematic." *Tesla Coil Design*, [www.teslacoildesign.com/construction.html](http://www.teslacoildesign.com/construction.html).
- [7] Fernandez, Diego P., et al. *Database for the Static Dielectric Constant of Water and Steam*. American Institute of Physics and American Chemical Society.
- [8] "Acetone." *Data Sheet*, Shell, [www.shell.com/content/dam/shell/static/chemicals/downloads/products-services/datasheet-acetone.pdf](http://www.shell.com/content/dam/shell/static/chemicals/downloads/products-services/datasheet-acetone.pdf). Table.
- [9] "Isopropyl Alcohol." *Data Sheet*, Shell, [www.panachem.com/msds/iso\\_propyl\\_alcohol\\_IPA.pdf](http://www.panachem.com/msds/iso_propyl_alcohol_IPA.pdf). Table.
- [10] "What is the Significance of Negative Resistance?" *Quora*, <https://www.quora.com/What-is-the-significance-of-negative-resistance>.

[11] "13X Molecular Sieve." *Delta Adsorbents*, Delta Enterprises, [www.deltaadsorbents.com/13x-molecular-sieve](http://www.deltaadsorbents.com/13x-molecular-sieve).

[12] *Molecular Sieve. Natural Zeolite*, [srorzeolite.org/en/alsaeda-script/uploads/2014/08/Zeolite\\_Molecular\\_Sieve\\_4A-287x300.gif](http://srorzeolite.org/en/alsaeda-script/uploads/2014/08/Zeolite_Molecular_Sieve_4A-287x300.gif).

[13] *Activated Carbon*. TIGG, <http://www.tigg.com/what-is-activated-carbon.html>.

[14] "Activated Carbon." *Capital Carbon*, [www.capitalcarbon.in/images/activated-carbon.gif](http://www.capitalcarbon.in/images/activated-carbon.gif).

[15] "Electronics and Chemicals." *Alibaba*, [alibaba.com](http://alibaba.com).

# Validating the Ion Slowing Model in the Geant4 Simulation Toolkit

Jonah Simpson

Brighton High School

Advisor: Dr. Christian Stoeckl

University of Rochester

Laboratory for Laser Energetics

Summer High School Research Program 2016

December 2017

## **Abstract**

Monte Carlo particle simulations are valuable because of their ability to accurately track multiple complex processes in specific geometries, but their applicability is constrained by the need to validate each physical process simulated in the code. The fast-ion energy-loss electromagnetic models in Geant4 were validated against the well-established, dedicated ion stopping simulation SRIM. The Geant4 toolkit was used to create a simple simulation of ion beams with energies in the range 1-20 MeV incident on various target materials. Tracking the position into the material and the kinetic energy of individual ions over many simulated particles allowed a comparison of the slowing down models. Geant4 and SRIM showed good agreement over the entire energy range in all target materials and with all the options for electromagnetic models available in the toolkit.

## **Introduction**

Laser-driven ion experiments at OMEGA EP are conducted to investigate the reactions of light ions created in a primary target as they interact with secondary targets, creating conditions like those in particle accelerators. A Monte Carlo model is suitable for simulating such experiments by tracking individual particles and reactions through specific experimental geometries to predict signals from detectors.

Geant4 is a toolkit for the Monte Carlo simulation of particle passage through matter [1]. It is provided as an object-oriented framework of C++ source. The source provides code for the simulation of particles, and each use case requires extending specific classes provided in the toolkit, allowing great flexibility in terms of experimental geometry, physical processes, data collection and more. However, reaching an accurate simulation of an experiment requires each of the processes simulated for each particle in the experiment to be validated.

This project aims to validate the Geant4 model for the slowing of fast ions in target materials. The slowing of fast ions is relevant to the interaction of ions generated in the primary target with the secondary target material. Further reactions leading to measurable results are in part dependent on the speed of ions in the material, which will vary with the slowing model.

### **SRIM – The standard of comparison**

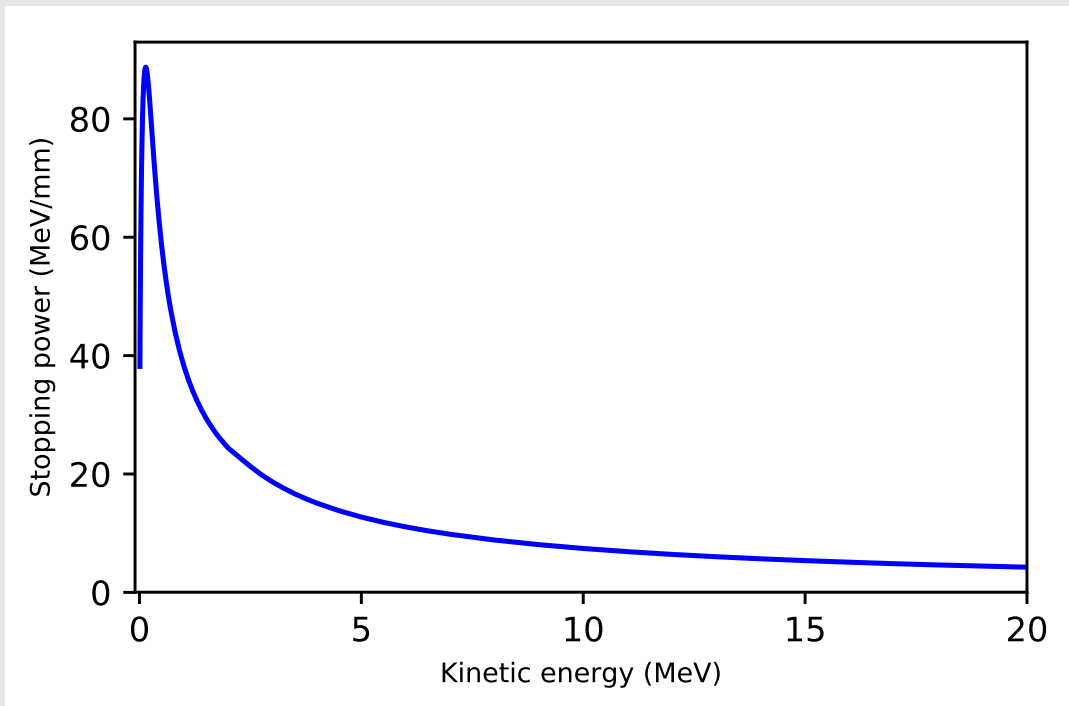
SRIM is a program dedicated to calculating the Stopping and Range of Ions in Matter [2]. Results from SRIM have been validated against experimental data for many ions and materials [3]. SRIM can create tables of the average stopping power as a function of ion energy in a given ion-material combination.

Stopping power,  $S$ , is the amount of energy that an ion loses per unit distance it travels through a material:

$$S(E) = -\frac{dE}{dx} \quad (1)$$

where  $E$  is energy and  $x$  is distance travelled. For a given ion-material combination, the stopping power is a function of the kinetic energy of the ion. This is because the relative speed of the ion and the electrons in the target material affects how much energy is transferred. For example, Figure 1 shows the stopping power of a deuteron in a carbon-deuterium (CD) compound material, from a data table generated with SRIM.

**Figure 1.** Deuteron stopping power in CD versus ion energy (from SRIM). The sharp peak in stopping power at a sub-MeV ion energy coincides with maximal loss in energy due to interaction with target material electrons. This peak is characteristic of all stopping power curves.



To compare with simulation of travelling particles, this information was used to model how an ion would slow in the material. To model the slowing of an ion, a script was written to calculate the energy of an ion as it passes through the material in discrete steps.

Given any ion energy, the stopping power at that energy level from the SRIM data was used to determine the energy decrease over a small step in distance to get a new energy value.

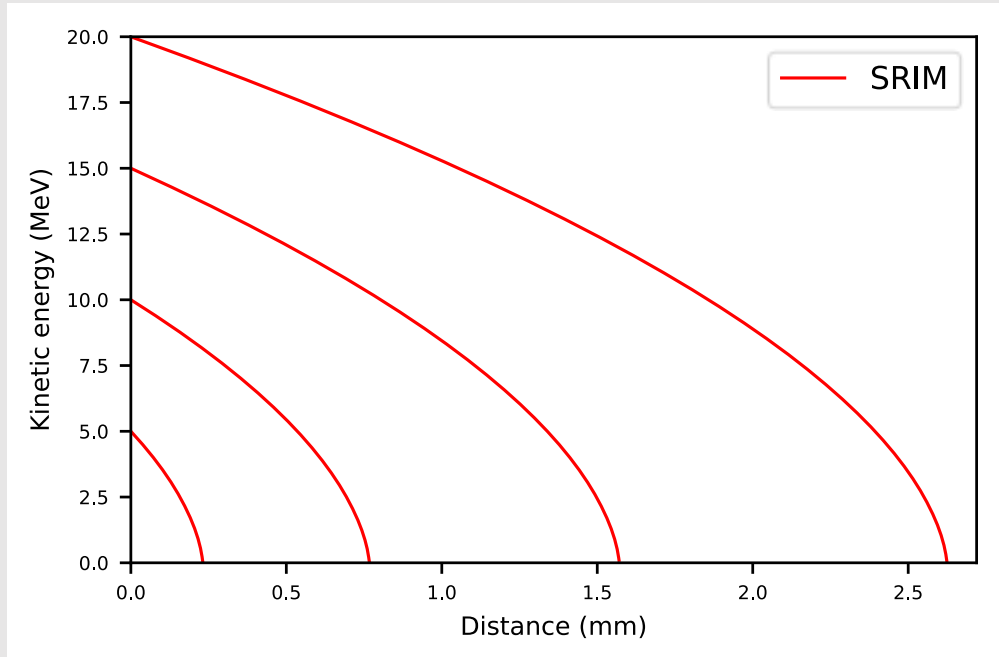
That is,

$$E_n = E_{n-1} - S(E_{n-1})\Delta x \quad (2)$$

where  $E_n$  is the ion energy at the current step of the simulation,  $E_{n-1}$  the ion energy at the previous step,  $S(E)$  the stopping power as a function of ion energy, and  $\Delta x$  the small step in distance. The initial energy  $E_0$  was set to a value in the range 1-20 MeV and then equation 2 was applied recursively to calculate ion energy as a function of distance travelled in the material.

For example, Figure 2 shows the slowing of a deuteron in CD starting at multiple energies, calculated using the SRIM data in Figure 1 with step sizes of  $10^{-3}$  mm.

**Figure 2.** Deuteron slowing in CD based on SRIM stopping power. Four particles were simulated with starting energies of 5, 10, 15, and 20 MeV. The increase in stopping power at low energies (see Figure 1) is reflected here in the increasingly sharp fall-off in kinetic energy as the ion slows.



## Geant4

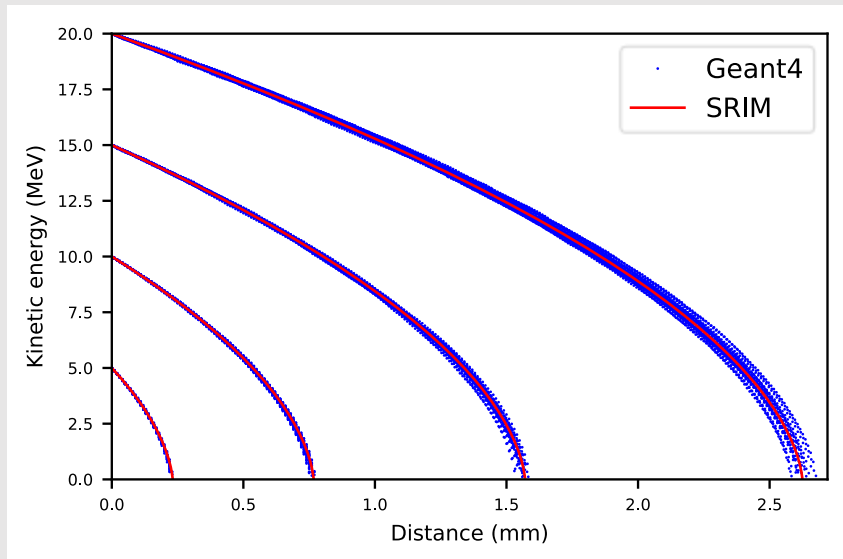
The SRIM model predicts the average slowing of ions in a material. In reality, ions stray from the average because the slowing process comprises an aggregate of many random interactions with target molecules. Geant4 does not deal with averages but rather simulates a single particle at a time, in discrete steps where processes such as electromagnetic slowing and nuclear reactions are applied during each step randomly, with a probability calculated from the cross section of the individual reactions. The strategy for comparing the two models is to generate the predicted averages with SRIM and to simulate many particles with Geant4 and confirm that the Geant4 simulation follows the SRIM model.

Because only the interactions of particles within a material were of concern in this project, the Geant4 experimental geometry consisted of a single cube of target material and particles were generated at the center of the cube with initial kinetic energy so that they were stopped within the material.

Geant4 allows user-defined code to be run at each step of a particle's simulation by defining a class that extends the provided *G4UserSteppingAction* class. To track the slowing of simulated ions, a class was defined that logged the position and kinetic energy of the current ion at each step in the simulation.

A separate script was created to calculate the path length for each ion from the logged positions in each simulation step. Graphs of kinetic energy versus distance travelled were directly compared with the ones generated by the SRIM reference data. For example, Figure 3 shows the Geant4 results for deuteron slowing in CD, overlaid with the SRIM model from Figure 2.

**Figure 3.** Deuteron slowing in CD according to Geant4 and SRIM. Red curves show the SRIM model as in Figure 2. Blue points represent individual ions in Geant4.



## Experimental Parameters

Parameters common to Geant4 and SRIM

To cover a wide range of possible experiments, simulations were run with varied ion type and target material. Ion types included: proton, deuteron, and triton. Target material types included: deuterium, tritium, helium-3, beryllium, carbon-12, and carbon-deuterium compound (CD). It was ensured that both simulations had the same definitions of materials with matching densities and molecular weight.

Geant4-specific parameters

Geant4 operates with a modular model of physics processes, allowing different combinations of physics processes to suit the experiment, so simulations were run with 7 different electromagnetic physics options, which are primarily responsible for fast ion slowing.

An overview of the applications of the different options is available from the SLAC National Accelerator Laboratory [4].

## Results

Stopping power tables were generated in SRIM for every ion-material combination described above, and those data were used to generate comparisons for simulations run in Geant4 with each EM physics option. The resulting graphs were overlaid and in every case showed good agreement between the SRIM and Geant4 models.

Figure 4 (a-g) shows the different physics options for a single ion-material combination.

**Figure 4.** Deuteron slowing in CD with different EM physics options

**(a)** *G4EmStandardPhysics*

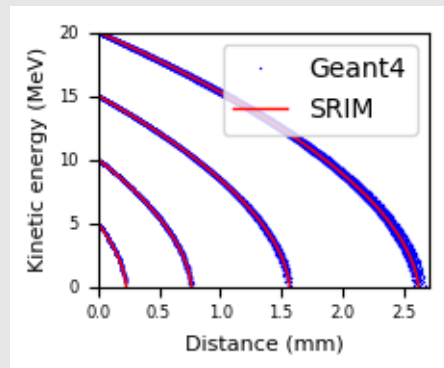
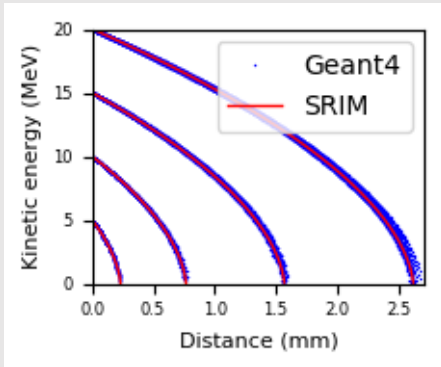
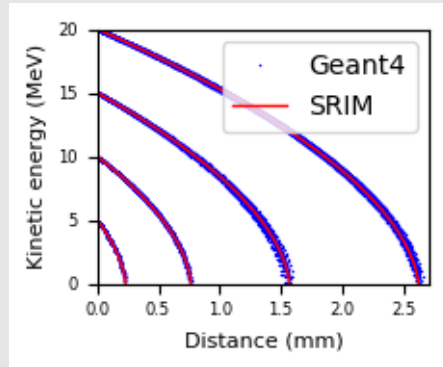


**Figure 4.** Deuteron slowing in CD with different EM physics options (continued)

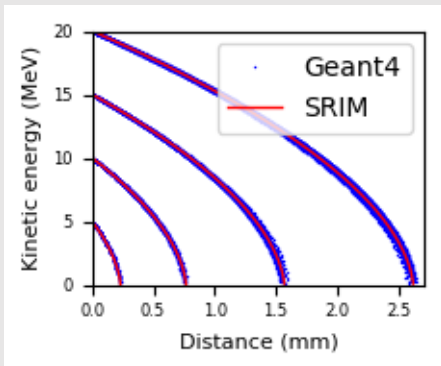
**(b)** *G4EmStandardPhysics\_option1*



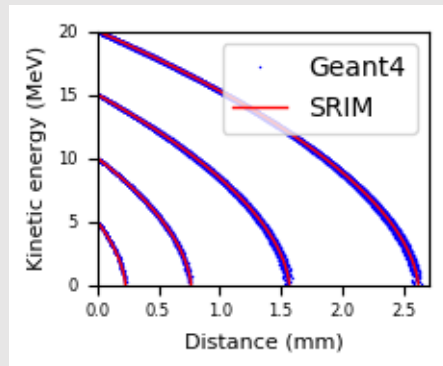
**(c)** *G4EmStandardPhysics\_option2*



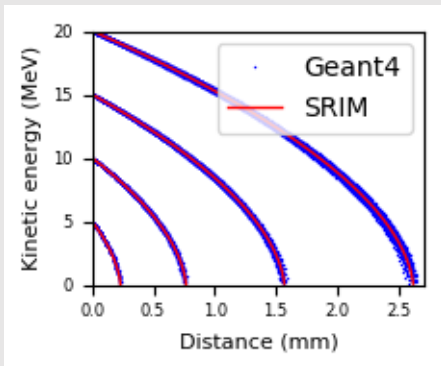
**(d)** *G4EmStandardPhysics\_option3*



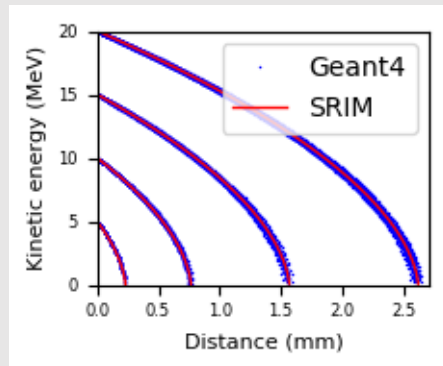
**(e)** *G4EmStandardPhysics\_option4*



**(f)** *G4EmLivermorePhysics*



**(g)** *G4EmPenelopePhysics*



Note that the results of the different electromagnetic physics options give almost identical results.

Figure 5 (a-r) shows the different ion-material combinations, all using the standard physics option.

**Figure 5.** Stopping power of all ions in all materials with *G4EmStandardPhysics*

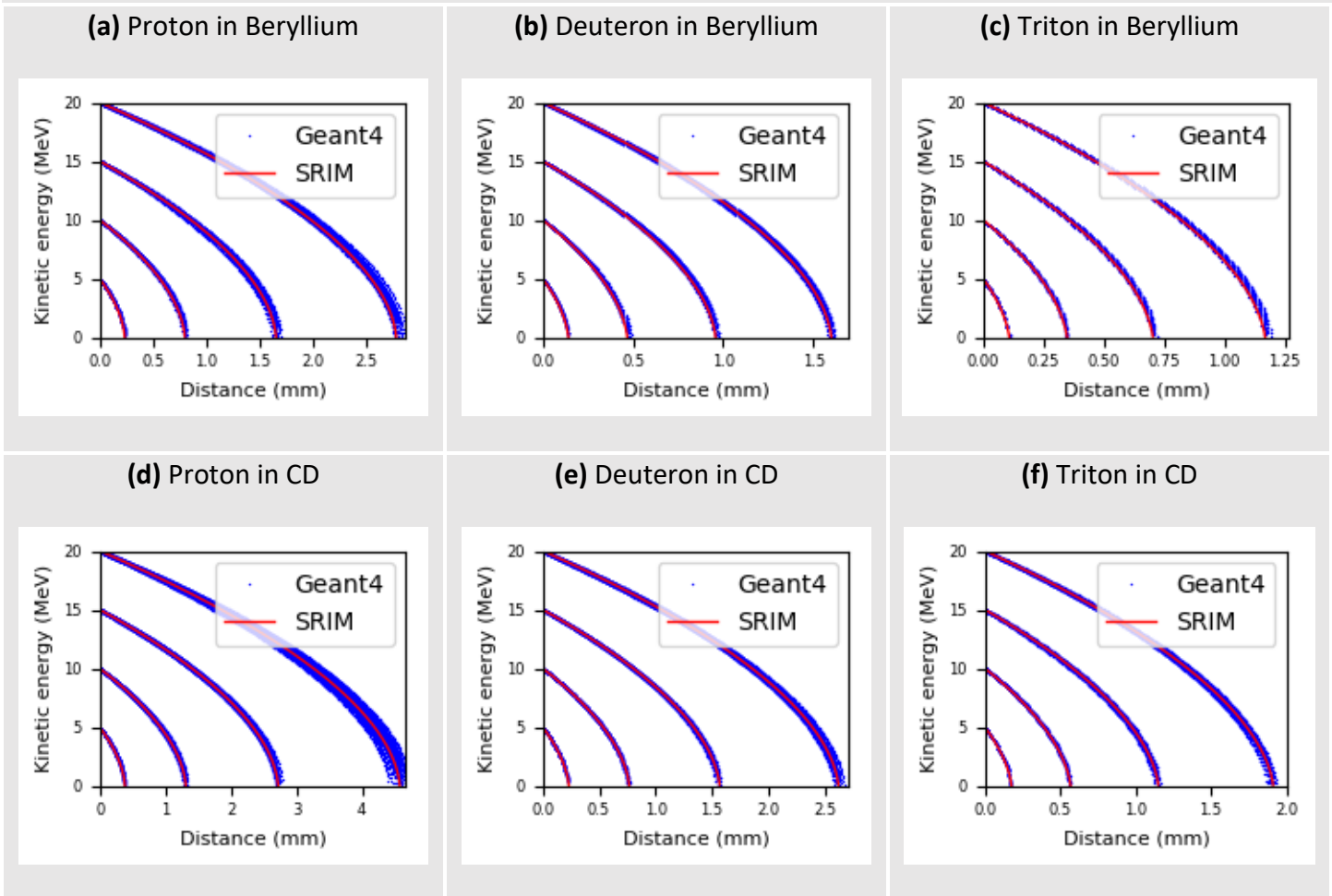
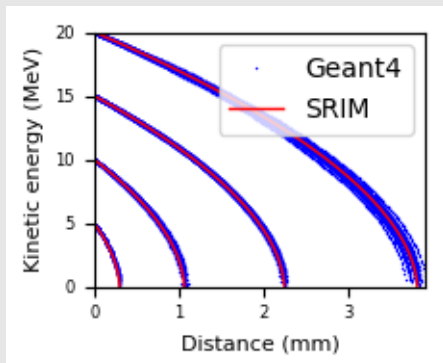
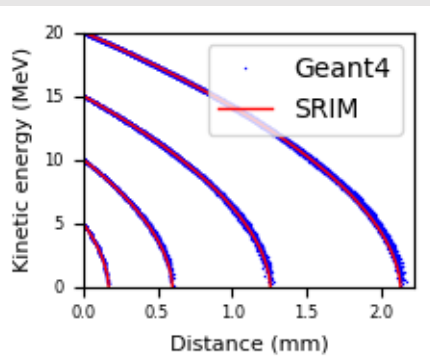


Figure 5. Stopping power of all ions in all materials with *G4EmStandardPhysics* (continued)

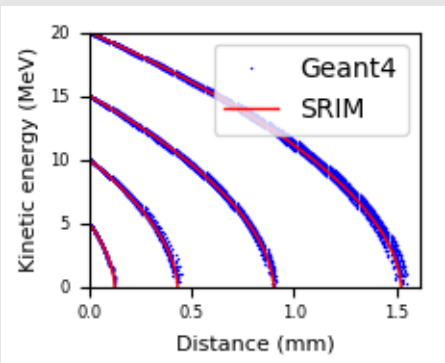
(g) Proton in Deuterium



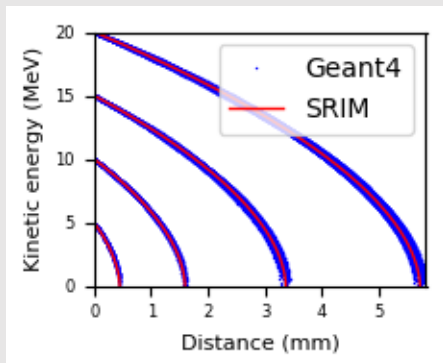
(h) Deuteron in Deuterium



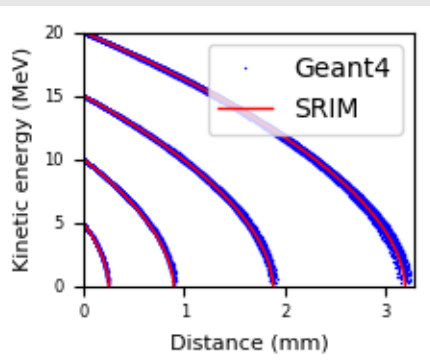
(i) Triton in Deuterium



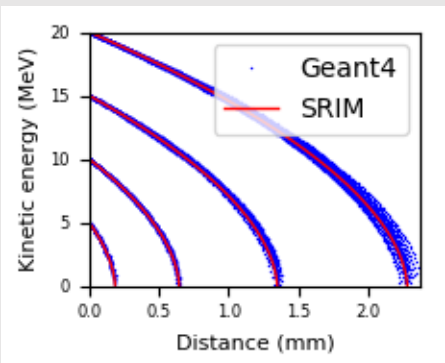
(j) Proton in Tritium



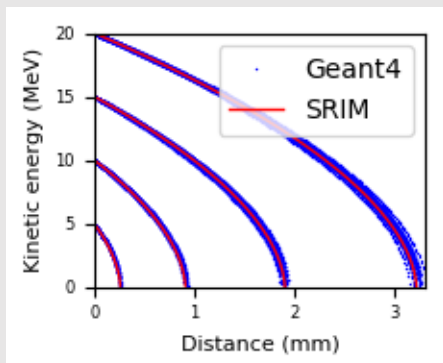
(k) Deuteron in Tritium



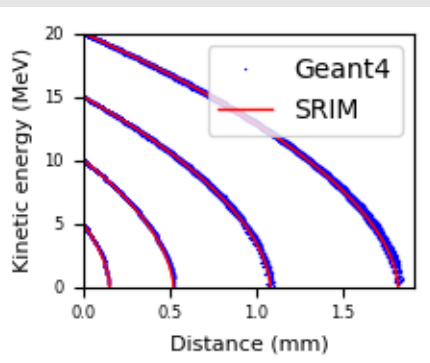
(l) Triton in Tritium



(m) Proton in Helium-3



(n) Deuteron in Helium-3



(o) Triton in Helium-3

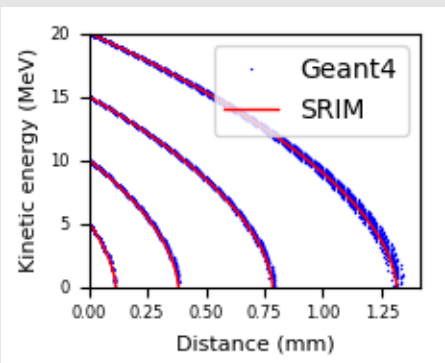
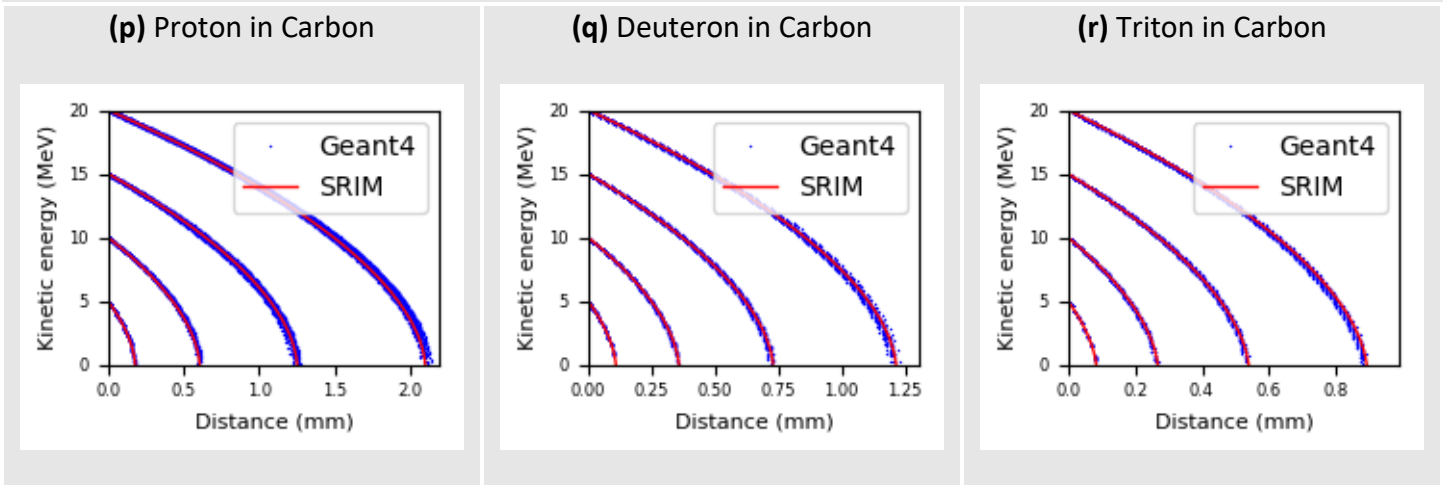


**Figure 5.** Stopping power of all ions in all materials with *G4EmStandardPhysics* (continued)



As with the different physics models, the different ion-material combinations gave almost identical results, all in agreement with the SRIM model. Additionally, the remaining combinations of other physics models with all the tested ions and target material did not differ noticeably in agreement between the Geant4 and SRIM simulations.

## Conclusion

The results indicate that for the tested parameters the Geant4 ion slowing model agrees well with SRIM, whose results have been independently validated. Should validation be necessary for different ions, other target materials, new physics models, or different particle kinetic energies, the methods used in this project are easily extensible to those cases.

## **Acknowledgements**

I owe complete thanks to my advisor Dr. Christian Stoeckl for guidance, to Manuel Stoeckl, who helped me to navigate the intricacies of Geant4, to my fellow interns for enjoyable lunch times, and to Dr. Craxton for running the program that introduced me to science in the real world.

## References

[1] [geant4.cern.ch](http://geant4.cern.ch)

[2] [www.srim.org](http://www.srim.org)

[3] [www.srim.org/PlotCit.htm](http://www.srim.org/PlotCit.htm)

[4] [geant4.slac.stanford.edu/SLACTutorial14/EMPhysics.pdf](http://geant4.slac.stanford.edu/SLACTutorial14/EMPhysics.pdf)

# **Impulse Response Calibration of a Neutron Temporal Diagnostic**

## **Using the Multi-Terawatt Laser**

Matthew Wang

Pittsford Sutherland High School

Pittsford, NY

Advisor: Dr. Christian Stoeckl

Laboratory for Laser Energetics

University of Rochester

Rochester, New York

April 2016

## **Abstract**

In inertial confinement fusion (ICF) experiments on OMEGA, the neutron production width is an important metric used to assess the quality of the implosions. In order to measure this width accurately, the impulse response of the neutron temporal diagnostic (NTD) system must be known precisely. The NTD uses a plastic scintillator that converts neutron energy into light, which is recorded by an optical streak camera capable of resolving temporal history. An NTD system was designed and built for the Multi-Terawatt (MTW) Laser, which uses x-ray pulses to simulate neutron production, in order to develop techniques to optimize its impulse response. The performance of this system was evaluated by varying the configuration of the laser, which included pulse duration, energy, focus condition, and target material, as well as by varying the NTD nose cone, which houses the scintillator. An important finding is that the measured impulse response using an aluminum nose cone was twice as fast as that using a tungsten nose cone. Techniques developed during this experiment will be used to optimize the impulse response of the NTD system on OMEGA.

## I. Introduction

Thermonuclear fusion, which does not generate nuclear waste, produces the most basic form of energy in the universe and has significant long-term application in the generation of electric power. One approach to controlled fusion, investigated at LLE, is ICF. In ICF experiments, shells are filled with either deuterium or deuterium-tritium mixtures and are compressed by direct laser illumination [1,2], soft x-ray radiation in a laser-heated hohlraum [3], or strong magnetic fields [4], resulting in thermonuclear fusion. As a measure of the quality of these experiments, the neutron production width must be known and recorded accurately [5]. However, the neutron temporal diagnostic (NTD) systems used to capture these events have a finite impulse response, which needs to be measured accurately. Impulse response, in this context, is defined as the width of the detected signal that results from an infinitesimally short pulse of neutrons. In this work, an NTD was designed and built for the MTW laser to develop techniques to optimize the impulse response of such systems. Although similar NTDs have been developed and implemented on larger lasers, including one on OMEGA, there are few shots readily available on the OMEGA laser system for experimentation. Thus, the brief cooldown time of the MTW laser, approximately half an hour, made it ideal for the experimentation conducted in this project.

## II. Experimental Setup

**Figure 1** illustrates the experimental setup of the MTW-NTD system and the optical relay path from the target chamber to the streak camera. The optical relay path is composed of a scintillator, housed in the nose cone, a lens barrel, two mirrors, a filter, a focus lens, and an optical streak camera.

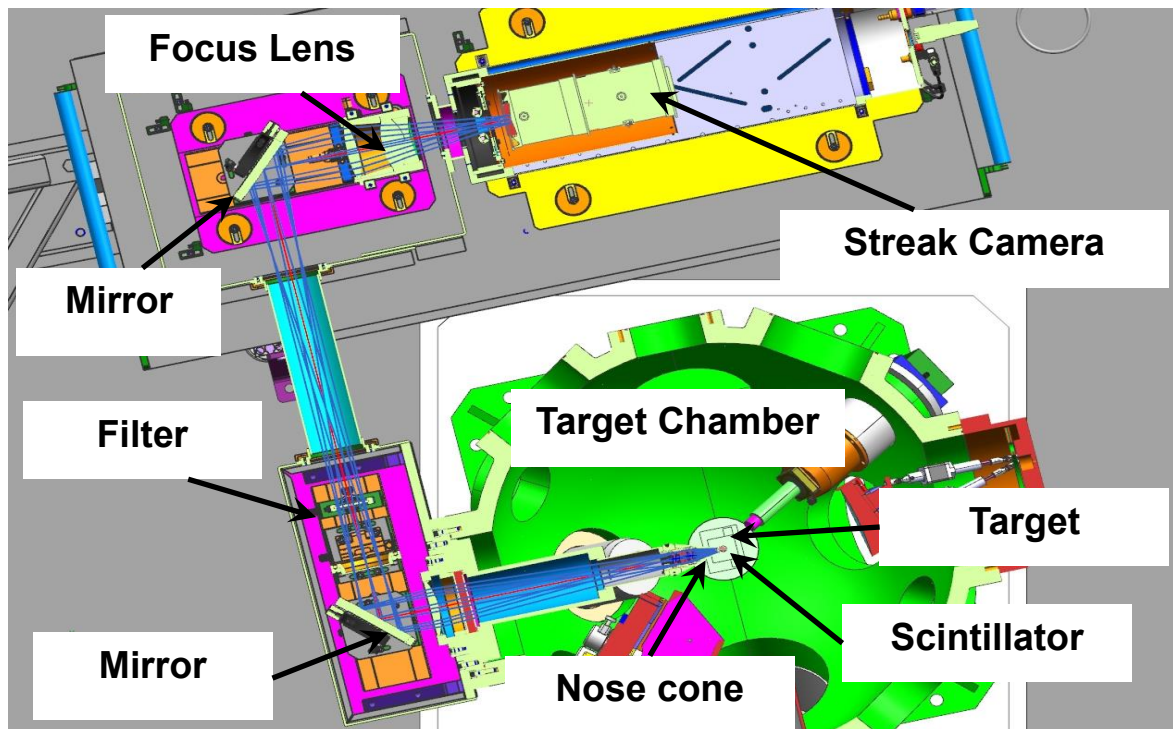


**Fig. 1:** CAD drawing of the MTW-NTD experimental setup. X-ray energy produced from the interaction between the target material and the laser pulse is converted into light by the scintillator, housed in the nose cone.

The targets used in this experiment included gold, copper, and aluminum targets, ranging from 500 by 500 by 3 microns to 500 by 500 by 20 microns. The x rays produced from the interaction of the MTW laser pulse with the target were converted into light by a BC-422 plastic scintillator, with a rise time determined to be less than 20

ps [6]. The light emitted by the scintillator traveled through the optical relay system, as illustrated in **Figure 1**, and ultimately was focused onto and recorded by an optical streak camera. **Figure 2**, from **Ref. 7**, describes the operation of a typical streak camera. The incident light on the photocathode is converted into electrons, the number of electrons being dependent on the intensity of the incident light for a given length of time. The electrons are accelerated by high voltage electrodes onto the phosphor screen, and are then converted back into light [7]. As the electrons pass through the streak tube, the voltage across the sweep electrodes is adjusted such that electrons that arrive at later times are deflected to a different spot on the phosphor screen, producing an image read by a CCD camera that is resolved in both the temporal and spatial directions.

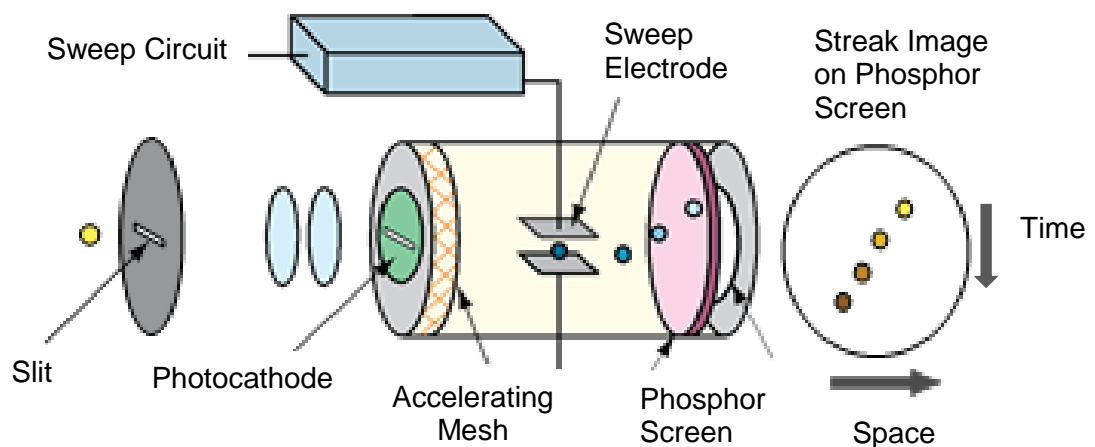


**Fig. 2:** Illustration of the components of an optical streak tube [7]. The optical streak camera is capable of converting incident light into electrons, which create an image on the phosphor screen after being deflected by the sweep electrodes.

LLE's ROSS P510 streak camera was used in this work. Extensive calibrations were performed for the streak camera, including correcting geometric distortions by

using a slow sweep, as well as calibration of the sweep speed and adjusting the initial biases of the electrodes to optimize focus [8].

### III. Data Collection

Over thirty shots of the MTW laser system were taken during a week of experimentation. **Figure 3** shows a CCD image produced from the first shot of the MTW-NTD laser and a corresponding lineout of intensity vs. space.

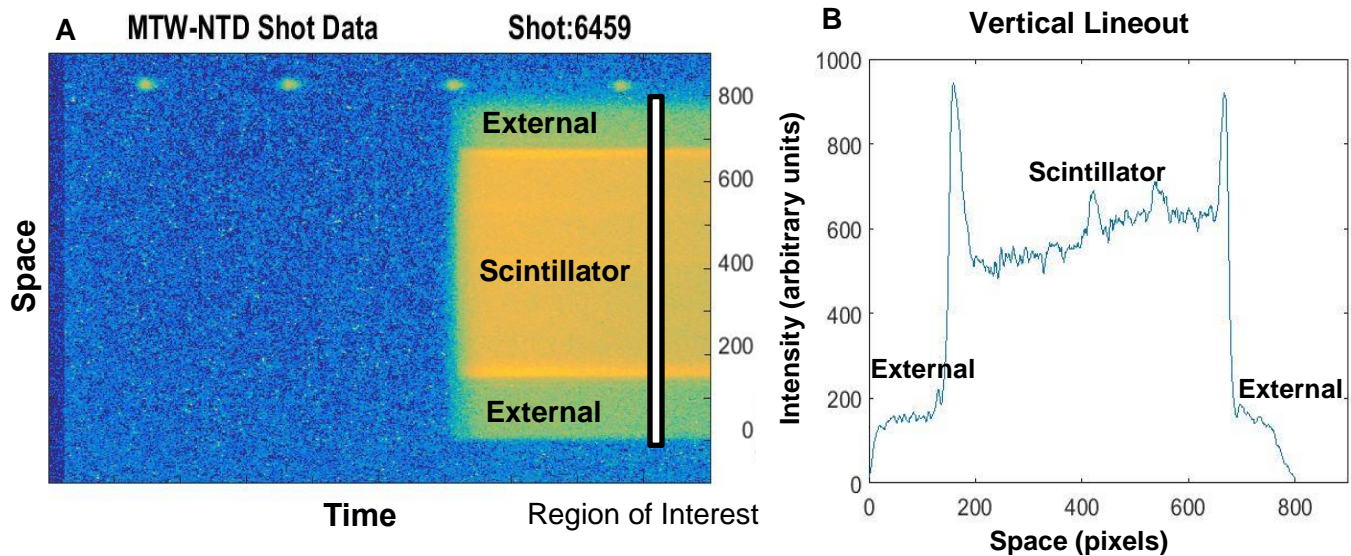


**Fig. 3:** (A) CCD image of the MTW laser shot. The x-axis indicates the temporal direction, while the y-axis represents the spatial direction. The brightness correlates to the intensity of the light produced. (B) Plot of the light intensity as a function of space. The external signal was associated with the presence of noise outside of the edges of the scintillator.

In **Figure 3A**, light produced from the scintillator is shown in the region from ~150 pixels to ~650 pixels on the y-axis. As shown in the image, around 850 pixels on the y-axis, a fiducial pulse of 506 ps was used to calibrate the time elapsed per pixel. The data reveals an unexpected signal produced from the region outside the scintillator, shown in the picture to be from 0 to ~150 pixels and from ~700 to ~800 pixels.

Furthermore, from **Figure 3B**, the plot indicated that the external signal was about 1/4 the intensity of the main signal. Another finding that was made from the first shot was regarding the leading edge of the scintillator signal. From the image a green-blue stripe could be seen before the characteristic orange-yellow scintillator signal.

As a result of these initial findings, subsequent changes in the experimental configuration were made to further investigate the sources of the external signal and the leading edge of the signal, ultimately to see if they would have an effect on the impulse response of the MTW-NTD system.

#### **A. Cherenkov Radiation**

Three shots were taken with an alignment nose cone. Since this nose cone did not contain a scintillator at the bottom, the resulting image should have revealed no signal. **Figure 4** shows the image produced from one of the alignment nose cone shots.

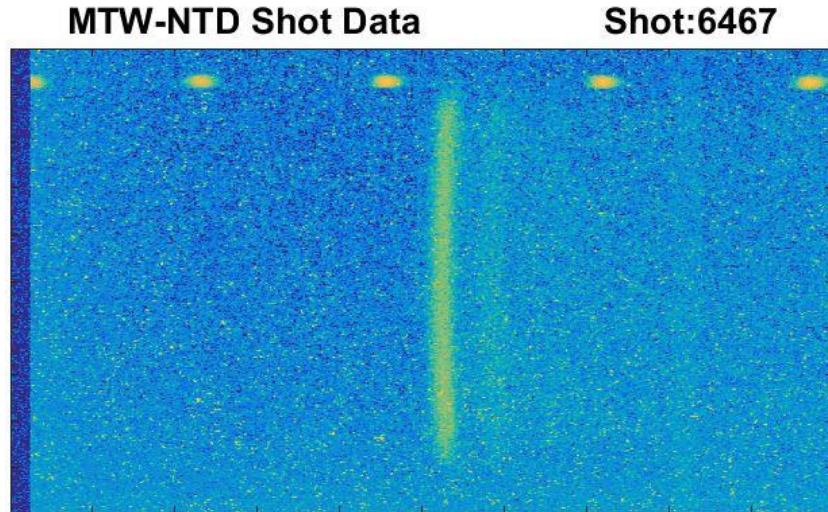


**Fig. 4:** *CCD image of an MTW laser shot with the alignment nose cone (no scintillator).*

The image indicated that a signal was still present even though there was no scintillator in the alignment nose cone. It was determined that this signal was produced from Cherenkov radiation in the nose cone lenses. Cherenkov radiation is light emitted from an electron when the electron travels through a medium faster than the phase velocity of light in that medium. As the production of energetic electrons is highly dependent on the laser intensity, other shots were taken with the alignment nose cone but with the laser defocused, to see if the intensity of the Cherenkov radiation would be affected. The laser was defocused by 50  $\mu\text{m}$  and by 100  $\mu\text{m}$ , and the corresponding intensity of the Cherenkov radiation is shown in **Figure 5**.

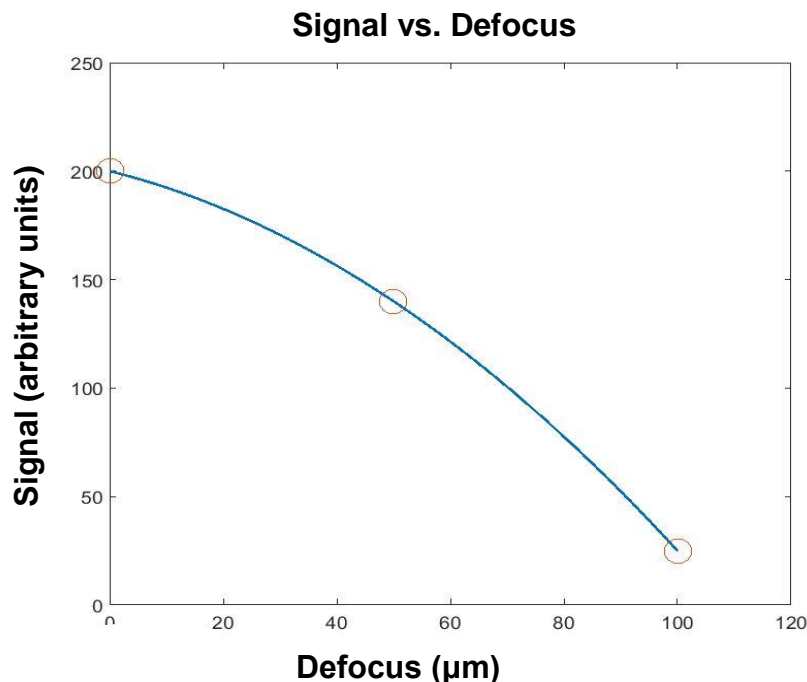


*Fig. 5: Plot of the signal intensity vs. defocus. These shots confirmed the presence of Cherenkov radiation.*

From these shots it was found that the intensity of the Cherenkov radiation could be significantly reduced by defocusing the laser by 100  $\mu\text{m}$ . As a result, subsequent shots were taken with the laser defocused by 100  $\mu\text{m}$ .

## B. External Signal

The external signal shown in **Figure 3A** was found to have been the result of scintillator light reflecting off the surface of the nose cone, as illustrated in **Figure 6**. The nose cones were then coated with a less reflective material, black plastic foil, which was shown to reduce the intensity of the external signal, as shown in **Figure 7**.

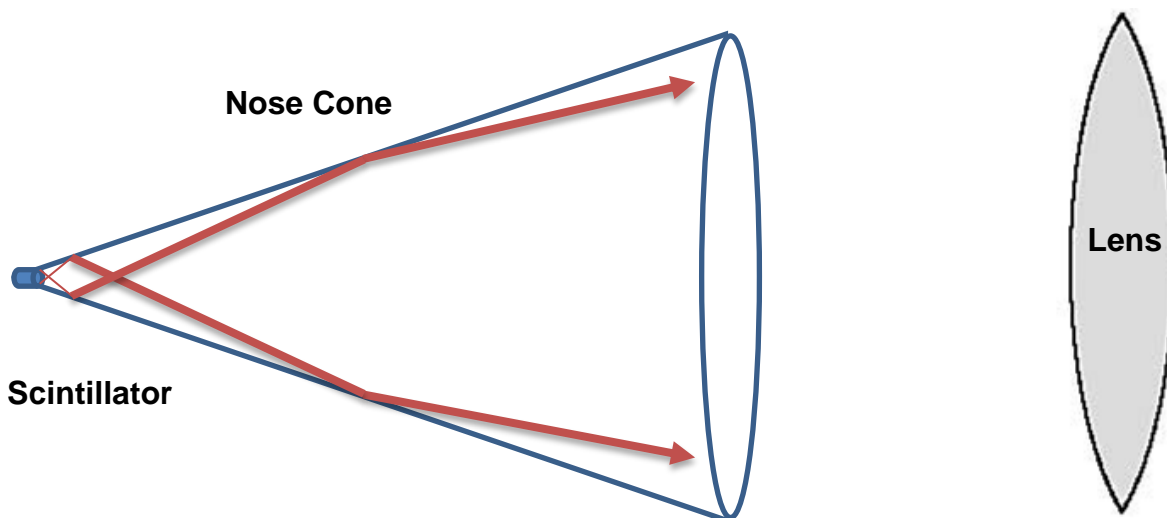


**Fig 6:** Schematic of the origin of the external signal produced by the scintillator and nose cone (enlarged). Light rays that reflected off the nose cone were not focused correctly and produced an external signal, shown in **Figure 3b**.

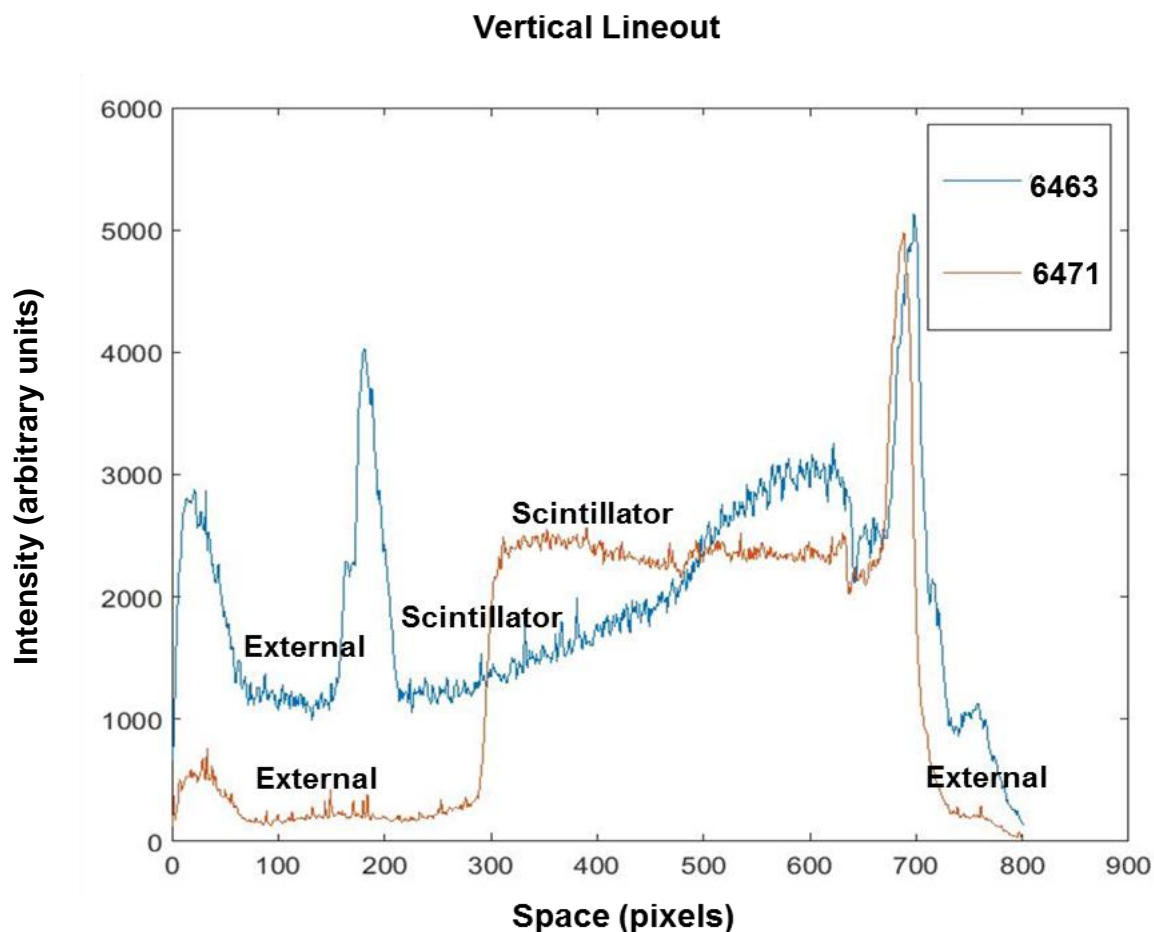


**Fig. 7:** Plot of the intensity vs. space for shots 6463 and 6471, one of which (Shot 6471) was taken with the nose cone coated with a less reflective surface. The external signal was significantly reduced in Shot 6471.

The ratio of the external signal from shot 6463, in the region ~75-150 pixels, to the scintillator signal, in the region ~200-675 pixels, is ~1:1.5. Compared to that for shot 6471, which indicated a ratio of the external to scintillator signal of ~1:8, the less reflective coating significantly reduced the amount of reflected scintillator light. After this finding all subsequent shots were taken with the nose cone coated with the black plastic foil.

## IV. Data Analysis

### A. Physical Modeling Equation

A physical modeling approach was used to remove the effect of the long scintillator decay. The equation is given by

$$N_i = S_i - \sum_{j=0}^{i-1} N_j \exp\left[\frac{-(i-j) \times \Delta t_p}{d}\right] \quad (1)$$

where the signal at pixel location  $i$ ,  $N_i$ , is given as the recorded signal  $S_i$  minus the sum of all earlier neutron signals, which decay exponentially at the scintillator fall time  $d$ , with  $\Delta t_p$  as the time separation of the two pixels [5]. In this work 1.4 ns was used as the scintillator fall time. The deconvolution of the signal can be seen in **Figure 8**.

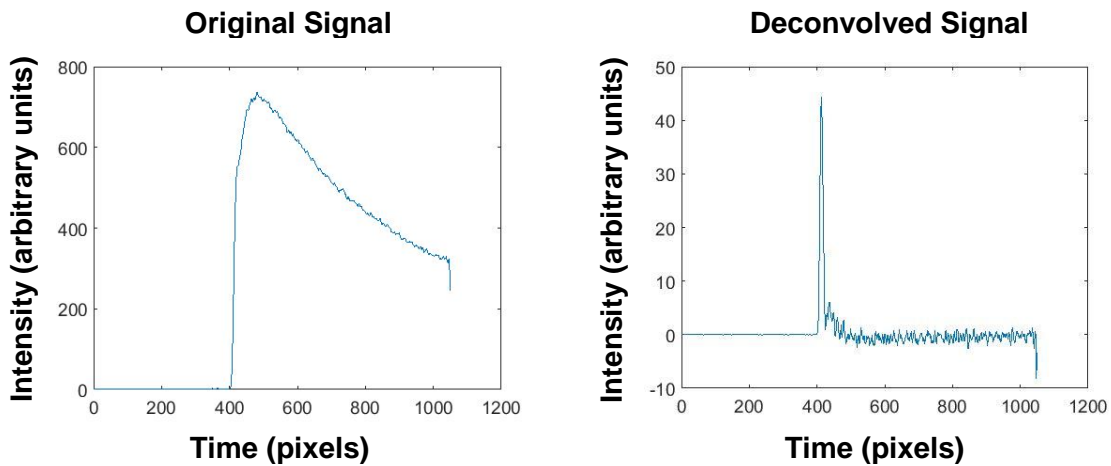


**Fig. 8:** Horizontal plots of the signal intensity vs. time. The deconvolution of the original signal produces an unfolded signal whose full width half maximum ( $\sim 22$  ps) could be determined.

A Gaussian fit was used to measure the full width half maximum (FWHM) of the unfolded signal in order to determine the impulse response of the MTW-NTD system.

## B. Experimental Findings

The most significant finding from this experiment was that an aluminum nose cone produced a shorter impulse response compared to that for a tungsten nose cone.

**Figure 9** shows the comparison of the tungsten and aluminum nose cones used in this work.

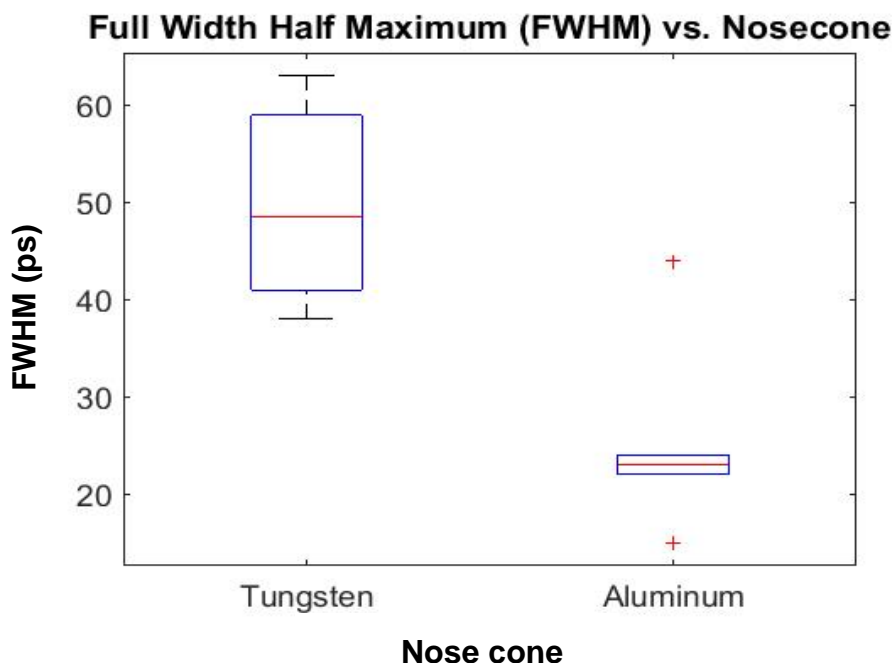


**Fig. 9:** Box plot comparing the impulse response for the aluminum and tungsten nose cones. The aluminum nose cone impulse response was measured to be twice as fast as the tungsten nose cone. (The “+” signs in the data for the aluminum nose cone represent experimental outliers)

The aluminum nose cone was measured to produce an impulse response of  $\sim 25 \pm 2$  ps, and the tungsten nose cone an impulse response of  $\sim 50 \pm 10$  ps. Besides nose

cone material, several parameters of the MTW-NTD setup were adjusted, including target material, pulse duration, defocus, and energy. As there were several parameters that differed between shots and since only thirty shots were taken, it was difficult to compare a significant number of shots that differed in only a single parameter.

Another finding that was made in this experiment was that the impulse response of the system using the aluminum nose cone was more consistent with a short pulse duration, shown in **Figure 10**. Although the average measured impulse response was ~23-25 ps for the two laser pulse durations, with a laser pulse ~1 ps, the range was measured to be ~4 ps, whereas with a laser pulse ~10 ps, the range was measured to be ~30 ps.

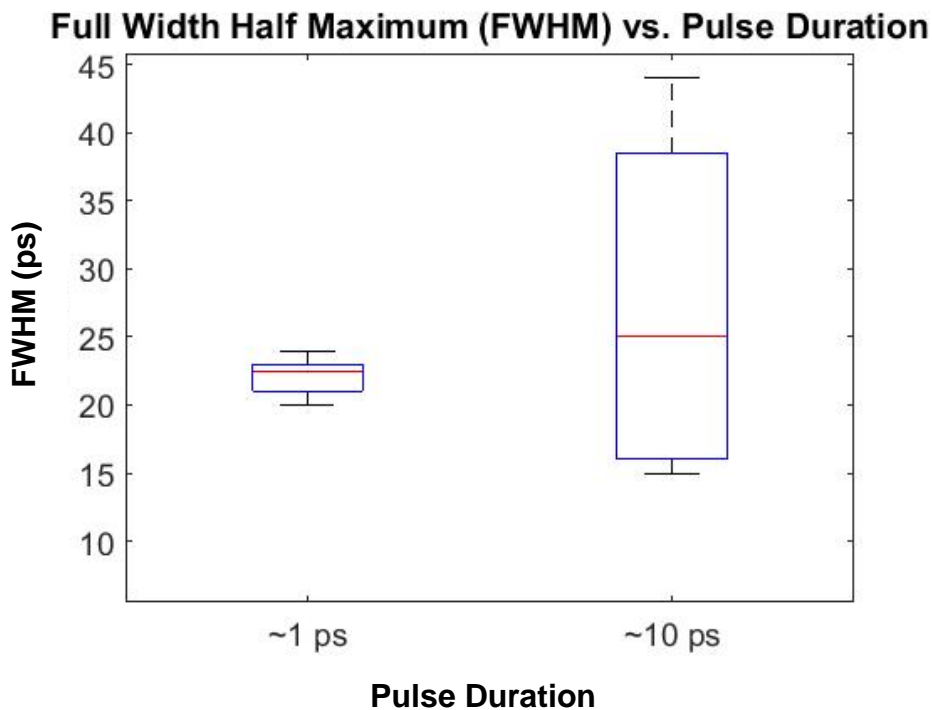


**Fig. 10:** Box plot of FWHM vs. Pulse Duration for the aluminum nose cone. The shorter pulse duration of the MTW laser system produced a more consistent impulse response.

Another notable finding of this experiment was the effect of defocusing the laser on the system performance, as shown in **Figure 11**. Although there were few shots with which to directly compare the effects of defocus on the measured impulse response, the defocused laser did produce a faster average impulse response,  $\sim 37 \pm 2$  ps compared to  $\sim 55 \pm 1$  ps. This suggests that the Cherenkov radiation had a negative impact on the MTW-NTD system performance, as its intensity without any defocus was  $\sim 200$  units, and with  $100 \mu\text{m}$  defocus it was  $\sim 20$  units (see **Figure 5**).

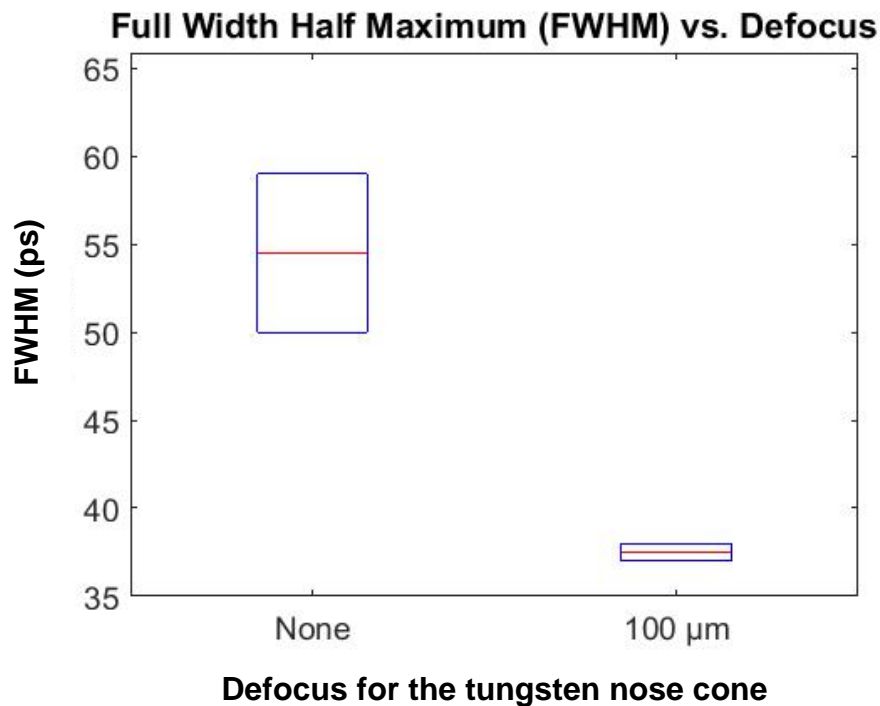


**Fig. 11:** Box plot of the FWHM vs. Defocus for the tungsten nose cone. Defocusing the laser by 100  $\mu\text{m}$  produced a faster and more consistent MTW-NTD impulse response.

Several adjustments made to the MTW setup yielded insignificant changes to the NTD performance. Some of these included the energy of the MTW laser shot, the target material, and the plastic nose cone coating. The lack of dependence on the coating indicated that the reflected light had very little effect on the measured impulse response of the system.

## V. Conclusions

A NTD system was designed and built for experimentation on the MTW laser system to develop techniques for optimizing the impulse response. During the data collection, Cherenkov radiation and an external signal were discovered in the CCD images. The intensity of both were reduced by defocusing the laser and by coating the nose cone with a less reflective surface. Cherenkov radiation was found to increase the measured system impulse response time, while the external signal had little effect on the response time. The most notable finding of this work is that the aluminum nose cone produced an impulse response of ~25 ps, whereas the tungsten nose cone produced an impulse response of ~50 ps. Many alterations in parameters, including laser energy and target material, yielded little improvement in system performance. Further investigations will be conducted to confirm and expand upon these findings, and ultimately such techniques will be implemented for use on OMEGA.

## VI. Acknowledgements

I would like to thank my advisor, Dr. Stoeckl, for encouraging me to ask questions about the theory underlying the research as well as for his support and guidance in each phase of the project. Dr. Stoeckl's unwavering enthusiasm helped me gain a considerably better understanding of the physics and theoretical background regarding the experiment. Also, many thanks to Joe Katz, whose help with hardware and the MTW-NTD assembly was instrumental to the project's success. Also, Joe's involvement with the project was extremely helpful, especially during the first week of the research when Dr. Stoeckl was unavailable.

I would like to thank Dr. Craxton for his work in providing us the resources and for helping guide us through the brief eight weeks of research. It is a testament to Dr. Craxton's tremendous efforts that this high school program has been so successful in educating high school students for so many years.

Finally, I would like to thank my fellow interns for their help and for creating a relaxed work environment. I especially wish to thank Jonah Simpson, whose assistance with writing the Matlab code was extremely helpful in compiling and analyzing the data.

## VII. References

1. J. Nuckolls, L. Wood, A. Thiessen, and G. Zimmerman, " Laser compression of matter to super-high densities: Thermonuclear (CTR) applications," *Nature* 239, 139 (1972).
2. R. S. Craxton, K. S. Anderson, T. R. Boehly, V. N. Goncharov, D. R. Harding, J. P. Knauer, R. L. McCrory, P. W. McKenty, D. D. Meyerhofer, J. F. Myatt, A. J. Schmitt, J. D. Sethian, R. W. Short, S. Skupsky, W. Theobald, W. L. Kruer, K. Tanaka, R. Betti, T. J. B. Collins, J. A. Delettrez, S. X. Hu, J. A. Marozas, A. V. Maximov, D. T. Michel, P. B. Radha, S. P. Regan, T. C. Sangster, W. Seka, A. A. Solodov, J. M. Soures, C. Stoeckl, and J. D. Zuegel, "Direct-Drive Inertial Confinement Fusion: A Review," *Phys. Plasmas* 22 (11), 110501 (2015).
3. J. D. Lindl, " Development of the indirect-drive approach to inertial confinement fusion and the target physics basis for ignition and gain," *Phys. Plasmas* 2, 3933 (1995).
4. S. A. Slutz, M. C. Herrmann, R. A. Vesey, A. B. Sefkow, D. B. Sinars, D. C. Rovang, K. J. Peterson, and M. E. Cuneo, "Pulsed-Power-Driven Cylindrical Liner Implosions of Laser Preheated Fuel Magnetized with an Axial Field," *Phys. Plasmas* 17 (5), 056303 (2010).
5. Stoeckl, C., et al. "Neutron temporal diagnostic for high-yield deuterium–tritium cryogenic implosions on OMEGA." *Review of Scientific Instruments* 87 (2016): 053501.

6. Lerche, R. A., and D. W. Phillon. "Rise time of BC-422 plastic scintillator < 20 ps." Nuclear Science Symposium and Medical Imaging Conference, 1991., Conference Record of the 1991 IEEE. IEEE, 1991.
7. *Guide to Streak Cameras*. Hamamatsu Photonics K.K., 2008.  
[https://www.hamamatsu.com/resources/pdf/sys/SHSS0006E\\_STREAK.pdf](https://www.hamamatsu.com/resources/pdf/sys/SHSS0006E_STREAK.pdf)
8. Donaldson, W. R., et al. "A self-calibrating, multichannel streak camera for inertial confinement fusion applications." *Review of Scientific Instruments* 73 (2002): 2606-2615.

*Simulations of Laser-Driven Magnetized-Liner Inertial Fusion*

**Leah H. Xiao**

Webster Schroeder High School

Advisor: **Dr. R. S. Craxton**

Laboratory for Laser Energetics

University of Rochester

November 2016

## 1. Abstract

Magnetized Liner Inertial Fusion (MagLIF) is being explored as a new method of producing fusion. MagLIF uses a cylindrical metal shell, or liner, containing deuterium fuel. A high electric current is run through the liner, forming a strong magnetic field and causing implosion of the cylinder. A preheating beam is fired down the axis of the cylinder to heat the deuterium so that when the liner implodes and the deuterium is compressed, the deuterium is able to reach the high temperatures needed for fusion. In this exploratory research work, simulations using the hydrodynamics code SAGE were conducted to help understand the physics of MagLIF. Simulations of MagLIF experiments on the OMEGA laser system at the University of Rochester Laboratory for Laser Energetics (LLE) without the preheating beam have demonstrated agreement with data from experimental shots. By varying the parameters of the beams used to implode the cylinder, the simulations have found the optimum conditions for achieving a uniform implosion with the OMEGA system. Simulations of upcoming shots on the OMEGA system with the incorporation of the preheating beam predicted temperature profiles of the heated deuterium-filled cylinder. SAGE was also used to simulate large-scale targets with dimensions similar to those of the Z-machine at Sandia National Laboratory. The simulated temperature profiles due to preheating are consistent with the experimental observations in four shots, a control shot and three variations. Simulations of the Z-machine with a higher deuterium density, as desired for future experiments, show that the proper temperature profile is achieved through the formation of a self-focusing density channel.

## 2. Introduction

Inertial confinement fusion (ICF) is a process that utilizes high powered lasers, X rays, ion beams or other energy means to compress and implode a target made up of a plastic or metal shell filled with deuterium-tritium fuel. The shell of the target ablates outward, compressing the contents inside the shell to reach temperatures of several keV (1 keV = 11.6 million degrees K). At the very high temperature and pressure, the nuclei can overcome the Coulomb force between them to achieve nuclear fusion. Most ICF research is done using lasers to implode the target.<sup>1</sup> Recently, an alternative method known as Magnetized Liner Inertial Fusion (MagLIF)<sup>2</sup> is being explored.

As illustrated in Figure 1, MagLIF utilizes a cylindrical target surrounded by a shell or liner that contains deuterium, which is heated with a laser beam called the “preheating beam” fired perpendicular to one circular end of the cylinder or “window” before implosion occurs. There are two different systems on which MagLIF experiments are currently run. The first is Sandia National Laboratory’s Z pulse power machine, and the second is the OMEGA laser system at LLE.

Sandia’s Z-machine uses an electric current pulse running through the liner to generate a strong magnetic field to implode the liner (Figure 1b). A second current is run through a set of external coils (Figure 1a) generating another magnetic field that becomes compressed when the deuterium compresses, which keeps the  $\alpha$ -particles released from the fusion contained within the cylinder. This containment contributes to the heating of deuterium to fusion temperature. The preheating beam (red arrow) is an essential part of MagLIF<sup>2,3</sup> because it heats the deuterium before implosion begins, allowing the deuterium to reach higher temperatures when compressed, increasing the number of fusion reactions. Additionally, the temperature needs to be high enough to maintain the current and the magnetic field. If the temperature drops too low, the current and thus the magnetic field dissipate.

Because the facilities needed to run the required current through the liner are large and expensive and there are a limited number of experimental shots that can be conducted (approximately one per day), small-scale MagLIF experiments are being carried out using

OMEGA, with the liner imploded by laser beam irradiation with beams known as “drive beams” instead of the electric current and magnetic field, as seen in Figure 1c.

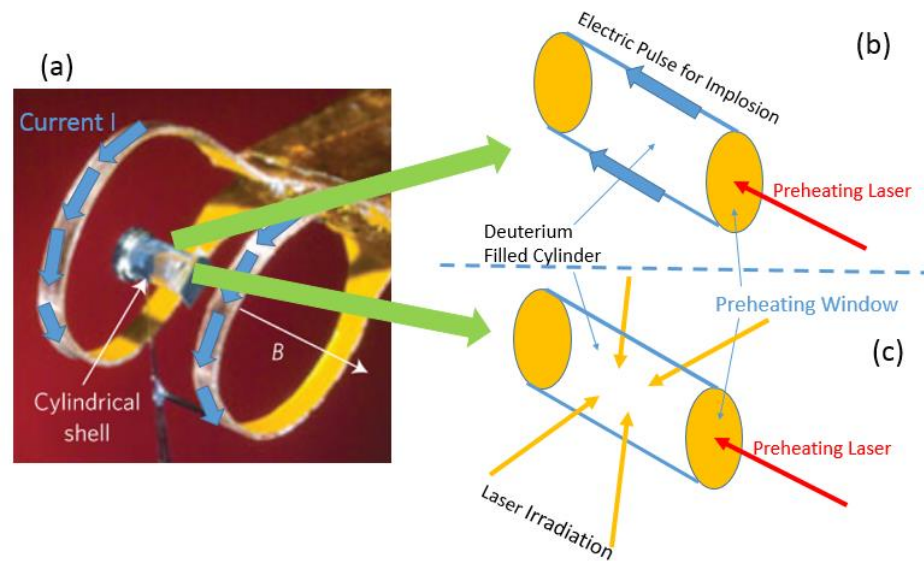


Figure 1: (a) Configuration of the MagLIF set up, showing a cylindrical liner (shell) filled with deuterium and coils that generate a magnetic field  $B$  along the axis of the cylinder when current is passed through. (b) Diagram of MagLIF with magnetic compression. The current is illustrated by the blue arrows, while the preheat beam is shown in red. (c) Diagram of the laser implosion configuration of MagLIF with the yellow arrows representing laser drive beams. The face of the cylinder where the preheat beam enters features a thinner wall called the window.

In this exploratory work, the hydrodynamics code SAGE<sup>4</sup> was used to understand aspects of the physics of MagLIF preheating and compression. This research demonstrates that SAGE is suitable to simulate these aspects of MagLIF. Proving this allows SAGE to be used to guide the designs for future MagLIF experiments.

### 3. MagLIF Experiments on the OMEGA System

Small-scale MagLIF experiments with laser beams irradiating the liner are being carried out using the OMEGA laser system. A detailed cross section of the liner and a 2D view of the upper half of the liner (which is rotationally symmetric about the  $z$ -axis) are shown in Figure 2.

The liner wall is made of CH (carbon-hydrogen, plastic). The thickness of the liner wall is  $20\ \mu\text{m}$ . The preheating window, which is approximately  $2\ \mu\text{m}$  thick, contains the high-pressure deuterium. There are four beams in Figure 2. Beam 1 and Beam 4 are symmetric about the middle plane of the cylinder, as are Beams 2 and 3. Each of the implosion beams illustrated actually represents ten beams that encircle the outside of the cylinder. MagLIF implosions on OMEGA use 40 beams.

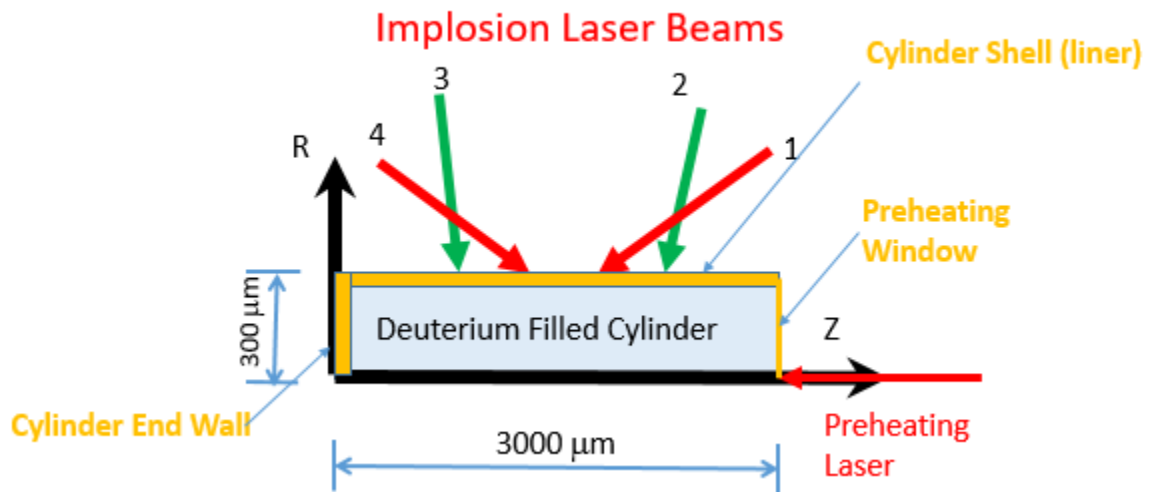


Figure 2: Cross Section of the MagLIF target used in the OMEGA system.

Simulations were conducted without the preheating beam to examine the speed and uniformity of compression (Section 3.1) and with the preheating beam to predict the results of future experiments (Section 3.2).

### 3.1 Experiments without Preheating

A series of experimental shots were conducted, without the preheating beam, to study compression. A simulation of one of these shots is shown in Figure 3, which illustrates implosion indicated by the shell surface collapsing inwards at  $1.4\ \text{ns}$  after irradiation starts. What is shown is the upper half of the cross section of the cylinder with only two groups of laser beams (Beam 1 and Beam 2 from Figure 2) pictured on one side of the cylinder for clarity. Density contours are shown in dark blue. The critical density, or the highest density that the beams can penetrate is shown in orange. When laser rays encounter areas of higher density, they refract away. The laser

wavelength is  $\lambda = 0.351 \mu\text{m}$ , the third harmonic of the Nd: glass laser whose wavelength is  $1.054 \mu\text{m}$ .

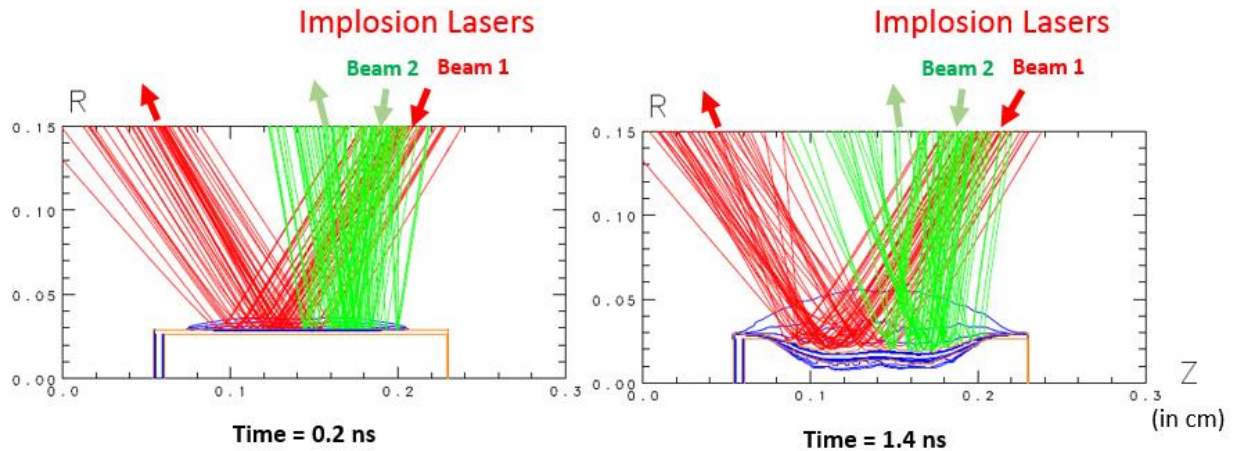


Figure 3: Two simulation snapshots showing two implosion beams (green and red) irradiating the liner and imploding the CH wall from experimental shot 79495. All units on such plots are in centimeters.

Figure 4 shows x-ray emission images from  $t = 1.6 \text{ ns}$  to  $t = 1.8 \text{ ns}$ . These images illustrate the speed of implosion, the portion of the cylinder that is compressed and the uniformity of the implosion. In Figure 4, the darker areas are from stronger emissions. The compression is fairly uniform, indicated by the smooth central region in each of the images. The x-ray emission comes from the hot plasma outside of the shell heated by the laser (Figure 3) and was used to determine the shell's location from experimental shot 79495. This was found by locating where the x-ray emission drops off sharply on the inside of the darker areas. In the top row of images in Figure 5, these radii were plotted for each  $z$ , creating an outline of the shell. The experimental images do not explicitly indicate a center of each cylinder, so the coordinates of the center of the cylinder needed to be found. This was done by trial and error to properly place the cylindrical edges, adjusting the coordinates of the center until the closest alignment between the red and blue dots was found.

The graphs of these points were compared with graphs of simulated shell center of mass plotted from SAGE calculations. The center of mass is the location that represents the mean position of mass in a system. D. Barnak<sup>5</sup> conducted a simulation of the x-ray emission based on a SAGE calculation that found that the x-ray emission is about  $47 \mu\text{m}$  offset above the simulated

center of mass, resulting in the offset between the dots (experimental results) and the black line (simulated center of mass) in the first row of images. When the predicted offset is eliminated, as shown in the second row of graphs, the dots from the experimental shot and the black line from the simulation align very well. The width of the flat compression of the x-ray emission is about the same as the width of flat compression of the simulated center of mass plot, which is about  $600\ \mu\text{m}$ .



Figure 4: *X-ray emission images<sup>6</sup> of implosion from experimental shot 79495 from 1.6 to 1.8 ns.*

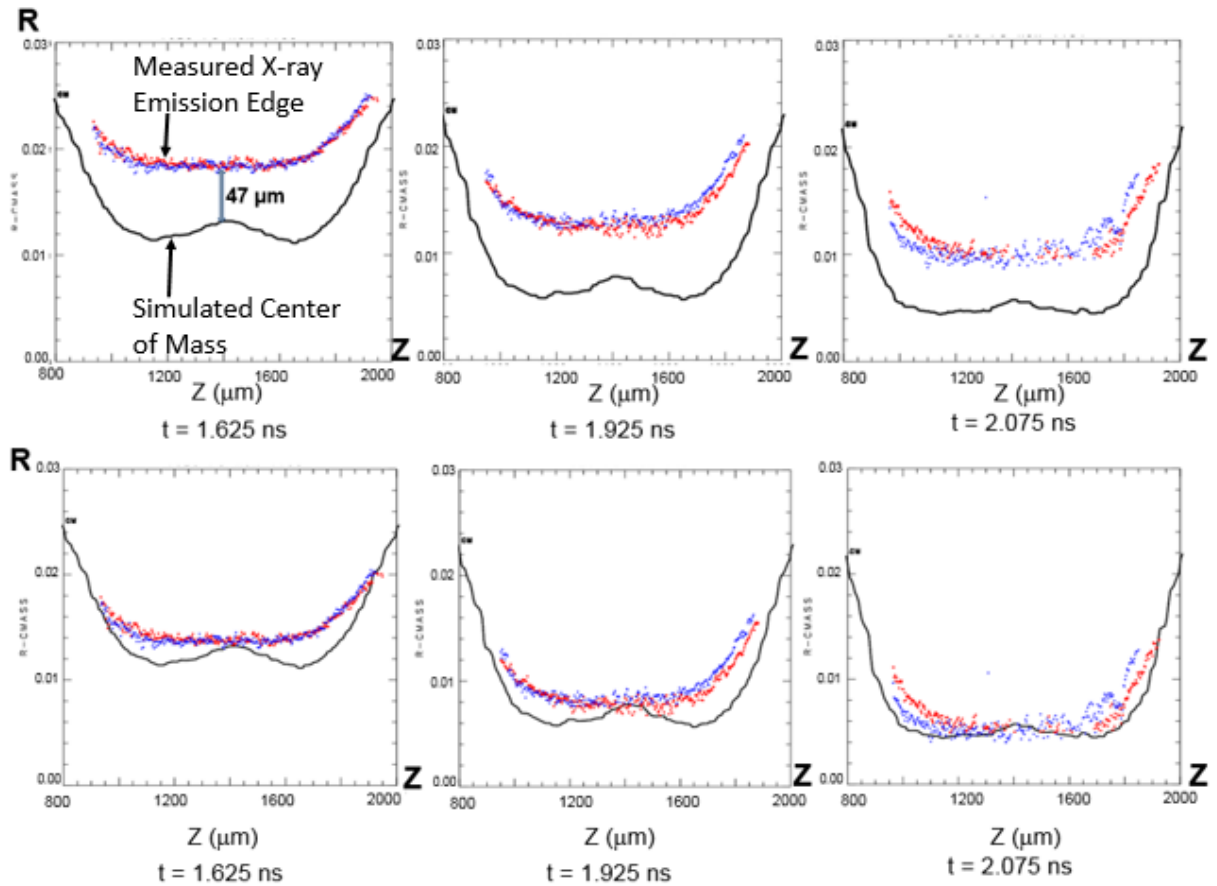


Figure 5: Top Row: Measured x-ray emission edge radius as a function of  $Z$  obtained from images such as those in Figure 4, plotted with SAGE predictions of center of mass. The red and blue dots show the x-ray emission from the opposite sides of the shell. Bottom Row: The x-ray radii have been reduced by  $47 \mu\text{m}$  to remove the predicted offset. In these images, the  $z$ -axis ranges from  $0.08$  cm to  $0.2$  cm and the  $r$ -axis ranges from  $0.0$  cm to  $0.03$  cm.

To compare the rate of compression, the experimental x-ray emission radii (from 8 images like those in Figure 4) and the simulated center of mass radii were plotted over time in Figure 6. The slope of each represents the rate of compression. The plots have very similar slopes, indicating similar implosion speeds. (The experimental implosion speed is  $2.1 \times 10^7$  cm/s and the simulated implosion speed is  $1.7 \times 10^7$  cm/s). Exact agreement is not expected as the separation between the x-ray emission radius and the center of mass radius changes over time. The results demonstrate that the velocity obtained from the x-ray emission radius gives a good indication of shell implosion velocity.

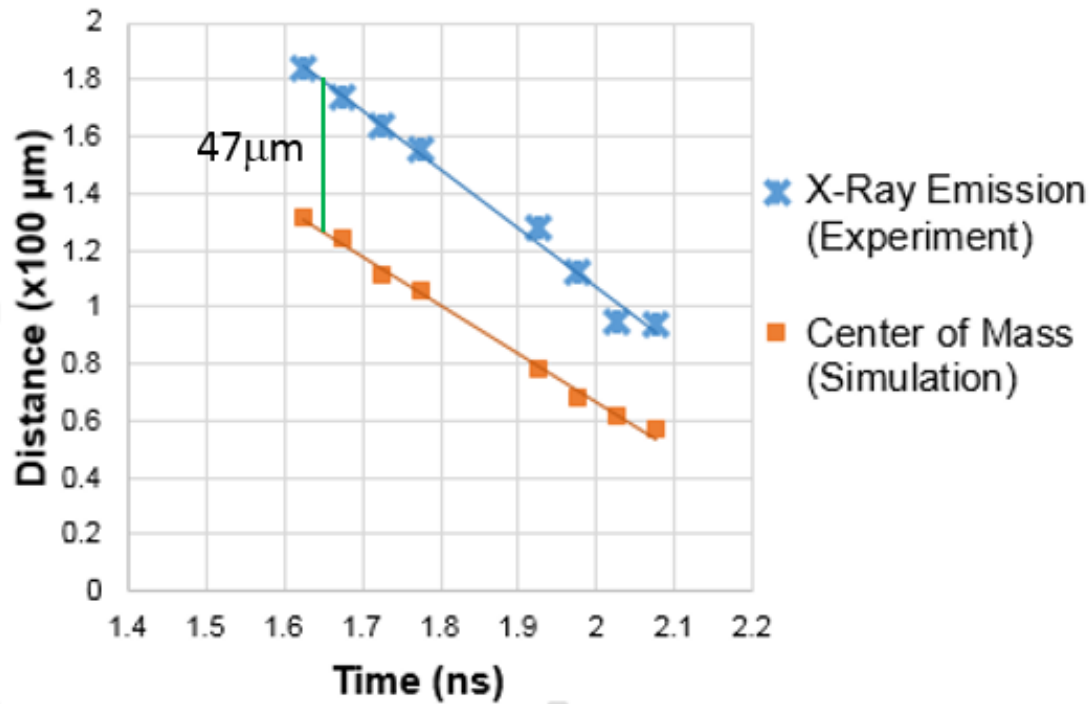


Figure 6: Experimental X-ray emission radii and simulated center of mass radii as a function of time, obtained from eight images such as those shown in Figure 4. The straight lines are regression fits.

A series of SAGE simulations was run to improve the liner shell implosion uniformity along the Z-direction. By shifting the beam pointings of beams 1 and 4 towards the outer sides of the cylinder in the z direction and shifting the beam pointings of beams 2 and 3 towards the center of the cylinder in the z direction and adjusting beam energy levels, significant improvements were made, as shown in Figure 7. The image on the left depicts the liner center of mass as a function of Z for one of the earlier runs. The liner's center of mass plot for times from 0.6 ns to 1.2 ns shows that the implosion is not uniform across the Z-direction. The graph on the right shows a more uniform compressed section during the implosion after optimization.

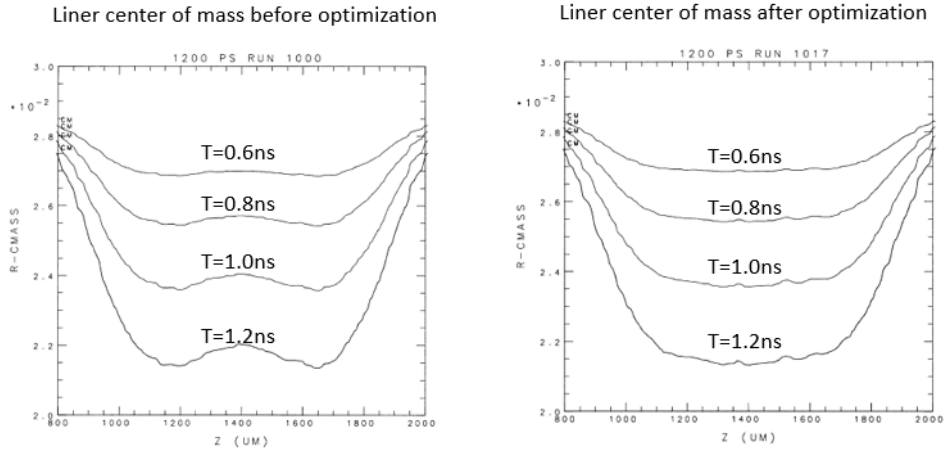


Figure 7: Center of mass radius as a function of  $z$  for 4 successive times, before and after optimization of the laser beam pointings. The  $z$ -axis ranges from .08 cm to 0.2 cm and the  $r$ -axis ranges from 0.02 cm to 0.03 cm.

### 3.2 Experimental Shots with Preheating

Results from planned laser driven MagLIF shots on OMEGA including the preheat beam were predicted using SAGE. A simulation at  $t = 1.4$  ns is shown in Figure 8. Implosion has not yet begun because the drive beams have just been initiated after the preheat beam has been firing for 1 ns. The planned set-up is comprised of a long tube that contains the deuterium, so in the simulation, the left end of the cylinder has been eliminated to reduce extraneous factors. The right end of the cylinder has been extended as well. The dark blue density contours on the right end arise from plasma created by the penetration and heating of the window. The density of the  $D_2$  changes as it is heated, causing some laser rays to refract toward the axis and some to refract towards the shell. The issue with the preheating beam hitting the shell, as demonstrated by Figure 8, is that when the shell is heated by the preheating beam, it creates plasma that expands inwards and mixes with the deuterium. Radiation loss scales as  $Z^2$ , or the square of the number of protons in the nucleus. Because the carbon radiates about thirty-six times more than the deuterium (beryllium, which is the preferred shell material for current-driven implosion, radiates about sixteen times more than deuterium), the temperature of the compressed fuel decreases because of the radiation energy losses, resulting in less fusion energy.

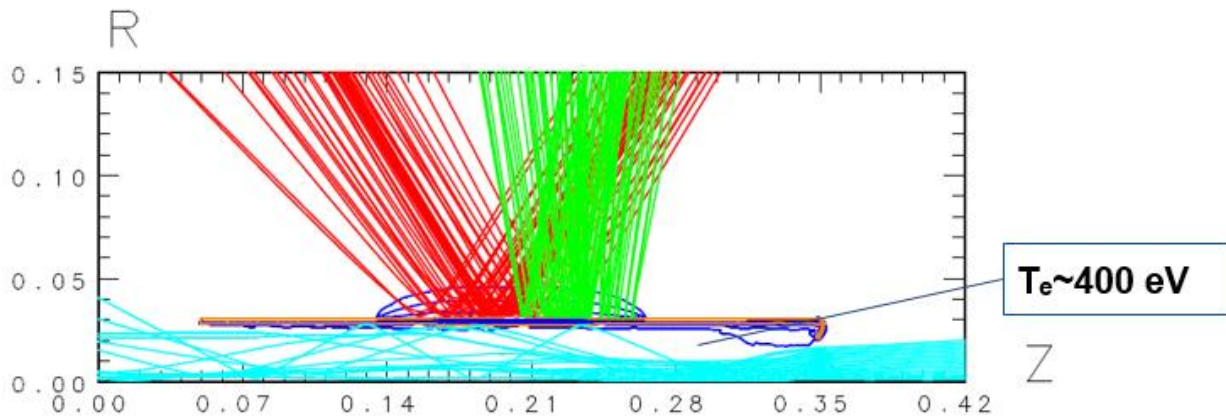


Figure 8: Simulation of a planned experiment on OMEGA at  $t= 1.4$  ns. In addition to the beams that drive the implosion (red and green), the preheating beam (teal) enters from the right.

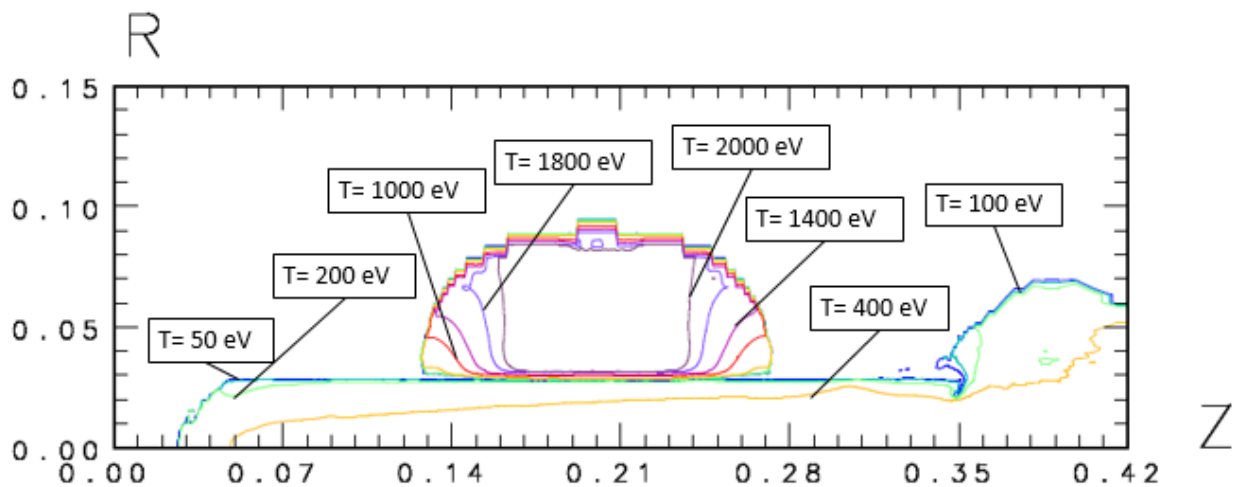


Figure 9: Temperature contours of an OMEGA simulation at the same time as Figure 8. The blue contour is 50 eV, the teal is 100 eV, the green is 200 eV, the yellow is 400 eV, the red is 1000 eV, the light purple is 1400 eV, the indigo is 1800 eV and the dark purple is 2000 eV.

Figure 9 shows temperature contours at the same time as Figure 8. The central region of the image has been heated by drive beams, which is why the temperature reaches around 2000 eV. In the deuterium, the hottest region is around the axis, which reaches around 400 eV. The temperature is above 200 eV for all of the deuterium in the cylinder, extending all the way up to

the shell. The temperature should be at least 100 eV by the time the cylinder starts compressing. This simulation shows that the preheating is sufficient, but could potentially cause plasma mixing due to rays striking the inner wall of the shell.

#### **4. Simulations for Large-scale Systems**

SAGE has also been used to simulate large-scale targets with dimensions similar to those of the Z-machine at Sandia National Laboratory. The Z-machine uses a cylindrical target approximately ten times the length and radius of the OMEGA target (the length changes from 0.1750 cm (Figure 3) to 1.2 cm, the radius changes from 300  $\mu\text{m}$  to 2600  $\mu\text{m}$  and the thickness of the shell changes from 30  $\mu\text{m}$  to 300  $\mu\text{m}$ ). In the Sandia Z-machine experiments the shell is imploded with a strong current pulse run through the metal liner in the z-direction. This current produces a magnetic field. Since SAGE does not have the capability of modeling the current and magnetic field driven implosion, laser beams are used to simulate the implosions caused by the electric current. Simulations were conducted to examine aspects of preheating on Z-machine experiments (Section 4.1) and predict the results of future large-scale experiments (Section 4.2)

##### **4.1 Experiments on Sandia's Z-machine**

A series of experimental shots were done on the Z-machine using a preheat beam with a second harmonic wavelength ( $\lambda= 0.527 \mu\text{m}$ , see Section 3.1) The beam diameter is determined by different phase plates, sheets of glass similar to frosted glass that focus the beam to specific radii. The preheat beam lasts for 2.0 ns. The effects of preheat beam energy, beam diameter and deuterium density were tested. The results are shown in Figure 10.

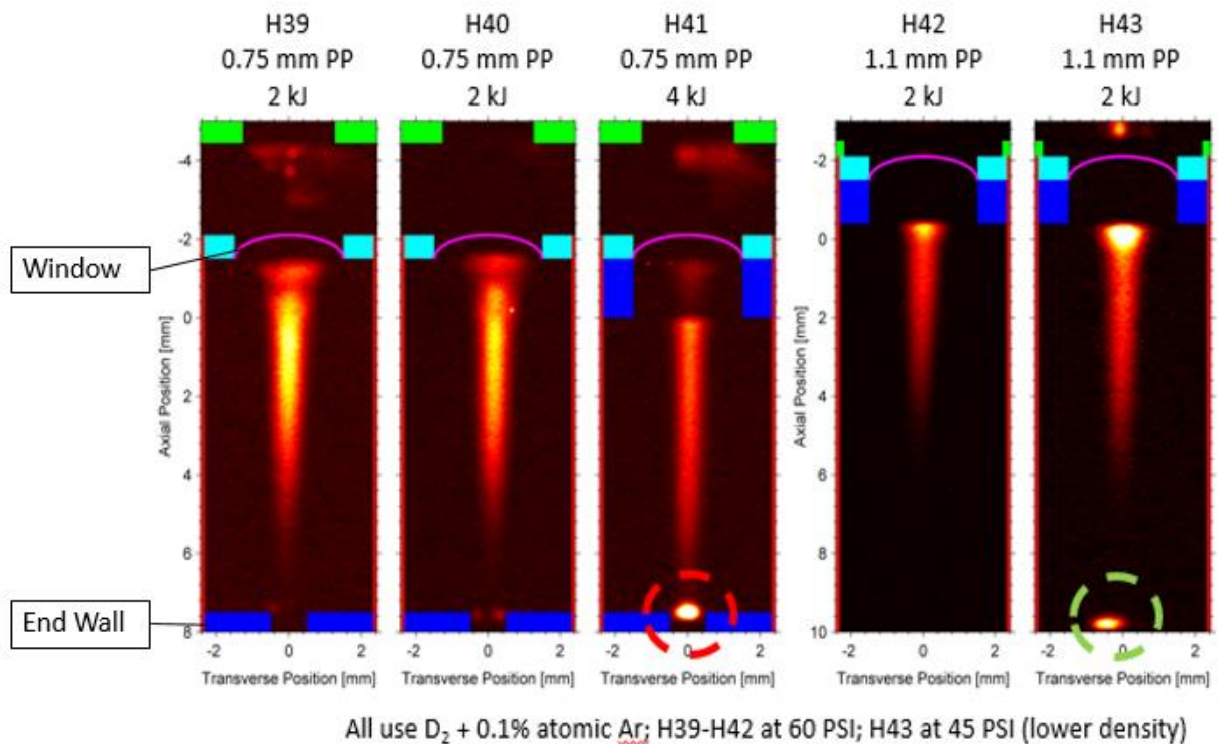
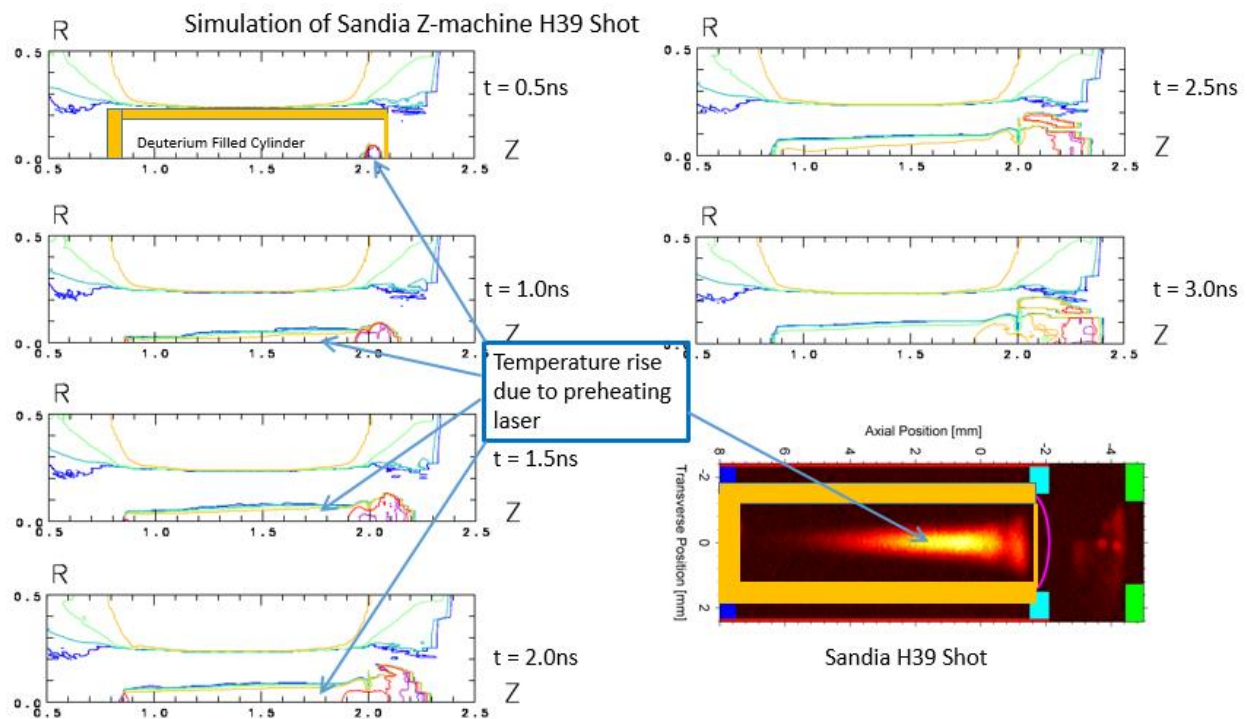


Figure 10: Time integrated images from experiments on the Z-machine showing x rays released from the heated deuterium, which are produced by a trace amount of argon in the deuterium. The yellow to red to black color scale shows the temperature change from high to low. H39 and H40 are the control shots and are nominally identical.

Time-integrated x-ray images<sup>7</sup> from these experiments are shown in Figure 10. In shots H39 and H40, the preheating laser energy is 2 kJ and the beam diameter is 0.75 mm. H41 has the same setting except that the preheating laser energy is doubled to 4 kJ. In H42, the diameter of the beam is increased from 0.75 mm to 1.1 mm, decreasing the intensity of the preheating laser. H43 is similar to that of H42, except that the density of the deuterium is lower. In two shots (H41 and H43), the preheating beam penetrates the deuterium more easily to reach the cylinder's end wall as indicated by the bright spot inside the red and green circles.

Figure 11 shows temperature contours from a simulation of shot H39. Temperature contours in areas beyond the shell (the shell location is indicated by yellow on the first temperature contour plot at  $t=0.5$  ns) are caused by drive laser heating and should be ignored when discussing the effect of the preheat beam. For this particular set of experimental shots,

implosion was not initiated. The incorporation of the drive beams in the simulation did not impact the results because the shell had barely begun to move at the time the preheat beam was firing. Following the end of the preheat beam firing, the temperature of the deuterium begins to cool off, as in the temperature contours at  $t=3.0$  ns. The narrow channel that is heated stays well away from the liner at all of the times in Figure 11, and temperatures in the channel generally range from 400 eV to 1000 eV when the preheat beam is on. The temperature profiles near the cylindrical axis in the simulation agree very well with the x-ray emission image. In Figure 11, where there are higher temperatures in the simulated temperature contours there are higher temperatures indicated by the x-ray images (indicated by the lighter colors, such as yellow, in the x-ray image on the lower right corner).



*Figure 11: Temperature contour plots from a simulation of the Sandia Z-machine H39 shot illustrating the temperature changes at times measured from when the 2-ns preheating beam is turned on ( $t=0$  ns). The lower right figure is the time-integrated experimental x-ray emission image, which corresponds to a combination of the simulations during the preheating laser firing. Yellow boundaries have been added to show the locations of the cylinder walls. As in Figure 9, in the simulated temperature contours, the blue contour is 50 eV, the teal is 100 eV, the green is 200 eV, the yellow is 400 eV, the red is 1000 eV and the purple is 1400 eV.*

Figure 12 shows a direct comparison between both the simulated temperature contours and the x-ray emission images of the control shot (shot H39) and the shot with twice the beam energy (shot H41). The higher laser power enables the beam to penetrate the entire length of the cylinder and hit the cylinder's end wall opposite the window. This creates a hot zone near the wall which can clearly be seen in the H41 simulation results in the red circle on the lower left and the experimental shot image in the red circle on the lower right. Some rays reflect off the end wall, heating the deuterium in that area twice, further contributing to the creation of the hot spot.

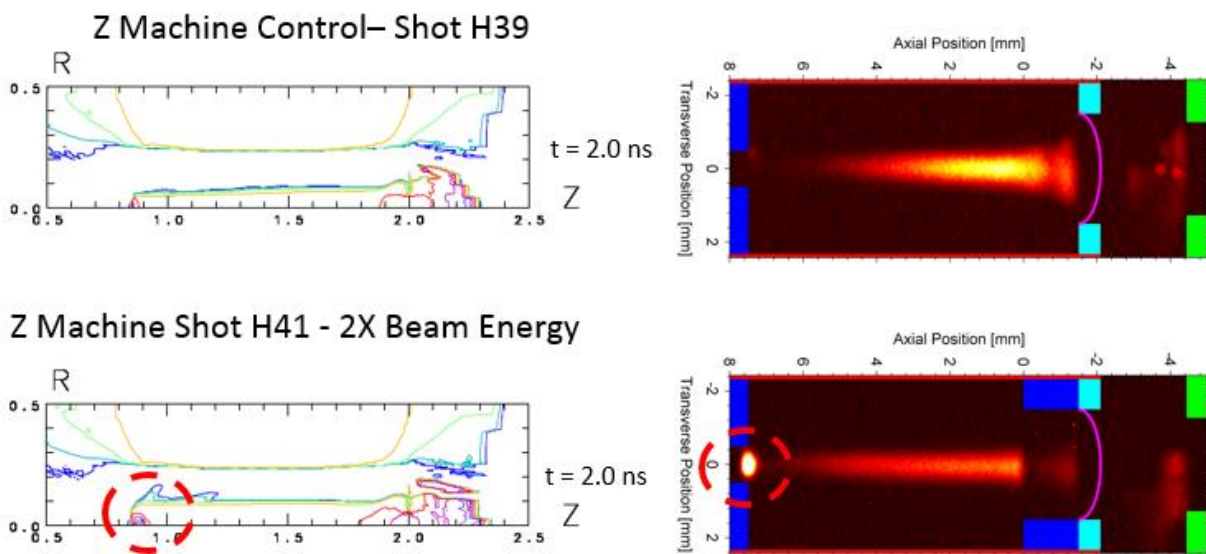
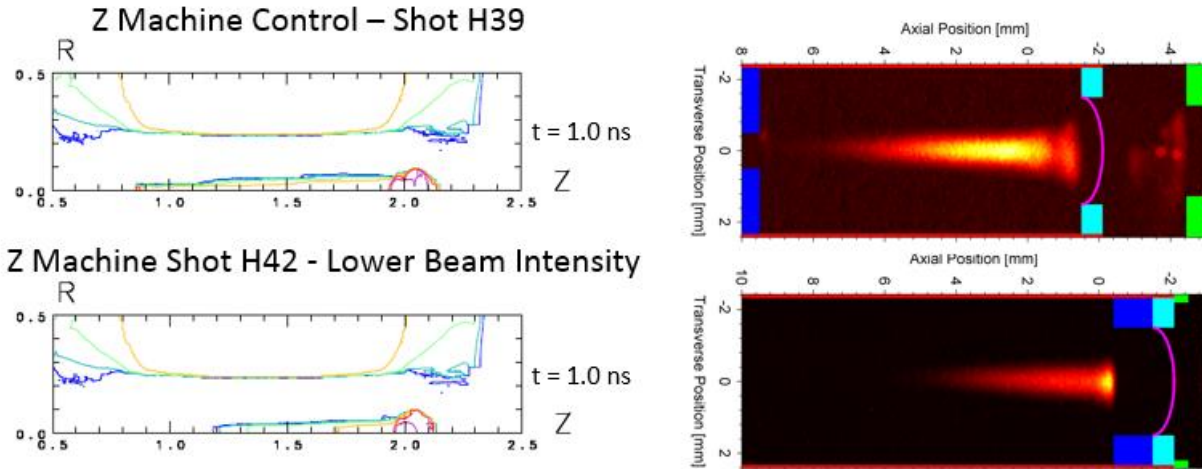


Figure 12: A comparison between Shot H41 with the control shot, Shot H39 at  $t = 2.0$  ns. In Shot H41, the preheating laser energy is doubled from 2 kJ to 4 kJ.

In Figure 13, the control (shot H39) is compared with a shot (H42) with a larger beam diameter. Because the beam is more widely distributed in the radial direction, the intensity of the beam lowers, which results in a narrower heated region, seen in both simulated and experimental results. There is actually a greater amount of heated area, but most of this area is below the lowest contour (50 eV), so it does not display.



*Figure 13: Comparison between Shot H42 and the control shot, Shot H39 at  $t=1.0$  ns, midway in the preheating pulse. In Shot H42, the phase plate diameter is increased from 0.75 mm to 1.1 mm, reducing the preheating laser energy intensity.*

From both the simulation and the experimental image, it can be inferred that the preheating beam in shot H42 does not penetrate as far into the deuterium, nor does it heat as wide of a range in the radial direction. In the simulation, the yellow temperature contour for 400 eV ends midway through the deuterium rather than occupying the whole length of the cylinder, while in the experimental image, the hot x-ray emitting region ends abruptly at around the same location that the simulation's strong heating ends.

Figure 14 compares two shots that both use the lower-intensity larger beam. Shot H42 is the control for this comparison. The other is shot H43, which lowers the density of the deuterium from 60 psi ( $0.664 \text{ mg/cm}^3$ ) to 45 psi ( $0.5 \text{ mg/cm}^3$ ). It can be seen from the simulation temperature profiles and the experimental images that the beam is penetrating more in the lower density setting, approximately 1 mm to 2 mm in each case. This is because the lower density deuterium does not absorb heat as well.

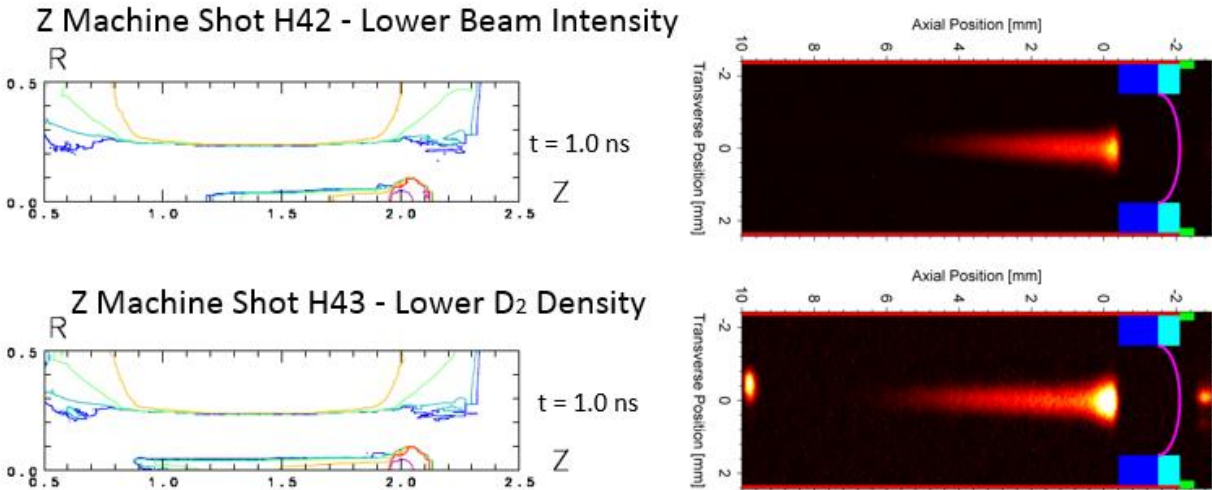


Figure 14: A comparison between Shot H43 and Shot H42. In Shot H43, the deuterium density is reduced compared to Shot H42 (from  $0.664 \text{ mg/cm}^3$  to  $0.5 \text{ mg/cm}^3$ ).

Through this series of comparisons, the validity of SAGE simulations is further demonstrated on the Sandia Z-machine.

## 4.2 Future Large-scale Systems

SAGE was used to simulate future Z-scale experiments, with the desired higher density of  $3 \text{ mg/cm}^3$  and a 2-ns third-harmonic preheating beam. Figure 15 illustrates such a simulation. There are only two drive beams used for implosion. For clarity, only one drive beam is shown (red). Only one ray of the preheating beam is shown (teal) to more easily view the behavior of the system while preheating is occurring. The energy of the preheat beam was given as 2 kJ. The preheat beam turns on 20 ns after the drive beams have begun firing (just after the shell has started to move). Multiple trials were run, testing different energies and positions of the drive beams along the z-axis to ensure that the shell imploded uniformly at around 80 ns, which is expected for a magnetically driven implosion. The drive beams were aimed at about the center of the cylinder in the z-direction. The total energy of both beams is 1.4 MJ (700 kJ for each drive beam).

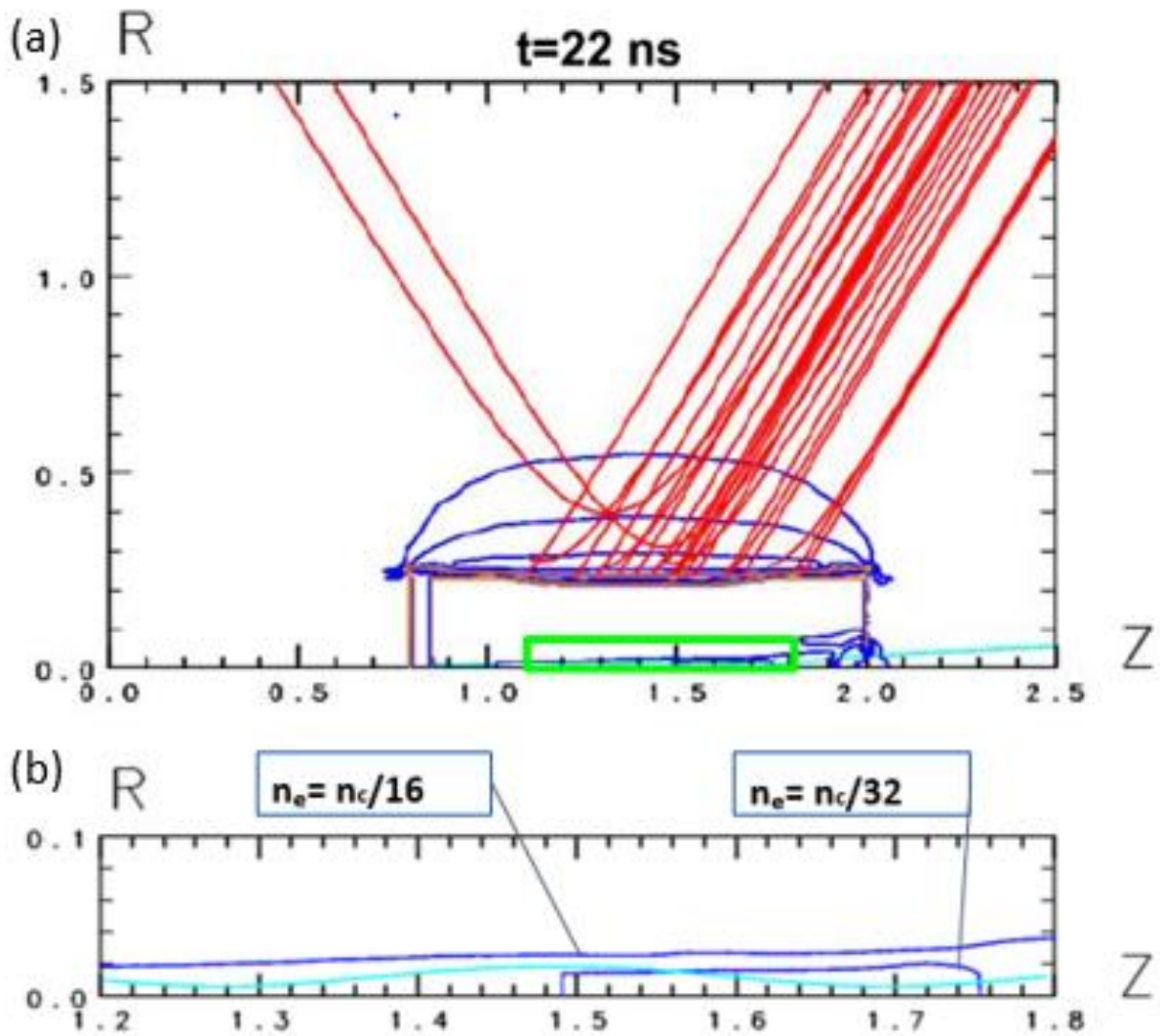


Figure 15: Example simulation of a future experiment with a higher density deuterium gas. Image 15a shows the liner being imploded by a laser beam with density contours in blue. Image 15b is an expansion of the area in the green box showing that the contour farther from the axis has a higher density than the contour closer to the axis, indicating the formation of a low-density channel.  $N_c$  represents the critical density. A sample laser ray (teal) is confined to the channel by refracting away from the higher-density contour.

Here, in contrast to the OMEGA simulation of Figure 8, it can be clearly seen that the preheating beam stays in a narrow channel along the axis of the cylinder, which avoids the preheat beam hitting the inside of the shell. When the deuterium near the axis is heated, it expands outwards toward the upper region. This leaves the region near the axis with a lower density. Figure 15b shows a typical ray of the preheating beam indicated in teal. When this ray refracts outwards, it encounters the higher density deuterium, which refracts it back towards the axis, keeping the beam focused near the axis of the cylinder. This is called whole-beam self-focusing.<sup>4</sup> The channel becomes more pronounced as time increases. The importance of the channel is that it allows the region of the cylinder near to axis to be heated effectively and uniformly without disturbing the shell.

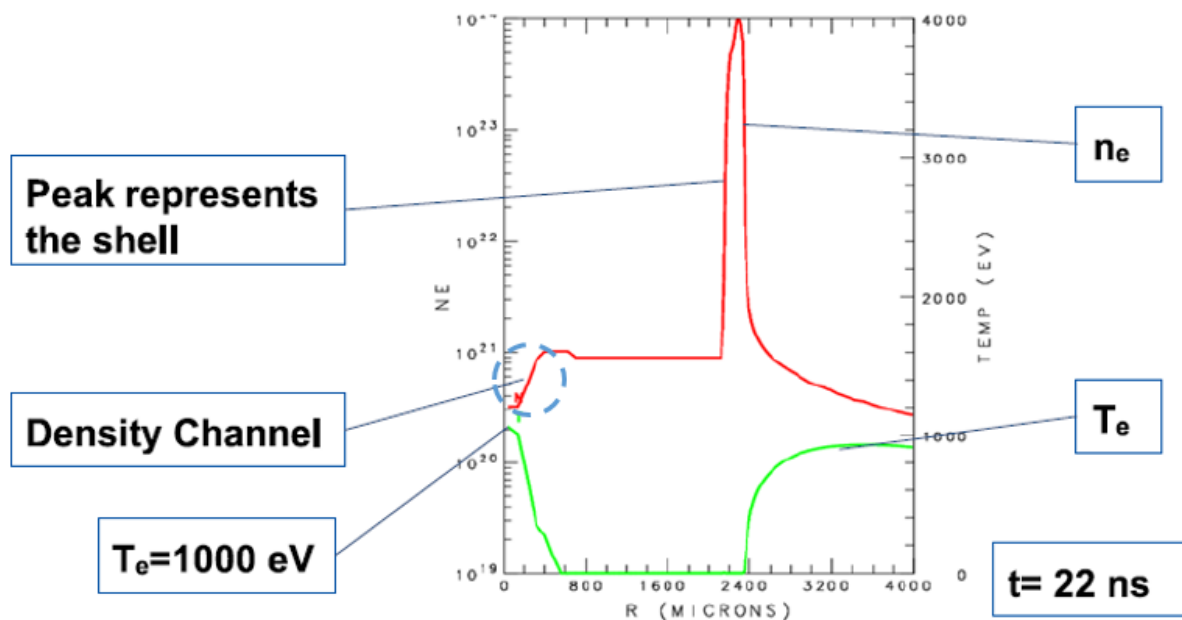


Figure 16: A one-dimensional graph in the radial direction at the midpoint along the z-axis of the cylinder. The red line represents density (in units of electrons/cm<sup>3</sup>) and the green line represents the temperature. The region in the blue circle illustrates the density channel.

Figure 16 helps to illustrate the density channel by plotting density (red) and temperature (green) in the radial direction at the midpoint of the cylindrical target. The density channel location is circled in blue. The density has a clear dip towards the center of the target when  $r$  is less than  $400 \mu\text{m}$ . This is consistent with the idea that the deuterium expands outwards, leaving the center of the cylinder less dense. Moving along the  $r$ -axis, the density rises and peaks at a

density higher than the initial density from about  $r=400\ \mu\text{m}$  to  $700\ \mu\text{m}$ . This is because the deuterium from the expansion is pushed outwards. From the temperature graph (green), it is clear that the temperature peaks on the axis, which is consistent with the theory that all the laser energy is deposited in the density channel containing the beam.

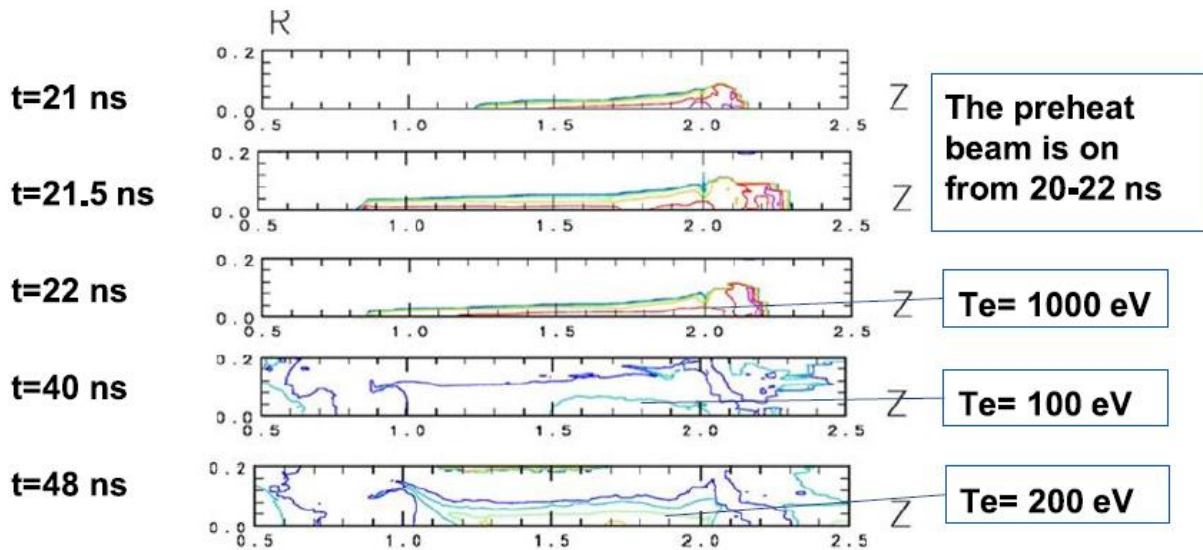


Figure 17: Temperature contours showing the temperature progression in the cylinder over time. The preheating beam was on from  $t = 20\ \text{ns}$  to  $22\ \text{ns}$ .

Figure 17 shows the progression of temperature of the deuterium contained in the cylinder over time. The first three strips ( $t=21\ \text{ns}$  to  $22\ \text{ns}$ ) show the temperature contours while the preheating beam is on. The deuterium is heated quickly along the axis to high temperatures of  $1000\ \text{eV}$ , all while being extremely well confined to the core of the cylinder. After the preheating beam switches off, the deuterium near the axis cools and the surrounding deuterium becomes hotter by thermal conduction, which is desired. This temperature change is indicated by the temperature contours at the  $40\text{-ns}$  plot. However, once the deuterium begins to be compressed due to the implosion of the liner, the temperature of the deuterium increases again to about  $200\ \text{eV}$  at  $48\ \text{ns}$ .

This preheating beam self-focusing and the effective heating of the center of the cylinder to an ideal temperature evenly along the axis without disturbing the shell is significant because it confirms the effectiveness of the preheating beam in the MagLIF approach and helps clarify the physics of the preheating mechanism.

## 5. Conclusion

This work showed that SAGE is an effective tool to model both OMEGA and Sandia Z-machine MagLIF experiments. A variety of MagLIF experiments have been modeled with different geometries and beam characteristics. Simulations of OMEGA experiments without a preheat beam demonstrate agreement with experimental observations. Simulations of upcoming OMEGA shots with the preheat beam predict temperatures of  $\sim 400$  eV. Simulations of Z-machine preheating show agreement with observations from experimental shots. Simulations of the Z-machine with a higher deuterium density, as desired for future experiments, show that the desired temperature profile is achieved through the formation of a self-focusing density channel. This is, to our knowledge, the first time that self-focusing has been reported in MagLIF physics.

## 6. Acknowledgments

This project was made possible by Dr. Craxton, whose support and assistance has guided me through this process. He has truly been an incomparable adviser. I would like to thank Mr. Barnak and Dr. Davies for providing the experimental data and images. I also would like to thank Dr. Enck for inspiring me to pursue physics outside of the classroom and encouraging me to apply for this internship. Lastly, I would like to thank the Laboratory for Laser Energetics for this incredible program that has been a wonderful learning experience.

## 7. References

- 
1. R. Betti and O. A. Hurricane, “*Inertial-confinement fusion with lasers*,” *Nature Physics* **12**, 435 (2016).
  2. S. A. Slutz et al., “*Pulsed-power-driven cylindrical liner implosions of laser preheated fuel magnetized with an axial field*.” *Physics of Plasmas* **17**, 056303 (2010).
  3. A. B. Sefkow et al., “*Design of magnetized liner inertial fusion experiments using the Z facility*.” *Physics of Plasmas* **21**, 072711 (2014).
  4. R. S. Craxton and R. L. McCrory, “*Hydrodynamics of Thermal Self-Focusing in Laser Plasmas*” *Journal of Applied Physics* **56**, 108 (1984).

5. D. Barnak, Private communication
6. J. Davies, Private communication
7. A. Harvey-Thompson, Private communication

*Development of a Digital Microscope for the Characterization of Defects in Cryogenic DT-filled*

*Targets*

**Joy Zhang**

Penfield High School

Advisor: Roger Janezic

Laboratory for Laser Energetics

University of Rochester

Rochester, NY

September 2017

## 1. Abstract

A digital microscope is being developed for the purpose of viewing submicron defects on the surface of cryogenic deuterium-tritium (DT) filled targets. The existing target characterization system is aperture limited by a protective shroud, limiting its resolution to 1.6  $\mu\text{m}$ . The microscope under development will eventually operate in a cryostat where targets can be viewed directly without the limitations of a protective shroud. This will allow the microscope to operate from a shorter working distance, improving its resolution to approximately 0.5  $\mu\text{m}$ . A U.S. Air Force resolution target was used to generate pixel-profile lineouts in order to quantify image quality during the optimization of illumination conditions. Using objectives of various magnifications, the optimal magnifying power of the microscope was determined. Additionally, the illumination conditions, including the wavelength, current, and exposure time of the light-emitting-diode (LED) light source, were optimized at ambient conditions. Under optimized conditions, a resolution of 0.5  $\mu\text{m}$  was confirmed using polymer microsphere standards and 0.5- $\mu\text{m}$ -diameter defects on a polystyrene (CH) cryogenic shell.

## 2. Introduction

Direct-drive inertial confinement fusion harnesses the potential of nuclear fusion as an abundant source of clean, safe energy through imploding cryogenic targets filled with solid DT fuel.<sup>1</sup> This can be done by placing the cryogenic DT-filled target (at 18 K) in the center of the OMEGA target chamber, where 60 high-energy pulsed beams are fired, causing the CH shell of the target to ablate outward.<sup>2</sup> This causes the DT fuel to compress rapidly and forcefully, generating the extreme densities and temperatures needed to initiate fusion reactions. Figure 1 shows two images of a typical cryogenic DT target, taken by the current target viewing system,

the optical Characterization Station, with two different focal points. Image (a) focuses upon the edge of the target shell and the ice layer that has formed within it and Image (b) focuses upon a defect upon the surface of the target shell.

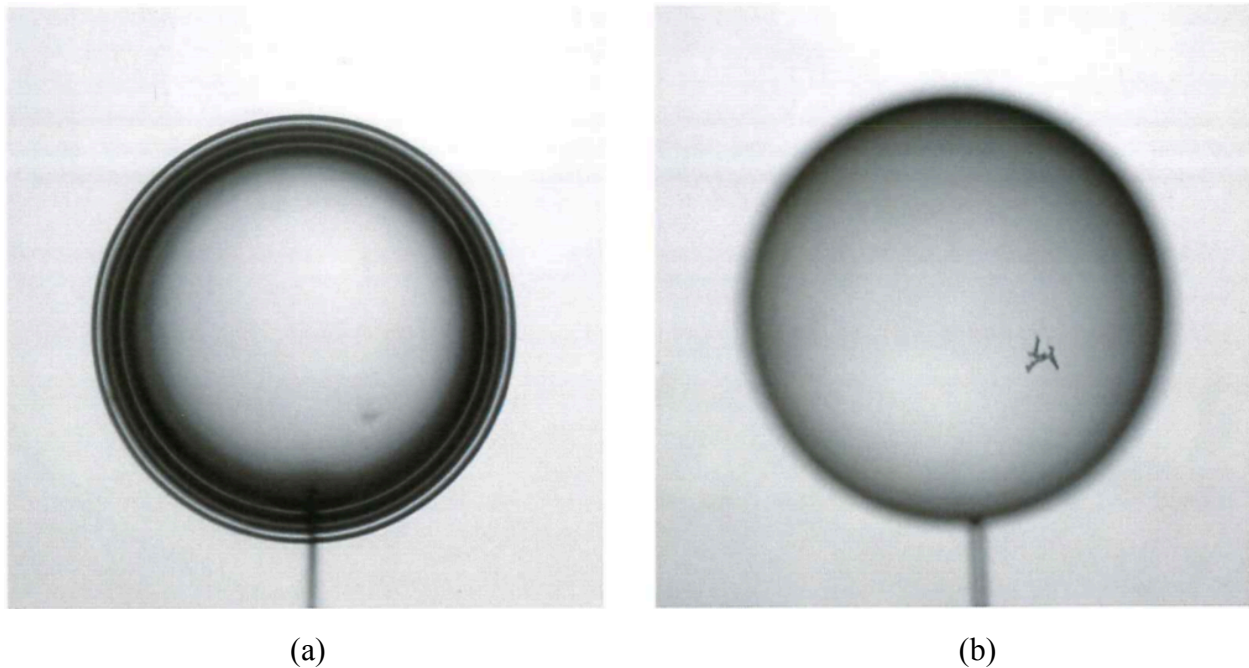


*Figure 1: Images of a CH cryogenic shell taken by the Characterization Station. Image (a) focuses upon the shell's edge and image (b) focuses upon a dendrite defect on its surface (from Ref. 4).*

In order to reach the desired densities and temperatures, the DT ice layer must be compressed uniformly, maintaining its spherical symmetry during the implosion. However, imperfections on the target's inner and outer surfaces may seed instabilities during implosion. In particular, the Rayleigh-Taylor instability causes non-uniformities in the interface between two materials of different densities to grow.<sup>1</sup> Therefore, in order to achieve desired core temperatures and densities, the target surface must contain minimal defects. However, there may be sub-micron defects on or within the shell surface that are currently not observed, consisting possibly

of metallic dust, condensable gases, or of some other material, that are hindering the desired densities and temperatures from being reached.<sup>3</sup> The Characterization Station does not possess a high enough resolving power to view these submicron defects. This is largely due to the existence of a protective shroud around the target, which maintains a cryogenic environment in order to allow the DT ice layer to form.<sup>3</sup> This protective shroud contains windows through which the Characterization Station views the target. However, these windows limit the cameras of the Characterization Station by requiring them to view the target from a distance, approximately 15 cm, which lowers their resolving power.<sup>5</sup> The measured resolution of the Characterization Station is approximately 3.1  $\mu\text{m}$ , making it unable to resolve defects as small as 0.5  $\mu\text{m}$  in diameter.<sup>5</sup>

### **3. Materials and Methods**

In order to overcome the limitations of the protective shroud, a digital microscope apparatus was designed, which is intended to view the inner and outer surfaces of the target from within the Fill and Transfer Station #2 (FTS#2) cryostat.

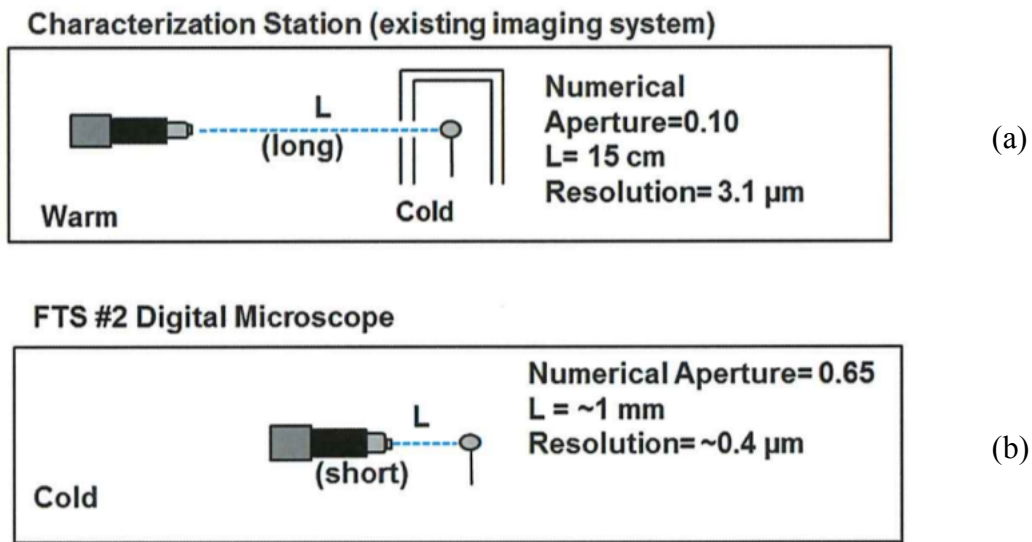


Figure 2: Comparison between the Characterization Station (a) and FTS #2 Microscope (b).

The cryostat maintains a cryogenic environment in order to ensure the survival of the target's DT ice layer in its cryogenic state, during which target characterization is conducted.<sup>3</sup> Figure 2 shows that, by viewing the target from within the cryostat, the digital microscope would be able to image the target directly, from a distance of approximately 1 mm.<sup>5</sup> Additionally, the microscope objective of the digital microscope contains a larger numerical aperture (NA=0.65) compared to that of the Characterization Station (NA=0.10).<sup>5</sup> Numerical aperture is a measurement of a microscope objective's ability to capture light and resolve fine details at a fixed distance. Therefore, the larger numerical aperture of the digital microscope suggests that it would have higher resolving power, which is supported by the equation

$$R = \frac{\lambda}{2NA} \quad (1)$$

where  $R$  is the resolution of the digital microscope, defined by the minimum distance between

two objects that is resolvable by an optical device,  $\lambda$  is the wavelength of the illumination source, and  $NA$  is the numerical aperture of the objective. It was projected that the apparatus designed for the FTS #2 digital microscope would provide a resolution of approximately  $0.4 \mu\text{m}$ .

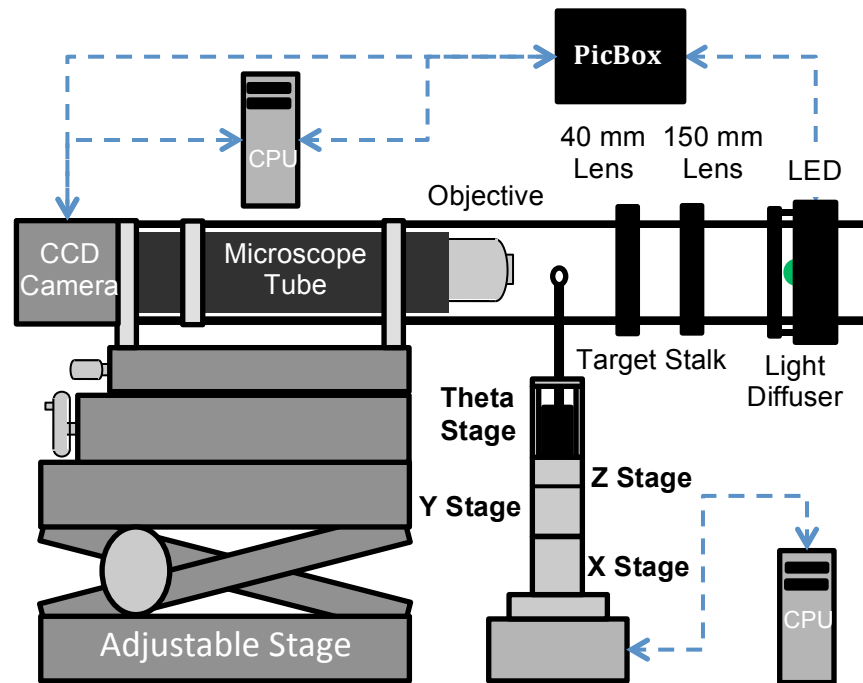
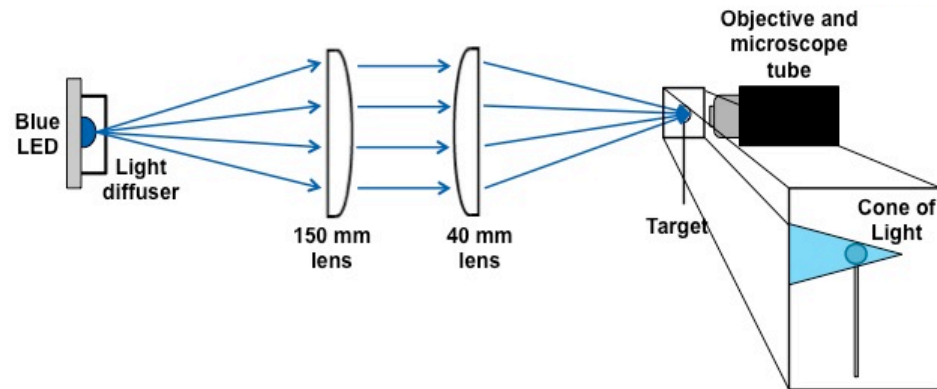


Figure 3: Box diagram of the microscope apparatus. The electronic communication pathways and the light path from the diffuser to the target are shown schematically.

The digital microscope shown in Figure 3 is composed of a microscope objective, a microscope tube, and a charge-coupled-device (CCD) camera. The digital microscope is mounted on an adjustable stage, which manipulates the objective's position. The target is illuminated by an LED, which emits light in rapid and continuous pulses. The LED's pulse rate is synchronized with the image capture rate of the camera by an LLE-designed "PicBox". This method utilizes the stroboscopic effect, in which the motion of an object is represented by a series of static snapshots that are repeatedly captured in synchronization with the pulses of light from the illumination source. The LED's rapid pulses stabilize the captured images of the target, mitigating the effects of the cryostat's vibration on the image. The PicBox and the CCD camera

are interfaced to a computer (CPU), which allows the camera to capture images and contains a set of controls which manipulate the LED's illumination settings such as the exposure time, the trigger rate, and the current.



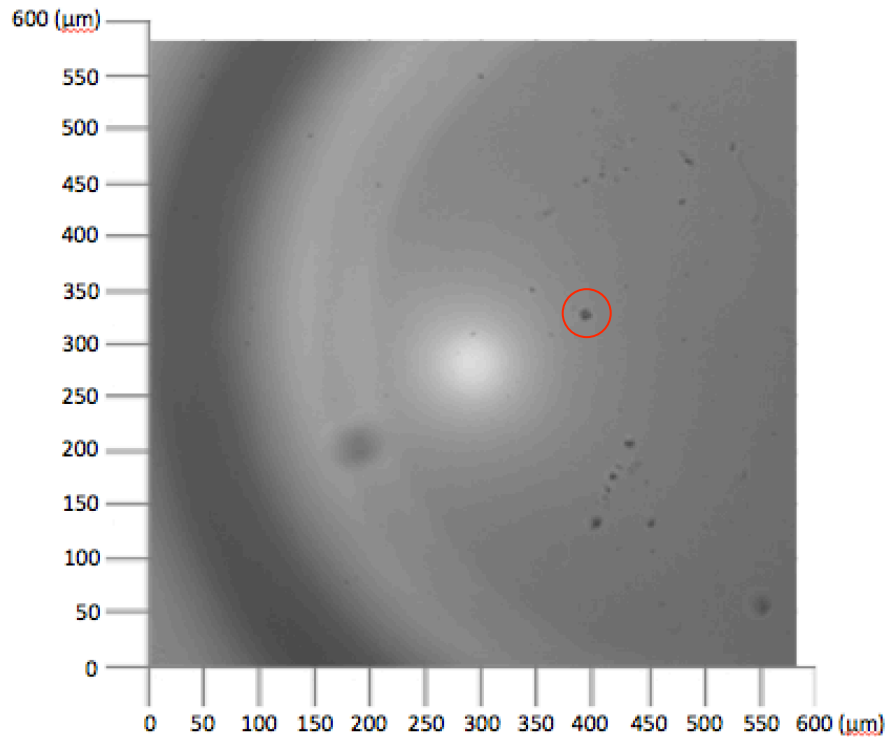
*Figure 4: Optical configuration for target illumination. The light pathway is shown schematically.*

Figure 4 shows the pathway of light from the LED to the target. The light from the LED is propagated by a holographic optical diffuser, which causes it to spread in order to provide consistent illumination. The light then passes through two plano-convex lenses. The first, which has an approximate working distance of 150 mm, collimates the light, making the rays accurately parallel. The light then passes through the second lens, with an approximate working distance of 40 mm, which focuses the light onto the target in order to illuminate it. Optimally, the cone of focused light illuminates the target tangentially as shown in the inset. This illumination system allows the apparatus to utilize the methods of bright-field microscopy.

The apparatus also includes a motion stage upon which the target stalk is mounted. The motion stage allows the target to be moved in the x-plane, y-plane, and z-plane, and also allows it to rotate (theta). The motion stage is interfaced to a computer, which contains a set of controls to move the target.

Figure 5 shows an image of an 8  $\mu\text{m}$  wall x 860  $\mu\text{m}$  diameter plastic CH “cryo” shell that

was taken by the digital microscope. The dark features upon the shell's surface are surface defects that were created during the target fabrication process. The defect that is encircled in red has a diameter of approximately  $8\ \mu\text{m}$ . This is the type of shell that would be filled to create cryogenic DT-filled targets.



*Figure 5. Typical image of a “cryo” shell employed for this study, captured with a 20x objective for the purpose of incorporating a larger view of the shell. The digital microscope’s focus is upon defects on the shell’s outer surface.*

The digital microscope’s working conditions were optimized in ambient conditions prior to its eventual placement in the FTS#2 cryostat. This ensured its ability to resolve  $0.5\text{-}\mu\text{m}$ -diameter defects at room temperature before optimization occurs at cryogenic temperatures. A standard 1951 US Air Force resolution target, shown in Figure 6, was used for this optimization.

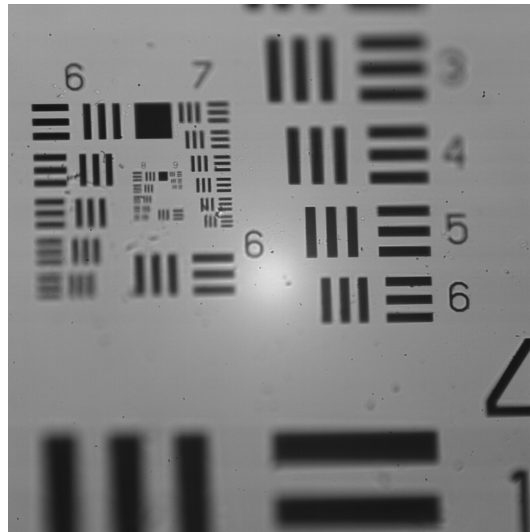


*Figure 6. Image of an Air Force resolution target, captured with a 40x objective.*

The resolution target is a plane of transparent glass that has a pattern of lines printed on it. These lines are organized into groups of three, which become progressively smaller towards the center of the target. The width of these lines decreases from  $2000\ \mu\text{m}$  to  $0.55\ \mu\text{m}$ . The resolution of the digital microscope was measured by determining the smallest distance between two lines that it was able to resolve.

Although the resolution target provided a fairly accurate estimation of the digital microscope's resolution, a more quantitative method to measure it was devised. Using an image of the resolution target that was taken by the digital microscope, a row of pixels that extended across a group of three lines was analyzed. The number of photons captured by each pixel was then graphed, generating a sine shaped curve, which is referred to as a pixel-profile lineout, shown in Figure 7. Then, the image's contrast ratio was calculated by dividing the highest number of photons collected by a single pixel by the lowest number of photons collected by a single pixel. Because contrast increases as resolving power increases, a higher contrast ratio

indicates a higher resolving power. For the image used to generate the pixel-profile lineout in Figure 7, the highest number of photons collected by a single pixel was 3270 and the lowest number of photons collected by a single pixel was 1038, yielding a contrast ratio of 3.2.

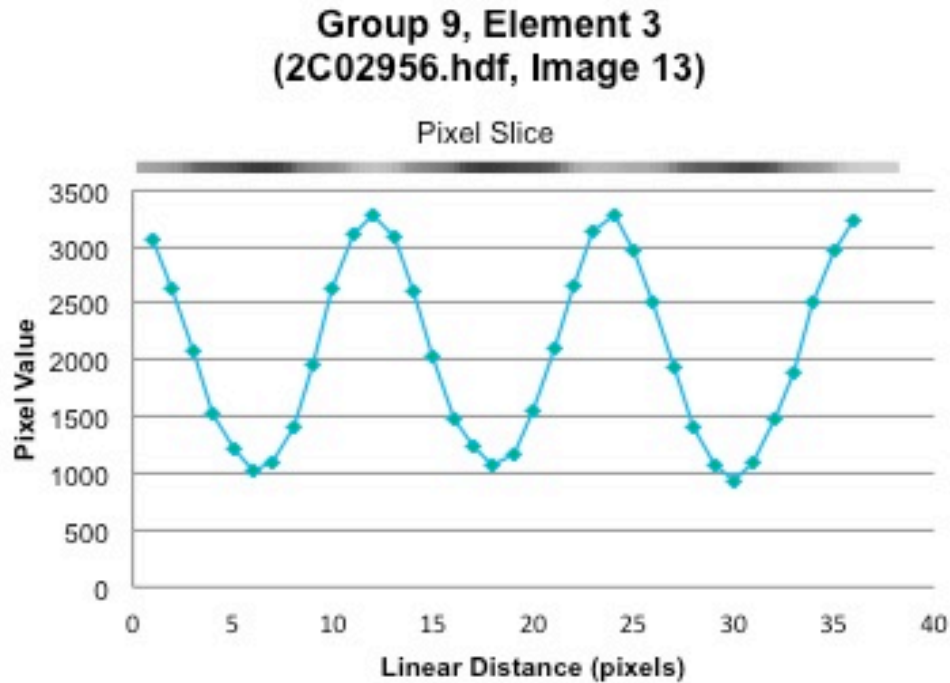


*Figure 7. Pixel-profile lineout of a line group on the U.S. Air Force Resolution Target. 7.9 pixels correspond to 1  $\mu\text{m}$  distance.*

Another application of the resolution target is its use in creating a pixel-to-micron conversion scale. This was done by using software to determine how many pixels were present between two lines on the resolution target, whose separation is accurately known. For example, one pair of lines had a separation of 60 pixels and a separation width of 7.81  $\mu\text{m}$ , which yielded a pixel-to-micron conversion of 7.67 pixels per  $\mu\text{m}$ .

Based on the average measurements of multiple line separations of different sizes for both the 20x and 40x objectives, it was determined that the conversion scale was approximately 4.2 pixels/ $\mu\text{m}$  for a 20x objective and 7.9 pixels/ $\mu\text{m}$  for a 40x objective. These measurements are

prone to slight error due to the resolving limitations of light microscopy, which may explain why the conversion scale for a 40x objective was not exactly twice as large as the conversion scale for a 20x objective, as would be expected. However, this conversion scale can be used to produce fairly accurate measurements of objects within the images captured by the digital microscope.

#### 4. Optimization

In order to establish the optimal working conditions for the digital microscope, various factors were considered, including the wavelength of the LED and the illumination settings. Because a 40x objective provides twice as much magnification as a 20x objective, it provides the digital microscope with a higher resolving power. Figure 8 shows a comparison between two images of the resolution target, one taken with a 20x objective and one taken with a 40x objective. The smaller line groups on the resolution target are much more resolvable with the 40x objective than they are with the 20x objective.

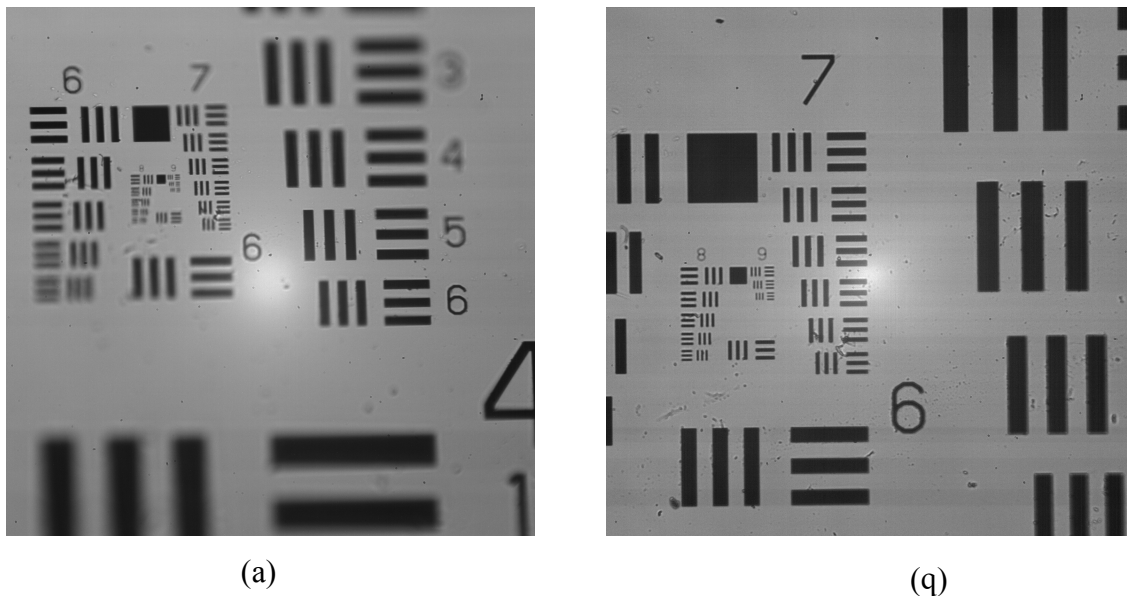


Figure 8. A comparison of images of the resolution target taken with a 20x objective (a) and a 40x objective (b).

It was calculated from Equation (1) that a 40x objective's numerical aperture of 0.65 would

yield a resolution of approximately  $0.4\ \mu\text{m}$  with green ( $525\ \text{nm}$ ) light illumination. This would make the goal of resolving  $0.5\ \mu\text{m}$  diameter defects feasible. Therefore, the 40x objective was utilized for most optimization operations.

#### 4.1. LED Wavelength Optimization

Prior to the optimization of the LED's wavelength, a green ( $525\ \text{nm}$ ) LED was used as the digital microscope's illumination source. According to the spectral response of the CCD camera (E12 device), shown by the red curve in Figure 9, the camera's ability to collect photons is optimal when illuminated by light with wavelengths between  $500\ \text{nm}$  and  $700\ \text{nm}$ .

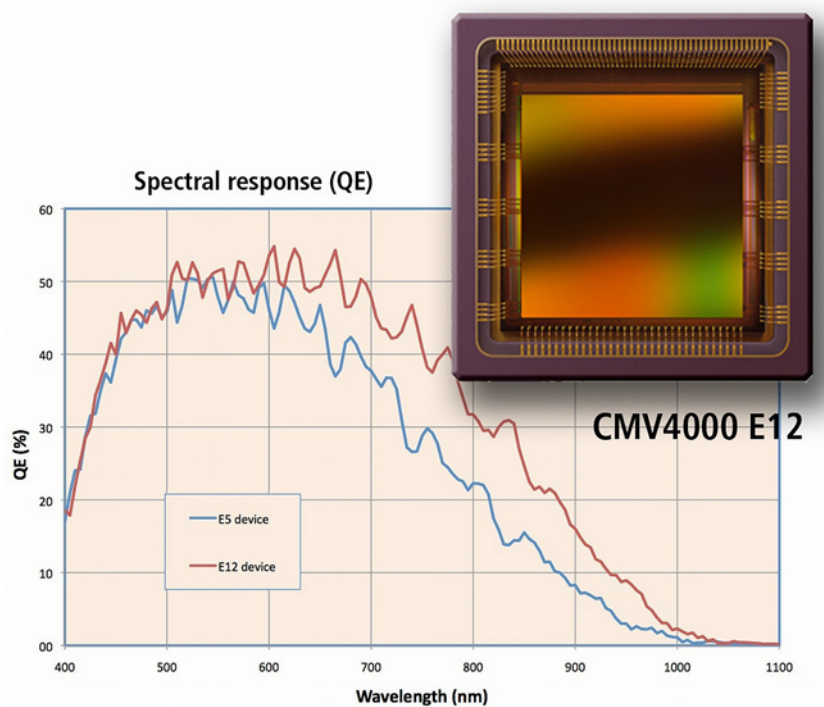


Figure 9. Spectral response graph for the complementary metal-oxide-semiconductor (CMOS) chip employed in the CCD camera (from Ref. 5). Quantum efficiency (QE) is shown as a function of wavelength of the illumination source. The chip design is shown in the top right corner.

However, according to Equation 1, as the wavelength of the LED decreases, the resolution value decreases as well, indicating a higher resolving power. Therefore, a blue LED, with a wavelength of 460 nm, was tested because it was predicted to yield a higher resolving power, although it is not considered optimal for the camera's spectral response.

Figure 10 shows the pixel-profile lineouts of resolution target images that were captured with the blue LED (right) and compared with lineouts of images taken with the green LED (left). Because the exposure time and current of the LED affect the resolution of the image, the images were taken over a range of exposure times and currents. The current for both LEDs ranged from 800 mA to 1400 mA while the exposure time ranged from 200  $\mu$ s to 3000  $\mu$ s. The contrast ratios at each setting were calculated for the pixel-profile lineouts. The highest contrast ratio for the blue LED was 4.0 at a setting of 1400 mA and 800  $\mu$ s. The highest contrast ratio for the green LED was 3.7 at a setting of 1000 mA and 600  $\mu$ s. Therefore, it was determined that the blue LED yielded a slightly higher resolving power. It should also be noted that the blue LED required a longer exposure time and higher current because of the camera's weaker spectral response due to the shorter wavelength.

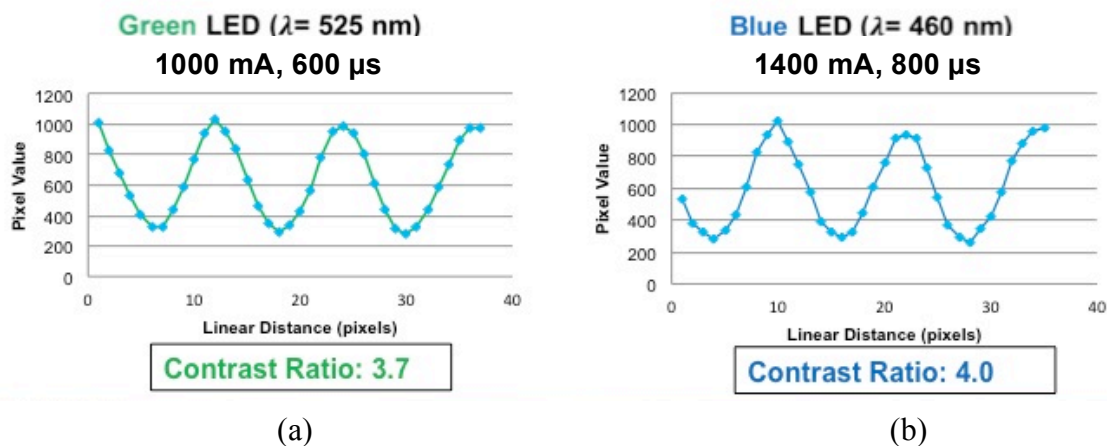


Figure 10. Pixel-profile lineouts of resolution target images taken by the green LED (a) and the blue LED (b). The same group of three lines was used to generate both lineouts.

#### *4.2 Current and Exposure Time Optimization*

The computer interfaced to the CCD camera and PicBox utilizes the LLE “Cryoview” software to capture images and manipulate the LED settings. Cryoview allows the operator to easily manipulate the LED’s current, exposure time (the length of each pulse from the LED), and trigger rate (the rate at which the LED pulses). The manipulation of these factors was expected to have an effect on the contrast ratio and image quality of the digital microscope. However, the trigger rate did not produce a profound effect on the image quality, and was therefore held constant at 5 Hz for the optimization process. During the optimization process, the current and exposure time were varied in order to determine which settings produced the highest image quality. The response of the contrast ratio to the variations of the LED’s current and exposure time is shown in Figure 11. Because both factors have an effect on the image quality, the exposure time was kept constant at 800  $\mu$ s while the current was varied. This exposure time was previously observed to produce moderate image quality. Current settings were tested within a range from 500 mA to 2,000 mA, beyond which the captured images exhibited poor image quality. Conversely, the current was kept constant at 1400 mA while the exposure time was varied. Exposure times were tested within a range from 200  $\mu$ s to 3,000  $\mu$ s, beyond which the captured images exhibited poor image quality.

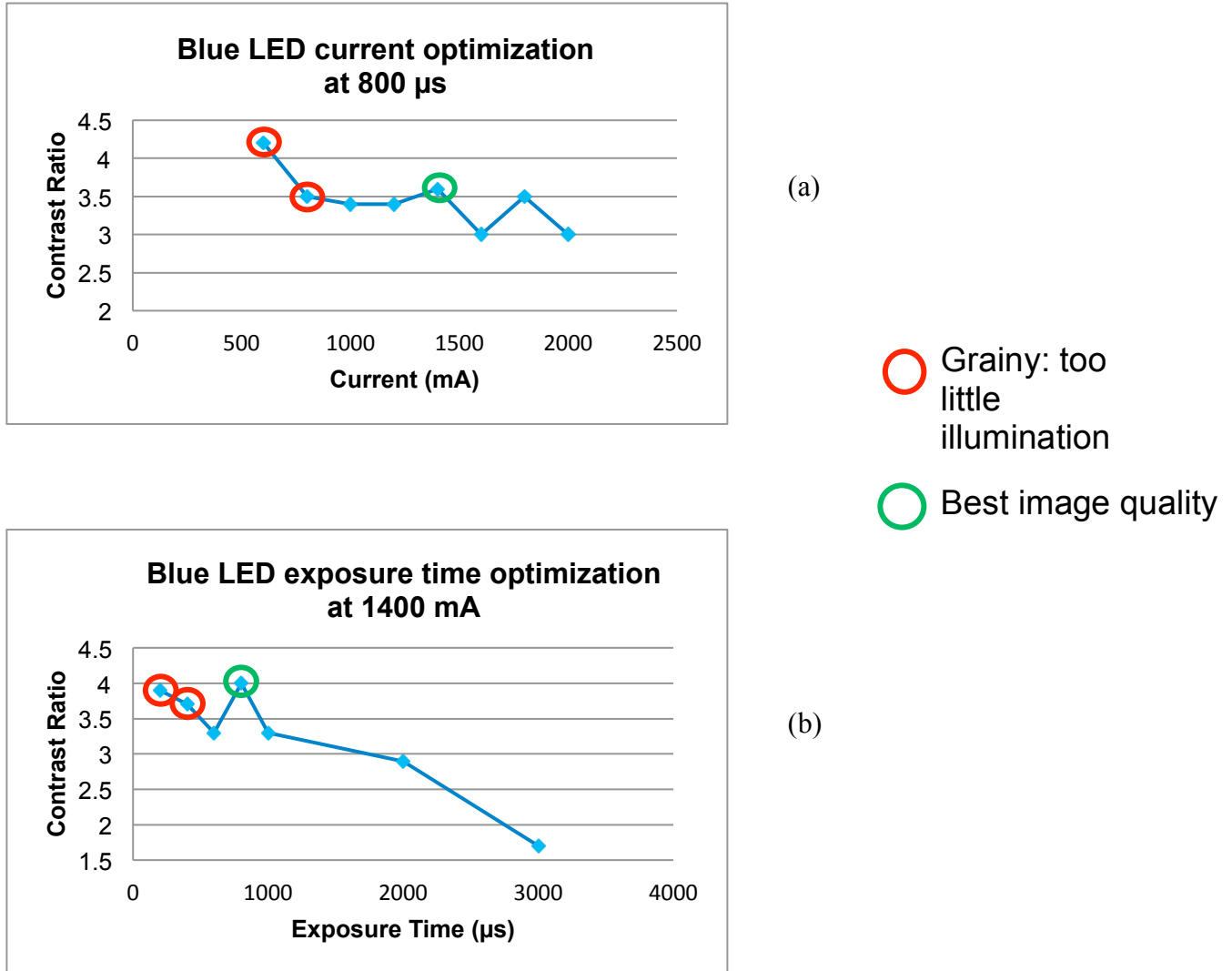


Figure 11. Contrast ratio as a function of LED current (a) and exposure time (b). The optimal current was found to be 1400 mA and the optimal exposure time was found to be 800  $\mu\text{s}$ .

By capturing images of the resolution target under these illumination settings and generating pixel-profile lineouts in order to determine the contrast ratio, it was determined that the optimal current setting at an exposure time of 800  $\mu\text{s}$  was 1400 mA while the optimal exposure time at a current of 1400 mA was 800  $\mu\text{s}$ . Although during both optimization operations, illumination settings at the lower end of the tested ranges produced similar or higher contrast ratios, many of the images captured under these settings were grainy due to insufficient illumination.

## 5. Imaging of 0.5- $\mu\text{m}$ microspheres and defects

After optimization operations were performed, 0.5- $\mu\text{m}$ -diameter polymer microspheres<sup>6</sup> were imaged as an independent assessment of the resolving power of the microscope. These microspheres were prepared upon standard microscope slides. Images of these microspheres were captured, and it was found that in order to view the microspheres clearly, the exposure time had to be increased to 1500  $\mu\text{s}$ . This may have been because the microspheres contain a shell that is relatively thick compared to the lines on the resolution target, requiring stronger illumination in order to be viewed. Under these conditions, the 0.5- $\mu\text{m}$ -diameter microspheres were resolvable. This was further confirmed by the fact that two of the spheres, which were located side by side, could be easily distinguished from one another.

It was determined that, according to the pixel-to-micron conversion scale (7.9 pixels/ $\mu\text{m}$ ), the diameter of each microsphere appeared to be much larger than 0.5  $\mu\text{m}$ . This was a result of Fresnel diffraction, which produces a circular diffraction pattern, making the objects appear much larger than they actually are. Therefore, it was determined that the exact location of the microsphere was somewhere within the center of the diffraction pattern. Figure 12 shows images of the microspheres, which were captured by the digital microscope and then analyzed using Matlab software to determine the actual location of the microsphere. Image (a) shows the original image of the microspheres. The black square within the image indicates the portion of the image that was extracted to produce image (b). Image (b) shows a light intensity map of the microspheres, in which a color gradient is used to show differences in light intensity across the image. The areas with lower light intensity indicated the presence of an object. The black square within image (b) indicates the single microsphere that was extracted to produce image (c). Image (c) shows a re-scaled light intensity map of the single microsphere and the diffraction

surrounding it. The white square indicates the exact location of the microsphere.

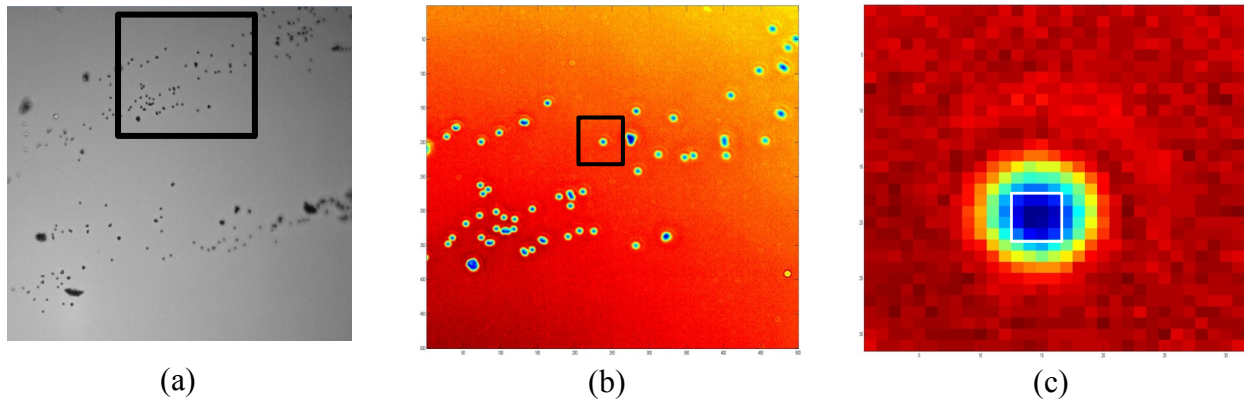


*Figure 12. Images of microspheres taken by the digital microscope and analyzed using Matlab. Image (a) shows the original image, taken with the blue LED and a 40x objective. Image (b) shows a light intensity map of a portion of the original picture. Image (c) shows a re-scaled light intensity map of a single microsphere from the original image (from Ref. 7).*

The ability of the digital microscope to resolve defects upon the surface of a CH cryo shell was then tested using the same Matlab analysis method. Figure 13 shows images of the CH cryo shell that were taken with a blue LED, a 40x objective, a current of 1400 mA, and an exposure time of 800  $\mu$ s. Image (a) shows the original image of the CH cryo shell, containing several defects upon its surface. The black square within the image indicates the portion of the image that was extracted to produce image (b). Image (b) shows a light intensity map of the defects. The black square within image (b) indicates the single defect that was extracted to produce image (c). Image (c) shows a re-scaled light intensity map of the single defect and the diffraction surrounding it. Upon analyzing these defects, it was found that, like the 0.5  $\mu$ m diameter microsphere, one particular defect contained a 4 $\times$ 4 pixel region within its center (shown by the white square). Therefore, according to the pixel-to-micron conversion scale, it was determined that this defect had an approximate diameter of 0.5  $\mu$ m, demonstrating that, under optimized conditions, the digital microscope was able to resolve 0.5  $\mu$ m diameter defects, within a room temperature setting.

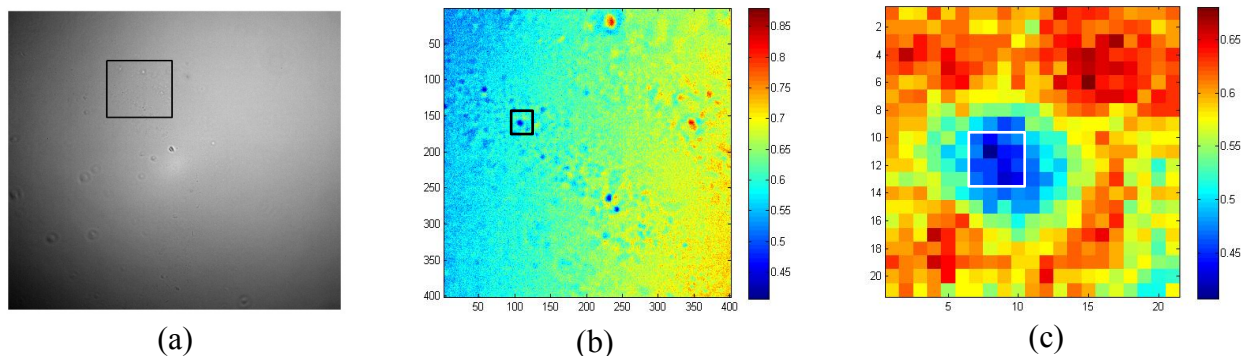


*Figure 13. Images of defects upon the CH cryo shell taken by the digital microscope and analyzed using Matlab. Image (a) shows the original image, taken with a blue LED and a 40x objective. Image (b) shows a light intensity map of a portion of the original picture. Image (c) shows a re-scaled intensity map of a single defect from the original image (from Ref. 7).*

## 6. Discussion

The digital microscope was able to demonstrate a resolving power of  $0.5\ \mu\text{m}$  with polymer microspheres and defects on the surface of a CH cryo shell. Additionally, it was determined that the optimal working conditions for the digital microscope utilized a 40x objective and a blue LED, with a current of 1400 mA, and an exposure time of  $800\ \mu\text{s}$ . These conditions produce the optimal resolving power ( $\sim 0.5\ \mu\text{m}$ ) for the digital microscope in a room temperature environment for a US Air Force Resolution Target.

However, it should be noted that different working conditions might be required for certain operations. For example, in order to view polymer microspheres, the LED's exposure time needed to be increased. Additionally, the working conditions may need to be adjusted in order to view CH cryo shells that are filled with DT fuel. The digital camera may also respond to the cryogenic environment and vacuum pressure within the cryostat differently than it does to the room temperature environment in which it was optimized. Its working conditions may need to be

adjusted according to the nature of the defects that it is viewing. Additionally, although the 40x objective was determined to provide the optimal magnification in order to view submicron defects, it also contains a much smaller depth of field than objectives with lower magnification. Therefore, the camera is only able to focus on a small portion of the target surface. Future work may be required to overcome these limitations and allow the camera to focus on larger portions of the target. Furthermore, because simply viewing target defects from the side has proven to be difficult due to the curvature of the target, a more efficient method for measuring the height or depth of target defects may need to be developed.

## **7. Acknowledgements**

I would like to thank Dr. Craxton for providing me with the wonderful opportunity to participate in the LLE Summer Research Program and conduct this research project. I would also like to thank my advisor, Roger Janezic, for all of his guidance throughout this process. Additionally, I would like to thank Dustin Comfort for his help in mechanical assembly, operational assistance, and the Matlab analysis, Dave Weiner for his optical engineering guidance, Mark Wittman for his microscope guidance and for supplying the microscope parts and the LED diodes, Larry O'Heron for his guidance with the CCD camera and its control interface, Michael Koch for his guidance with the FTS #2 system and cryogenic DT targets, Sal Scarantino for his help with mechanical assembly and for supplying the motion stages, Chad Fella for his guidance with target characterization and the target positioner, Vinitha Anand for her guidance with the LED and CCD camera synchronization equipment, Brian McIntire for supplying the polymer microspheres, and Sam Morse for his guidance with my final presentation.

## 8. References

- <sup>1</sup>R.S. Craxton et al., “Direct-Drive Inertial Confinement Fusion: A Review.” *Physics of Plasmas* 22, 110501 (2015).
- <sup>2</sup>T.C Sangster et al., “Cryogenic DT and D<sub>2</sub> Targets for Inertial Confinement Fusion.” *Physics of Plasmas* 14, 058101 (2007).
- <sup>3</sup>“Chapter 1: CTHS Overview,” *Cryogenic Target Handling System Operations Manual, Volume IV – CTHS Description* (LLE) 1, 3 (2004)
- <sup>4</sup>R. Janezic, private communication
- <sup>5</sup>R. Janezic et al., (2016, June). “Planning meeting for High School Summer Student Project involving an FTS #2 Digital Microscope for Defect Evaluation,” presentation at High School Summer Student Preparation Meeting.
- <sup>6</sup>Thermo Fisher Scientific, Waltham, Massachusetts, 02451
- <sup>7</sup>D. Comfort, private communication